Universität Hamburg

DER FORSCHUNG | DER LEHRE | DER BILDUNG

# Construction of a novel strontium quantum simulator

Dissertation
zur Erlangung des Doktorgrades
an der Fakultät für Mathematik, Informatik und Naturwissenschaften
Fachbereich Physik der Universität Hamburg

vorgelegt von

**Meny Menashes**

Hamburg
April 2025

**Gutachter/innen der Dissertation:**

Prof. Dr. Ludwig Mathey
Dr. Guillaume Salomon

**Zusammensetzung der Prüfungskommission:**

Prof. Dr. Ludwig Mathey
Prof. Dr. Henning Moritz
Prof. Dr. Ralf Riedinger
Dr. Christoph Becker
Dr. Guillaume Salomon

**Vorsitzende/r der Prüfungskommission:**

Prof. Dr. Ludwig Mathey

**Datum der Disputation:**

13.05.2025

**Vorsitzender des Fach-Promotionsausschusses PHYSIK:**

Prof. Dr. Markus Drescher

**Leiter des Fachbereichs PHYSIK:**

Prof. Dr. Wolfgang J. Parak

**Dekan der Fakultät MIN:**

Prof. Dr.-Ing. Norbert Ritter

## Acknowledgments

When I moved to Germany at the end of 2021, I did not know the amount of effort it would take to build a machine of this capacity in three and a half years. Through that time, I have learn many new aspects of physics that were only known to me theoretically, and I have never designed and constructed them to be applicable for cooling and trapping atoms. This journey was full of new aspects of fundamental experimental physics, building tools that are now being used in our laboratory. For these reasons, I would like to thank first my supervisor, Guillaume Salomon, who showed me how experimental work is done and contributed to my understanding of the physics of ultracold atoms and particularly strontium. I am sincerely grateful for his thorough review of my thesis and his valuable input on my writing. Although crafting the dissertation was challenging for me, I am sure that carefully examining every aspect was not easy for him either. I would like to thank Henning Moritz, who, almost four years ago, responded to my email and gave me the opportunity to leave my country and travel to Hamburg. It was a great honor to have discussions with him that were not always physics-related but helped me profoundly. I want to thank my dear colleague Leon Schäfer, with whom I shared an office and who helped me with german language barriers when I could not understand specific terms. To my other colleague Thies Plaßmann, who is doing an amazing job holding the lab together, and I admire his work ethic, coming over the weekend to do measurements at the same time I was writing my thesis. I thank Cesar Cabrera, with whom I had many a fruitful discussion and was able to explain things to me in the most basic way possible. To Benjamin Abeln, Jose Antonio Vargas, Rene Henke, and Hauke Biss, I thank you for helping me with my corrections on the thesis and for giving me feedback when I needed. I want to thank the entire support of the CUI, especially Jutta Voigtmann, who gave me a bit more air to breathe and was very understanding of my situation last year. I would like to thank the support of the workshop and Stephan Fleig, as well as the purchasing department, with Melanie Grundner. Both of them assisted me when it came to building new elements and ordering parts for our experiment. Finally, I would like to thank my family, my mom, dad, and sister Hanna, David, and Maayan, for their support, and to Alina, thank you for being there for me with love and care.

# Abstract

This thesis details the design and construction of a novel quantum simulator platform using ultracold strontium atoms. We establish key experimental infrastructure—including a high-flux atomic source, an ultra-high vacuum environment, and a cost-effective laser delivery system—to manipulate strontium's internal degrees of freedom. These techniques were developed for cooling and trapping all four stable isotopes, enabling diverse investigations into both bosonic and fermionic physics.

Our experimental approach begins with a blue magneto-optical trap (MOT) operating on the broad ${}^1S_0 \rightarrow {}^1P_1$ transition at 461 nm, which efficiently captures and cools thermal atoms from a strontium oven. The atoms are subsequently transferred to a red MOT based on the narrow intercombination line at 689 nm, where precise frequency modulation and spectral broadening techniques allow us to achieve temperatures below $1\,\mu$K.

Central to the simulator's capabilities is the integration of a 3D accordion lattice that provides dynamic control over lattice spacing. The lattice in the vertical gravity direction design and construction is described to give an overview of its confinement efficiency. Specifically, the realization of a 2D trap is needed to study spin models in reduced dimensionality. Our approach involves a single-atom imaging setup enabled by a high numerical aperture objective microscope and a single-photon camera. This platform allows us to probe many-body phenomena at the single-atom level.

To accommodate spin detection with our microscope, we introduce an optical Stern-Gerlach scheme to spatially resolve the atomic nuclear spin during free-fall. This technique can help engineer a spin-dependent potential and leverage the $SU(N > 2)$ symmetry of ${}^{87}$Sr for exploring the interplay between magnetism and interactions within a Fermi-Hubbard model framework.

# Zusammenfassung

Diese Dissertation beschreibt das Design und den Aufbau einer neuartigen Plattform für Quantensimulationen mit ultrakalten Strontiumatomen. Wir entwickeln zentrale experimentelle Komponenten – einschließlich einer Hochfluss-Atomquelle, eines Ultrahochvakuum-Systems und einer kosteneffizienten Laserstrahlführung – um die inneren Freiheitsgrade von Strontium gezielt zu kontrollieren. Die entwickelten Methoden ermöglichen das Kühlen und Einfangen aller vier stabilen Isotope und eröffnen damit vielseitige Untersuchungen sowohl in der bosonischen als auch in der fermionischen Physik.
Der experimentelle Ablauf beginnt mit einer blauen magneto-optischen Falle (MOT), die auf dem breiten Übergang ${}^1S_0 \rightarrow {}^1P_1$ bei 461 nm basiert und thermische Atome effizient aus einem Strontiumofen einfängt und vorkühlt. Anschließend erfolgt die Überführung in eine rote MOT auf der schmalen Zwischenzustandslinie bei 689 nm. Durch präzise Frequenzmodulation und spektrale Verbreiterung werden Temperaturen unterhalb von $1\,\mu$K erreicht.
Ein zentrales Element des Simulators ist die Integration eines dreidimensionalen „Accordion"-Gitters, das eine dynamische Kontrolle des Gitterabstands erlaubt. Der Aufbau und die Konstruktion des vertikalen Gitters entlang der Gravitationsrichtung werden beschrieben, um die Effizienz der Einschlussbedingungen darzustellen. Insbesondere ist die Realisierung einer zweidimensionalen Falle entscheidend, um Spinmodelle in reduzierter Dimensionalität zu untersuchen. Unser Ansatz umfasst ein Einzelatom-Bildgebungssystem, bestehend aus einem Große NA-Objektivmikroskop und einer Einzelphotonenkamera. Diese Plattform ermöglicht es, Vielteilchenphänomene auf der Ebene einzelner Atome zu untersuchen.
Um die Spindetektion mit dem Mikroskop zu ermöglichen, führen wir ein optisches Stern-Gerlach-Verfahren ein, das die räumliche Aufspaltung des nuklearen Spins während des freien Falls erlaubt. Diese Technik kann dazu verwendet werden, spinabhängige Potentiale zu erzeugen und die $SU(N > 2)$-Symmetrie von ${}^{87}$Sr auszunutzen, um das Zusammenspiel von Magnetismus und Wechselwirkungen im Rahmen des Fermi-Hubbard-Modells zu erforschen.

# Contents

# Chapter 1

# Introduction

At the turn of the 19th century, when theories of atomic particles began raising many questions, physicists started to doubt the classical models of the time. It soon became apparent that nature is governed not by classical mechanics but by quantum principles. This paradigm shift led to groundbreaking theoretical developments—from Enrico Fermi's quantum statistical model [1] to Dirac's equation and the discovery of Bose-Einstein condensation (BEC) [2, 3]. Although early technology could not fully probe the quantum behavior of matter, several breakthrough phenomena in the latter half of the 20th century—such as superconductivity, superfluidity, and the quantum Hall [4, 5] effect—laid the foundation for our modern understanding of quantum phases. At the end of the 20th century, the emergence of ultracold atoms provided direct evidence of fundamental quantum states. Experiments, such as the observation of Bose-Einstein condensation in sodium atoms [6] and the realization of quantum degenerate Fermi gases [7] have confirmed key aspects of many-body quantum theory and complemented established frameworks like BCS theory [8, 9].

Fermions, the building blocks of everyday materials, have attracted wide interest from understanding the behavior of neutron stars and quark-gluon plasmas to efforts in developing a new standard model. Recently, the focus has shifted toward condensed matter physics, where designing materials with tailored properties and novel phases remains a central challenge. In conventional solid-state systems, directly observing the real-time dynamics of individual electrons is highly challenging. The electrons are tightly coupled to a fixed lattice of ions, and strong electron-electron correlations give rise to complex collective behavior. These factors, in combination with high-energy scales, render the direct imaging of single-electron motion, or even their spin dynamics, extremely difficult using standard experimental techniques. Ultracold atomic systems and specifically quantum gases, offer much lower energy scales with enhanced tunability over interaction strengths and deterministic spatial arrangements. These factors allow for the direct observation of individual particle dynamics and offer a promising alternative for simulating elaborate quantum systems [10].

For instance, ultracold atomic simulators can implement the Fermi-Hubbard model [11], which captures phenomena such as Mott insulating behavior and antiferromagnetic ordering at low temperatures. Other theoretical models, like the transverse Ising model [12], have been invoked to describe exotic disordered states, such as spin glasses [13]. Moreover, the use of magnetic fields to shift the scattering length via Feshbach resonances [14, 15] has enabled studies of the BEC-BCS crossover [16] in bulk systems.

Combined with high-resolution microscopy for single atom and spin detection [17] and

dynamically controlled tweezer arrays for local addressing [18], atomic quantum simulators provide a powerful tool for exploring many-body phenomena. In our system, we harness these techniques by integrating a 3D accordion lattice with a tweezer array. This configuration enables spin-resolved detection at the single-atom level and allows for the precise engineering of lattice geometries.

Choosing an atomic species is a story of its own, as it defines the range of physical phenomena that can be explored. Early quantum gas experiments relied on alkali elements due to their high neutral abundance, optical cooling transition, and closed cycling transitions. The first reason offers cost-efficient experiments, while the other two have the advantage of using commercially available lasers to send many photons, creating scattering events with a low probability of decay into unwanted states and facilitating efficient cooling and trapping. However, with the tremendous improvements in laser technology, research groups worldwide have extended ultracold experiments to a wider variety of elements. For instance, Dysprosium, a rare-earth element, has the highest magnetic moment of all other atoms, making it ideal for studying dipole-dipole interaction [19]. Other exotic metals, such as mercury (Hg) [20], have a large nuclear charge that enables studies of charge-parity-time (CPT) violations via electric dipole moment measurements [21]. In this thesis, we focus on strontium, an earth-alkali atom that offers a narrow-line cooling transition and metastable energy levels with lifetimes exceeding 100 seconds. These unique properties and others underscore why strontium is an excellent candidate for quantum simulation and computation.

## 1.1 Energy and length scales in ultracold systems

In many-body quantum systems, the interplay between energy and length scales fundamentally determines the observable phenomena. Two such platforms are solid-state materials with atoms being tightly bound to each other, and ultracold gases where temperatures are near absolute zero. In most ultracold gas experiments, the particles are remarkably isolated, while being almost immobilized by their low kinetic energies, which can be tuned and precisely measured. Operating in a low-temperature regime where thermal fluctuations are virtually eliminated makes them an ideal platform for the observation of quantum many-body phenomena, for example, coherent dynamics [22]. Unlike in rigid matter, where the fierce interactions and the structure quantum nature create interesting properties such as superconductivity and insulation [23]. These effects and more are desirable, but extremely difficult to study, which is why one can use quantum gases to simulate these phases. To see why this is the case, we start with a classical gas at room temperature ($T = 300\,\mathrm{K}$). Assuming a simple Maxwell-Boltzmann distribution, we can find that the mean velocity of the ensemble is:

$$\langle v \rangle = \sqrt{\frac{3k_B T}{m}}, \tag{1.1}$$

where $\langle v \rangle$ is the mean particle velocity, $m$ is the particle mass, and $k_B$ is the Boltzmann constant. By plugging in some numbers, we can see that the velocities of the particles are in the order of hundreds of meters per second. By using well-known cooling and trapping techniques [24], these gases can become slow enough to be imaged many times with fairly simple cameras and optics. In contrast to solid-state materials, where the electrons in the bands set the energy, with characteristic energies in the range of meV to eV. This corresponds to temperatures in the hundreds to thousands of Kelvin, meaning that imaging dynamics of

| Parameter | Condensed Matter | Ultracold Atoms |
|---|---|---|
| Temperature (Energy) | 100K - 1000K (meV-eV) | nK – $\mu$K (peV-neV) |
| Interparticle Spacing | $\sim$ Angstroms ($\sim$0.1 nm) | $\sim$ Micrometers ($\sim$1–10 $\mu$m) |
| Dynamics Timescale | Femtoseconds to picoseconds | Milliseconds to seconds |
| Tunability | Fixed lattice constants | Dynamical, tunable |
| Imaging Techniques | Indirect (transport, scattering) | Direct (quantum gas microscopy) |

Table 1.1: Comparison of Energy and Length Scales between Condensed Matter and Ultracold Atomic Systems

electron-electron interactions is done at the short times scales (femtoseconds to picoseconds), and thermal fluctuations at room temperature are significant. In addition to the significantly faster dynamics, the characteristic length scale of crystalline solids, defined as the distance between neighboring atoms or ions, is typically on the order of a few angstroms and remains untunable. The rapid dynamics and elevated energy scales may obscure the fine structures of many-body interactions, impeding observation of quantum phase transitions. Going back to ultracold atoms, temperatures are routinely brought down to the nanoKelvin to microKelvin range, and the characteristic interparticle separation reaches the micrometer scale. Under these conditions, the quantum behavior can be explored and tuned to create novel many-body phenomena of these degenerate gases. In Table 1.1, we summarized the difference in scales between the two types of systems. By mimicking similar structures of solids but with the ability to image their positions and dynamics with ordinary instruments (microscopes and cameras), we can uncover the fundamental physics behind these quantum systems.

### 1.1.1 Quantum gas of strontium

Having established the stark contrast between the energy and length scales in ultracold atoms and those in conventional condensed matter systems, we now turn our attention to the emergence of quantum behavior in degenerate gases and specifically in strontium. At the heart of this transition is the thermal de Broglie wavelength,

$$\lambda_T = \sqrt{\frac{2\pi\hbar^2}{mk_BT}}\ ,\ \rho_{\mathrm{PSD}} = n\lambda_T^3 \tag{1.2}$$

which characterizes the spatial extent of an atom's wavefunction. As the temperature decreases, the phase-space density $\rho_{\mathrm{PSD}}$ increases and can become comparable to or exceed the average interparticle separation. In Equation 1.2, $\hbar$ is the reduced Planck constant, and $n = N/V$ is the density of the gas. In the regime where the phase-space density is on the order of unity, the overlap of atomic wavefunctions leads to behavior governed by quantum statistics, which is expressed by the momentum and spatial distribution as:

$$n(\mathbf{r},\mathbf{p}) = \frac{1}{e^{H(\mathbf{r},\mathbf{p})/(k_BT)} + \eta}, \tag{1.3}$$

Here $H(\mathbf{r},\mathbf{p})$ is the Hamiltonian of the system, with $\eta = -1$ for bosons, $\eta = +1$ for fermions and zero for classical gas. This density divination from the classical functional form ($\eta = 0$ ) marks the onset of quantum degeneracy, where the atoms begin to exhibit collective quantum phenomena, such as Bose-Einstein condensation [25, 6] and Fermi degeneracy [7]. These two

options can have distinctly different distribution shapes, which depend on the spin degree of freedom. Fermions, which possess half-integer spin $\hbar/2$, and bosons, characterized by integer spin $\hbar$, exhibit intrinsically different behaviors. Although spin effects are not apparent in everyday phenomena, cooling an atomic ensemble reveals their quantum nature governed by the spin-statistics theorem [26]. At these ultralow temperatures, the gas wavefunction evolves along different trajectories based on spin. Bosons, whose wavefunctions are symmetric, enjoy being in the same quantum state and tend to condense into the lowest energy state [25, 6]. As a macroscopic number of atoms condense into the ground state, they form a state of matter known as a Bose-Einstein condensate (BEC). The characteristic temperature at which these quantum phase transitions occur is referred to as the critical temperature and is given by

$$k_B T_C \sim \frac{\hbar^2}{m} n^{2/3} \tag{1.4}$$

The temperature here is quite similar to the Fermi gas critical temperature, but their properties are very different. For fermions, the antisymmetric nature of the wavefunction prevents identical particles from occupying the same state, forcing them to fill higher energy levels up to the Fermi energy $E_F$. This principle underlies electron degeneracy pressure in stars [27] and Pauli blocking in Fermi gases [28]. In fermions, the temperature of the cloud is normalized by the Fermi temperature $T_F = E_F/k_B$, and deviation from the thermal behavior usually occurs at $T/T_F < 0.5$ [29]. As an alkaline earth element, strontium was not the first pick for inducing quantum degeneracy. Nevertheless, the first observation of BEC in strontium atoms was demonstrated in 2009 by both the Innsbruck and Rice research groups [30, 31]. In both cases, the isotopes they used were $^{84}$Sr, and they measured temperatures for these phase transitions at $T_C \approx 0.4$ $\mu$K with around $\sim 0.5 \times 10^6$ atoms. Their accomplishment paved the way for degeneracy with the only stable fermion of strontium is $^{87}$Sr, and a year after the realization of the first $^{84}$Sr BEC, a degenerate Fermi gas was also achieved by the Rice group [32]. In fermions, the temperature scales with the Fermi energy, and the group measured $k_B T/E_F \approx 0.25$, with a signature Fermi-Dirac velocity distribution, which is the onset of a degenerate Fermi gas. As the complete theory of degenerate quantum gases is extensive (see [33, 34] for Bose gases and [35, 36] for Fermi gases), our focus is on showing why strontium is a good candidate for quantum simulations. By combining the intrinsic properties of strontium with a high-resolution quantum gas microscope, the reader will see the kind of many-body physics to be explored with strontium quantum degenerate gases.

## 1.2 Quantum Simulation

A key motivation for building a quantum simulator is captured in Richard Feynman's famous remark [37]:

> *"Nature isn't classical, dammit, and if you want to make a simulation of nature, you'd better make it quantum mechanical, and by golly, it's a wonderful problem because it doesn't look so easy."*

Nearly fifty years later, this insight has spurred global research into constructing large-scale quantum machines. To see why simulating a quantum system is so challenging, we can think of the following scenario. Taking an ensemble of half-integer spin particles (Fermions), the Fock space dimensionality with each addition of a particle increases by a factor of two; if we have a

2D lattice of $N \times N$ particles, then the total possible configuration is $2^{N^2}$. Setting $N = 20$, the computational power needed to simulate all these spins is impossible with any known classical computer. Since Feynman's theoretical idea quantum simulation has enabled the estimation of the ground state of water molecules [38], the discovery of novel phases such as spin-liquids [39], and the demonstration of quantum processors that outperform classical systems by executing tailored quantum algorithms exponentially faster [40, 41]. Specifically in neutral atoms, digital quantum platforms have low infidelities (below 0.5%) [42], local controllability over the entire system, and rapid state preparation and read-out times (below 10 $\mu$s for Rydberg qubits) [43]. Such quantum systems have been suggested to solve optimization problems, such as the maximum independent set problem [44], through techniques like the Quantum Approximate Optimization Algorithm (QAOA) and quantum annealing [45]. In this work, we focus on the analog aspect of ultracold atoms, which functions as a macroscopic quantum simulator. By arranging the spin particles in specific orientations and introducing interactions, a quantum simulator can discover novel phases of matter. A good example is the supersolid; this state of matter was theorized back in the 1960s, but without any experimental proof, that is, until 2019 when several ultracold atomic experiments showed its existence in a quantum gas [46, 47]. Moreover, analog quantum simulators are appropriate candidates for applications in domains such as material science, particularly in the study of superconductivity through the phenomenon of superfluid emergence [48]. In the context of superconductivity, one needs to be able to replicate the natural periodic structure that exists in condensed matter. Optical lattices are clear candidates to form conditions similar to those in solid superconductors [49], but generating them and observing the atoms inside the lattice requires optical accessibility. This is possible with quantum gas microscopes as a tool for observing ultracold atoms. Having high optical resolution that can distinguish single atoms and simultaneously create the trapping potential where they reside, they become a key feature in quantum simulators [50].

### 1.2.1 Quantum gas microscopy

Quantum gas microscopy has emerged as a groundbreaking technique that enables the real-space, single-atom resolution imaging of ultracold quantum gases in optical lattices [51]. Unlike early distractive methods such as electron microscopy [52], which, despite their atomic-scale resolution, suffer from invasiveness and are typically limited to high-density crystalline samples, optical imaging techniques exploit specific atomic transitions to localize atoms in optical lattices.

In quantum gas microscopy, the resolution is determined not by the physical size of an atom (typically on the order of the Bohr radius, $a_0 \approx 5.29 \times 10^{-11}$ m), but rather by the wavelength of the light used to probe the atomic transition. This wavelength, often in the visible or near-ultraviolet range, sets the diffraction-limited resolution of the imaging system. Traditional quantum gas detection methods include momentum and real space imaging, these are fairly simple to implement and require a small number of shots to have single-atom resolution with high fidelity ($> 95\%$) [53]. To reach such high accuracy in detection necessitates first high optical excess, where most microscopes numerical aperture (NA) ranges from $0.4 - 0.9$, depending on their distance from the atom plane.

When trapping atoms in optical lattices, they need to sit near their 3D motional ground state to be individually resolved. This condition is required because at high motional energy states, the scattered light from the atom is less deterministic, and the momentum spread can become on the order of the optical lattice's lowest spacing at half its wavelength [54].

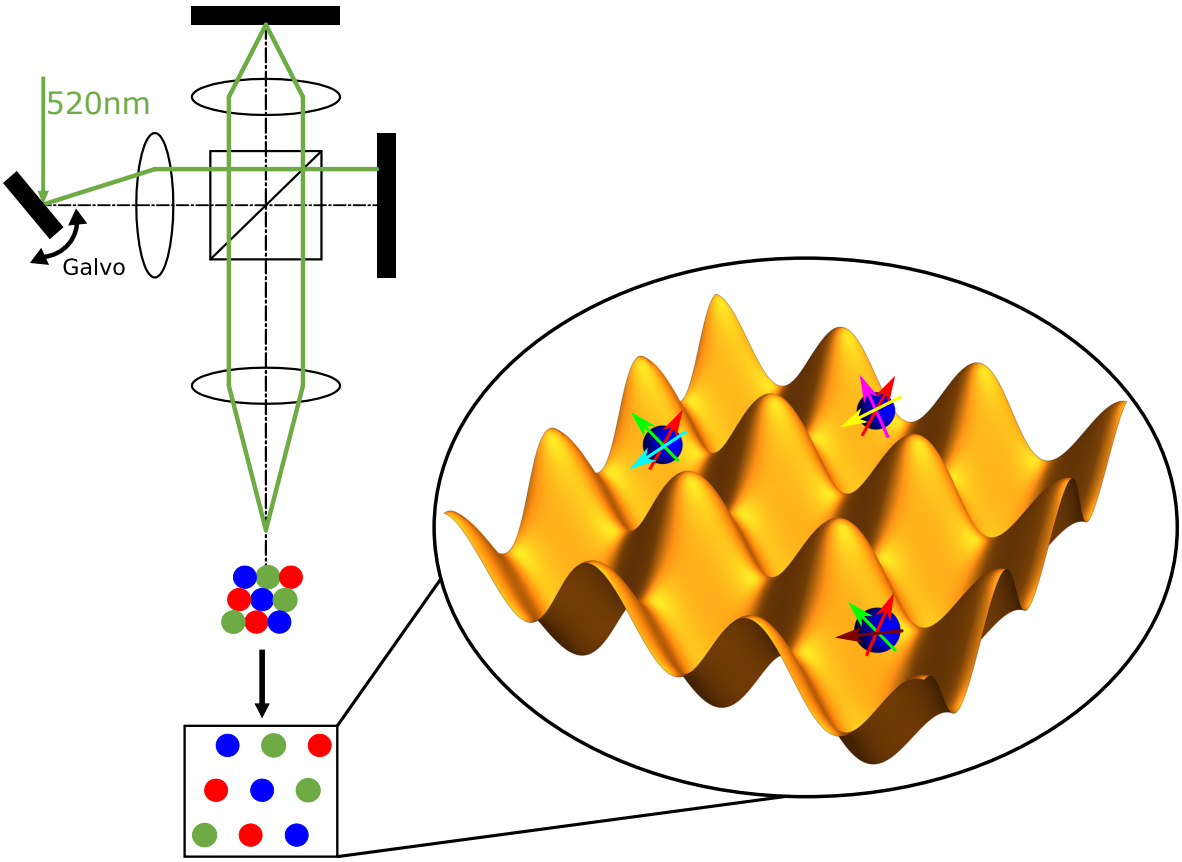


Figure 1.1: Quantum gas microscopy of the $SU(N)$Fermi-Hubbard model. The 520 nm light that enters the microscope can be angled with a galvo mirror, shifting the spacing of the lattice potential. In the circle inset is a 3D illustration of an $SU(N)$ spin model where each site can have up to $N$ different spins (marked by different colors).

The density resolution problem can be mitigated by cooling the atom to degeneracy and pinning the atoms in deep trapping depths. Several other options to obtain a sub-wavelength resolution using a microscope include the use of non-linear atomic response [55], or utilizing the so-called dark state and its interaction with light fields [56]. To characterize the quality of single-atom imaging with a microscope, the point spread function (PSF) method is employed [57]. Meant for fluorescence imaging, this technique is used when one needs to determine the focusing abilities of the imaging system. Specifically in single-atom microscopy, the amount of an atom's fluorescence spreads in space (blurring), and whether we can resolve it from its neighboring particle. Even with high-resolution microscopy, the imaging system PSF is typically on the order of several hundred nanometers, leading to overlap between signals when the interatomic spacing is comparable to the PSF size. This overlap degrades the imaging fidelity and hampers our ability to resolve single atoms. Our solution is creating an optical lattice with a tunable spacing, easing the imaging by increasing the spatial distance between atoms in neighboring sites, making the PSF size much smaller compared to the lattice spacing. By sending a red-detuned optical lattice via the objective, one creates an "egg-carton"-like potential where atoms can be pinned with the optical potential and later expanded for imaging. Referred to as an accordion lattice, we desire to realize such an expanded light trap using a

galvanometer mirror in an optical setup as illustrated in Figure 1.1. The sequence starts with a tightly confined lattice where atoms can tunnel between sites, and contact interaction happens. Afterward, the lattice follows a fast adiabatic expansion, and with higher spacing, the imaging of the atoms takes place. This method, already accomplished by the Harvard group by transmitting the lattice through the microscope [58], demonstrates lattice spacing at the diffraction limit. By expanding the lattices and taking fluorescence images, the group was able to reach high-resolution pictures with fidelities above $> 99\%$ single-atom in a lattice. The limitation of their imaging technique is its inability to spin-resolve the atom in the lattice. For our strontium simulator, releasing the atoms from the enlarged lattice, we can apply a spin-dependent force scheme (like optical Stern-Gerlach), where using the microscope can resolve the 2D density filling, which is what one wants to be able to study many-body physics with high magnetic ordering.

### 1.2.2 Exploring many-body physics at the single-atom level

Conventional condensed matter experiments, such as those performed on high-temperature superconductors like YBCO (Yttrium-Barium-Copper-Oxide), probe many-body phenomena at energy scales defined by the atomic lattice, where superconductivity emerges around $T \approx 70\,K$. In contrast, ultracold Bose and Fermi gases operate at temperatures on the order of 200 nK with interparticle separations in the micrometer regime, representing a dramatic 6–7 orders of magnitude difference in energy and length scales. Despite the scale difference, critical behavior and phase diagrams are similar and observed across both platforms. We can see that by considering a unit-less parameter $T_C/T_F$, which is the ratio between the critical and Fermi temperatures. This ratio scales the high density of electrons in a metal (and other systems with fermions), making it a generic parameter, useful for predicting critical changes on the macroscale. Remarkably, by inducing interaction (via Feshbach resonance [59]), a Fermi gas can enter the superfluid phase around $T_C/T_F \sim 0.15$, which is comparable to high-temperature superconductors at $T_C/T_F \sim 0.05$. This fact categorizes Fermi gases as genuine high-temperature superfluids [35], and offers to study quantum phase transitions in a diluted environment without interaction complications. Quantum gas microscopy of Fermi gases is a complementary tool for understanding the underlying mechanism of superconductivity via superfluidity in ultracold gases [60, 48]. Unlike traditional condensed matter probes, which rely on indirect measurements (e.g., transport or scattering experiments), quantum gas microscopy provides the capability to image individual atoms and resolve local correlations in real space. Through the direct visualization of single-atom occupancy and dynamics, access is granted to the many-body correlations that underpin superfluidity and other collective phenomena. Beyond merely imaging individual constituents of a quantum many-body system, microscopes can tightly focus beams to allow for manipulation at the single-particle level. Such local addressing and site-resolved imaging opens the door to more exotic options such as studying strongly correlated materials [61] or testing doping effects and their dynamics compared to solid-state materials [62]. In particular, using the $^{87}$Sr isotope which has a nuclear spin $I = 9/2$ and thus provides $N = 2I + 1 = 10$ nuclear spin states offers a unique opportunity to study magnetism in $SU(N)$ models along with other many-body phenomena. The following subsection discusses these promising experimental proposals in detail.

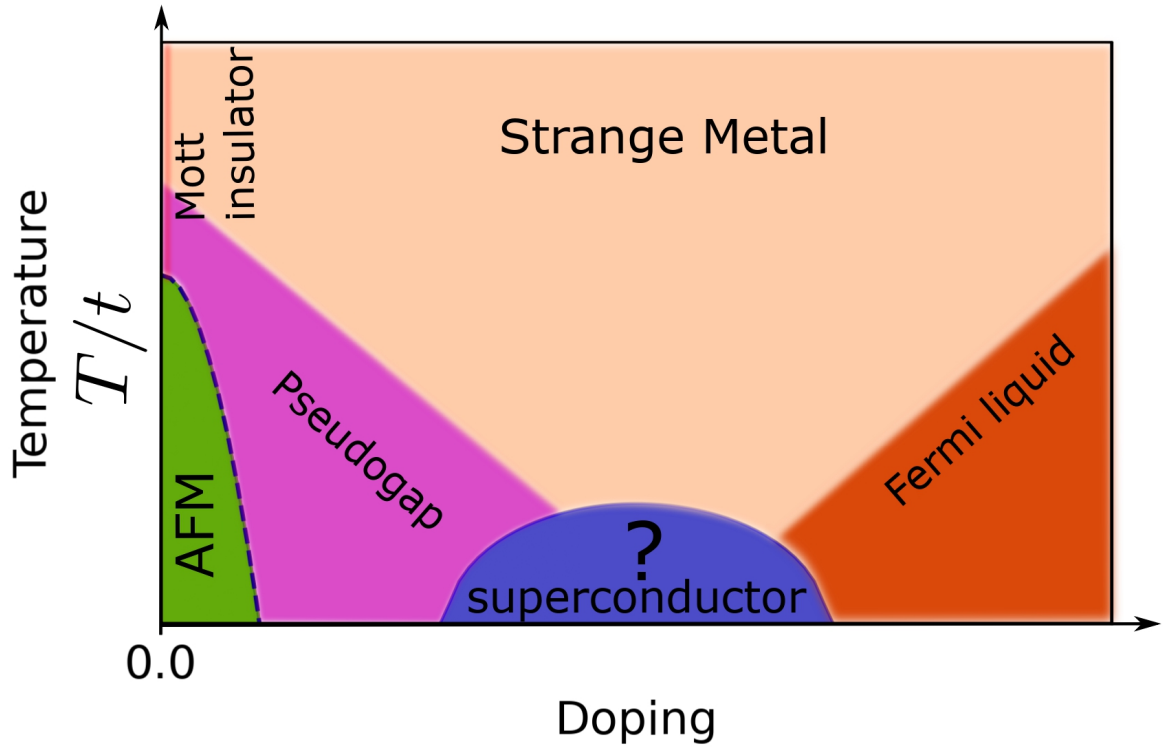


Figure 1.2: Schematic plot of the $SU(2)$ Fermi-Hubbard phase diagram. As doping increases, the system undergoes various phase transitions. Experimental observations have confirmed phases such as the Mott insulator and antiferromagnet at relatively high temperatures. However, superconductivity has not been observed so far(if it exists at all in the single band FHM), likely due to the extremely low temperatures required for its emergence. Note that the domain of each phase is not to scale.

### 1.2.3 The $SU(N)$ Fermi-Hubbard Model

The Fermi-Hubbard model (FHM) in its simplest form is a toy model that aims to study strongly correlated many-body quantum systems, such as electrons in different materials, and how exotic phases of matter can emerge [63]. Originally developed in condensed matter physics to describe the dynamics of electrons in a crystalline lattice [64], the model has become a cornerstone of atomic physics, especially with the advent of quantum simulation using ultracold atoms in optical lattices [11, 65]. These experimental realizations involve loading a degenerate Fermi gas into a periodic potential, where the interplay between atomic tunneling and on-site interactions leads to the emergence of complex quantum phenomena such as magnetism, metal-insulator transitions, and other quantum phases.
The Hamiltonian of the Fermi-Hubbard model is given by:

$$\hat{H}_{FH} = -t \sum_{\langle i,j\rangle,s} \left(\hat{c}^{\dagger}_{i,s}\hat{c}_{j,s} + \text{h.c.}\right) + \frac{U}{2} \sum_{i,s\neq k} \hat{n}_{i,s}\hat{n}_{i,k} + \sum_{i,s} V_i \hat{n}_{i,s} \tag{1.5}$$

Here, $\hat{c}^{\dagger}_{i,s}$ and $\hat{c}_{j,s}$ are the fermionic creation and annihilation operators, respectively, that create or annihilate a fermion with internal state $s$ (e.g., spin or hyperfine state) at lattice

sites $i$ and $j$. These operators obey the standard anticommutation relations, reflecting the fermionic nature of the particles. The parameter $t$ represents the tunneling amplitude, which characterizes the kinetic energy of the fermions as they hop between neighboring lattice sites $\langle i, j \rangle$, while h.c. denotes the Hermitian conjugate. The second term describes the on-site interaction energy, where $U$ quantifies the interactions between two fermions occupying the same lattice site. The number operator $\hat{n}_{i,s} = \hat{c}^{\dagger}_{i,s}\hat{c}_{i,s}$ measures the population of fermions in internal state $s$ at site $i$. The last term is harmonic confinement per site and is tunable by changing the trapping depth in the lattice.
This Hamiltonian highlights the competition between kinetic energy, driven by tunneling, and interaction energy, governed by on-site repulsion. The model can be extended to have $SU(N)$ symmetry by considering alkaline-earth atoms. In these atoms, the decoupling of the electronic and nuclear spin degrees of freedom in the ground state is a consequence of the negligible spin-orbit coupling in low-lying states. This decoupling leads to scattering lengths that are essentially independent of the nuclear spin, thereby endowing the system with an approximate $SU(N)$ symmetry (with $N$ equal to the number of nuclear spin states). In contrast, alkali atoms exhibit strong spin–exchange interactions that render their scattering lengths state-dependent, typically restricting their symmetry to $SU(2)$ [66, 67]. To see the relation to the model, we need to look at the interaction term, which is proportional to the $s$-wave scattering length $a_s$, with the on-site interaction energy given by:

$$U \sim \frac{4\pi\hbar^2}{m} a_s \tag{1.6}$$

where $m$ is the atomic mass. By having an equal scattering length, the atoms interact similarly no matter their spin state. This unique feature of alkaline–earth systems facilitates the exploration of exotic quantum phases and many-body phenomena, as demonstrated in experiments with ultracold ytterbium and strontium [68, 69]. Working with $^{87}$Sr, with its spin-independent scattering length and rich internal structure with up to ten accessible nuclear spin states, allows for the realization of a two-dimensional $SU(N)$ Fermi-Hubbard model with $N \leq 10$. In addition, recent proposals suggest that advanced entropy redistribution schemes could be implemented to create low-entropy regions by isolating a central subsystem while using the surrounding $SU(N)$ mixture as a thermal reservoir [70]. Such strategies offer promising avenues for reaching the low temperatures required to explore magnetic ordering and exotic quantum phases in strongly correlated systems.

Dealing with 2D systems, one of the goals of the FHM is to understand the physics behind high-temperature superconductivity [71]. In the context of FHM, the $N$ parameter gives rise to different kinds of magnetic ordering. We can see that by setting $N = 2$ and looking in systems that have one particle per site, meaning half-filling. Doping the optical lattice, i.e., shifting the on-site atomic density away from half-filling (where the notable Mott insulator phase lives [72]), significantly enriches the resulting phase diagram, leading to the emergence of multiple predicted quantum phases [73]. This behavior arises from the competition between magnetic ordering and contact interactions as the system deviates from half-filling, resulting in phase transitions characterized by diverse ground-state properties. The theoretical phase diagram presented in Figure 1.2 shows that when the normalized temperature ($T/t$) decreases and the doping increases, the antiferromagnetic behavior disappears, and the system enters the pseudogap regime [74]. State-of-the-art experiments in optical lattices under various doping conditions have realized exotic quasi-particles such as Nagaoka polarons in triangular geometries [75] and achieved unprecedented ultralow temperatures [76], albeit primarily within the

framework of the $SU(2)$ Fermi–Hubbard model. The $SU(N)$ fermionic model has already been studied with optical lattices in several groups [77, 78], however, without a microscope. Our goal is to use the $^{87}$Sr high nuclear spin dimension to see the role this enlarged spin symmetry space takes in the interplay between magnetism and the doping particles. As we showed, doping already presents a very exciting phase diagram in $SU(2)$-symmetry, so moving towards high spin dimension, we can reach uncharted territories in $SU(N)$ magnetism.

**$SU(N)$ magnetism and quantum spin models**

Alkaline-earth metals have been proposed as candidates for many quantum spin experiments with high $SU(N > 2)$-symmetry [79, 80, 69]. Owing to their high nuclear spin that decouples from the electronic structure, both $^{173}$Yb and $^{87}$Sr have a ground state with all $m_F$-states having equal scattering length. Essentially, the high spin symmetry $N > 2$ can create an environment where there is no one clear ground state of the system, and the spins can rearrange in a unique formation depending on the value of $N$ [81, 66]. This includes the symmetry breaking of spin order, spin dimerization, and charge-conjugation [82]. Especially interesting is the magnetic ordering, which in the $SU(2)$ Fermi-Hubbard model requires the entropy to be on the same order as exchange coupling between neighboring magnetic moments (usually nearest neighbors) in the lattice. Recently, this experimentally challenging limit was achieved by the Harvard group in a $SU(2)$ F-H square lattice (with $T/t = 0.05$ at $U/t = 8$) [76]. The higher spin dimensionality of $N$ offers prospects to improve compared to alkalies, but it is at least as challenging to reach these values. Studies have shown that the temperature of the lattice can decrease with $N$-dependence [83], and even specific protocols where the higher nuclear spin states store the system heat have been shown to reach lower entropy with numerical simulations [70]. Although promising, the spin entropy required for ordering also decreases with lower spin dimension $N$, so without a proper reshuffling scheme, it is not clear if one can reduce entropy with higher spin symmetry.

## 1.3 Thesis Overview

Many other groups have shown the ability to trap and manipulate all of Sr stable isotopes [84] and still are doing so [85, 86]. Thus, our focus will not be to present a full detailed review of the physical properties of strontium nor how quantum simulators are designed and built, as the theory and experimental results have been firmly established. The main goal of the thesis is to give the reader a clear description of our strontium-based simulator and its capabilities and advantages over other state-of-the-art strontium machines. The thesis starts with a chapter dedicated to the examination of strontium and its intrinsic properties. The focus will be on atomic attributes pertinent to our system, including electronic energy levels, and presenting important optical cooling and trapping transitions. Particular attention will be given to the distinctive hyperfine structure present in the fermion $^{87}$Sr isotope and its magnetic nuclear ground state, which can potentially enhance the study of the $SU(N > 2)$ Fermi-Hubbard model. The second section will present the experimental apparatus with its atomic source, ultra-high vacuum, magnetic coils, and blue laser systems. The blue laser system is fully described both before and after coupling to fiber and delivered around the vacuum and science cell, with a focus on the techniques of frequency stabilization and locking, the Zeeman slower, the 2D MOT, and the 3D MOT. The chapter concludes with an exposition of our repumping system and strategy, which includes the utilization of the magnetically metastable

$^3P_2$ state serving as a reservoir to increase the atom numbers. This is subsequently assessed by their recapture in the blue MOT. In the third chapter, the 689 nm narrow line transition is presented and showcases the different regimes that atoms go through as they are cooled by the red MOT. A layout of the red laser system is given. We report on the final temperature and atom number of the final red MOT of $^{87}$Sr and $^{88}$Sr atoms.

The fourth chapter presents the next step taken as the red MOT ends, where the atomic cloud is transferred to an optical dipole trap we refer to as the dipole reservoir trap. During the procedure, two more beams are applied to the atoms, a highly confined dimple beam and a light-shifting transparency beam. These lights are designed to bring the ensemble to quantum degeneracy through light shielding the atoms inside the dipole trap. The latter section of the chapter will elaborate on the development and analysis of an accordion optical lattice, which will be used to create 2D gases. The 1D vertical lattice's design is crafted and assessed through a combination of simulation and image analysis to determine its optical constraints prior to setting it up on the experimental table and directing it toward the atoms. The final chapter begins with the current status of the machine and gives an outlook on our single-atom imaging and optical Stern-Gerlach technique that can be used for spin detection to study, for example, the $SU(3)$ Fermi-Hubbard model.

# Chapter 2

# Strontium in a nutshell

In this chapter, we will delve into the physical properties of strontium, the atomic species at the heart of this work, and describe how it can be trapped and cooled to form a degenerate quantum gas.

## 2.1 Atomic and nuclear characteristics

Belonging to the alkaline-earth group, Strontium exhibits electronic and nuclear characteristics that are essential for laser cooling and trapping. Positioned in the second group of the periodic table, Strontium, along with other divalent atoms such as Ytterbium (Yb), has two valence electrons. This electronic structure introduces symmetry considerations in the electronic wavefunctions, as opposed to alkali elements such as Lithium (Li) and Potassium (K), which have only one valence electron. In Strontium's two-electron system, the exchange symmetry of these electrons results in two possible solutions for the overall spin wavefunction. These solutions are categorized as singlet (symmetric) and triplet (anti-symmetric) states, which can be expressed as seen below:

$$|\Psi_s\rangle = \begin{array}{c} |\uparrow\uparrow\rangle = |S=1, m_S=1\rangle \\ \frac{(|\uparrow\downarrow\rangle + |\downarrow\uparrow\rangle)}{\sqrt{2}} = |S=1, m_S=0\rangle \\ |\downarrow\downarrow\rangle = |S=1, m_S=-1\rangle \end{array} , |\Psi_a\rangle = \frac{(|\uparrow\downarrow\rangle - |\downarrow\uparrow\rangle)}{\sqrt{2}} = |S=0, m_S=0\rangle \quad (2.1)$$

where $\Psi_s(\Psi_a)$ represents the symmetric (anti-symmetric) wavefunction and $S, m_S$ are the full electronic angular momentum and the magnetic quantum number, respectively (we use the arrow notations $\uparrow, \downarrow$ to represent the spin of each electron). The singlet state corresponds to $S = 0$, while the triplet states correspond to $S = 1$. This splitting into singlet and triplet states is central to the energy level structure as it provides multiple transitions that are exploitable for cooling, excitation, and trapping. These transitions will be discussed further in the next section.

Beyond its electronic configuration, strontium has intriguing nuclear properties. There are four stable isotopes in addition to over 20 unstable ones. Notably, $^{90}$Sr, with a half-life of nearly 30 years, is widely used in medical and nuclear applications due to its radioactive nature and behavior as a bone seeker [87, 88].

| Isotope | Natural Abundance (%) | Atomic Mass (Da) | Statistics | Nuclear Spin ($I$) |
|---|---|---|---|---|
| $^{84}$Sr | 0.56 | 83.913 | Bosonic | 0 |
| $^{86}$Sr | 9.86 | 85.909 | Bosonic | 0 |
| $^{87}$Sr | 7.00 | 86.908 | Fermionic | 9/2 |
| $^{88}$Sr | 82.58 | 87.905 | Bosonic | 0 |

Table 2.1: Properties of stable Strontium isotopes, including their natural abundance, atomic mass, quantum statistics, and nuclear spin [89].

Among the stable isotopes, three are bosonic, with nuclear spin $I = 0$, while $^{87}$Sr is fermionic, possessing a nuclear spin of $I = 9/2$. The total angular momentum $\mathbf{F}$, which arises from the coupling of nuclear spin $\mathbf{I}$ and total electronic angular momentum $\mathbf{J} = \mathbf{L}+\mathbf{S}$, is given by $\mathbf{F} = \mathbf{I} + \mathbf{J}$.

In the singlet ground state ($\mathbf{J} = 0$), the fermionic isotope $^{87}$Sr exhibits $2I + 1 = 10$ hyperfine sublevels, or $m_F$ states.

As shown in Table 2.1, the natural abundance of Strontium isotopes varies significantly, with $^{88}$Sr being the most abundant, making up more than 82%. The abundance of $^{86}$Sr and $^{87}$Sr is nearly an order of magnitude lower, and $^{84}$Sr is even rarer by over two orders of magnitude. These variations in abundance play a crucial role in experimental setups, influencing signal-to-noise ratios during spectroscopy and imaging, especially when working with less abundant isotopes such as $^{84}$Sr or $^{87}$Sr. Differences in isotopic abundance, along with the nuclear and electronic characteristics, affect the number of atoms and, therefore, the phase space density of the cloud under equal experimental conditions. Thus, the choice of isotope is pivotal in optimizing experimental designs, particularly for precision measurements and imaging of low-density samples. In our work, we address these issues by initially loading $^{88}$Sr atom, optimizing the signals we attend to measure, and then moving to other isotopes.

## 2.2 Energy levels scheme and optical transitions

In divalent atoms, the ground state, $^1S_0$, is magnetically insensitive due to the absence of a magnetic dipole moment. For bosonic isotopes, which possess no nuclear spin, this results in a complete lack of hyperfine structure, making the ground state insensitive to magnetic fields via the Feshbach resonances [15]. However, some research groups have successfully induced bound states through optical means, primarily in $^{88}$Sr using the intercombination transition at 689 nm [90].

Contrary to the behavior of atoms interacting through the electron's Bohr magneton $\mu_B$, the fermionic isotope $^{87}$Sr, characterized by a nuclear spin of $I = 9/2$, demonstrates a weak coupling to external magnetic fields as it is proportionally related to the nuclear magneton $\mu_N$. This results in a decreased sensitivity when compared to alkali atoms, differing by approximately $\mu_B/\mu_N \approx 1840$ [91]. As a consequence, separating the hyperfine sublevels in a standard Stern-Gerlach experiment would necessitate magnetic fields on the order of several Teslas. Nevertheless, recent advancements have demonstrated that an optical Stern-Gerlach effect provides an effective means for hyperfine level separation, opening new possibilities in hyperfine-resolved experiments [92].

Due to the different energy level structures arising from the absence (bosonic isotopes) or presence (fermionic isotopes) of hyperfine splitting, the optical transitions of each isotopic

species will be discussed separately in the following sections.

### 2.2.1 Bosonic case ($F = J$)

In bosonic isotopes, two types of transitions are relevant: spin-allowed transitions, such as $^1S_0 \rightarrow {}^1P_1$, and spin-forbidden intercombination transitions, like $^1S_0 \rightarrow {}^3P_J$, each with unique properties.

The spin-allowed transition from $^1S_0$ to $^1P_1$ occurs at a wavelength of 460.8 nm and is often referred to as the "blue" transition. It has a relatively broad linewidth of $\Gamma = 2\pi \times 30.5$ MHz, which makes it suitable for initial laser cooling stages and imaging applications [93]. Atoms excited to the $^1P_1$ state have a short lifetime of just a few nanoseconds, with the vast majority (99.99%) decaying back to the $^1S_0$ ground state. The resulting fluorescence serves as a useful tool for spectroscopy and for stabilizing lasers on the $^1P_1$ transition [94].

However, the blue transition is not close and allows a small fraction of atoms to decay into the $^1D_2$ state. Reported measurements of the associated branching ratio vary between 1:20,000 and 1:50,000 [94, 95, 96, 97][1]. The $^1D_2$ state possesses a significantly extended lifetime, approximately 300 $\mu$s [95]. As a consequence, the cooling rate of these atoms is reduced. One can exploit the intermediate $^1D_2$ state by finding a transition to re-excite the atoms and bring them back to the blue cooling cycle. This approach has been proven successful by [98] and uses the transition to pump atoms in the Zeeman slower (ZS) and will be described briefly in the repumping section.

As they decay via the $^1D_2$, atoms eventually populate the $^3P_J$ triplet states, notably $^3P_1$ and $^3P_2$, with a population ratio of 2:1, respectively. Atoms in the $^3P_2$ state are effectively lost from the cooling cycle and require repumping to re-enter it. Conversely, atoms in the $^3P_1$ state decay back to the ground state with around 20 $\mu s$ lifetime and return to the cooling cycle.

The $5s5p$ manifold, encompassing the $^3P_{0,1,2}$ states, exhibits the LS-coupling structure and provides narrow and ultra-narrow linewidths for intercombination transitions due to dipole selection rules impeding transitions by a single photon [99]. Three key transitions exist between the singlet ground state $^1S_0$ and the triplet states $^3P_J$, each with significant implications in precision measurements and quantum simulations.

The transition $^1S_0 \rightarrow {}^3P_0$, often known as the "clock transition," plays a pivotal role in atomic clocks and quantum information storage [100, 101]. In the absence of a magnetic field, the 698 nm transition is forbidden by both spin exchange and angular momentum conservation, leading to an exceptionally narrow natural linewidth of 1 mHz. This doubly forbidden nature renders the transition accessible only through hyperfine mixing, which allows otherwise forbidden transitions to occur by mixing singlet and triplet characters [102].

Next, the $^1S_0 \rightarrow {}^3P_1$ transition at 689 nm is less restrictive, being forbidden only by electronic spin flip; however, due to spin-orbit coupling, it has a linewidth of "only" 7.4 kHz, which in comparison to alkali metals such as lithium and potassium is three orders of magnitude smaller [103, 104]. This transition is critical for narrow-line cooling, facilitating magneto-optical trapping (MOT) techniques that bring Sr atoms closer to quantum degeneracy, a subject elaborated on in the Red MOT chapter.

Finally, the $^3P_2$ state functions as a "reservoir" where atoms can be stored for extended periods—exceeding 100 seconds—due to its extremely low decay rate to the ground state.

[1] The discrepancy between measurements of the blue transition decay channel remains an open question

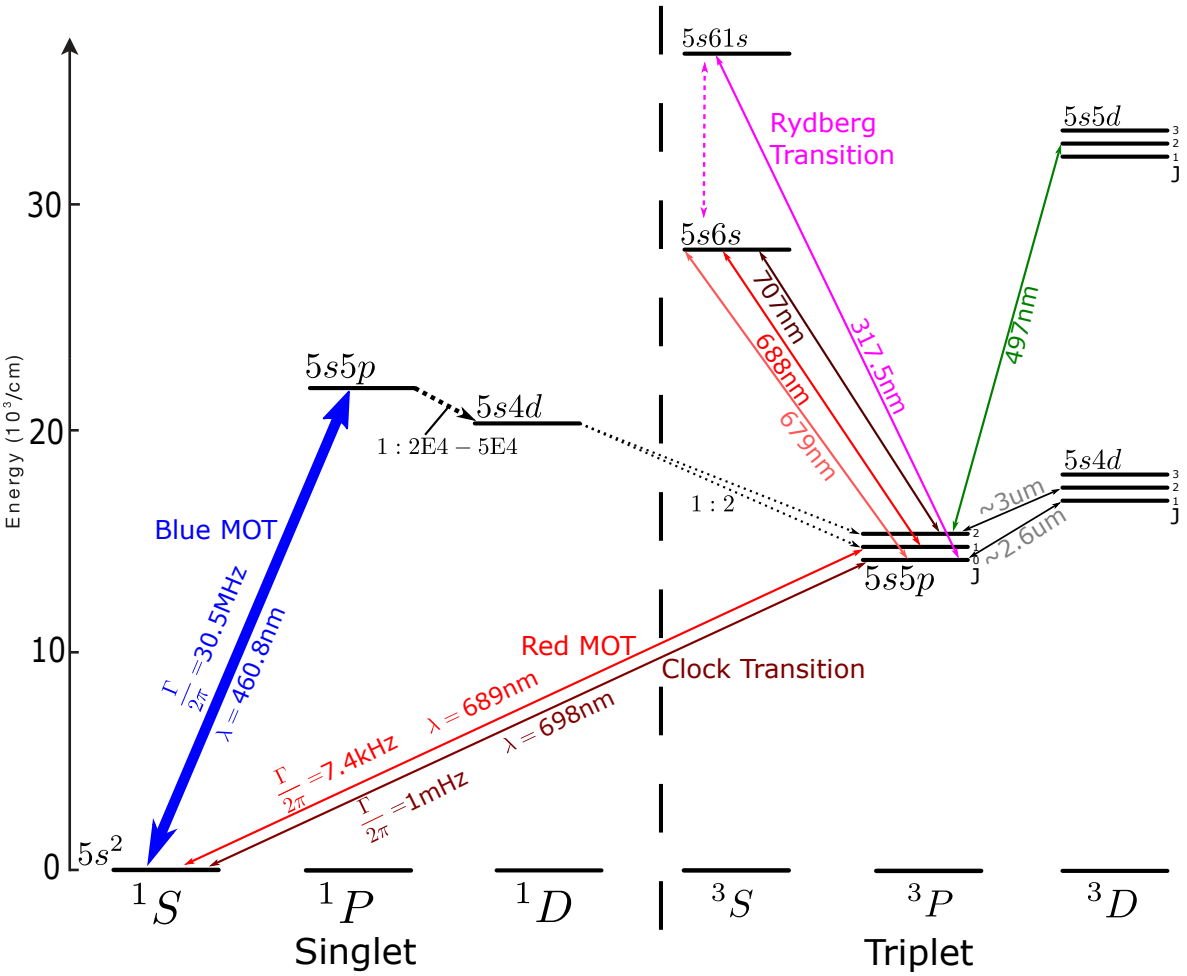


Figure 2.1: The energy level scheme and relevant optical transitions in $^{88}$Sr.The diagram shows the most relevant transitions and their linewidths and branching ratios[93].

This stability is further enhanced by its high magnetic moment ($J = 2$), which not only suppresses decay—since the $^1S_0 \rightarrow {}^3P_2$ transition is forbidden by both spin exchange and angular momentum conservation—but also renders the state magnetically trappable. The transition proceeds predominantly via magnetic-quadrupole (M2) coupling, making it highly sensitive to external magnetic and quadrupole fields. This sensitivity enables quantum simulation experiments that explore magnetic qubits under tunable external fields or probe quadrupolar interactions [105].

In Table 2.2, one can see the relevant transition shifts in this work for each isotope together with lifetime estimations. No concrete measurement of the magnetic transition shift ($^1S_0 \rightarrow {}^3P_2$) for the two bosonic isotopes was found in the literature.

### Repumping

During the cooling process, a significant fraction of atoms inevitably escapes the cooling cycle and becomes trapped in long-lived metastable states, necessitating repumping via intermediate states to reintegrate them into the cooling scheme. As illustrated in Figure 2.1, several

| Transition | $^1S_0 \rightarrow {}^1P_1$ | $^1S_0 \rightarrow {}^3P_1$ | $^1S_0 \rightarrow {}^3P_0$ | $^1S_0 \rightarrow {}^3P_2$ | $^3P_1 \rightarrow {}^3S_1$ |
|---|---|---|---|---|---|
| Lifetime ($\tau$) | 5.22(3) ns | 21.4 $\mu s$ | 120 s | 500 s | 13.92 ns |
| $^{84}$Sr | -271 | -351.5 | -349.6 | - | $\approx 200$ |
| $^{86}$Sr | -125 | -163.8 | -162.9 | - | $\approx 100$ |
| $^{87}$Sr | -46.5 | -62.18 | -62.17 | 62.93 | 62.91 |
| $^{88}$Sr (CF) | (650,503,200) | (434,8290,700) | (429,228,066) | (446,647,243) | (435,731,560) |

Table 2.2: Main optical transition frequencies (in MHz) between ground state to excited P orbitals for each isotope compared to the $^{88}$Sr isotope transition in the () brackets, which is referenced as zero due to its high abundance. The reference data was taken from [84, 89].

repumping options exist, each with unique benefits and challenges. The choice of repumping transitions must consider factors such as the availability of suitable laser sources, ease of implementation, and the necessity for closed transitions to minimize additional atom losses.

Several repumping techniques are commonly employed in the field, although not all are practical for our experimental setup. One widely used option involves a green 497 nm transition; although repumping via the green transition is appealing, the scarcity of high-intensity, single-mode lasers at that wavelength limits its utility. Similarly, methods involving mid-infrared transitions within the $3D$ manifold—such as the $^3P_2 \rightarrow {}^3D_2$ transition at approximately 3 $\mu$m, or repumping from the $^3P_0$ state via a 2.6 $\mu$m line—pose significant challenges due to the need for specialized optics and detectors, as well as difficulties in beam alignment caused by the limited visibility of IR light.

In contrast, the most widely accepted and practical repumping scheme employs two laser wavelengths in the visible spectrum. In our system, we utilize a 707 nm laser to drive the $^3P_2 \rightarrow {}^3S_1$ transition, which has a lifetime of approximately 22 ns; atoms decay from the $^3S_1$ state back into the $^3P_{0,1,2}$ manifold with branching ratios of roughly 1:3:5. To prevent atoms from being trapped in the clock state ($^3P_0$), we employ a second laser at 679 nm to repump the $^3P_0$ state via the $^3P_0 \rightarrow {}^3S_1$ transition, thereby ensuring that the atoms are returned to the cooling cycle through the $^3P_1$ level. This dual-laser approach, relying solely on visible wavelengths, is favored not only for its ease of implementation and cost efficiency but also for its proven performance in similar experimental configurations [106].

An alternative repumping option worth considering is the direct excitation of the $^1D_2 \rightarrow 8p^1P_1$ transition using a 448 nm laser. High-power laser systems (>1.5 W) at this wavelength are readily available, providing a viable means of repumping atoms directly from the $^1D_2$ state. Recent measurements by the Schreck group have demonstrated a potential increase in atomic flux in the Zeeman slower by approximately 60% when employing this technique [98], suggesting it could be a valuable addition to our experimental setup.

### 2.2.2 Fermion Case ($F = I + J$)

The $^{87}$Sr isotope Fermion has a nuclear spin $I = 9/2$, leading to a complex hyperfine structure characterized by numerous hyperfine states that arise from the coupling between the nuclear spin and the electronic angular momenta. The hyperfine splitting introduces additional levels for the atoms to decay and be excited into, significantly enriching the atomic structure compared to the bosonic isotopes. The resulting splittings between different hyperfine states (F-states) vary substantially, ranging from sub-megahertz to several gigahertz, depending on the electronic configuration and specific coupling constants. These GHz hyperfine shifts can

be addressed with acoustic-optic modulators (AOMs) or electro-optic modulators (EOMs) and are typically employed to shift the laser frequencies dynamically to match the required transitions.

The hyperfine energy shifts at zero magnetic field of $^{87}$Sr are reported in Figure 2.2. These energy splittings are predominantly attributed to the magnetic dipole moment and higher-order multipole contributions arising from the nuclear $g_I$ factor. The unperturbed hyperfine structure is governed by the intrinsic properties of the nucleus, including its magnetic dipole and electric quadrupole moments, which interact with the magnetic field generated by the electron cloud surrounding the nucleus.

To obtain the frequency shifts for each hyperfine state in both singlet and triplet manifolds, we applied the modified Breit-Wills (MBW) theory [107, 108]. This approach, combined with empirical parameters from previous experimental studies [93], enables accurate determination of the hyperfine structure. The MBW theory models the magnetic interactions between the electron and the nucleus by considering dipole, quadrupole, and, if necessary, higher-order terms like the octupole interaction[2]. Under the magnetic field $\mathbf{B}$, the atom internal Hamiltonian reads:

$$H_{hf} = -\mu_B \Big( g_s \, \mathbf{S} + g_l \, \mathbf{L} \Big) \cdot \mathbf{B} \; - \; \mu_N \, g_I \, \mathbf{I} \cdot \mathbf{B}, \tag{2.2}$$

In Equation 2.2, the hyperfine Hamiltonian is expressed in terms of the electron spin $\mathbf{S}$, orbital angular momentum $\mathbf{L}$, and nuclear spin $\mathbf{I}$. Here, $\mu_B$ and $\mu_N$ are the Bohr and nuclear magnetons, respectively, while $g_s$, $g_l$, and $g_I$ are the corresponding g-factors. This equation encapsulates the magnetic coupling between the atomic magnetic moments and an external magnetic field $\mathbf{B}$, thereby giving rise to the observed hyperfine structure.

The hyperfine Hamiltonian is typically simplified by assuming that hyperfine splittings are small compared to fine structure separations, allowing the use of the total electronic angular momentum as a good quantum number, and by considering only first-order Zeeman interactions alongside second-order magnetic dipole and electric quadrupole contributions [107], yielding the expression:

$$H_{hf} = H_D + H_Q = \hat{A}(\mathbf{r}) \mathbf{I} \cdot \mathbf{J} + \hat{B}(\mathbf{r}) \frac{3(\mathbf{I} \cdot \mathbf{J})^2 + 3\mathbf{I} \cdot \mathbf{J} - 2IJ(I+1)(J+1)}{4IJ(2I-1)(2J-1)} \tag{2.3}$$

where $\hat{A}(\mathbf{r})$ and $\hat{B}(\mathbf{r})$ represent the spatial dependence of the magnetic dipole and electric quadrupole interactions, respectively. Radially averaging the Hamiltonian yields the hyperfine energy shift:

$$\Delta E_{hf} = h\delta_{hf} = h\frac{GA(^{3,1}L_l)}{2} + hB(^{3,1}L_l)\frac{3G(G+1) - 4IJ(I+1)(J+1)}{8IJ(2I-1)(2J-1)}, \tag{2.4}$$
$$2G = 2\left\langle \mathbf{I} \cdot \mathbf{J} \right\rangle = 2 \cdot \frac{1}{2} \left\langle \mathbf{F}^2 - \mathbf{I}^2 - \mathbf{J}^2 \right\rangle = F(F+1) - I(I+1) - J(J+1)$$

where $G$ quantifies the degree of hyperfine coupling. The coefficients $A(^{3,1}L_l)$ and $B(^{3,1}L_l)$ denote the hyperfine splitting parameters, which have units of frequency and indicate how the

[2]For the precision level required in our experiments, contributions from the octupole term can be safely neglected. However, higher-order corrections can be calculated if needed.

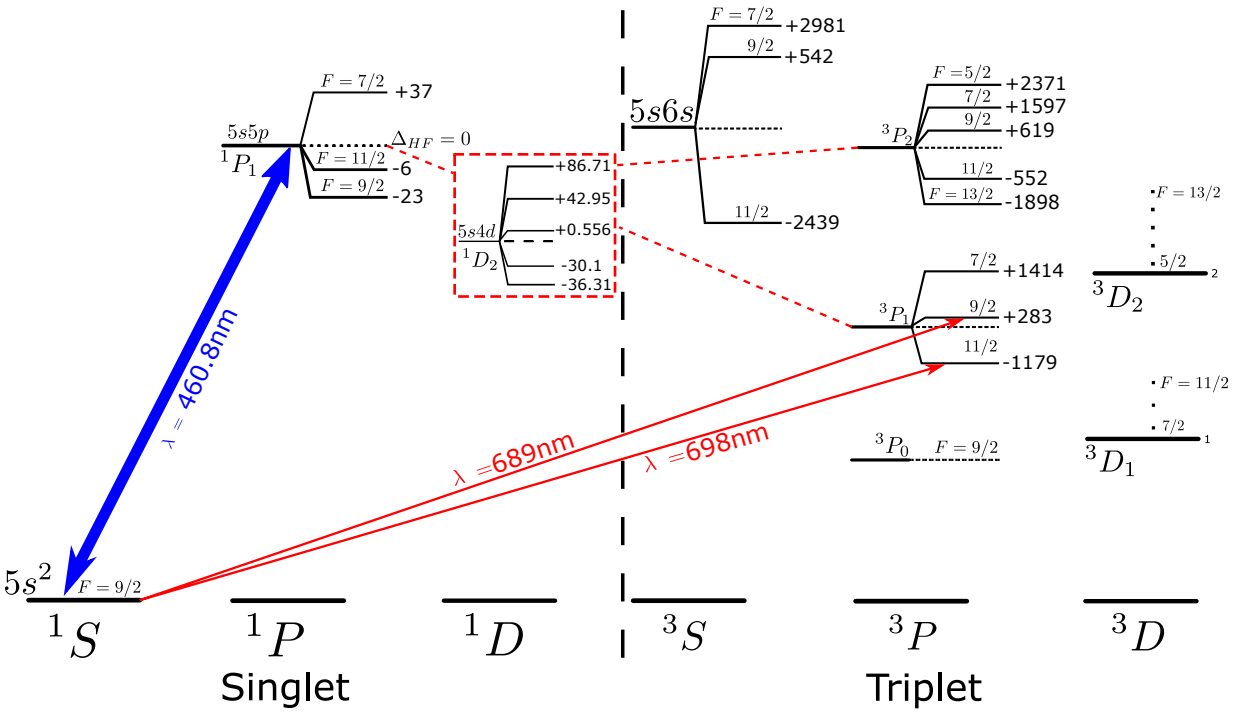


Figure 2.2: The energy level scheme and relevant optical transitions in $^{87}$Sr. The diagram lists the most relevant transitions and their linewidths and branching ratios.

F-states are separated for each singlet ($^1L_l$) and triplet ($^3L_l$) state. Determining $A$ and $B$ is described in detail in [107, 109], with further refinements based on experimental data provided in [93] and presented in Table 2.3. The parameters $A(^1D_2)$, $B(^1D_2)$ of the intermediate state hyperfine splitting are taken from [110], which uses the RF double resonance method, and are also presented in Table 2.3. The $^1D_2$ hyperfine split levels are less commonly addressed in the literature and may cause more atomic loss via the decay channels to the $^3P_J$ manifold [84]. Using the hyperfine interaction coefficients ($A$, $B$) and Equation 2.4 for each manifold, we can evaluate the splitting in MHz. The results are depicted in Figure 2.2, which shows the separation between hyperfine levels in different states relevant to our work.

The hyperfine structure of the $^3P_1$ state is well-resolved, which facilitates high-resolution spectroscopy on the intercombination line. The larger hyperfine splittings allow for selective excitation of individual hyperfine components, thereby enhancing the precision of spectroscopic measurements. The detailed structure of this state, together with the $^3S_1$ state, has been experimentally determined with high accuracy, offering valuable reference points for theoretical models and comparisons across different experimental setups.

The $^3P_2$ state presents unique hyperfine characteristics that provide deeper insights into the nuclear structure of alkaline-earth atoms such as strontium. The hyperfine splittings in this state can be used to probe the nucleus, revealing details about higher-order electromagnetic moments. Precision measurements of these splittings allow for the determination of the nuclear octupole moment, contributing to our understanding of the internal distribution of charge and magnetization within the nucleus. These measurements have been conducted by the Munich group [105] with a precision of approximately 10 kHz. These findings underscore the potential

| Transition State | $A$ (MHz) | $B$ (MHz) | $F$ | $g_F$ | Shift (MHz) |
|---|---|---|---|---|---|
| $^1S_0$ | 0 | 0 | 9/2 | 0 | 0 |
| $^3S_1$ | -542 [111] | -0.1(5) [111] | 7/2 | -4/9 | 2980.9 |
| | | | 9/2 | 8/99 | 542.1 |
| | | | 11/2 | 4/11 | -2439.1 |
| $^1P_1$ | -3.4(4) [93] | 39(4) [93] | 7/2 | -2/9 | 36.98 |
| | | | 9/2 | 4/99 | -22.83 |
| | | | 11/2 | 2/11 | -5.63 |
| $^3P_0$ | 0 | 0 | 9/2 | 0 | -62.17 |
| $^3P_1$ | -260.084 [112] | -35.658 [112] | 7/2 | -1/3 | 1414.252 |
| | | | 9/2 | 2/33 | 283.653 |
| | | | 11/2 | 3/11 | -1179.212 |
| $^3P_2$ | -212.765 [112] | 67.84 [112] | 5/2 | -6/7 | 2371.222 |
| | | | 7/2 | -1/7 | 1597.138 |
| | | | 9/2 | 2/11 | 618.691 |
| | | | 11/2 | 51/143 | -551.517 |
| | | | 13/2 | 6/13 | -1898.081 |
| $^1D_2$ | -5.5734(4) [110] | 55.421(6) [110] | 5/2 | -4/7 | 86.709 |
| | | | 7/2 | -2/21 | 42.955 |
| | | | 9/2 | 4/33 | 0.556 |
| | | | 11/2 | 34/143 | -30.098 |
| | | | 13/2 | 4/13 | -36.305 |

Table 2.3: Hyperfine parameters for the laser cooling and repumping transitions in $^{87}$Sr, including the dipole interaction constant $A$, quadrupole interaction $Q$, total angular momentum $F$, Landé g-factor $g_F$, and frequency shift from resonance in MHz. The values for $A$ and $Q$ are taken from .

of $^3P_2$ hyperfine spectroscopy in refining nuclear models and providing stringent tests for atomic theory.

### Fermion repumping scheme

Another important aspect in our experiment is the repumping transitions, as the additional hyperfine detunings relative to the respective $^{88}$Sr add a layer of complexity. This difficulty of repumping the fermion $^{87}$Sr is attributed to three reasons. Firstly, During the blue MOT stage, the cooling cycle predominantly drives the $F = 9/2 \rightarrow F = 11/2$ transition, but the small hyperfine splittings in the $^1P_1$ state (comparable to its natural linewidth) means that all three split state $F' = \left(\frac{7}{2}, \frac{9}{2}, \frac{11}{2}\right)$ are populated. All three contribute to the decay to the triple $^3P_J$ state, leaving us with the second problem, which is the branching ratio from the $F'$-state to the extensive hyperfine structure of the $^3P_2$ manifold via the $^1D_2$ level. Lastly, only the $F = 5/2$, $F = 11/2$, and $F = 13/2$ states are magnetically trappable, with $F = 13/2$ being

maximally probable to be trapped as it has the highest $F$ number. This phenomenon lies in the $F = 7/2$, and $F = 7/2$ states' weak magnetic coupling strength due to their small Landé g-factor, which is almost six times smaller [93]. All these facts make the repumping scheme on the $^3P_2 \rightarrow {}^3S_1$ inefficient, which predominantly stems from specific hyperfine states of the $^3P_2$ manifold, such as $F = 11/2$ and $F = 13/2$, remaining unaddressed. We observe this in the Blue MOT; the 707 nm transition shows limited efficiency when its detuning is fixed and shifted relative to the hyperfine splittings of $^{87}$Sr. As shown in Figure 2.2, the $^3S_1$ state is split over 5 GHz, while the natural linewidth of this state is on the order of only a few MHz.

To preferentially repump atoms into these states, the 707 nm transition can be detuned from the blue side (centering at approximately 423.91236 THz) and dynamically modulated its frequency over a 3 GHz bandwidth with a 1 ms repetition time. This approach enhances the repumping efficiency for the higher-lying trappable states ($F = 11/2$ and $F = 13/2$), thereby loading a robust reservoir in the long-lived $^3P_2$ state. Subsequent repumping from this reservoir increases the MOT atom number by a factor of 4–5, as atoms lost via the less-trappable $F = 7/2$ and $F = 9/2$ channels are minimized. Additionally, the $^{87}$Sr, due to its hyperfine structure, experiences inhomogeneous magnetic forces across its $^3P_1$ $m_F$ sublevels, leading to uneven trapping and greater atom loss compared to bosonic isotopes. In the blue MOT chapter, a detailed explanation of our repumping technique will be presented.

### 2.2.3 Other Relevant Transitions

While the most commonly employed transitions in Strontium experiments have been extensively discussed, a vast array of specialized level schemes can be utilized for more specific applications. Below, we detail several light transitions relevant to our experimental setup:

**Rydberg Atom Laser** - The $^{88}$Sr isotope is particularly well-suited for exploring Rydberg physics, a regime in which an atom is excited to a high principal quantum number ($n \gg 1$), significantly increasing its dipole interaction strength. This occurs because the electron occupies an energy state much farther from the nucleus [113]. Neutral Rydberg atoms have garnered intense interest in the atomic physics community due to their diverse applications, ranging from qubits in quantum computing processors [44] to the study of novel phases of matter [39].

In $^{88}$Sr, Rydberg states can be accessed through a series of optical and near-infrared transitions [114] or via a single ultraviolet photon at 317 nm(shown in Figure 2.1), exciting the atom from the $^3P_1$ clock state to a Rydberg state [115]. This UV-based excitation pathway provides a compelling platform for encoding long-lived qubits within an optical array, leveraging the extended lifetime of the clock state. Furthermore, Rydberg interactions in geometrically frustrated 3D lattices offer an avenue to investigate quantum spin liquid phenomena, building on analogous studies conducted in alkali atoms within 2D systems [116].

**Accordion Lattice at 520 nm** - Recent findings identify 520 nm as a magic wavelength, where the polarizability of the $^1S_0$ ground state matches that of the metastable $^3P_1$ for $\pi$-transition, making it desirable for creating a state-independent trap. This discovery has facilitated the use of optical tweezers [94] for simultaneous trapping and imaging of atoms within the trap. Optical tweezers enable the dynamic reordering [117] and shuffling of atoms [118], converting a randomized initial configuration into a deterministic arrangement. Beyond tweezers, the same wavelength can be employed to create optical lattices, offering high trapping depths while allowing simultaneous cooling via the 689 nm narrow-line transition.

**Tweezer Light at 813 nm** - To achieve a high-resolution, low-entropy deterministic ar-

| $a_0$ | $^{88}$Sr | $^{87}$Sr | $^{86}$Sr | $^{84}$Sr |
|---|---|---|---|---|
| $^{88}$Sr | -1.4 | 55 | 97.4 | 1790 |
| $^{87}$Sr | 55 | 96.2 | 162.5 | -56 |
| $^{86}$Sr | 97.4 | 162.5 | 823 | 31.9 |
| $^{84}$Sr | 1790 | -56 | 31.9 | 122.7 |

Table 2.4: Scattering lengths $a_s$ (in units of the Bohr radius $a_0 \approx 0.053\,\text{nm}$) for different combinations of Strontium isotopes. Data adapted from [124].

rangement of atoms, our setup integrates a tweezer array with a quantum gas microscope. The 813.4 nm wavelength is particularly advantageous as it is a magic wavelength for both the $^1S_0 \rightarrow {}^3P_0$ clock transition first demonstrated by the Tokyo group [119] for an optical clock lattice. This ensures compatibility with precision experiments involving the clock transition [120] and as an intermediate state employed for Rydberg excitation [121].

In our setup, an ECDL at 813 nm is amplified to 2 W using a TA. The beam is shaped into a tweezer array via an SLM, enabling configurable atomic patterns, as detailed in the Master's thesis of Leon Schäfer, with further developments in his forthcoming dissertation.

## 2.3 Isotopes Interaction Properties

A key factor in ultracold atomic systems is the role of atomic collisions, which drive momentum exchange and thermalization processes crucial to achieving quantum degeneracy. At low temperatures, where only s-wave collisions are relevant for distinguishable fermions and bosons away from scattering resonances, interactions are fully characterized by a single parameter—the s-wave scattering length $a_s$. This parameter embodies the phase shift of the incoming wavefunction relative to the outgoing one due to interatomic forces.

In several alkali atoms, the magnetic field sensitivity of ground-state atoms allows for tunable scattering interactions via Feshbach resonances, wherein the external magnetic field shifts the relative energy difference between the bound state and incoming pair of atoms, which leads to a modification of the scattering length $a_s$. This allows for resonantly enhanced interactions and enabling studies in phenomena such as three-body loss mechanisms, [122] and the more spectacular BEC-BCS crossover [123] which gave raise to the study of novel physics as one changes the interaction strength by tuning the scattering length [16]. However, in alkaline-earth atoms like Strontium, the spinless ground state is nearly magnetically insensitive, and the scattering length $a_s$ depends on the binding energy of the lowest vibrational mode of the interatomic molecular potential.

In these systems, interatomic potential parameters, such as the Van der Waals coefficients $C_n$, govern the scattering properties and yield isotope-dependent scattering lengths, as mass differences between isotopes influence the molecular binding energy. Precision measurements of the $Sr_2$ molecular potentials, combined with quantum calculations of the wavefunctions, have provided accurate values for these scattering lengths, as shown in [124] and summarized in Table 2.4.

From the data in this table, several observations can be made regarding the suitability of Strontium isotopes for ultracold experiments. With a near-zero scattering length, $^{88}$Sr has minimal collisional interactions, making it well-suited for applications in precision measurement and quantum metrology. However, this low scattering length complicates evaporative

cooling due to slow thermalization, and thus, $^{88}$Sr cannot reach quantum degeneracy independently. Nevertheless, it has been cooled to degeneracy through sympathetic cooling with other isotopes. Exhibiting a large scattering length, $^{86}$Sr undergoes substantial three-body recombination loss, which can limit phase-space density in evaporative cooling sequences. This high $a_s$ introduces rapid density-dependent losses, challenging the stabilization of Bose-Einstein condensates in experimental setups. Despite having the lowest natural abundance, $^{84}$Sr has favorable scattering properties for efficient evaporative cooling, and due to its scattering length, exhibits favorable conditions to generate Bose-Einstein condensation [125]. The only stable fermion $^{87}$Sr provides robust interaction parameters for degenerate Fermi gas studies and potential quantum simulation applications [32].

While elastic scattering between strontium atoms in their ground state offers attractive features for advanced quantum simulations, experimental investigations have demonstrated that inelastic scattering processes in excited states severely limit their stability on the timescales required for ultracold experiments [126]. Such inelastic scattering between metastable states $^3P_2$ and $^3P_0$, in particular, two-body inelastic collisions, induce rapid trap loss and unwanted heating, thereby impeding efficient evaporative cooling and reducing the achievable phase-space density. For instance, in bosonic $^{88}$Sr, the decay pathways result in insufficient atom retention for effective cooling, whereas in fermionic $^{87}$Sr, the presence of multiple hyperfine levels further complicates the decay dynamics and exacerbates atom loss [105, 84].

# Chapter 3

# Experimental apparatus and blue MOT

In this chapter, we provide an overview of our experimental setup for the laser cooling and trapping of Strontium atoms. Our system integrates an effusive atomic oven, an ultra-high vacuum environment, a precisely aligned laser delivery network, and a custom magnetic trapping assembly that is geometrically matched to fit our glass science chamber and the delivered light beams.

We first describe the overall architecture of the light delivery system, which is critical for directing and tuning the blue cooling beams. Next, we characterize the performance of the blue MOT in both 2D and 3D configurations across the stable isotopes of strontium. Finally, we introduce the repumping and recapturing scheme employed to enhance the atom number, setting the stage for subsequent experimental investigations.

## 3.1 Experimental apparatus overview

### 3.1.1 Cold strontium atomic source

The first step towards cooling strontium atoms is to generate an atomic flux directed into the science chamber, which operates under UHV conditions. Achieving this requires a meticulously engineered system that delivers a stable, high-flux beam, provides the necessary optical access, and maintains strict vacuum integrity.

While several groups have developed custom stationary setups for ultracold Strontium [84, 93, 127], these systems often require extensive laboratory space and heavy mounting configurations, which limit flexibility for integrating new experimental components. As demand for compact and efficient ultracold atom systems has grown, commercial cold atom beam sources are now readily available, offering compact, modular solutions that simplify the setup of new cold atom experiments.

We opted for a pre-assembled cold atomic beam source from AOsense as shown in Figure 3.1, which meets our requirements for a mobile, space-efficient setup with robust vacuum performance. This choice allowed us to bypass the lengthy design and assembly process of a custom system while providing the flexibility to mount the full vacuum system on a linear rail [128], enabling easy repositioning across the optical table without interfering with optical and magnetic setups around the science chamber. The system, spanning approximately 40

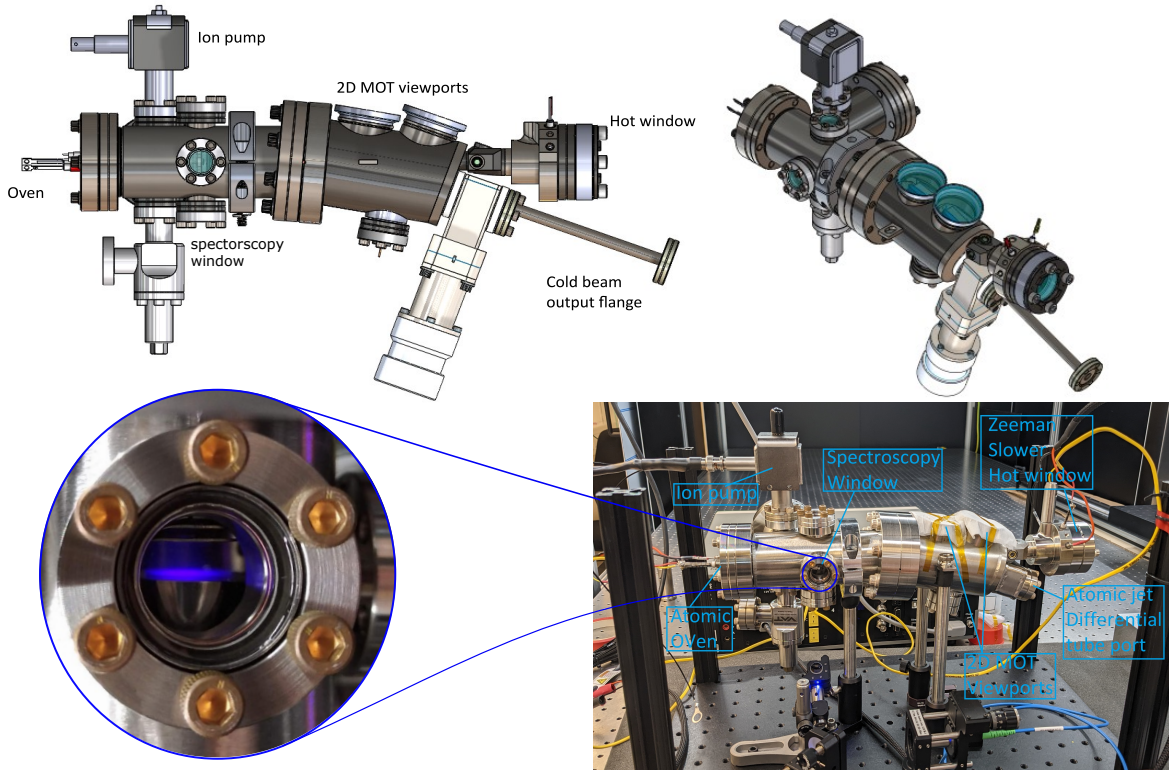


Figure 3.1: Schematic of the AOsense atomic beam system. The apparatus consists of a temperature-stabilized oven followed by a Zeeman slower section starting at the hot window and two angled 2D MOT modules that deflect the cold atom beam toward the differential pumping tube exit. The hot window facing the oven output is temperature stabilized and illuminated by a Zeeman slower beam for efficient deceleration of high-velocity atoms. At the bottom, we see a picture of the assembly being tested (right image) and a spectroscopy measurement of strontium atomic flux at an oven temperature of 420 °C in the left circle inset.

cm from the oven output to the science cell, delivers a stable cold atom flux, in a temperature range from 360-500 °C. The system specifications are found in the AOsense datasheet [129].

The system comprises the following key components:

- **Atomic beam source** – As seen in Figure 3.1.
- **Temperature control unit** – featuring an SRS PTC10 controller for precise thermal regulation.
- **Mounting parts and accessories** – providing the necessary tools to operate the assembly.

After mounting the main body on the table, we connected the oven and hot window to the PTC10 temperature controller. The atomic beam source was first tested using 460.8 nm resonance light to verify the flux operation and atomic species as shown in Figure 3.1 (bottom panels). Before sending atoms from the oven to the 2D MOT section, several system benchmarks must be met. The AOsense source chamber operates at approximately $1 \times 10^{-8}$ mBar, necessitating high pumping speed to achieve UHV in the science cell. This was accomplished

by first connecting the AOsense to our main vacuum system with the science cell, which was initially pumped and baked. Using a differential pumping tube, we attached the atomic source and vacuum system, equipped with a getter and ion pumps. After the attachment, the vacuum quality was verified with a residual gas analyzer (RGA), and using our ion pump[1] reading with electrical analogy we estimating that the pressure in the glass cell is reduced to below $1 \times 10^{-11}$ mBar.

When the oven is activated, the atomic beam trajectory, in the absence of any 2D MOT or other light pressure, leads directly to the hot window. This window can become coated rapidly, compromising the transmission for the Zeeman slower light. Thus, the hot window must be connected to the temperature controller and heated to a specified temperature, which is contingent on the oven's operating temperature. The oven temperature can be adjusted only after these prerequisites are satisfied, thereby enabling the measurement of the thermal atomic flux. Subsequently, we couple the blue laser light to all relevant viewports and optimize the atomic stream into the science cell and the number of atoms in the 3D MOT. Each of these steps involves distinct challenges, which will be discussed in detail in the following sections.

### 3.1.2 The effusion oven

At atmospheric pressure, Strontium requires a vaporization temperature of approximately $T_{\text{vap}} = 1650\,K$. However, in the reduced-pressure environment of our system, the required temperature to initiate the effusion process is significantly lower, around 300°C. This allows the oven to operate at relatively low temperatures to produce a steady atomic beam of Strontium.

Due to commercial confidentiality, limited technical details about the AOsense setup are available. Nonetheless, we know that operating the oven at a temperature of 420°C yields an atomic flux of approximately $8 \times 10^{13}$ atoms/s. This was confirmed by both a theoretical estimation Appendix A and by the manufacturer specifications [130].

The oven and hot window are controlled by an SRS PTC10 temperature controller. The device is connected to the system via high-power cables, ensuring the necessary current and voltage levels to maintain stable operation, with the oven drawing up to 15 W. Proper insulation is in place to protect users from electrocution hazards.

Before activating the oven, we preheat the sapphire AR-coated hot window, which is capable of withstanding temperatures up to 800°C. To prevent Strontium deposition on the hot window, it must first be heated to an initial temperature of 260°C, which correlates with an oven temperature of 360°C. For a higher atomic flux, we must incrementally increase the hot window temperature in steps of $\Delta T_{\text{HW}} = 15$°C, allowing each increase to stabilize before proceeding, thereby preserving the AR coating and minimizing thermal stress on the hot window. For our final operational oven temperature of 430°C, the hot window is set to 335°C.

To avoid repetitive heating and potential damage to the AR coating, we maintain the hot window temperature continuously, even when the oven is inactive. Despite these precautions, challenges arose with the hot window's reliability, which subsequently impacted the performance of the Zeeman slower. These issues will be addressed in detail in the Zeeman slower section.

Similarly to the hot window, we ramp up the oven temperature gradually, targeting a final temperature of 430°C. This is done in steps of $\Delta T_{\text{oven}} = 75$°C with a stabilization period of 15 minutes per increment to allow the PID control circuit to stabilize. Additionally, the

[1] Agilent VacIon Plus 20 and SAES D500

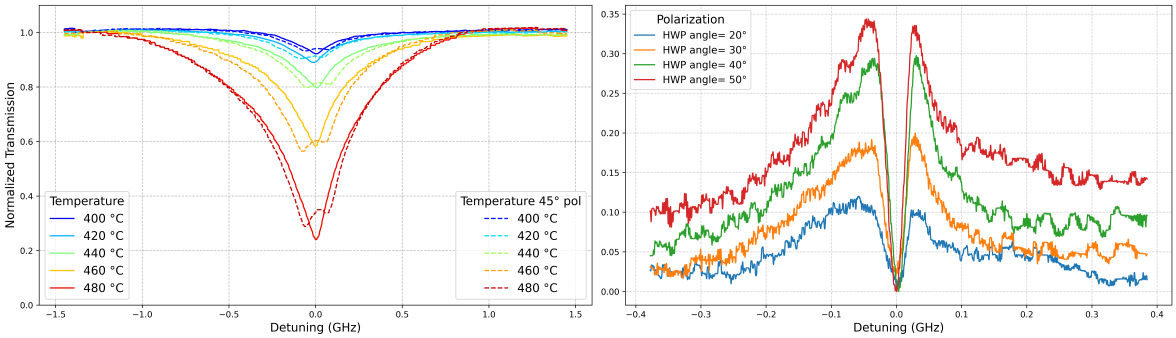


Figure 3.2: Doppler absorption signal for different oven temperatures and beam polarizations. By using blue resonance light we can measure the atomic optical density for different oven temperatures. A second experiment tested the beam polarization on the absorption signal. By changing the light polarization from 0° to 45°(wrt to the optical table), the central deep is split into two 30 MHz side valleys reflecting the Zeeman $m_J$-states splitting of the $^1P_1$ energy level.

temperature ramp rate is limited to $dT/dt = 0.1°\text{C/s}$, taking approximately two hours to reach full operating conditions.

While the oven is rated for a maximum temperature of 520°C, we limit it to 430°C to prolong its operational life and avoid thermal strain on the components. Operating the oven at reduced temperatures diminishes the production of atomic vapor, thereby decreasing the atomic flux while resulting in a greater residual quantity of strontium remaining in the oven. The PTC10 controller's programmability allows us to automate the oven's on/off sequence, facilitating remote control and simplifying daily operation.

Our first check-up of the system was to measure the Doppler absorption profile at the oven output plotted on the left panel of Figure 3.2. A monochromatic 460.8 nm laser beam—resonant with the $^1S_0 \rightarrow {}^1P_1$ transition—is directed through the spectroscopy window. Initially, the beam waist is 1mm and 5 mW power, it has 0° linear polarization wrt to the optical table. Its frequency is then scanned across the resonance while the transmitted light is monitored by a photodetector. This measurement of the absorption signal is made for varying oven temperatures, providing feedback on the atomic beam flux coming directly out of the oven.

This measurement was also performed by the manufacturer and provided to us as a reference to diagnose potential malfunctions during shipping or installation. Since both measurements were conducted on the same system under comparable parameters but with different instruments and environmental conditions, slight deviations are expected. Our optical density measurements (left plot on Figure 3.2) show a discrepancy of approximately 5% compared to the AOsense reference data, which lies within the estimated measurement uncertainties. Additionally, we characterized the polarization dependence of the Doppler absorption signal by placing a $\lambda/2$ waveplate before the spectroscopy window and rotating it in 10° increments. This procedure gradually varied the linear polarization angle of the probe beam, selectively addressing the Zeeman sublevels of the $^1P_1$ excited state manifold. In the crossing section, where the light beam integrates with the flux main isotope, which is $^{88}$Sr, the magnetic field is unknown. However, it can be estimated using the splitting of the $m_J$ states shown in Figure 3.2. To do this, we need to send polarized light such that we address predominantly the $m_J = \pm 1$ states. The behavior arises from the coupling of the electric field polarization

to the $m_J = \pm 1$ Zeeman sublevels, which are split due to residual magnetic fields around the spectroscopy window. By observing the absorption signal on a photodiode, we see the effect is most pronounced between 0° and 45°, where the central absorption dip exhibits the largest polarization-dependent variation. To emphasize the influence of polarization on the absorption profile, the zero-polarization signal was subtracted from all subsequent measurements. The resulting differential signal (right panel of Figure 3.2) reveals two side peaks at approximately ±30 MHz, whose amplitudes increase with the polarization angle, peaking at 45° before diminishing to zero at 90°. Using the B-field Zeeman shift $\Delta\nu = m_J g_J \tilde{\mu}_B B$, which represents the energy frequency shift due to the magnetic field $B$. Here $g_J = 1$ is the Landé g-factor, and the $\tilde{\mu}_B = 1.4$ MHz/G is the Bohr magneton. From the two peaks positions, we can extract the frequency shift, which is around $\Delta\nu \approx 36.9$ MHz. Then, from the B-field Zeeman shift equation, we get a magnetic field of around $B \approx 26.3$ G, as expected due to the Zeeman slower magnets. This behavior underscores the critical importance of maintaining a well-defined polarization state for accurate laser frequency stabilization.
Notably, all polarization measurements were conducted with the oven maintained at 430°C set via the PTC driver to ensure a consistent effusive jet of strontium atoms. This controlled thermal environment guarantees a stable atomic beam, which is subsequently directed into the UHV system for laser cooling and trapping.

### 3.1.3 Vacuum and magnetic field systems

A robust UHV environment is essential for performing quantum gas experiments as it minimizes interactions with residual gas molecules that can degrade measurement coherence. In our system, the AOSense atomic source chamber operates at approximately $1 \times 10^{-8}$ mBar. The vacuum system consists of two distinct differential pumping stages. In the first stage, an 8 cm-long, 1 cm-diameter pumping tube connects the output of the AOSense to a CF40 cube, which serves as the initial pumping chamber and is evacuated using a 200 L/s SAES getter pump. A custom gasket then connects this cube to a second chamber, a custom 5-way bucket that is differentially pumped by a 500 L/s ion getter pump, as well as a compact Agilent ion pump (20 L/s) used to further reduce outgassing. Additionally, the vacuum assembly was baked and characterized using a Residual Gas Analyzer (RGA) to confirm that the residual gas composition meets our stringent requirements. Based on measured lifetimes of atoms trapped in an optical tweezer (exceeding 150 s), we estimate that the background pressure in the glass cell is below $1 \times 10^{-11}$ mBar, which is satisfactory for quantum gas experiments. The relatively lightweight vacuum assembly is mounted on a manual linear translation stage, allowing the vacuum chamber to be decoupled from the surrounding optical setup, a feature that greatly facilitates precise laser beam alignment around the science chamber. In this configuration, the atomic beam is maintained at a height of 29 cm above the optical table, while an additional mounting platform—constructed from a custom breadboard with a 12.7 cm hole pattern and positioned 25 cm above the table in the X–Z plane—ensures that light is accurately delivered to the atoms at the desired level.

Surrounding the science chamber (SC), a custom in-house water-cooled magnetic coil system was constructed (see Figure 3.3). The primary coils form a diamond-shaped anti-Helmholtz configuration that produces a magnetic field gradient with a minimum at the science cell center, where the atoms are positioned. Each primary coil is fabricated from hollow copper tubes, looped in series and encapsulated in insulating epoxy, then mounted on a non-magnetic, hardened fiberglass frame to protect the SC's glass cell. A continuous flow of

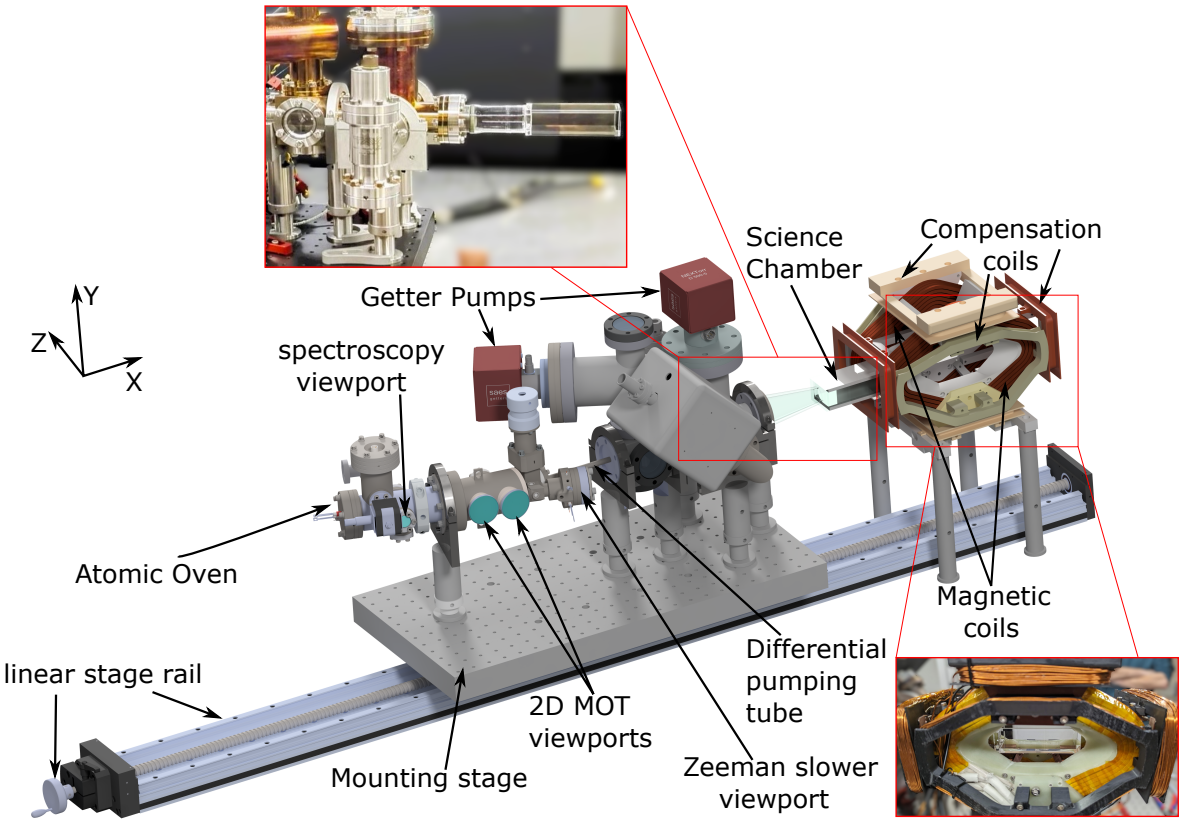


Figure 3.3: Overview of the experimental setup. The apparatus comprises three primary sections: the AOSense atomic beam source, a differential pumping stage, and the science chamber. The AOSense source is connected to the differential pumping stage, which ensures ultra-high vacuum conditions in the science chamber, placed on the right side of the rail. The SC is positioned within a pair of custom-made, diamond-shaped, water-cooled anti-Helmholtz magnetic coils, providing a gradient field for atomic manipulation. Six additional winded Helmholtz coils, without active temperature stabilization, allow for fine magnetic field adjustments. The entire vacuum assembly, excluding the magnetic coils, is mounted on a mechanical linear rail system, enabling translational movement of the full vacuum system. The total length of the vacuum system, from the atomic oven to the SC, is under 0.5 meters. Note that the magnetic coils are set after the rail and not as shown in the image. In the insets are pictures of the real science cell and magnetic fields system.

approximately 1.5 L/min of deionized water, cooled via a heat exchanger, maintains the coil temperature at a stable 17°C.

The coils are driven by a *DELTA ELEKTRONIK SM30-200* high-current supply with a maximal current of 200 A.[2] For rapid switching of the magnetic field, we employ a switching circuit based on IGBTs and varistors; this circuit enables the field to be turned off from full current to zero in approximately 500 $\mu$s.

In addition, six compensation coils are installed on custom 3D-printed mounts to generate Helmholtz offset fields for fine positional adjustments of the atoms. They are independently

[2]We notice that optimal current for trapping $^{88}$Sr is at 120 A and for $^{87}$Sr at 140 A

| **Parameter** | Longitudinal (X) | Vertical (Y) | Horizontal (Z) |
|---|---|---|---|
| Anti-Helmholtz Gradients [(G/cm)/A] | -0.16 | 0.3 | 0.33 |
| Max Anti-Helmholtz Gradients [G/cm] | -19.2 | 36.0 | 39.6 |
| Helmholtz Offset Field [G/A] | 0.9 | 1.8 | 1.8 |
| Max Helmholtz Offset Field [G] | 4.5 | 4.5 | 2.25 |

Table 3.1: Magnetic field parameters at the atom position, measured with the system retracted around the geometric center of the coils. The anti-Helmholtz gradients were measured at an optimal current of 120 A for the $^{88}$Sr isotope, while the Helmholtz offset fields are derived from a maximum current of 2.5 A.

driven up to 2.5 A using a constant current controller,[3] which controls their strength, and with an H-bridge, we can also change the field direction when needed. Their output offset fields and anti-Helmholtz gradients were characterized and summarized in Table 3.1.

These magnetic components, along with the vacuum assembly, were designed and characterized by my colleague Thies Plassmann; a comprehensive presentation of the full system is forthcoming in his future work.

## 3.2 Blue laser system

The blue laser system is central to the cooling and trapping processes, addressing the $^1S_0 \rightarrow {}^1P_1$ transition at 460.8 nm. The laser light is delivered to the apparatus through a series of optical elements, including mirrors, lenses, and waveplates, designed to control the beam's intensity, polarization, and alignment precisely. A detailed presentation is provided below concerning the laser system employed for modulating both the frequency and amplitude of the beams directed at the atoms.

### 3.2.1 Laser source and controller

Advancements in laser technology have introduced new tools for atomic physics, including modern laser diodes (LDs) that were previously unavailable. Our primary light source for the blue laser system is a recent model from *MOGLabs*, featuring a tunable Littrow external cavity diode laser (ECDL) coupled to an injection lock amplifier diode (ILA).

The MOGLabs laser module comprises two main sections, as shown in Figure 3.4. The first section is the ECDL, which generates approximately 200 mW of power at 230 mA current [131]. It operates with a mode hop-free range (MHFR) of $3 - 4$ GHz, depending on the operating frequency. Directly after the ECDL, an optical isolator is placed, attenuating back-propagating light to protect the diode. The beam after is then split into a 20/80 ratio, where the majority of the power (80%) is directed to a free-space output port for locking and imaging setups, while the remaining 20% (around 30 mW) is injected into the ILA. Within our blue laser system, the frequency-locked ILA beam output is nearly 700 mW when operated at 700 mA under temperature stabilization of $\Delta T \approx 0.02°$C. Together, these components yield a combined output of over 900 mW with highly adjustable frequency characteristics.

[3] *Thorlabs* LD3000R - Laser Diode Driver

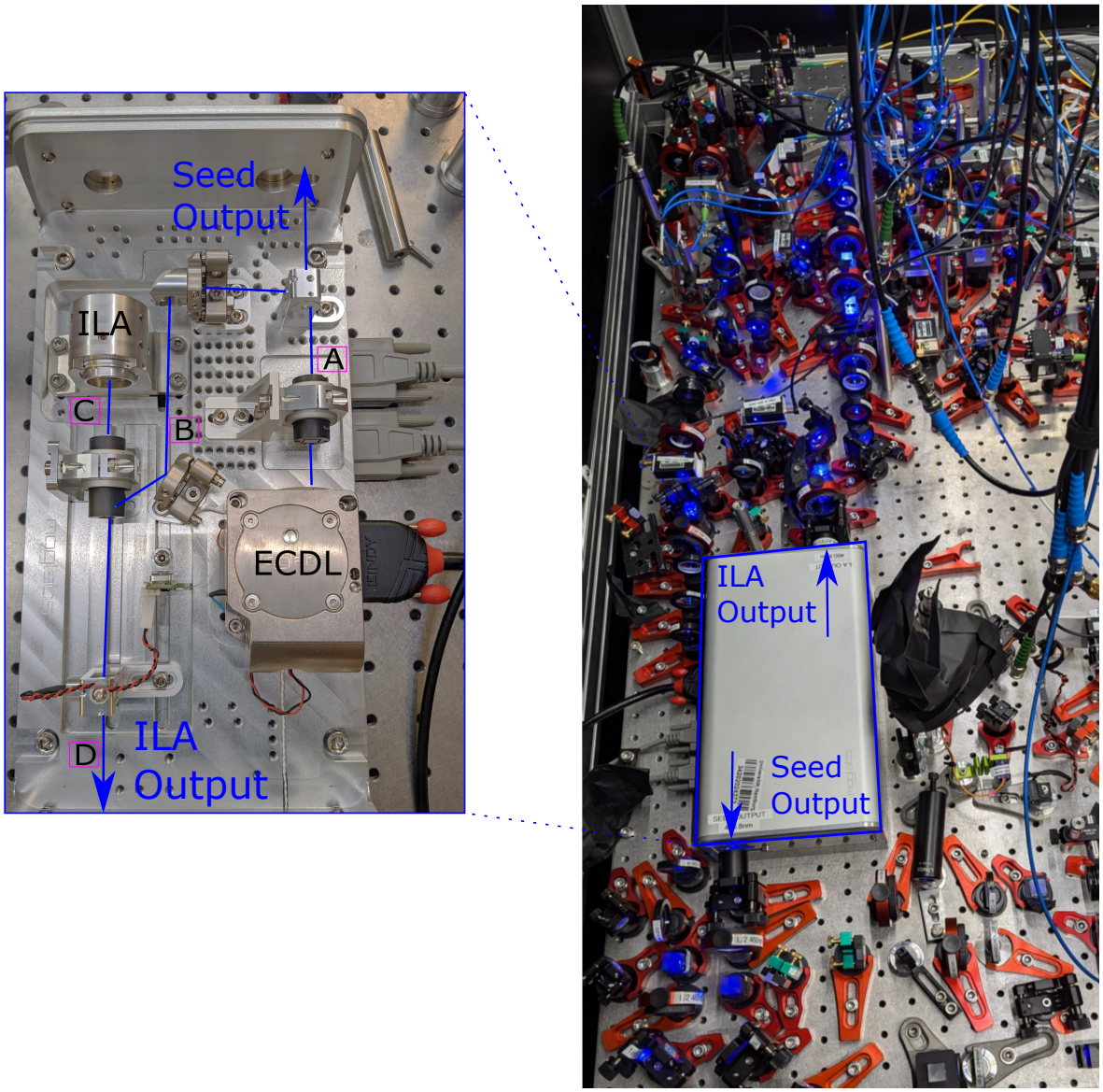


Figure 3.4: The Moglabs laser module and the blue laser delivery system. The ECDL output passes through an optical isolator before reaching an 80/20 beam splitter. Most of the laser power is directed outside the module for use in the laser system, while the rest of the portion is sent to an Injection Lock Amplifier (ILA), boosting the power by an additional 700 mW (both beams represented by blue lines). The ILA is controlled by a separate driver, which features an auto-relock option for stable long-term operation. Beam monitoring points A-D are used to ensure the proper functioning of both the ECDL (points A and B) and the ILA (points C and D). The module is mounted on our small laser table, and the entire blue light delivery setup is based around it on the table, as seen on the right side. Note the inverted direction of the module on the table and inset.

The ECDL and ILA are controlled by independent drivers. The ILA driver regulates temperature and current, and it features an auto-relocking function to ensure continuous

| Arm Name | BW [MHz] | Detuning | Power [mW] | AOM Path |
|---|---|---|---|---|
| Lock (pump) | ±150 | 0 | 25 | $1^{st}$ DP, $2^{nd}$ SP |
| Lock (probe) | ±150 | 0 | 5 | $1^{st}$ DP, $2^{nd}$ SP |
| Imaging | ±24 | 0 | 0.5-5 | DP |
| 2D MOT | ±24 | -30 MHz $\sim \Gamma$ | 80 | DP |
| 3D MOT (per beam) | ±25 | -30 MHz $\sim -\Gamma$ | 70-90 | DP |
| Zeeman | ±38* | -590 MHz $\sim -20\Gamma$ | 0-120 | two SP |
| Mini-Zeeman | ±25* | -80 MHz $\sim -2.5\Gamma$ | 3-5 | two SP |

Table 3.2: Frequency BW and detuning of the AOMs, for each arm of the blue system optimized for the $^{88}$Sr MOT. The power column is the power for each beam before it is coupled to the fiber. The two only single pass (SP) AOMs of the mini/Zeeman can be shifted in frequency but involving recouping of their fibers*.

operation, which is critical since the blue ILA at high power is sensitive to current fluctuations that can induce mode hops and cause it to unlock from the ECDL injection. The ECDL driver offers precise control over current, piezo adjustment, and temperature tuning and incorporates feed-forward modulation to extend the mode-hop free tuning range. It also includes a built-in double-integral proportional-derivative (PIID) locking mechanism essential for robust frequency stabilization.

The laser module is mounted on a compact optical table, with the two laser outputs directed to different parts of the experiment. The ECDL output feeds into two paths, one is to a modulation transfer spectroscopy setup intended for frequency stabilization and the other for an imaging fiber port for absorption and fluorescence imaging. The ILA output provides higher power for the Zeeman and mini-Zeeman slower beams, as well as the 3D MOT (via three fibers) and the 2D MOT (via a single fiber).

The full beam paths, including the AOM frequencies, typical powers, and frequency references relative to the $^1S_0 \rightarrow {}^1P_1$ transition frequency of $^{88}$Sr, are detailed in Figure 3.5.

### 3.2.2 Blue Laser table Setup

The design of the blue light system required careful consideration of the specifications provided by AOsense to achieve optimal cold atomic flux. While power requirements are straightforward and do not necessitate extensive analysis, the laser frequencies are crucial. These frequencies must be adjusted to be able to address all isotopes and ensure that all related beams are appropriately shifted. To optimize the atomic signal in the Blue MOT, one can derive a relationship between the laser frequencies for different components of the system. The lock frequency serves as the reference point and is aligned with the resonance frequency of the isotopes in choice. By shifting the lock frequency to the resonance of a different isotope, all other beams are simultaneously adjusted. This feature is critical for optimizing MOT settings when exploring Zeeman detuning or imaging various isotopes. In Table 3.2, we can see the frequency tunability set for each beam using the AOM and also the set-point of the light with respect to $^{88}$Sr isotope.

The AOMs signals are generated and controlled by a software-managed *Wieserlabs FlexDDS-NG* Rack driver. The driver provides precise frequency, amplitude, and phase control over all beams as specified here [132].

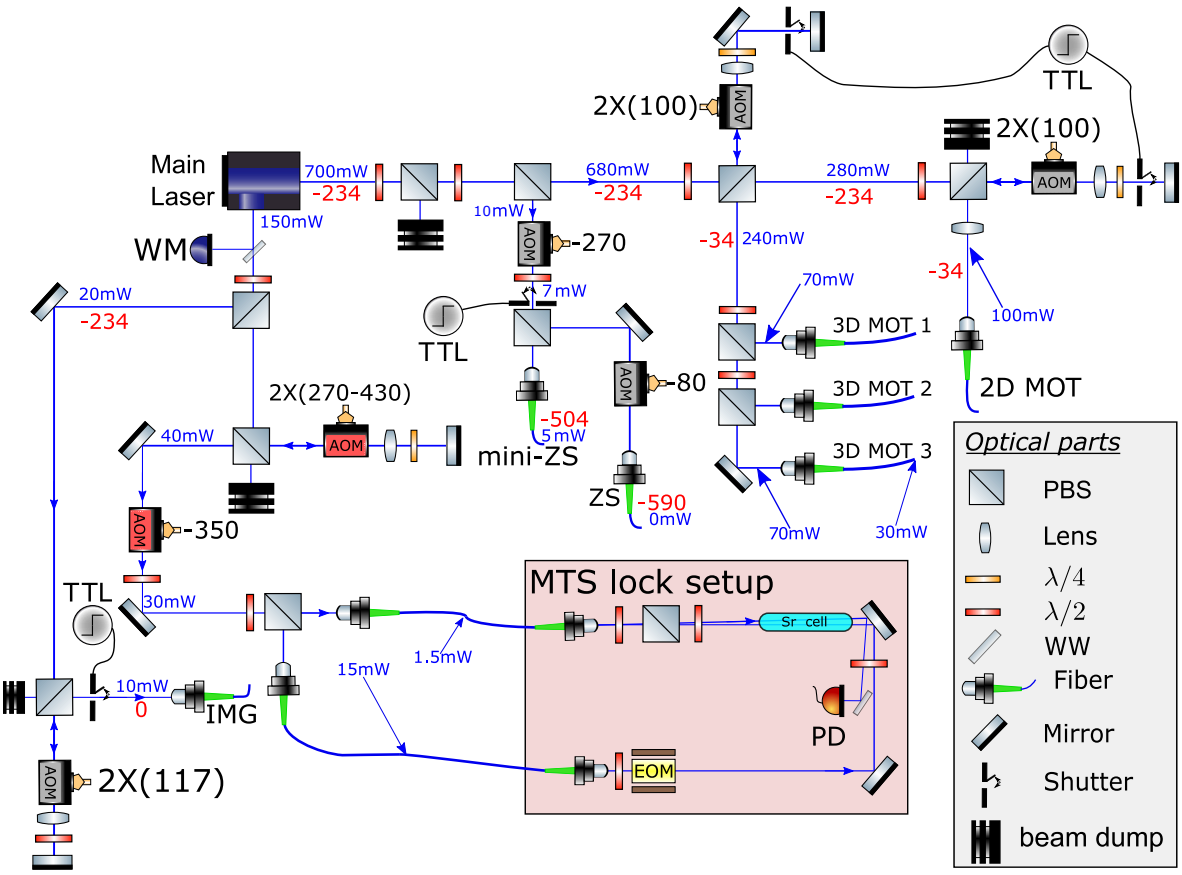


Figure 3.5: Complete blue laser system setup from the 460.8 nm Moglabs laser. The diagram details all beam paths prior to fiber coupling, including the MTS lock configuration, which stabilizes the laser frequency. Power levels at each port are indicated in blue (in mW) and are dynamically adjusted based on system requirements. Frequency shifts from the sub-Doppler resonance of the $^1S_0 \rightarrow {}^1P_1$ transition are labeled in red(in MHz). Key optical and electrical components are shown, with the wavemeter actively monitoring the bare laser diode frequency. The red-labeled AOMs are broadband, while the gray AOMs are narrower in bandwidth, with their primary operating frequencies noted in black beside each.

To meet the specific amplitude requirements of different AOMs for optimal diffraction efficiency, we employ 1 W or 2 W RF amplifiers [4]. The DDS is connected via a LAN network using the TCP/IP protocol, allowing us to control and program it remotely through a Python-based software driver. This script enables both off-experiment configurations and real-time tunability of all AOMs within the experimental sequence. Due to the limited number of DDS channels and the requirement for each AOM to receive a dedicated signal, we also designed and built in-house RF drivers based on amplitude- and frequency-tunable voltage-controlled oscillators (VCOs). These drivers, constructed using SMD chips on electronic breadboards, can be externally triggered and controlled. They include internal frequency limit options to ensure operational safety and versatility. The development of these VCO drivers was initiated by a former Bachelor student, Immo Dede, as detailed in [133], and has been further expanded

[4] Mini-Circuits ZHL-1A+ or ZHL-1-2WX-S+

in ongoing work by Leon Schäfer. These efforts have proven instrumental in enhancing the flexibility and robustness of our blue light delivery system.

### 3.2.3 Frequency stabilization of the blue laser

Without any frequency stabilization, lasers in our lab typically drift by several MHz per minute or more. These drifts render it impossible to reproduce measurements accurately. To properly address an optical transition with a natural linewidth $\Gamma$, the laser must be stabilized to a precision significantly finer than $\Gamma$, which is around a few tens of MHz, ensuring optimal resonant coupling. In the case of Strontium atoms, locking the laser to the ${}^1S_0 \rightarrow {}^1P_1$ transition ensures precise and reproducible experimental conditions. Several methods can be used to stabilize the frequency of a laser. These include cavity locking [134, 135], using a hollow cathode lamp [136], or employing a spectroscopy cell. Among these techniques, the choice depends heavily on the linewidth of the transition; narrower linewidths make it more challenging to achieve stable locking due to the need for precise frequency control.

The blue transition has a broad linewidth of approximately 30.5 MHz. This relatively large linewidth allows for straightforward stabilization techniques. Several locking techniques exist to lock on an atomic transition from saturated absorption spectroscopy (SAS) in vapor cells[24], to polarization spectroscopy, exploiting the optical pumping of atoms by a linearly polarized beam, which induces circular birefringence[137]. Due to its relatively simple requirements that match our laboratory capabilities, we choose a Modulation Transfer Spectroscopy (MTS) scheme[138], engineering a pump-probe configuration to generate a sub-Doppler signal. A cavity-based approach would be excessive for this linewidth, and using a spectroscopy cell is facilitated by our setup, which includes an atomic source and a viewport allowing laser light to interact with the atomic beam, as shown in Figure 3.1.

### 3.2.4 Modulation transfer spectroscopy Lock on the ${}^1S_0 \rightarrow {}^1P_1$ Transition

The specific MTS scheme employed in our system is adapted from [139], where a pump beam and a probe beam are used to interrogate the atomic vapor transversely to the atomic jet. The pump beam is modulated using an Electro-Optic Modulator (EOM), creating sidebands 66 MHz away from the carrier frequency. This modulated light is then sent into the vacuum cell while the probe beam simultaneously interacts with the atomic vapor. Through the four-wave mixing process, nonlinear interactions induce sidebands in the probe beam, which are subsequently detected by a photodetector (PD).

The electric field of the modulated pump beam can be mathematically expressed as:

$$E(t) = E_0 e^{i(\omega_0 t + \mu \sin(\omega_m t))} = E_0 e^{i\omega_0 t} \left[ \sum_{n=-\infty}^{\infty} J_n(\mu) e^{in\omega_m t} \right], \tag{3.1}$$

where $\mu$, $\omega_0$, and $\omega_m$ represent the modulation index, carrier frequency, and sideband frequency, respectively. The second equality is obtained via a Bessel function expansion, where $J_n(\mu)$ are Bessel functions of the first kind. The modulation process effectively transfers the modulation from the pump to the probe beam, yielding sidebands characterized by the Lorentzian profile of the dipole transition. This results in a beat signal on the PD, which consists of the probe field mixed with the sidebands induced by the pump. In the Fourier

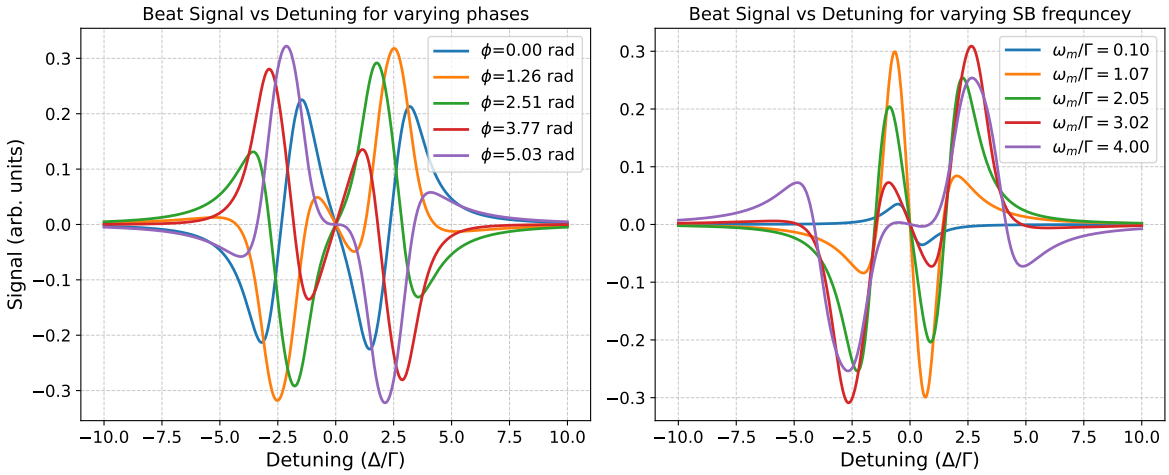


Figure 3.6: Simulation of MTS beat signals for the ${}^1S_0 \rightarrow {}^1P_1$ transition, illustrating signal variation with modulation phase and sideband frequency. In the left panel, signals are shown for varying phase values between $\phi = 0$ to $\phi = 8\pi/5$ where we set $\omega_m/\Gamma = 1$; here $\Gamma$ is the natural linewidth of the atomic transition, displaying the in-phase and quadrature components as the phase progresses. The right panel presents the beat signal as a function of detuning for different sideband modulation frequencies, with values ranging between $\omega_m/\Gamma = 0.1$ to $\omega_m/\Gamma = 4.0$, the phase is set to $\phi = \pi/3$.

domain, the intensity of the beat signal can be expressed as [140]:

$$I(\omega) = |\hat{E}(\omega)|^2 = \frac{A_0}{\sqrt{\Gamma^2+\omega^2}} \sum_{n=-\infty}^{\infty} J_n(\mu)J_{n-1}(\mu)\times \tag{3.2}$$
$$\left[\left(L_{(n+1)/2} + L_{(n-2)/2}\right)\cos(\omega t+\phi) + \left(D_{(n+1)/2} + D_{(n-2)/2}\right)\sin(\omega t+\phi)\right],$$

where the Lorentzian functions are defined as:

$$L_n = \frac{\Gamma^2}{\Gamma^2+(\Delta - n\omega_m)^2}, \quad D_n = L_n \times \frac{(\Delta - n\omega_m)}{\Gamma}.$$

Assuming the modulation index $\mu < 1$, we can neglect higher-order terms in the series expansion, resulting in a simplified expression for the beat signal spectrum on the PD:

$$I(\omega) \approx \frac{A_1}{\sqrt{\Gamma^2+\omega_m^2}}\times \tag{3.3}$$
$$\left[L_{-1} - L_1 - L_{-1/2} + L_{1/2}\right]\cos(\omega_m t+\phi) + \left[D_{-1} + D_1 - D_{-1/2} - D_{1/2}\right]\sin(\omega_m t+\phi),$$

where $A_1 = A_0 J_1(\mu)J_0(\mu)$ represents an amplitude factor dependent on the light intensity and atomic density. The parameters $\Gamma$ denote the natural linewidth of the atomic transition and $\phi$ the phase shift introduced by the detector with respect to the modulation field applied to the pump beam.

By adjusting the ratio of the modulation frequency $\omega_m$ to the atomic linewidth $\Gamma$, it is possible to manipulate the in-phase and out-of-phase components of the beat signal, thus enhancing the lock signal's sensitivity. This is particularly relevant when $\omega_m/\Gamma > 1$, as the

| Beam | Frequnecy shift [MHz] | PAF [mW] | Waist [mm] | $I_{\text{beam}}$ |
|---|---|---|---|---|
| Lock (pump) | 0 | 15 | 0.5 | $100\, I_{\text{sat}}$ |
| Lock (probe) | 0 | 1.5 | 0.5 | $10\, I_{\text{sat}}$ |
| Imaging | 0 | 0.1–1 | 1.2 | $I_{\text{sat}}/10$ |
| 2D MOT | -35 | 35 | $2.5 \times 12.5$ | $2\, I_{\text{sat}}$ |
| 3D MOT (per beam) | -35 | 10–12 | 5 | $2\, I_{\text{sat}}/3$ |
| Zeeman | -590 | 50–60 | 3 | $8\, I_{\text{sat}}$ |
| Mini-Zeeman | -80 | 1–2 | 2.5 | $I_{\text{sat}}/2.5$ |

Table 3.3: Delivery parameters for each arm of the blue system. The frequency shift is measured at the fiber output and reference compared to the lock point of the laser. The power after fiber (PAF) is measured after a cleaning PBS cube, and the waist size indicates the approximate Gaussian beam waist ($1/e^2$) at the vacuum entrance position. The intensity is expressed in units of the saturation intensity $I_{\text{sat}} \approx 40.5$ mW/cm$^2$.

phase $\phi$ and sideband structure significantly impact the error signal used for stabilization. This behavior can be observed in Figure 3.6, which illustrates the effect of varying these parameters on the beat signal shape. Such flexibility in shaping the signal is crucial for optimizing the lock performance and stability. From our simulations, we have determined the necessity of designing an EOM (Electro-Optic Modulator) circuit with a modulation frequency, $\omega_{\text{EOM}}$, approximately equal to the natural linewidth of the blue transition, $\Gamma_{\text{Blue}}$. Additionally, electronic control over the phase of the signal is required to ensure precise modulation. To address this consideration, we built a custom-made EOM and its additional circuitry. The characterization of this EOM is detailed in full in the Appendix B. The next essential step is to generate two distinct blue laser beams. The beams enable the four-wave mixing interaction with the atomic sample.

### 3.2.5 Probe and Pump Beam Delivery

The MTS technique requires two independent, counter-propagating beams to interact with the atomic sample. Initially, we intended to construct a dedicated spectroscopy cell instead of using the main atomic source. However, after integrating the AOsense system, we identified the potential to use the perpendicular two-window spectroscopy port and designed our locking setup around this feature. For this setup, as seen in Figure 3.5, we allocated 80 mW of blue light from the main ECDL output, which was directed through a double-pass (DP) AOM configuration. The AOM used [5] operates at a center frequency of 350 MHz with a bandwidth of 150 MHz. This DP configuration is crucial, as it allows precise frequency shifts necessary for addressing various Strontium isotopes, with resonance frequencies separated by approximately 275 MHz.

Following the DP stage, a secondary SP AOM of the same model provides a fixed offset frequency shift of 350 MHz. The beam is then split using a polarizing beam splitter (PBS) cube, directing one path to the pump fiber and the other to the probe fiber. These two fibers, each 10 meters in length, transmit the beams from the blue laser table to the experiment table, where they are positioned on opposite sides of the spectroscopy windows.

For optimal polarization, a cleaning PBS cube is placed at the fiber output with a $\lambda/2$

[5] G&H 3350-199 AOMO

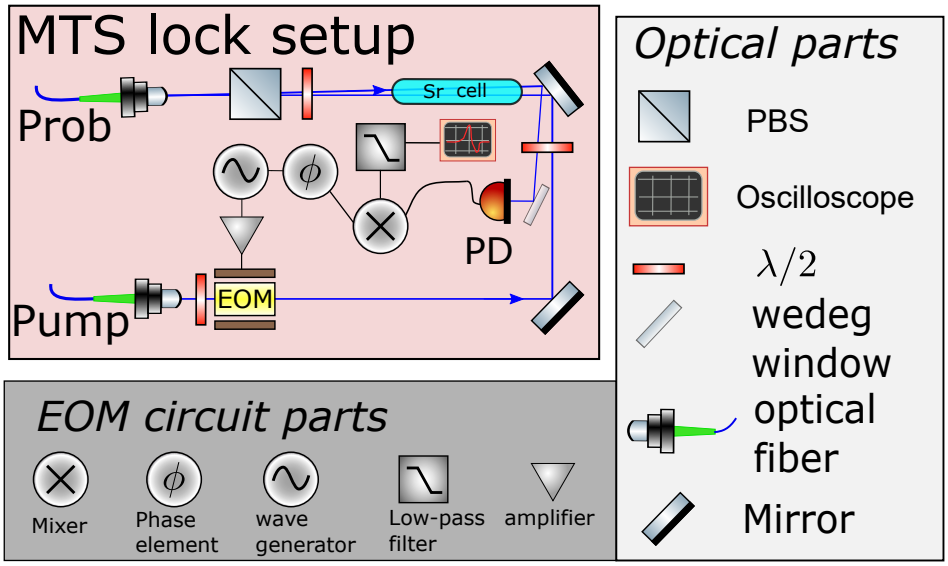


Figure 3.7: Modulation transfer spectroscopy setup. The two beams are split on the laser table and sent to two different optical fibers. The ratio between the beams is around 1:10, favoring the pump, and the probe signal is measured on a fast photodiode (>100 MHz BW). The signal is divided between the oscilloscope and the blue laser driver, where, together with the PIID options, the optimal lock point is found.

waveplate, eliminating unwanted $\pm\sigma$ transitions and thus providing a clean linear polarization for the probe beam [6]. The probe beam is then aligned into the vacuum chamber and directed to a fast photodiode.

The pump beam is also polarization selective to accommodate the requirements of the EOM, which is sensitive to the electromagnetic field direction of the propagating light. After the EOM, the pump beam transversely interacts with the atomic jet and is subsequently directed to a beam dump.

Measurement adjustments have shown that an optimal locking signal is achieved with a power ratio of approximately 1:10 between the probe and pump beams, with both beams maintaining a waist size of 0.5 mm, with about 16 mW for both beams. The two-beam configuration around the AOsense spectroscopy window is shown in Figure 3.7, including in the illustration as well are electronics in the demodulation circuit connected to the EOM and the fast photodiode, converting the sub-Doppler signal into an error signal. The beams parameters are reported in Table 3.3.

### 3.2.6 The sub-Doppler and lock signals

Utilizing the AOsense spectroscopy window, by probing the transverse flux of the atomic jet, one can already observe at an oven temperature of 350 °C a sub-Doppler signal. The MTS technique, which takes advantage of the Doppler effect, yields a bare momentum distribution of the atomic ensemble. By optically pumping the ground state, a distinct secondary peak emerges at the center of the Doppler-broadened signal. This sub-Doppler peak represents the

[6] As presented in the Doppler absorption testing section, a magnetic field exist around the spectroscopy window and by rotating the probe polarization, side peak do rise around the transition line center.

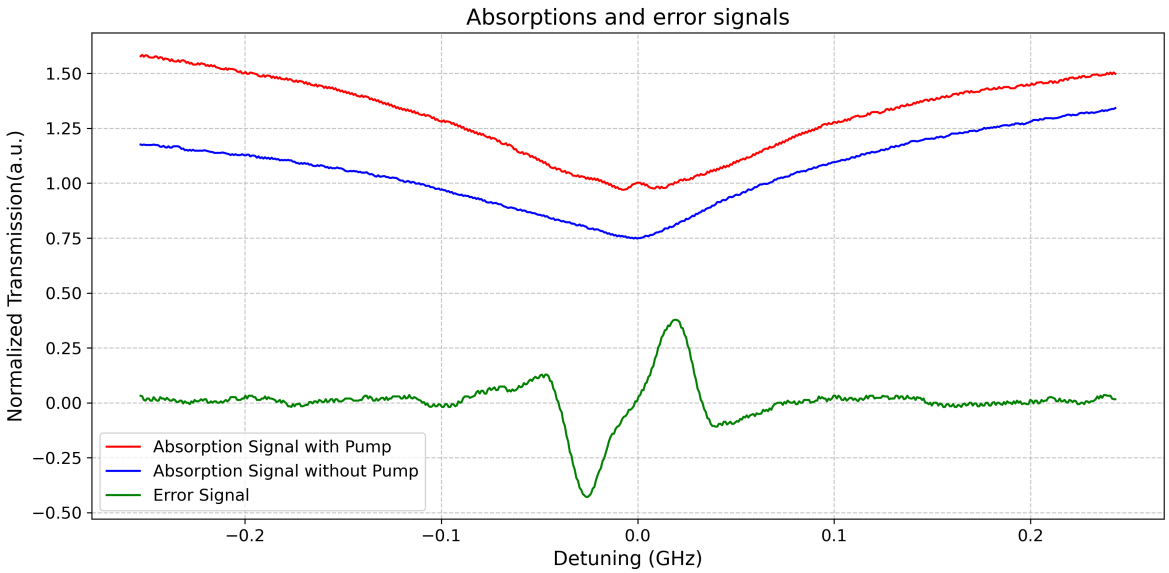


Figure 3.8: Comparison of absorption signals under different conditions. For an oven temperature of 430 °C, the single is dominated by the $^{88}$Sr isotope. The Doppler absorption signal is observed in the blue curve with the pump beam blocked with a 500 MHz scan around the resonance. Unblocking the pump causes the sub-Doppler peak to rise, as shown in the red curve. The green curve depicts the generated error signal, which is critical for stabilizing the laser frequency. The Y-axis is the voltage conversion from the probe beam transmission power sent to the PD. It is normalized by the gain factor of the photodiode, and the signals are vertically shifted for clarity.

intrinsic linewidth of the $^1P_1$ transition and corresponds to the level to which the laser is ultimately stabilized.

In Figure 3.8, we observe that blocking the optical pumping beam eliminates the sub-Doppler peak and the associated error signal, which originates from the gradient of the smaller peak.

The error signal is generated by mixing the photodiode signal with the modulated sine wave applied to the EOM at a frequency of 67.2 MHz. The resulting down-converted DC signal corresponds to the derivative of the absorption signal, shown in green in Figure 3.8. The locking point for the blue transition was validated by analyzing the error signal, processed through a low-pass filter with a cutoff below 1 kHz before being sent to the feedback input of the Moglabs laser driver and locked precisely at the zero crossing of the central slope.

The amplitude and quality of the error signal are influenced by both the linewidth of the transition and the electronic response of the circuit. To optimize the error signal, we adjust the phase introduced in the EOM circuit. This phase can be manipulated by varying the cable length between the EOM and the mixer. Proper phase alignment enhances the amplitude and steepness of the error signal, ensuring robust locking even when the modulation transfer spectroscopy (MTS) condition $\omega_{\text{res}}^{\text{EOM}}/\Gamma_{\text{blue}} < 1$ is not perfectly fulfilled. With the optimized phase and the proportional-integral-derivative (PID) module built into the laser driver, reliable frequency locking is achieved when the error signal has a minimum peak-to-peak amplitude of 12 mV.

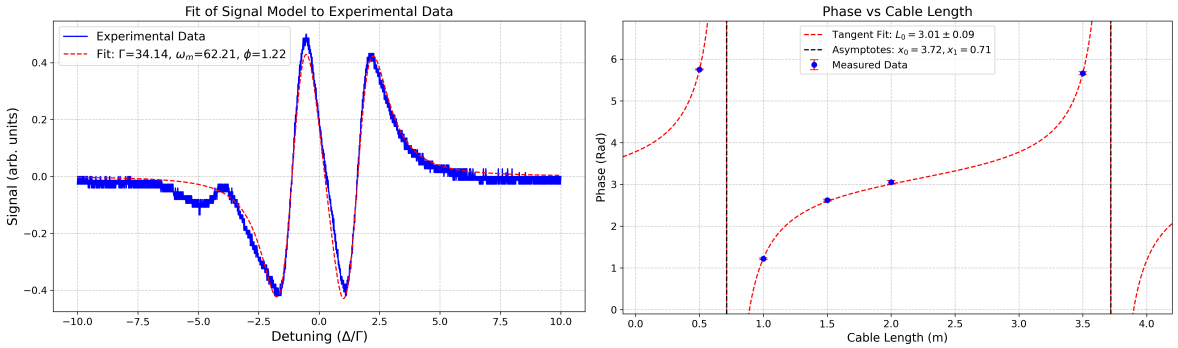


Figure 3.9: Error signal fit and phase evolution with cable length. The left panel presents the measured error signal obtained using the downconversion circuit with a 1 m cable between the mixer and oscillator. The red dashed line represents the fitted modulation transfer spectroscopy (MTS) beat signal for the $^1S_0 \rightarrow {}^1P_1$ transition, normalized to the corresponding linewidth. The right panel shows the extracted phase shift as a function of cable length, obtained by fitting the error signal model to experimental data. The phase evolution is modeled using a tangent function, yielding a full phase rotation corresponding to approximately $3.01 \pm 0.09$ m of cable.

In order to optimize the robustness of the lock, we investigated the effect of the phase; we recorded multiple datasets while varying the cable length between the EOM and the mixer. For each dataset, we ensured that the modulation bandwidth matched $\pm 10\Gamma_{\text{blue}}$ and verified this condition using a wavelength meter to monitor the laser frequency ramp.

In the left panel of Figure 3.9, we present an experimentally measured error signal over a frequency scan of approximately 1 GHz, with the oven temperature set to 430 °C. The MTS model was used to fit the error signal, with the linewidth and modulation frequency as free parameters bounded to ±15% of their known values. This flexibility accounts for power broadening, small EOM resonance fluctuations, residual nonlinear polarization effects, and signal contributions from other isotopes, such as $^{86}$Sr, which overlap with the dominant $^{88}$Sr signal. Indeed, in the experimental data, a pronounced mismatch at $\Delta/\Gamma_{\text{blue}} = -5$ arises due to absorption from $^{86}$Sr, the second most abundant isotope. Despite these challenges, the fit achieves a reduced chi-squared value of $\chi^2 \approx 1.16$, indicating good agreement with the experimental data, and the extracted parameters remain within 10% of their nominal values.

The fitted phase values were subsequently extracted for five different cable lengths to study the correlation between phase and length. As shown in the right panel of Figure 3.9, the phase evolves periodically with cable length, as expected for a signal propagating in a transmission line. The data confirm that increasing the cable length by integer multiples of a characteristic length returns the phase to its initial value. Specifically, phase measurements for 0.5 m and 3.5 m cables yield similar results. To model this behavior, we employed a simple trigonometric tangent function:

$$\phi(x; A, B, C) = A \tan(Bx + C) + \pi \tag{3.4}$$

Where $A, B$, and $C$ are free fitting parameters. The reason to choose this function is the noticeable periodicity of the error signal shape as we increased the cable length. Despite the limited sampling, the fit captures the observed phase evolution well, with a reduced chi-

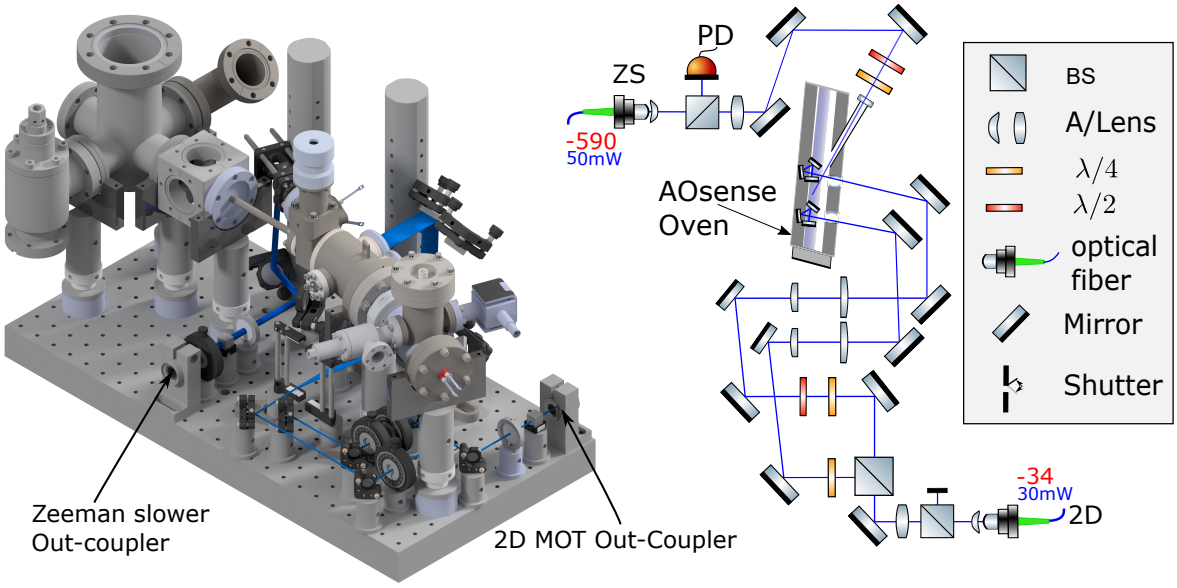


Figure 3.10: 2D and 3D schematic representations of the Zeeman slower (ZS) and 2D MOT setups integrated into the experimental system. The 3D representation illustrates the beam paths for one of the two 2D MOT beams and the Zeeman slower beam. The optical fibers exit through custom-designed out-coupler mounts (indicated by black arrows) placed at different sides of the stage, marking the beams' initial points. Not present in this figure are the pump and probe beams used for the locking setup.

squared value of $\chi^2 \approx 1.66$. From this model, we deduce that the characteristic cable length for a full $2\pi$ phase rotation is approximately $L_0 \approx 3.01$ m. Using different cables and touching the EOM resistance were all helpful in making the locking more stable and managing to shift the setpoint, thus imaging all four different isotopes in the 3D MOT while keeping the laser locked during the experiment.

### 3.2.7 Zeeman slower, mini-Zeeman & the 2D MOT

The beam delivery for the ZS and 2D MOT is fundamentally different. The Zeeman slower beam requires a power of approximately $P_{ZS} \approx 60\,\text{mW}$ and a detuning of $\Delta_{ZS} \approx -20\Gamma \approx -600\,\text{MHz}$ from the atomic resonance. In contrast, the 2D MOT beams demand a combined power of $P_{2D} \approx 30\,\text{mW}$ for both beams, with a detuning of $\Delta_{2D} \approx \Gamma \approx -30\,\text{MHz}$. Initially, the Zeeman slower arm incorporated two AOMs, which allowed us to achieve the required detuning and power.

After exiting the fiber, the Zeeman beam is shaped to match (see in Table 3.3 for detailed parameters) the conditions for optimal atomic deceleration (as given by AOsense) and sent to the hot window as shown in Figure 3.10. Its intensity is approximately $8I_{\text{sat}}$, and its polarization is adjusted to right-hand circular using a combination of $\lambda/4$ and $\lambda/2$ waveplates to properly address the Zeeman-split levels.

As shown in Figure 3.10, the beam delivery and shaping are depicted in both the 3D illustration and 2D schematic, highlighting the layout of the optical elements.

Custom-designed outcoupler mounts (indicated by the black arrows in the figures) are placed on the linear rail stage. For the 2D MOT, the beam is first cleaned with a PBS

and split into two paths using another PBS. One of these paths is rotated with a half-wave plate to match the polarization of the other, and quarter-wave plates convert both to circular polarization.

The resulting beams are then shaped by a cylindrical telescope into elliptical profiles with a 5:1 aspect ratio (favoring the table-parallel axis) and directed into the 2D MOT viewports via a custom periscope. Within the AOsense source, three internal mirrors reflect the beams to establish a light-pressure region that effectively cools and deflects the atomic jet toward the differential pumping tube. Together with several permanent neodymium magnets, we generate our 2D MOT configuration as both beams have an RHC polarization coming into the vacuum.

### 3.2.8 3D MOT beams delivery

Trapping the atoms as they exit the cube requires a beam configuration suitable for efficient magneto-optical trapping. A three-beam configuration was implemented, where each beam is retro-reflected.

The 3D MOT beams are derived from the main blue laser system, with each beam shaped to a gaussian waist of approximately 0.5 cm and have peak intensity on the order of $I_{\text{sat}}$ (see Table 3.3). The beams are arranged to propagate at angles of $+35°$ and $-35°$ relative to the cell in the X-Z plane, and the third beam is sent in-plane through a dichroic mirror. This 3D MOT beam configuration, as illustrated in Figure 3.11, is dictated by the spatial constraint set by a high-resolution vertical objective microscope. The microscope with NA $\approx 0.55$, is mounted within 1 mm size and located below the chamber.

Additionally, based on numerics and given the relatively high longitudinal velocity of the atoms entering the 3D MOT region, we introduced a counter-propagating beam in the cell with the atomic jet (named "mini-Zeeman slower). This beam operates as a Zeeman slower in the MOT quadrupole field and allows for to enhancement of the number of trapped atoms by a factor of five. This beam is specifically employed to slow atoms emerging from the AOsense source with longitudinal velocities of approximately 50 m/s. In our configuration, the mini-Zeeman beam is directed into the glass science chamber parallel to the longitudinal axis and works in conjunction with three retro-reflected MOT beams.

The mini-Zeeman beam itself is characterized by a smaller waist of 0.25 cm and operated at a peak intensity of $I_{\text{sat}}/4$, which ensures sufficient photon scattering for effective deceleration. Its detuning is set to $-2.5\ \Gamma$, with optimal values determined experimentally via simulations of atomic phase-space trajectories. These results confirm that incorporating the mini-Zeeman beam effectively boosts the MOT's capture efficiency by specifically addressing the high-velocity atomic class. To obtain the required polarization states, the incoming and back-reflected beams were configured to have opposite circular polarizations, as dictated by the radiation force condition of a MOT in Equation 3.8. Polarization alignment was verified using a polarimeter[7] positioned along the beam direction to replicate the atomic perspective, as seen from above the cell.

### 3.2.9 Imaging setup and techniques

The imaging beam is derived from the blue laser system and is controlled by a DP AOM. It is detuned near the ${}^1S_0 \rightarrow {}^1P_1$ resonance, and a mechanical shutter blocks any residual

[7] Schäfter+Kirchhoff Polarization Analyzer SK010PA

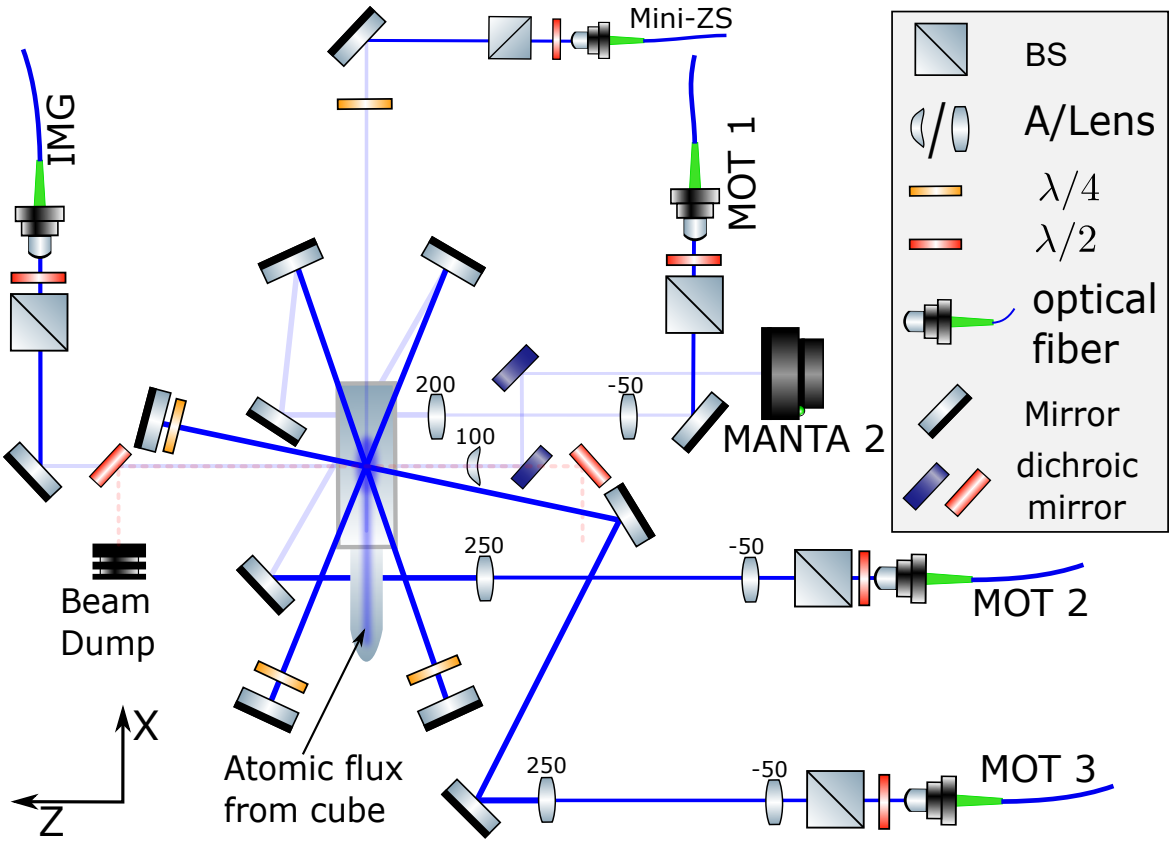


Figure 3.11: Optical layout of the 3D MOT, imaging, and mini-ZS setup around the SC. The figure depicts the paths of the three 3D MOT beams, the mini-Zeeman beam, and the imaging beam. MANTA 2, one of two MANTA cameras used for imaging, captures the X-Y plane, while the other MANTA camera (not shown) images the X-Z plane. The path of the 1040 nm dipole trap, indicated by a red dashed line, passes through the dichroic mirrors used for imaging. Note that shaded lines are only done for higher visibility and the repumping beams are not shown in this figure.

resonant light to prevent unwanted excitation of the atomic cloud. The beam supports both fluorescence and absorption imaging modalities; its delivery path is depicted in Figure 3.11, with key beam parameters detailed in Table 3.3.

### Fluorescence imaging

Fluorescence imaging is performed by exciting the atoms with the 3D MOT (and repumping beams for a stronger signal, which depends also on the exposure time), thereby inducing emission from the ${}^1S_0 \rightarrow {}^1P_1$ transition. This method allows monitoring the atomic cloud and is particularly useful for initial alignment and frequency optimization. In our setup, an *Allied Vision MANTA G-201B* camera, paired with a 100 mm lens, dichroic mirror, and a 460 nm bandpass filter, collects the emitted light with an effective numerical aperture of approximately 0.125. This configuration provides high-quality images of the cloud and aids in adjusting beam parameters to maximize trapping efficiency.

**Absorption imaging**

For absorption imaging, a square pulse (up to 120 $\mu$s) synchronizes the imaging beam with the camera, enabling spatially resolved measurements of the atomic cloud. The method relies on the Beer–Lambert law[141]:

$$\frac{I_{\text{fin}}}{I_{\text{init}}} = e^{-n_{2D}(\mathbf{r})\sigma}, \tag{3.5}$$

where $I_{\text{init}}$ and $I_{\text{fin}}$ are the incident and transmitted light intensities, $n_{2D}(\mathbf{r})$ is the column density of atoms, and $\sigma$ is the imaging cross-section. In practice, the density is determined by recording three intensity images—one without atoms, one with atoms, and one with a known background—allowing us to compute:

$$n_{2D}(\mathbf{r}) = -\frac{1}{\sigma} \ln\left(\frac{I_2 - I_0}{I_1 - I_0}\right). \tag{3.6}$$

In addition to the horizontal imaging setup, our system integrates a microscope objective (NA $\approx 0.55$) from *Special Optics* for high-resolution imaging. This microscope projects images onto both a secondary MANTA camera and/or an ANDOR Ixon Ultra 897 EMCCD from *Oxford Instruments*, the latter providing the single-photon sensitivity necessary for single-atom resolution.

## 3.3 The blue MOT

The first crucial milestone in the trapping and cooling sequence was the successful observation of atoms in a blue MOT. After assembling and aligning the necessary optical components, we began capturing data directly from the atomic ensemble.

The blue MOT operates on the broad ${}^1S_0 \rightarrow {}^1P_1$ transition at 461 nm. The laser is frequency locked to the resonance of the selected isotope to ensure stable operation. Auxiliary beams are independently shifted to achieve the optimal detuning necessary for maximizing atomic flux. This configuration results in an optimized atom number density within the MOT.

In this chapter, we detail both the theoretical framework and the experimental characterization of the blue MOT. We describe the optimized trapping parameters and configurations that enable efficient atom capture across various strontium isotopes. Fluorescence and absorption imaging results illustrate the performance of the blue MOT under different operating conditions, while lifetime measurements validate its stability. Moreover, we emphasize the necessity of the magnetic reservoir stage in enhancing loading rates and overall atom capture performance.

### 3.3.1 Theory of a broadband MOT

Before presenting the blue delivery system, which enables us to observe both 2&3D MOT, one should understand the conditions under which magneto-optical trapping works. When a two-level atom, traveling with velocity $\mathbf{v}$, resides in its ground state and encounters a laser photon possessing energy $\hbar\omega_L$, it absorbs the photon and undergoes excitation to a higher energy state. Through the principles of energy and momentum conservation, a correlation between the laser frequency and the atom's energy and velocity is established:

$$\omega_L = \omega_0 + \mathbf{k} \cdot \mathbf{v} + \frac{\hbar k^2}{2m} \tag{3.7}$$

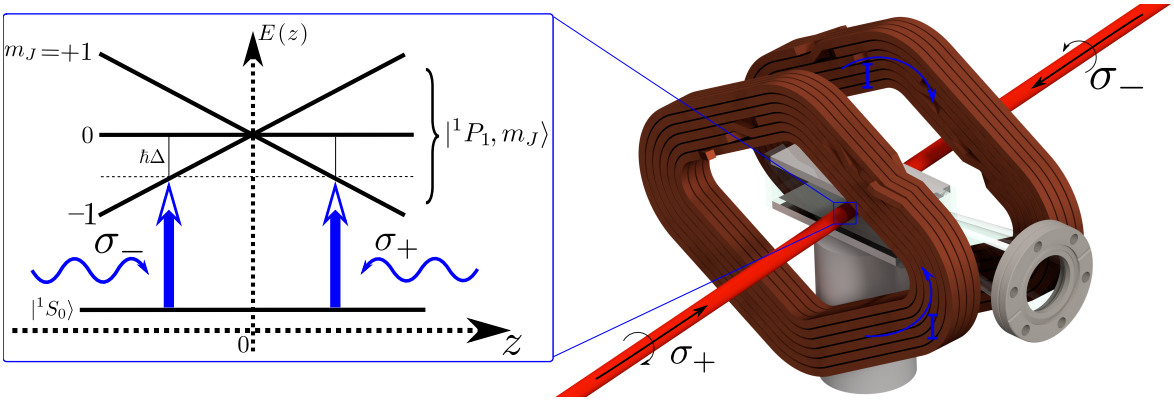


Figure 3.12: MOT working principle and setup schematics. The left panel presents the operating principle of an MOT that can be understood in a 1D model. An atom interacts with two counterpropagating beams red detuned from the $^1S_0$ to $^1P_1$ transition. A quadruple magnetic field lifts the degeneracy of the $^1P_1$ Zeeman states. Thanks to the magnetic field and the beam polarizations, an atom at $z < 0$ scatters more photons from the beam propagating towards $z > 0$ than from the opposite one, creating a restoring force towards $z = 0$. The right side is a 3D image of our diamond-shaped magnetic gradient field coils with our glass cell in the middle. To ease the image, we added only a single beam to show how the blue MOT beam intersects with the atoms. In blue arrows, we see that the current in the coils is opposite in the direction of the beam polarization.

where $m$ and $\mathbf{k}$ are the atom's mass and the wave vector of the incident light, and the final term represents the recoil shift caused by the photon's momentum. By carefully tuning the detuning $\Delta = \omega_L - \omega_0$ of the laser frequency relative to the atomic transition, it becomes possible to exert a velocity-dependent force, decelerating atoms and reducing their thermal motion[24]. For typical thermal velocities, and most transitions in alkali atoms as well as for the blue transition in strontium the recoil shift term in Equation 3.7 is negligible compared to the Doppler shift, particularly for transitions with lifetimes on the order of $\tau \sim 100\,\text{ns}$ and lower, and the detuning becomes $\delta = \Delta + \mathbf{k} \cdot \mathbf{v}$. As the atom absorbs and emits photons, in spontaneous emission, it can lose energy depending on the detuning, this process cools it down and slows the atom. We can see that by looking at the radiation pressure force[142]:

$$F_{\text{rp}} = \hbar k\Gamma \frac{\Omega^2/4}{\delta^2 + \Omega^2/2 + \Gamma^2/4} = \frac{\hbar k\Gamma}{2} \frac{s}{1+s} \xrightarrow{s\ll 1} \frac{\hbar k\Gamma}{2} s \tag{3.8}$$

Here, $\Omega$ and $\Gamma$ are the Rabi frequency and atomic natural linewidth, respectively (we assume low saturation parameter in the last transition). As an atom decelerates, its Doppler shift decreases, which in turn alters the effective detuning between the laser frequency and the atomic transition. For red-detuned light, this generally results in a reduced scattering force. However, the extent of this reduction depends on both the initial velocity of the atoms and the specific value of the detuning. We define the saturation parameter $s$ in Equation 3.8 as:

$$s = \frac{\Omega^2/2}{\Gamma^2/4 + \delta^2}, \quad s_0 = \frac{I_L(\mathbf{r})}{I_s} = \frac{2\Omega^2}{\Gamma^2} \tag{3.9}$$

where $I_L(\mathbf{r})$ is the laser intensity, and $I_s = \frac{\hbar\omega^3\Gamma}{12\pi c^2}$ is the saturation intensity. These parameters establish the relationship between light intensity and the scattering process for a

two-level system. The saturation intensity for our ${}^1S_0 \rightarrow {}^1P_1$ is $I_s \approx 40[\mathrm{mW/cm^2}]$. So far, no magnetic field has been introduced, and the use of only light to cool atoms is referred to in the literature as molasses cooling [143]. Applying a spatially dependent magnetic field $B(\mathbf{r})$ causes the atomic energy level to split into Zeeman levels, with the shift correlated to the magnetic field strength. This effect alters the Doppler cooling shift, bringing a Zeeman shift into the game and trapping the atom in the center of the gradient field. To see why this is the case, let's look at a single beam entering the science chamber between our diamond-shaped collies and hitting the atom on the 1D Z-axis as illustrated on the right side of Figure 3.12. If the beam is polarized $\sigma^+$ and we retro-reflect it such that the back-propagating beam is $\sigma^-$, then a ground state atom on the left side of the magnetic field feels a greater radiation force. This force is minimized as the atom moves towards the zero gradient field, and symmetrically, the right side atoms feel the opposite circular polarized beam and them too are also pushed inward. The atomic detuning writes:

$$\delta_\pm = \Delta \pm \mathbf{k}\cdot\mathbf{v} \pm \mu_E \nabla |\mathbf{B}| \cdot \mathbf{r}, \tag{3.10}$$

where $\nabla|\mathbf{B}|$ is the 3D magnetic field gradient, written as

$$\nabla |\mathbf{B}| = \left(|\partial_x B_x|, |\partial_y B_y|, |\partial_z B_z|\right)$$

coupled to an effective magnetic moment $\mu_E = g_J \mu_B/\hbar \approx 1.4$ MHz/G, where $\mu_B$ is the Bohr magnetron and $g_J$ is the Landé g-factor, which depends on the Zeeman level it's linked to. Assuming a 1D gradient field and placing this new Doppler shifts Equation 3.10 into the Equation 3.8 we get:

$$\begin{aligned} F_{\mathrm{1D,MOT}} = F_{\mathrm{rp},+} + F_{\mathrm{rp},-} &= \frac{+\hbar k \Gamma s_0/2}{1 + s_0 + \left[\frac{2(\delta_+)}{\Gamma}\right]^2} + \frac{-\hbar k \Gamma s_0/2}{1 + s_0 + \left[\frac{2(\delta_-)}{\Gamma}\right]^2} \\ &\approx \frac{\Delta}{\Gamma} \frac{8\hbar k s_0}{1 + s_0 + \left[\frac{2\Delta}{\Gamma}\right]^2} (k v_z + \mu_E |\partial B_z| z) \end{aligned} \tag{3.11}$$

where $v_z$, $z$ is the velocity and displacement in the z-direction, and the last approximation is done under the assumption of a slow moving atom near the center of the trap $k v_z,\ \mu_E |\partial B_z| z \ll \Gamma\sqrt{1+s_0}$, which fits with our blue broad linewidth. We see that depending on the detuning, we get a repulsive $\Delta > 0$ or an attractive $\Delta < 0$ force, and the latter is needed to trap and cool the atoms. Our anti-Helmholtz MOT coils configuration as seen in Figure 3.12 can generate a gradient, up to $B' \approx 55[\mathrm{G/cm}]$ on the $Z$-axis at the center of our MOT[8]. If we add two more beams in the same way, we get a 3D MOT, and with only two beams, we have a 2D MOT as it is built into our AOsense atom source.

### 3.3.2 Characterization of the 2D MOT Signal in the First Vacuum Cube

Initial characterization focused on investigating the impact of the 2D MOT beams on the atomic stream entering the vacuum chamber. This was achieved by sending an absorption beam transversely to the atomic jet direction through a window in the CF40 cube immediately after the DPT at the AOSense source output. The frequency was varied around the blue cooling transition, and the absorption signal was recorded at an oven temperature of $T = 430$ °C.

[8] We do not use such strong gradient field at the moment, but is possible to generate this magnitude

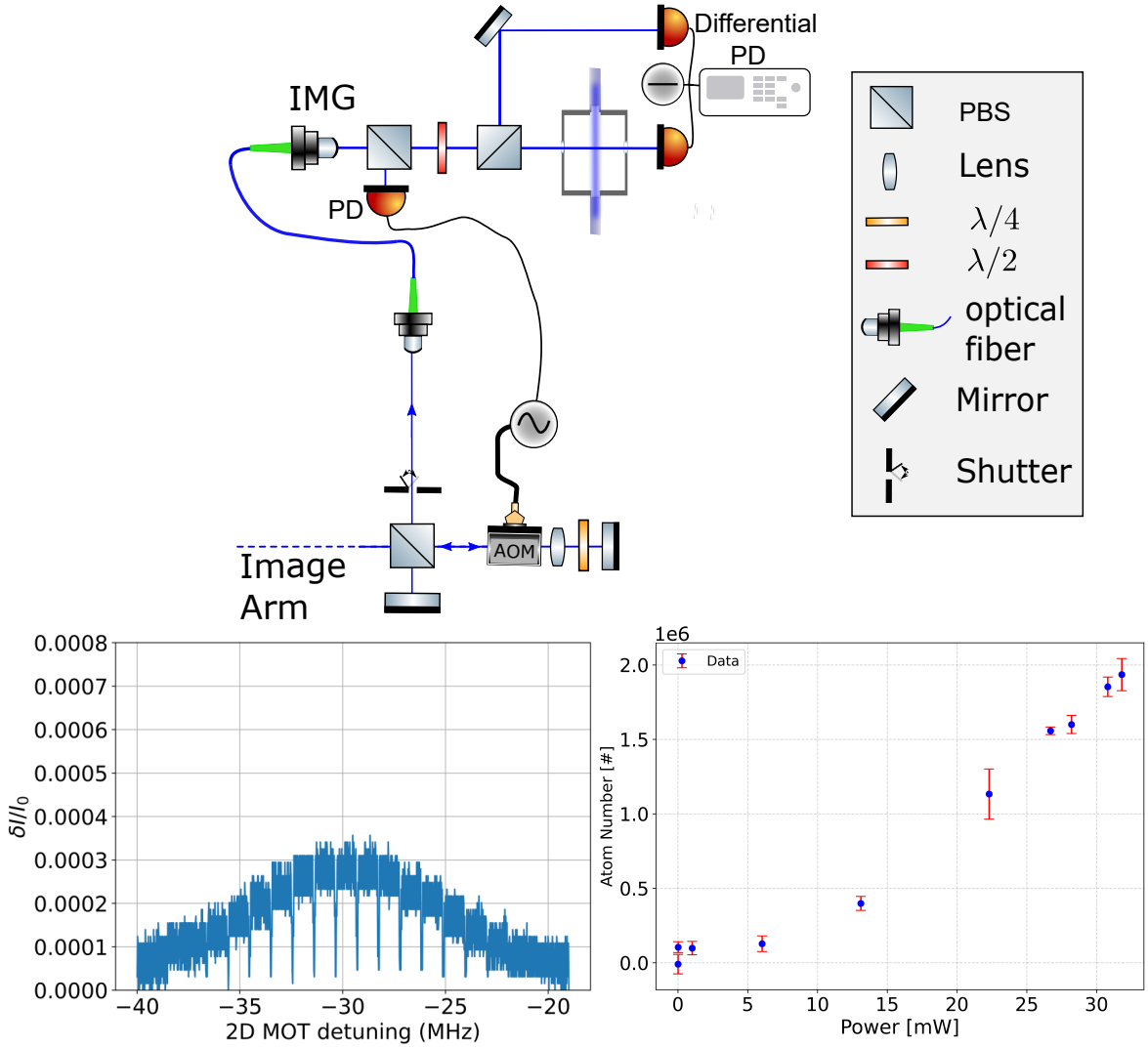


Figure 3.13: Schematic of the differential absorption setup and characterization of the 2D MOT in the first vacuum cube and main SC. The left Top panel illustrates the optical setup, where the imaging beam is split by a PBS, with one path traversing the vacuum cube and the other serving as a reference. These two beams are then directed onto a balanced photodiode for differential measurement. The absorption intensity, denoted as $\delta I/I_0$, is measured for different imaging beam powers, as seen in the bottom left plot. The image displays the time-dependent differential absorption signal, obtained by varying the 2D MOT detuning at a frequency of 2 Hz. While not shown in the diagram, a power stabilization circuit is implemented to mitigate the effects of minor power drifts on the measurement. In the last plot (right bottom), the number of atoms trapped in the 3D MOT is measured as a function of the 2D MOT power for a detuning of $-30$ MHz.

The presence of atoms in the first vacuum cube, after the output aperture and differential pumping tube, was initially confirmed by observing a fluorescing cloud using resonant light illumination, indicating that the atomic beam was propagating towards the science chamber. To quantify the atomic beam density, a differential absorption setup was implemented, as

depicted in the top panel of Figure 3.13. This setup uses the resonant imaging beam, which is split by a PBS. One beam passes through the atomic beam and is detected on a balanced photodiode system, while the other serves as a reference. The two signals are electronically subtracted ($\delta I = I_0 - I_a$) where $I_0, I_a$ are the bare intensity and the absorption intensity, respectively, and the imaging beam power is stabilized using a closed-loop digital PID controller acting on the AOM, reducing fluctuations from 15% to 4% on the photodiode. As the atoms come out of the differential tube, they expand as they pass through the pumping chamber, and to figure out their density, one should choose a beam that is on the order of the flux size cross-section we interrogate with. For us, it was roughly 5 mm. We use 1 mW of power in this beam to stay well below saturation intensity. This absorption spectroscopy method is commonly used in cold atom experiments. Optimal atomic beam flux was achieved by balancing the power between the two 2D MOT beams, with the first beam receiving 70% of the total power and the second beam 30%. The polarization of the first 2D MOT beam proved to be a critical parameter influencing absorption, while the second beam's polarization exhibited a smaller effect. Despite the Zeeman slower beam's fluorescence dependence on its polarization and power, neither parameter influenced the absorption signal. Notably, the only cooling and trapping effects were found to originate from the first 2D MOT section, as evidenced by the persistence of the absorption signal even in the absence of the Zeeman beam.

The power and beam size we use gives $I_{\text{im}} \approx 0.07 I_{\text{sat}}$ while still giving us a sufficient absorption signal on the photodiode. The absorption signal was used to determine the atomic density and flux by measuring the change in the photodiode signal when the 2D MOT was on or off while sweeping the 2D MOT frequency. The photodiode signal initially increased, followed by distinct dips corresponding to the discrete scanning steps of the 2D MOT frequency sweep. The depth of these dips, relative to the signal when the 2D MOT was off, was used to quantify the absorption and, thus, deduce the atomic beam density. Scanning the 2D beam frequency and observing the light reflected from the mirrors inside the AOsense 2D section assist in finding the resonance by the maximal absorption point. This acted as our reference point to optimize the detuning for these beams. The absorption spectrum as seen in Figure 3.13 left bottom figure, showed a smooth increase peaking around $-\Gamma_{\text{blue}}$, followed by a decrease as the 2D MOT frequency approached the resonant frequency. To quantify the atomic density from our absorption measurements, we employed the Beer-Lambert law. In the low-absorption regime, this law simplifies to a relationship between the column-integrated density, $n_c(x, y)$, and the fractional absorption of the probe beam.

A rough estimate can be obtained by using the low absorption approximation of the Beer-Lambert law [24], which relates the density to the change in intensity of the probe beam:

$$n_c(x, y) = -\frac{2\pi}{3\lambda^2}\left(1 + \left(\frac{2\delta}{\Gamma}\right)^2\right) \ln\left(\frac{I}{I_0}\right), \tag{3.12}$$

where again $n_c(x, y)$ is the column integrated density, $\delta$ is the detuning from the resonant frequency, and $\Gamma$ is the linewidth of the atomic transition. For resonant excitation ($\delta = 0$) and in the low absorption regime, this simplifies to:

$$n_c(x, y) \simeq \frac{2\pi}{3\lambda^2}\frac{\delta I}{I_0}, \tag{3.13}$$

where $\delta I = I_0 - I$ is the absorbed intensity. By applying this approximation to our absorption measurements seen in Figure 3.13 spectra, we obtained a column-integrated atomic

| Parameter | Probe Beam | Zeeman Beam |
|---|---|---|
| Waist Size pre-vacuum (mm) | 0.6 | 2 |
| Max power pre-vacuum (mW) | 25 | 80 |
| Frequency Range (MHz) | ±600 | discretize ±150 |
| Focusing beam diameter | 1.2 mm → 0.44 mm | 4 mm → 3.3 mm |
| Polarization | Linear (horizontal) | Right-hand circular |

Table 3.4: Beam parameters for the Zeeman spectroscopy measurements. Note that focusing of the beam in the atom position is estimated using an optical simulation, and the polarization was measured with a polarimeter right before the vacuum.

density of approximately $3.25 \times 10^5\,\mathrm{cm}^{-2}$. In our measurements, the longitudinal velocity of the atomic beam was determined by recording the signal delay in the cube chamber after the 2D MOT beams were switched on, yielding a velocity of approximately 40 m/s. Given a beam diameter of 1 cm at the center of the cube, we estimate the atomic flux to be on the order of $3 \times 10^9$ atoms per second.

This value remains approximately one order of magnitude lower than expected, which is not surprising in the absence of a functional Zeeman slower. According to the manufacturer's specifications, an operational Zeeman slower should enhance the atomic flux by roughly a factor of 15, highlighting the critical role of the Zeeman slower.

### 3.3.3 Investigation of the Zeeman slower performance

The Zeeman slower (ZS) is a critical component that decelerates the atomic beam emerging from the AOSense oven, from velocities around 400 m/s down to approximately 40 m/s, thereby enhancing the capture efficiency of the 2D MOT and increasing the loading rate of the 3D MOT. In a Zeeman slower, the spatially varying magnetic field $B(z)$ induces a Zeeman shift that compensates for the Doppler shift as atoms slow down, maintaining resonance with the cooling light. This resonance condition is expressed as [144]:

$$\delta = \frac{\mu B(z)}{\hbar} - \mathbf{k} \cdot \mathbf{v},$$

which maximizes the radiation pressure force on the atoms. By directing the beam through the differential pumping tube into our experimental cube, our observations indicate that the ZS beam has not produced a significant effect on the atomic density. This unexpected result has motivated a detailed investigation into the Zeeman slower's performance.

The first observation was that no atom signal enhancement in the cube was seen for Zeeman detunings ranging from –450 to –690 MHz relative to the blue transition) without observing the expected modulation in the atomic signal. To probe the effect of the Zeeman beam more directly on the atomic velocity distribution emerging from the Zeeman slower section, we designed and constructed a tunable ECDL capable of scanning over a GHz range. This approach enabled us to perform dedicated Zeeman spectroscopy measurements. The key beam parameters used in these experiments are summarized in Table 3.4. In our setup, the probe beam is power-stabilized to avoid fluctuations in the observed signal and focused through the entire system to hit the side of one of the inner vacuum walls near the 2D MOT window. It maintains a linear horizontal polarization, and the scattered light that makes it out of the 2D viewport is collected via two f=200 2-inch lenses in a series. A 460 nm Bandpass

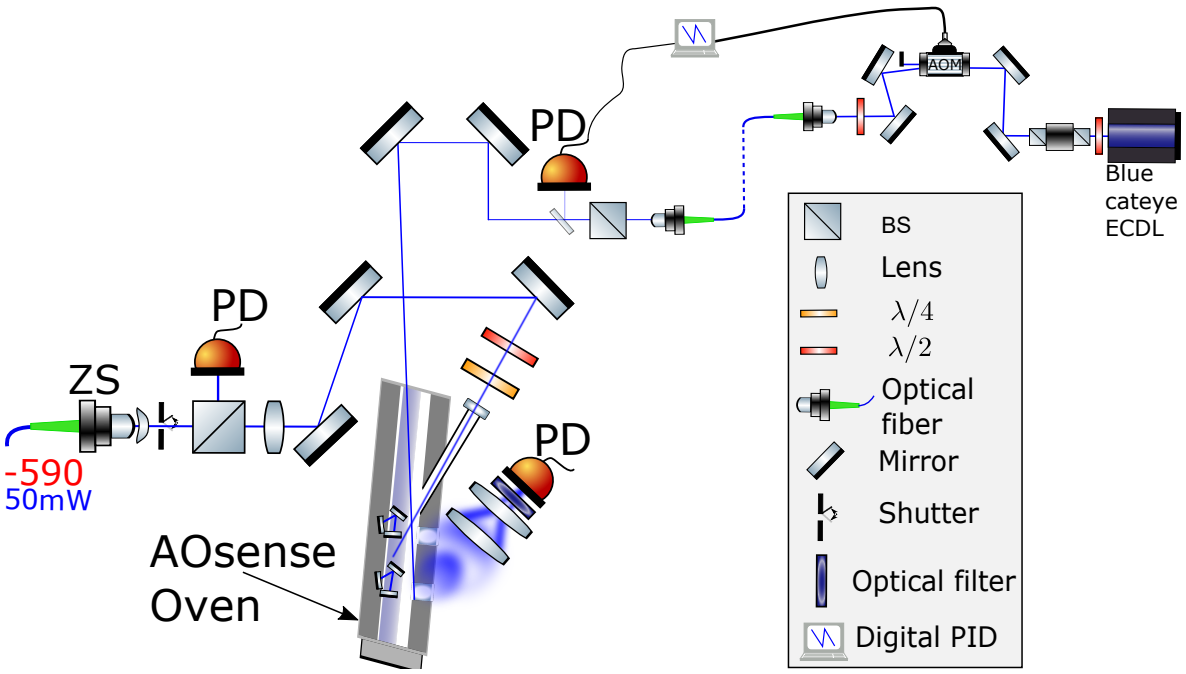


Figure 3.14: Setup for spectroscopy at the Zeeman section output. A homebuilt ECDL with about 2 GHz mode-hop free tuning range is directed from the glass cell towards the oven output. It hits an internal corner in the vacuum system near the Zeeman slower section output, and the scattered light is collected on a photodetector. While the ECDL laser is modulated over about 0.9 GHz, a Zeeman beam is directed through the hot window towards the oven, with a tunable detuning of 300 MHz bandwidth to evaluate its influence on the atomic flux.

filter[9] was added before the PD to filter any stray light and improve the SNR. The Zeeman beam is slightly focused over the range Zeeman slower section from 4 mm to 3.3 mm and set to right-hand circular polarization. The architecture of this experiment is illustrated in Figure 3.14, showing both of the beams' paths.

Velocity spectroscopy measurements were then performed to evaluate the impact of the ZS on the atomic beam at temperatures of 430 °C and 450 °C. A probe beam was scanned across a 1 GHz frequency range, with the resulting signals captured using a custom imaging system. While fluorescence is visible in front of the oven, indicating photon scattering, only a small fraction of atoms were shifted in velocity distribution as seen on the left of Figure 3.15. By detuning the Zeeman beam frequency discretely using the blue laser lock point, the position of the deep changes over the momentum distribution. The difference signal was obtained with the Zeeman beam being on and off. We then extract from the data the velocity class the Zeeman address, in the frequency domain, by finding the maximal gradient position. The same analysis should also make visible to which lower velocity class the addressed atoms are shifted to. Looking at Figure 3.15 left panel, this effect is on the scale of the entire momentum distribution quite small but noticeable the deep around 0.7 GHz is followed by a slight increase at a lower frequency (0.64 GHz), meaning that indeed atoms were decelerated, but too small of a fraction and by less than 10% of their original velocity. We can repeat it for varying

[9] *Thorlabs* FBH460-10

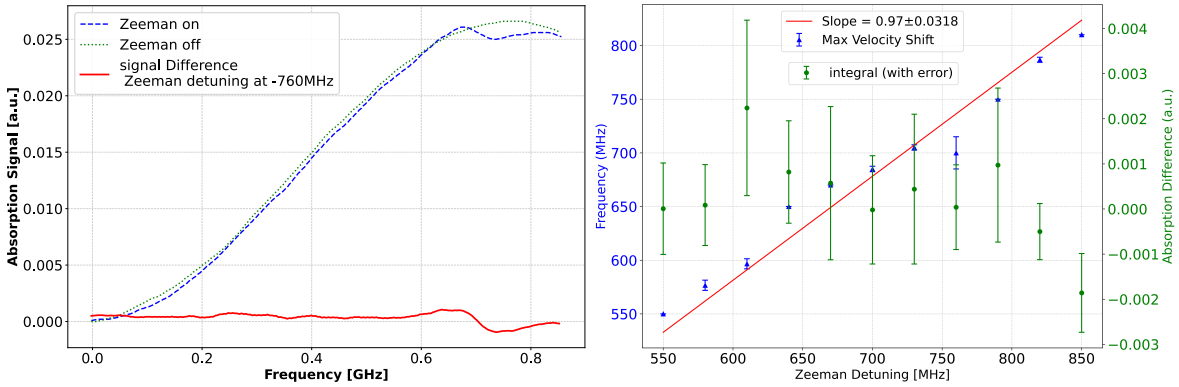


Figure 3.15: Zeeman slower velocity distribution for different beam detuning at an oven temperature of 430 °C. On the left panel, the probe beam spectrum with and without Zeeman. The subtraction of the two signals is presented in red, and by analyzing its maximal gradient and amplitude for different Zeeman detuning, its effect becomes apparent, as seen in the right plot. The slope position represents the class of atoms the Zeeman addresses (blue arrows), and by integrating over the low-frequency region, shows the atom shifted to the low-velocity class(green circles). Using linear fit for the slope position and atomic frequency class, we get an almost 1:1 relation between them, indicating that the beam does interact with the atomic jet. However, the fact that we see no increase of atomic signal for low velocity class means that the Zeeman is ineffective.

Zeeman beam detuning (-550 to -850 MHz), the results are presented in the right plot of Figure 3.15, showing a linear correlation (seen by a linear fit in red) between Zeeman and atomic distribution frequencies. Additionally, we integrate from zero to 0.35 GHz over the difference signal.

This region of integration should show a population increase as atoms are decelerated by the Zeeman beam, reaching lower speeds. However, no apparent effect was seen in the lower class velocity from the number of atoms. This result suggested two possible scenarios: either the magnetic field gradient of the ZS was not correctly configured, thus preventing effective deceleration of the atoms, or insufficient light power was reaching the atoms from the HW, resulting in inadequate deceleration for capture by the 2D MOT.

It is suspected that the hot window is coated significantly, attenuating the transmission of the 461 nm light as it enters the vacuum system. An attenuation of at least a factor 20 has been estimated by comparing the fluorescence of the probe beam and Zeeman beams in their crossing region for the same detuning and power. The strong influence of the 2D MOT field on the fluorescence, combined with the beam angle, introduces variables that make precise quantitative comparisons challenging. Therefore, while these observations point toward a potential issue with the HW, further quantitative measurements are required to confirm the origin of the observed attenuation. Unfortunately, at the time of this writing, AOSense still has not acknowledged an issue with the system they shipped, and did not provide any measurements for our system before shipping.

Despite thorough testing, including adjustments to frequency detuning, beam alignment, and polarization, the Zeeman slower failed to produce measurable effects on the atomic beam's velocity. Future work will focus on increasing the atom flux by other means such as transverse cooling in the vacuum cube before the SC, repumping schemes using 688 nm laser in the glass

cell, and optionally more exotic ideas such as using a 2.92 $\mu m$ repumping from the hot window to push atoms back to the cycle[145]. And at the moment, a new source is being developed to ship the current one back for examination and readjusting to match original specifications similar to [146].

### 3.3.4 Characterization and Optimization of the 3D Blue MOT

After seeing atoms in the pumping cube section, our focus now is shifted towards trapping atoms in the 3D MOT in the science chamber.

With atoms traversing from the 2D MOT through our vacuum cube and into the SC, a faint fluorescence signal was initially observed during continuous operation of the 2D MOT, with the oven maintained at 450 °C. This preliminary signal was captured using a MANTA camera coupled with a basic 4f optical imaging system. This initial observation enabled us to improve the MOT NoA and lifetime by several orders of magnitude. Key improvements included precise alignment of the beams to mitigate the effects of interference fringes resulting from the non-coated SC glass cell, as well as the implementation of repumping light during the imaging phase. The optimal beams parameters can be seen in Table 3.2. To assess the number of atoms within our MOT, we employed fluorescence imaging, a well-established technique for characterizing cold atomic systems [24, 96].

We observed that the fluorescence signal reaches saturation at longer exposure times. This can be attributed to atomic decay into the metastable reservoir in the absence of repumpers, as described in [96], and that the MOT exhibits a finite lifetime.

To estimate the number of trapped atoms, my colleagues performed the following experiment. In the absence of repumpers, we switched off the source and integrated the fluorescence of the MOT over time afterwards. Assuming all atoms during the imaging have been lost due to decay outside of the blue transition. The total signal is directly correlated to the total atom number. The number of scattered photons ($\Theta_s$) is described by:

$$\Theta_s = \Gamma_s(\Delta)\, N\, T_{exp}, \tag{3.14}$$

where $\Gamma_s(\Delta)$ is the scattering rate, $N$ is the NoA, and $T_{exp}$ is the exposure time. Assuming isotropic scattering, the fraction of photons captured by our imaging system ($\Theta_C$) is determined by the optical cross-section ($\sigma$) and can be approximated using the NA:

$$\Theta_C = \Theta_s \frac{\sigma}{4\pi f^2} \approx \Theta_s \frac{\pi d^2}{4\pi f^2} \approx \Theta_s \frac{(\mathrm{NA})^2}{4} \approx 0.004 \times \Theta_s, \tag{3.15}$$

where $d$ and $f$ are the radius and focal length of the imaging setup, respectively, and the numerical aperture is calculated as $\mathrm{NA} = \sin(\arctan(d/f)) = \sin(\arctan(12.7/100)) \approx 0.126$. This approximation is valid under the assumption of small angles. The detected photon count ($N_c$) is then related to the number of captured photons by the quantum efficiency (Q) and the camera gain (g):

$$N_c = Q g\, \Theta_C. \tag{3.16}$$

The camera gain was calibrated by measuring the variance and mean pixel values over a homogeneous area under varying light intensities. By leveraging the Poissonian statistics of photon scattering, we know that the variance of the number of photoelectrons is equal to the number of photoelectrons, thus, the variance of the detected counts scales linearly with the gain parameter: $\mathrm{var}(N_c) = g\, N_c$.

In reality, the blue MOT is not a closed two-level system due to the decay channel into the metastable reservoir. To account for this, we assumed that the number of atoms within the 3D MOT decayed exponentially over time with a decay time constant $t_0$:

$$N(t) = N_0\, e^{-t/t_0}. \tag{3.17}$$

The total number of scattered photons over time is then given by:

$$N_c(t) = \Gamma_s\, N_0 \int_0^T e^{-t/t_0}\, dt = \Gamma_s\, N_0\, t_0\, (1 - e^{-T/t_0}), \tag{3.18}$$

where $\Gamma_s = \frac{\Gamma}{2}\frac{s}{1+s}$ is the scattering rate, with $s$ being the saturation parameter, and $t_0 = \alpha\frac{1+s}{s}$ is the decay time constant, where $\alpha = 1.56 \times 10^{-3}$ s, as determined in Ref. [96]. For long exposure times, the scattered photons saturate to a value of $N_c = \frac{\Gamma}{2}N_0 t_0$, which is independent of light power, exposure time, and detuning, requiring only knowledge of the decay rates of the blue transition and the decay channel to the reservoir. This allows us to obtain a rough estimate of the number of atoms in our blue MOT using fluorescence imaging.

The blue laser system enables flexible isotope addressing by tuning the lock frequency via a DP AOM in the probe-pump path. Frequency shifts within 20 MHz allow switching between isotope transitions while preserving lock stability, enabling blue MOT operation for different Strontium isotopes.

To demonstrate the versatility of the system, we trapped all strontium isotopes by shifting the lock point as shown in Figure 3.16. For this measurement, the magnetic field gradient was ramped to 16.6 G/cm along the X-axis, the standard operating value for the high-gradient MOT configuration. The 2D MOT, 3D MOT, and mini-ZS beams were activated to load atoms into the blue MOT. The ZS beam was deliberately inactive due to its observed lack of effect. To maximize the atomic signal, we individually tuned the repumping beams for each isotope during the imaging period.

Following the repumped MOT loading phase that saturates for all isotopes after approximately 1 second, the 2D MOT and Zeeman blue beams are deactivated. The atoms are then imaged by recording the fluorescence signal of the scattered photons while both repumping and 3D MOT beams are on, with exposure times ranging from 1 ms to 10 ms, depending on the isotope. We then rapidly ramp down the magnetic field (around 0.1 ms) and wait for the atoms to disperse for another 100 ms before reactivating all imaging-related beams to acquire a reference image. The atom image is then subtracted from the reference image to provide a less noisy image and remove unnecessary artifacts from the atomic cloud background, from which the atom number is calculated using Equation 3.18 and the camera and imaging parameters (imaging time, camera gain, etc). This configuration offers higher signal collection efficiency than absorption imaging, making it particularly suitable for detecting low-density atomic clouds in the MOT.

By shifting the lock point of our blue laser system using a locking AOM with a total scan range of 300 MHz, we can capture all stable Strontium isotopes. The resonance peaks, obtained from Gaussian fits, are presented in Figure 3.16.

Additionally, for less abundant isotopes such as $^{87}$Sr and $^{84}$Sr, the Blue MOT absorption signal saturates at a lower value, which hampers robust evaporative cooling toward quantum degeneracy. To address this challenge, atoms are first accumulated in a magnetic reservoir trap during the MOT phase. However, efficient repumping is essential to transfer these atoms back to the ground state for continued cooling. For all bosonic isotopes, the measured resonance

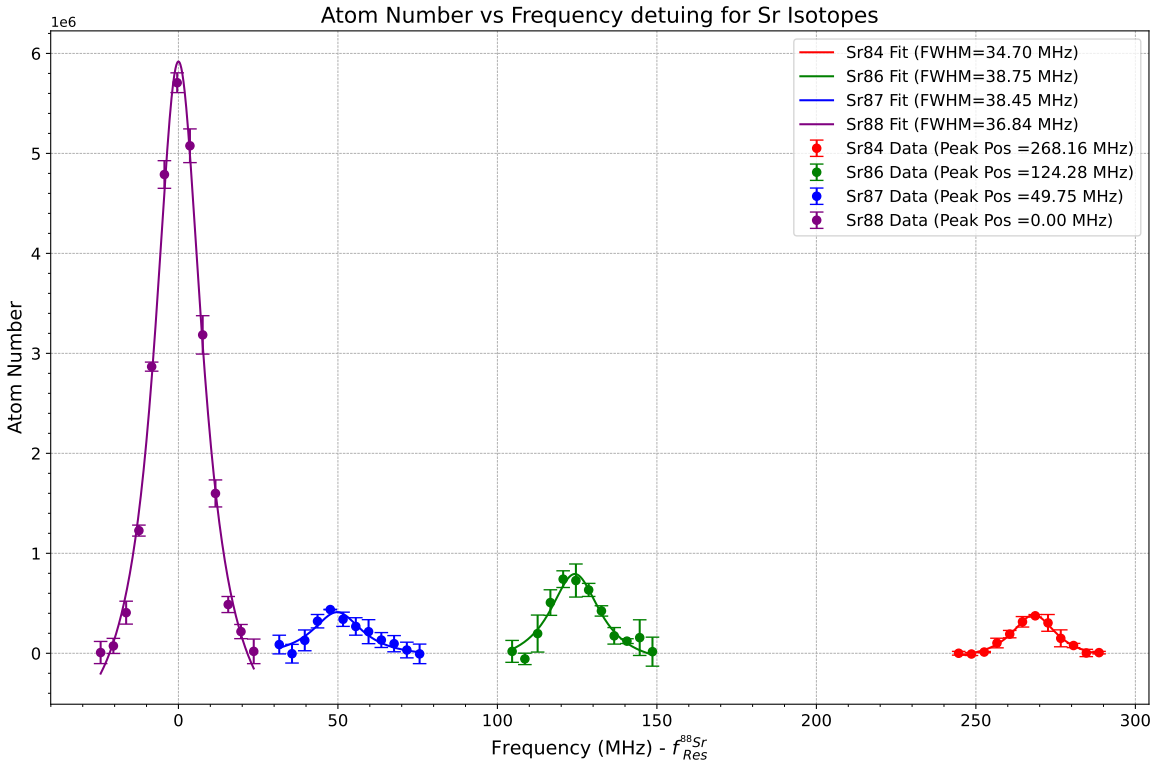


Figure 3.16: Atom number as a function of laser detuning for all stable Strontium isotopes. The data were fitted to Gaussian profiles, from which the FWHM and peak positions were extracted. The fitted FWHM values for all isotopes are shown in the legend, and the peak positions are reported relative to the $^{88}$Sr resonance. The extracted values for peak position and width all match within a few percent of the known theoretical and experimental values. Note that the relative peak heights of $^{84}$Sr and $^{87}$Sr do not reflect the natural abundances of these isotopes, as experimental parameters such as loading time and imaging duration were optimized independently for each isotope(more information in the text).

peak positions and widths are in close agreement with previous reports, with deviations under 1%, where the $^{88}$Sr and $^{86}$Sr, have a peak height difference (showcasing the natural abundance difference) of 7.6(6)% within 10% of the expected value [147] which can be attributed to the time difference between measurements that may have caused a drift in beam power and frequency. For the other two isotopes $^{84}$Sr and $^{87}$Sr, the measurements were performed under different experimental conditions due to their lower natural abundance and increased loss mechanisms [84]. Such variability reinforces the use of a repumping strategy involving the reservoir magnetic state that will be discussed in the repumping section.

## 3.4 Repumpers and Shutter System

The $^1S_0 \rightarrow {}^1P_1$ cooling transition, while effective for initial laser cooling, is not a closed cycle; a significant fraction of the excited-state atoms decay through the $^1D_2$ state, populating the metastable $^3P_2$ reservoir state. While atoms in the $^3P_1$ state quickly decay back to the ground

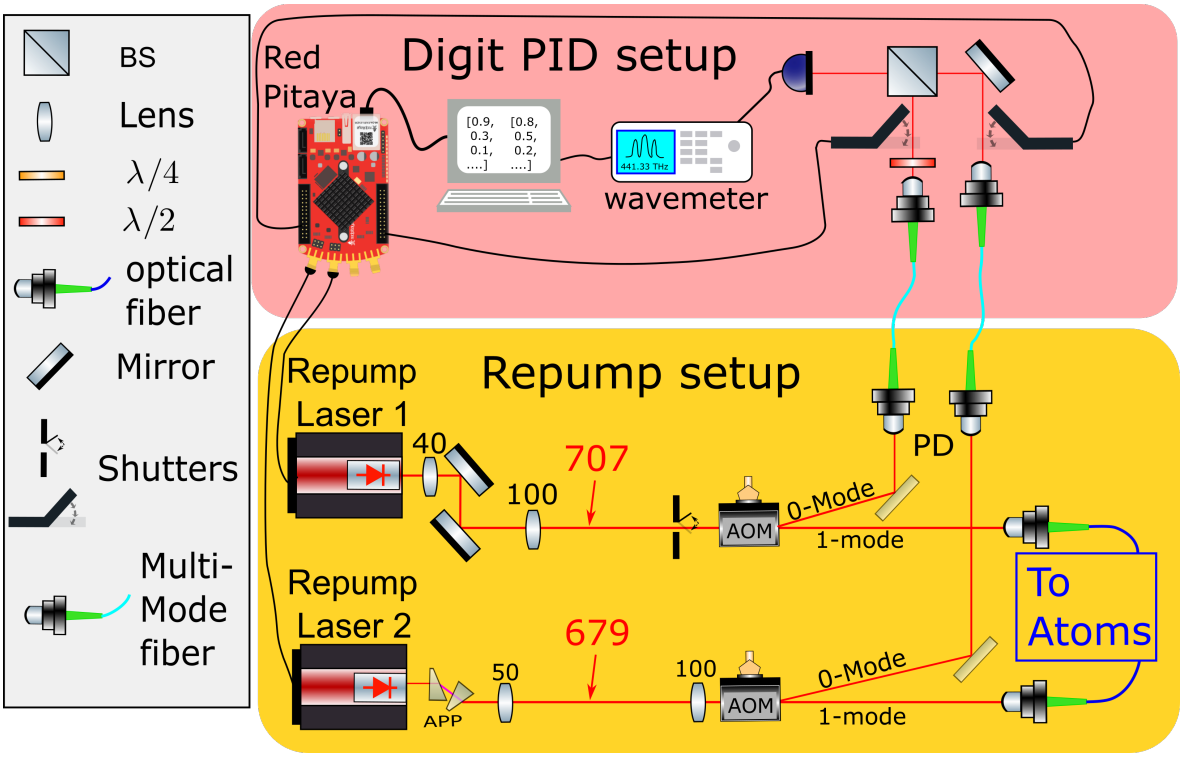


Figure 3.17: Schematic of the repumping and digital PID systems. The figure shows an illustration of the optical setup containing two Toptica lasers and the associated optics used to generate the 707.2 nm and 679 nm repumping beams. Each beam is guided through two AOMs, which produce a first-mode diffracted beam sent to PM fibers aligned on the SC and a zero-mode beam sent to multi-mode fibers for further frequency stabilization using a wave meter. Each beam path incorporates a mechanical shutter, remotely controlled by a trigger signal generated by a Red Pitaya, which allows control over the light that reaches the wavemeter input.

state (with a timescale of approximately 22 $\mu s$), atoms in the $^3P_2$ state can persist for several minutes [148]. This decay channel into the $^3P_2$ state thus limits the effective lifetime of the atoms within the blue MOT cycle.

The $^3P_2$ state, being magnetically sensitive, interacts with the quadrupole field of the MOT. When addressing the fermionic $^{87}$Sr isotope, the coupling between the atomic magnetic moment and the magnetic field gradient depends on the magnetic quantum number $m_F$, such that some states are lost from the trap while others accumulate in the reservoir. However, the long-lived nature of the $^3P_2$ state can be utilized as a metastable reservoir. This approach can compensate for a lack of our initial flux by employing longer waiting times to accumulate atoms in the reservoir before recapturing them in the blue MOT, thus achieving higher atom numbers at the expense of longer experimental cycles [149]. To ensure the successful reloading of the blue MOT from the reservoir state, it is essential to maintain precise control and timing of the repumping light. The repumpers must be sequentially activated, deactivated, and modulated in frequency to properly repump the atom back to the ground state. To achieve this level of control, we implemented a combined system of mechanical shutters and digital locking setups. This configuration enables precise control of both the laser frequency and

| | $^3P_0 \rightarrow {}^3S_1$ | $^3P_1 \rightarrow {}^3S_1$ | $^3P_2 \rightarrow {}^3S_1$ |
|---|---|---|---|
| wavelength (frequency) | 679.29 nm (441.3329 THz) | 688 nm ($\approx$ 435.8 THz) | 707.20 nm (423.9137 THz) |
| Transition Linewidth | 1.416 MHz | 4.297 MHz | 6.68 MHz |
| Saturation Intensity | 0.59 mW/cm$^2$ | 1.725 mW/cm$^2$ | 2.469 mW/cm$^2$ |

Table 3.5: Relevant parameters for the $^3P_J \rightarrow {}^3S_1$ transition related to our repumping and transparency beams. The data was taken from [99]

its activation, all managed through a custom-built graphic user interface (GUI), allowing for real-time monitoring of the laser lock throughout the experiment.

### 3.4.1 Repumpers setup of the two lasers and the live adjustment

Our initial repumping system, based on two home-built cat-eye ECDLs, was eventually replaced with two Toptica lasers (model) and a newly designed optical path, as illustrated in the left panel of Figure 3.17. The new lasers offer significant advantages, including a higher mode-hop-free range (MHFR) tuning capability exceeding 20 GHz compared to the 3-4 GHz achievable with our previous home-built design. Additionally, they provide a 3.5-fold increase in the light intensity at the atoms.

The impact of the repumping lasers is substantial, as without them, the imaging signal becomes nearly undetectable for both $^{87}$Sr and $^{84}$Sr and is reduced by more than an order of magnitude in luminosity for the other isotopes. The $^3P_J$ triplet states can be excited to the $^3S_1$ state by three different wavelengths, two of which are essential for our repumping scheme. The $^3S_1$ state provides decay channels to both the metastable $^3P_{0,2}$ states, creating a possibility of losing atoms in the MOT cycle. The repumping scheme implemented here involves two laser wavelengths at 707.2 nm and 679 nm. The 707.2 nm laser pumps atoms from the $^3P_2$ state to the $^3S_1$ state, which then decays to the $^3P_1$ state, from which atoms quickly decay to the ground state. The 679 nm laser is strategically employed to mitigate repumping leaks into the long-lived $^3P_0$ clock state, as atoms can decay from the $^3S_1$ to the $^3P_0$ state. The parameters associated with two of our repumping transitions and as well as the $^3P_1 \rightarrow {}^3S_1$ line, which can be used to repump the atom to the reservoir[150], are presented in Table 3.5.

To provide real-time frequency monitoring of our lasers, our setup includes an additional monitoring arm. This arm utilizes the residual 0-order light from the AOMs that quickly controls the light reaching the atoms. Coupling the zero-order beam into simple multi-mode fibers [10], we can direct it to a beam combination setup on a separate table. This approach allows us to capture a small fraction of the residual light from our four lasers (the blue and red lasers and the two repumpers) and then use a single in-coupler to direct them to our WM. This setup allows for monitoring each laser frequency separately. A shutter system, controlled by a Red Pitaya Field Programmable Gate Array (FPGA) device (STEMlab 125-14), enables us to selectively choose which light is sent to the wavemeter. More details about the shutters and digital locking setup can be found in Appendix A.

[10] Using a cheaper multi-mode fiber is permissible here as deviations in polarization, frequency, or single-mode of the repump lasers were not visible on the wavemeter monitor or within its resolution, but sufficient for our purposes.

On the main experimental table, both repumping beam fibers are mounted in front of the science cell and aligned with the blue MOT beams. We measured the power as 14 mW with a beam diameter of 0.8 cm for the 707 nm laser and 11 mW with the same beam size for the 679 nm laser. These numbers represent saturation intensity of $I/I_{\text{sat},707} \approx 5.64$ for the 707 nm and $I/I_{\text{sat},679} \approx 18.54$ for the 679 nm transition, respectively.

### 3.4.2 Repumping from the Metastable Reservoir

To increase the phase-space density, we exploit the ${}^1D_2 \rightarrow {}^3P_2$ decay channel, utilizing the long lifetime of the ${}^3P_2$ state to accumulate atoms in a metastable reservoir for periods of tens of seconds. This magnetically sensitive metastable state acts as a storage space for atoms decaying from the MOT, with its trapping efficiency dependent on the flux, 3D MOT temperature and beam power, and the natural decay rate. By waiting approximately 0.5 seconds, we can accumulate atoms number of around $10^5$ with the ${}^{87}$Sr isotope, and up to $6 \times 10^6$ with the ${}^{88}$Sr isotope as seen in Figure 3.16. During this loading period, the 707 nm repumping beam is blocked using a mechanical shutter, as even small amounts of light can de-pump atoms from the reservoir. To image atoms accumulated in the reservoir trap, we employ a depumping scheme. After loading the reservoir state, we deactivate the 2D MOT and mini-Zeeman slower beams and subsequently unblock the repumping beams. At the same time, we ramped up the magnetic field gradient to 36 G/cm in the vertical direction. The 3D MOT beams are activated to recapture the atoms, enabling effective imaging of the recaptured cloud.

Using this method, we measure the atomic population in the recaptured blue MOT for all isotopes.

To maximize the atomic signal, atoms were loaded into the long-lived reservoir state over several seconds, with all repumping beams fully blocked during the loading period. Following the loading phase, the blue beams were turned off, and the atoms were held for 1 second in the reservoir. At this point, the 3D MOT beam frequency was shifted closer to resonance for optimal fluorescence imaging. The repumping beams were then unblocked, and a 60 ms stabilization delay ensured the shutters were fully open and stable before imaging. Fluorescence imaging was performed using both the repumping beams and the 3D MOT beams with a duration time of 8 ms and with exposure times ranging from 1 ms to 7 ms, depending on the isotope. We used a MANTA camera (positioned to image from the side of the SC), which collected photons through an $f = 100$ mm lens and a dichroic mirror combined with a blue bandpass filter. This approach resulted in a significant relative increase in the number of trapped atoms, particularly for the fermionic ${}^{87}$Sr and bosonic ${}^{84}$Sr isotopes, which initially exhibited lower capture efficiencies.

To enhance the atom number in our ${}^{87}$Sr system, we compared two repumping configurations by varying the detuning of the 707 nm laser. In the first configuration, the 707 nm and 679 nm repumpers were applied continuously during a 7 ms imaging period of the blue MOT. During the entire experiment, the 707 nm repumper frequency was swept over a 4 GHz range (where for each frequency step we also modulated the laser with 1.2 GHz span to be able to get a signal), and the resulting increase in atoms—reflected in the MOT fluorescence—allowed us to identify the optimal recycling frequency.

In the second configuration, atoms were first loaded into the ${}^3P_2$ reservoir for 5 seconds with both repumpers blocked. Then, the 707 nm and 679 nm lasers were unblocked, and after a 60 ms delay, the MOT was imaged while scanning the 707 nm frequency with a repumping

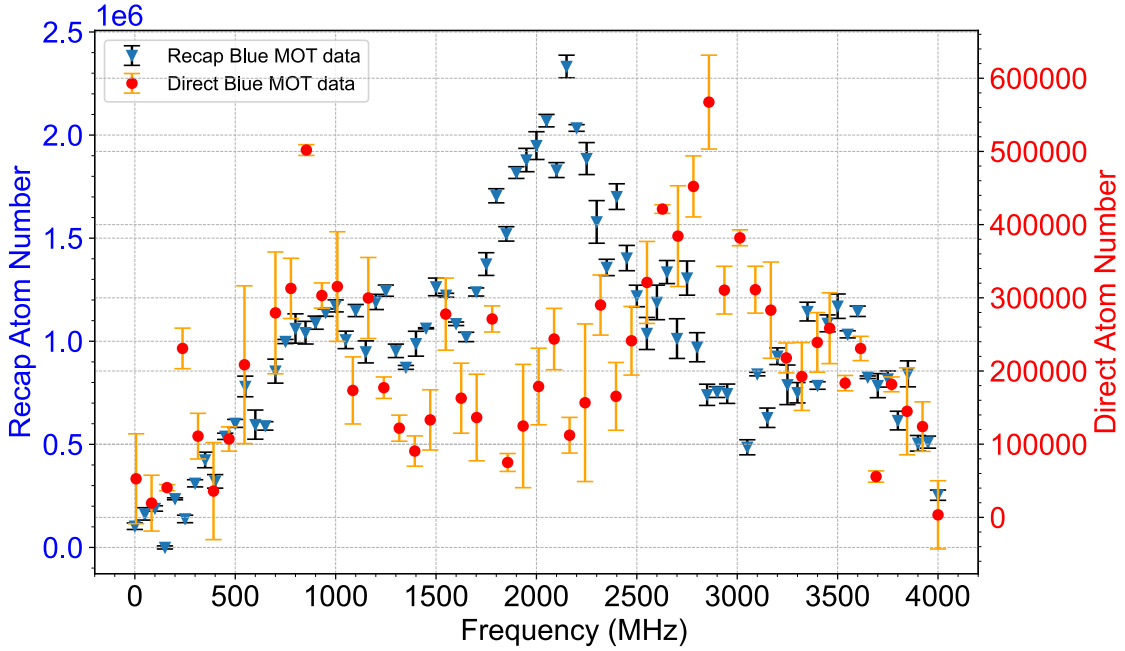


Figure 3.18: Recapture and direct blue MOT vs 707 nm repump detuning.We see in the plot above two measurements done by measuring the number of atoms in the blue MOT, where one is recaptured from the reservoir state (blue arrows) and the other is the direct blue MOT (red circles). We note the different Y-axis for each measurement.

pulse of 7 ms. This sequence revealed a repumping spectrum for the reservoir that is distinct from that observed during continuous MOT operation, as illustrated in Figure 3.18. Each frequency data point was averaged over three measurements to ensure reproducibility.

Our measurements show that the optimal repumping frequency for steady-state MOT operation differs from that maximizing the reservoir depumping efficiency. These observations suggest that dynamically adjusting the 707 nm repumper detuning during the loading sequence can improve the final atom number transferred into the long-lived $^3P_2$ reservoir.

Another idea presented here involves the 688nm light, which excites atoms on the $^3P_1 \rightarrow {}^3S_1$ transition. Although not yet implemented in our system, previous experiments [150, 111] have shown that repumping schemes employing 688 nm light can enhance the reservoir atom number by redirecting decay pathways away from the ground state. In our approach, the 688 nm laser is tuned to drive the $^3P_1 \rightarrow {}^3S_1$ transition. This excitation prevents atoms, which decay from the $^1D_2$ state in a 2:1 ratio to $^3P_1$ and $^3P_2$, from returning directly to the ground state; instead, they are forced into the metastable $^3P_0$ and $^3P_2$ states. In the papers, the researchers quantified this effect by monitoring the fluorescence from the blue MOT under varying intensities of 688 nm light. At intensity of $I_{s,688} \approx 51$ [mW/cm$^2$], the fluorescence signal decreased by up to 70% for $^{88}$Sr and 40% for $^{87}$Sr, respectively. These measurements suggest that optimal timing and intensity of the 679 nm and 688 nm repumping lasers can substantially enhance the reservoir atom number by up to a factor of three, thereby providing a larger initial atom number for transfer to the 3D red MOT.

# Chapter 4

# From Blue to Red: Sr cooling advantage

Having demonstrated decent atom numbers within the recapture blue MOT using the reservoir protocol ($N \approx 10^7$) with $^{88}Sr$ atoms. We now focus on the unique advantage presented by Strontium as compared to alkaline elements, namely its narrow intercombination transition $^1S_0 \rightarrow {}^3P_1$. This specific transition enables a subsequent phase of laser cooling that can achieve temperatures in the sub-microkelvin range, using laser cooling only [151].

While the intercombination transition enables cooling to the microkelvin regime, its narrow linewidth introduces unique challenges for laser stabilization and trapping dynamics. In this regime, isotope-specific effects become prominent and emerge for fermions compared to bosons. At a narrow line MOT, single-photon light scattering can shift the atoms out of resonance, imposing a fundamental limit on the minimum achievable temperature well before quantum degeneracy or significant collisional effects emerge. This chapter elaborates on the operation of our red MOT system, engineered to achieve temperatures below 1 $\mu$K and atomic cloud lifetimes on the scale of seconds. We detail our approach for transferring atoms from the blue MOT to the red MOT at a wavelength of 689 nm, utilizing controlled spectral broadening and a frequency transition to a red-detuned state [152]. The discussion encompasses the red laser system, including its frequency locking mechanism and dual AOM arms for isotope tuning, along with power amplification improving the capturing efficiency of atoms within the MOT. The chapter concludes with an analysis of the measurements of optimal temperature and atom counts at the end of the red MOT sequence.

## 4.1 Loading from a broad to narrow linewidth MOT

After loading atoms into the blue MOT and assuming maximal damping, the time required for the atomic motion to relax to the Doppler cooling limit is approximately $\tau = \frac{m}{\alpha} = \frac{\hbar}{4E_r s_0}$, where $s_0, E_r$ are the situation parameter and the recoil energy, respectively. This simplified picture, considering our MOT beams intensity, gives a lower bound of $\sim 10\mu$s, but typical relaxation times are on the order of ms. At the end of the cooling sequence, as the cloud reaches the Doppler temperature limit, the gas particles remain in a relatively fast velocity class ($v > 500\,\mathrm{mm/s}$). Further cooling of the atoms can be done in many ways, such as evaporation cooling [153] or sympathetic cooling [154]. In strontium, another transition at 689 nm is generally used to lower the atomic temperature by three orders of magnitude compared

to their final temperature in the blue MOT. Utilizing this red light transition, we can create a second MOT and transfer the atoms into it. Subsequently, in the red MOT, the atoms are cooled to below 1 microkelvin due to the narrow linewidth of this transition. Nevertheless, the distinct operational mechanisms between the red and blue MOTs introduce complexities in achieving these temperatures. To elucidate these distinctions, we explain the fundamental principles governing the trapping and cooling processes of strontium.

### 4.1.1 Doppler limit and recoil temperature for strontium

The essence of laser cooling in a MOT is based on the Doppler effect, as explained in subsection 3.3.1. The effect is caused by coupling a laser light with a moving atom. In the atom reference frame, the photon frequency is shifted to the red or the blue, depending on their (atom and photon) propagation direction. Known as the Doppler shift, this phenomenon allows for momentum transfer, creating a velocity-dependent force that slows the atom. Recalling Equation 3.7 and adding the Zeeman shift due to the magnetic gradient field, we get that the total detuning in the MOT is spatially and velocity dependent, which is at the origin of cooling and trapping. We can use this detuning condition in the MOT as follows:

$$\delta = \Delta + \mathbf{k}\cdot\mathbf{v} + \tilde{\mu}_B\vec{\nabla}\mathbf{B}\cdot\mathbf{r} + \frac{\hbar k^2}{2m} \tag{4.1}$$

The terms appearing in Equation 4.1 are the laser detuning, followed by the Doppler shift and the Zeeman shift with $\tilde{\mu}_B \approx 1.4$ MHz/G being the reduced Bohr magneton. The final term represents the recoil shift caused by the photon's momentum, usually on a few kHz scale. The recoil shift is negligible for the blue transition but not for the red, with a much narrower linewidth. To understand the difference between these two transitions, we start with the fundamental limits of Doppler cooling. The minimum temperature achievable is determined by the balance between the cooling force and the momentum diffusion due to the stochastic recoil of spontaneously emitted photons. This minimum temperature, referred to as the Doppler temperature limit ($T_D$), is defined by [155]:

$$T_D = \frac{\hbar\Gamma}{2k_B}, \tag{4.2}$$

where $\Gamma$ is the natural linewidth of the cooling transition. In strontium, two transitions are predominantly utilized for Doppler cooling: one at 460.8 nm ($^1S_0 \rightarrow {}^1P_1$), referred to as "blue transition" and the other at 689.4 nm ($^1S_0 \rightarrow {}^3P_1$), referred to as "red transition". The blue transition has a linewidth of $\Gamma_{\text{blue}} = 2\pi \times 30.5\,\text{MHz}$ and a Doppler limit of 720 $\mu$K, which provides a strong cooling force for capturing atoms from a thermal source. Under the assumption of a maximal scattering rate of $\Gamma/2$ and a homogeneous MOT beam configuration, we can estimate the MOT maximal capture velocity as [73]:

$$v_{\text{max,c}} = \sqrt{\frac{2\pi\hbar D\Gamma_{\text{blue}}}{m\lambda_{\text{blue}}}} \approx 137\ \text{m/s}, \tag{4.3}$$

Where $D = 10\,\text{mm}$ is the MOT beam size and $m$ is the atomic mass of $^{88}$Sr. This upper bound determines the atomic velocity classes trappable by the MOT light. This high capture velocity is typically well matched to the atomic flux delivered from a Zeeman slower and the 2D MOT.

| **Parameter** | **Blue Transition** $^1S_0 \rightarrow {}^1P_1$ | **Red Transition** $^1S_0 \rightarrow {}^3P_1$ | **Formula** |
|---|---|---|---|
| Wavelength | 460.862 nm | 689.449 nm | $\lambda$ |
| Transition Linewidth | 30.5 MHz | 7.42 kHz | $\Gamma/2\pi$ |
| Doppler Temperature | 720 µK | 179 nK | $T_D = \hbar\Gamma/2k_B$ |
| Saturation Intensity | 40.7 mW cm$^{-2}$ | 3 µW cm$^{-2}$ | $I_s = \pi hc\Gamma/3\lambda^3$ |
| Atomic Mass | 87.62 u | 87.62 u | $m$ |
| Max acceleration | 980 000 m s$^{-2}$ | 150 m s$^{-2}$ | $a_{max} = h\Gamma/2m\lambda$ |
| gravity Recoil | 96 566 | 15.6 | $R_g = \hbar k\Gamma/2mg$ |
| Recoil Temperature | 515 nK | 230 nK | $T_r = \hbar^2k^2/2mk_\mathrm{B}$ |
| Recoil Velocity | 11.4427 mm s$^{-1}$ | 9.3435 mm s$^{-1}$ | $v_r = \sqrt{\frac{2k_BT_r}{m}}$ |
| Recoil parameter | 0.000 35 | 0.64 | $\epsilon_r = \hbar k^2/m\Gamma$ |

Table 4.1: Key parameters for the blue and red transitions used in Strontium MOT experiments. The values are taken from [99].

The red transition, with a linewidth of $\Gamma_{\mathrm{red}} = 2\pi \times 7.5$ kHz and a Doppler limit of 179 nK, enables sub-Doppler cooling to temperatures near the recoil limit of 460 nK. However, the narrow linewidth poses challenges for capturing fast-moving atoms.

To address the challenges imposed by the narrow red intercombination line, it is instructive to consider both the Doppler temperature and the recoil temperature. The recoil temperature, which quantifies the momentum imparted by a single photon, is given by

$$T_r = \frac{\hbar^2k^2}{2mk_B}, \tag{4.4}$$

where $k = \frac{2\pi}{\lambda}$ and $m$ is the atomic mass. Table 4.1 summarizes the key parameters, including the Doppler and recoil temperatures for the blue and red transitions.

From these scales, the recoil parameter $\epsilon_r$ is defined as the ratio of the recoil energy to the natural linewidth. In many alkali systems, $\epsilon_r \ll 1$ means that scattering photons will not affect the resonance condition, maintaining efficient cooling throughout the sequence. However, for strontium's narrow red transition, $\epsilon_r$ approaches unity. Consequently, during the absorption-emission cycle, a single photon recoil can shift an atom out of resonance, thereby limiting further cooling unless the spectrum is broadened [152]. For strontium, the ratio between the Doppler scattering rate and the recoil energy (or Doppler to recoil temperatures) highlights the difference between the two MOTs:

$$\frac{T_{D,\mathrm{blue}}}{T_{r,\mathrm{blue}}} = \frac{\hbar\Gamma_{\mathrm{blue}}}{E_{r,\mathrm{blue}}} \approx 700 \gg \frac{T_{D,\mathrm{red}}}{T_{r,\mathrm{red}}} = \frac{\hbar\Gamma_{\mathrm{red}}}{E_{r,\mathrm{red}}} \approx 0.39, \tag{4.5}$$

Here, $E_r = k_BT_r$ is the recoil energy and can be deduced from Table 4.1. The broad linewidth of the blue transition enables efficient initial cooling over a wide velocity range. However, without additional frequency broadening, the narrow linewidth of the red transition limits its capture range, making direct capture from the blue MOT ineffective [156].

To overcome these constraints, we employ a frequency-modulated laser to generate a frequency comb that effectively broadens the cooling spectrum. This broadened light interacts

with faster-moving atoms, extending the capture range of the red MOT. As a result, the distinct cooling regimes in the blue and red MOTs give rise to markedly different dynamics in the trapped atomic clouds.

Not only is the cooling aspect different between the narrow and broad lines, but trapping also has a big part in shaping the MOT. Unlike the blue (and general broad-lines) MOT, in red MOT, the maximum acceleration provided by the cooling force is only about 15 times greater than gravitational acceleration. This proximity with the force from gravity makes the MOT highly sensitive to the saturation parameter. At high intensity, the equilibrium point between gravity and the MOT beam force is shifted away from the trap center, creating sagging of the cloud. On the other hand, excessive reduction in beam intensity can cause atoms to fall out of the trap.

### 4.1.2 Theory of Narrow-Line MOT

While previous sections focused on reducing atomic velocities via Doppler cooling in a broad-line MOT, effective laser cooling also requires spatial confinement. In the MOT, a combination of near-resonant laser cooling and a spatially varying magnetic field produces a restoring force that traps atoms. As detailed in the broad-line MOT section, this interplay mediated by the Zeeman effect confines the atomic cloud. In the narrow-line MOT, these principles still apply, though the reduced linewidth and capture range necessitate a more complex scheme for the efficient atomic trapping.

For narrow-line transitions, such as the $^1S_0 \rightarrow {}^3P_1$ transition of Strontium at 689 nm, the cooling dynamics differ markedly from those in broad-line MOTs. The narrow linewidth ($\Gamma = 7.5\,\mathrm{kHz}$) gives rise to unique thermodynamic and mechanical regimes, where the interplay between the power-broadened linewidth ($\Gamma_E = \Gamma\sqrt{1+s_0}$), single-photon recoil ($\omega_r$), and laser detuning ($\Delta$) governs the system's behavior. This section focuses on the theory of narrow-line MOTs, particularly the three operational regimes defined by the saturation parameter $s_0$ and the ratio $\Delta/\Gamma_E$, as well as the impact of gravity.

In the reference frame of a moving atom, the total force in the MOT comprises gravitational and Doppler. The MOT beams in the presence of a magnetic B-field that breaks translational symmetry create a restoring force on top of the cooling force, a restoring force, that allows us to trap them. These contributions can be written as follows:

In the reference frame of a moving atom, the total force within the MOT consists of both gravitational and Doppler components. The MOT beams in the presence of a magnetic B-field that breaks translational symmetry create a restoring force on top of the cooling force that allows us to trap them. These components can be mathematically represented as follows:

$$\mathbf{F}_{\mathrm{tot}} = \mathbf{F}_{\mathrm{g}} + \mathbf{F}_{\mathrm{Doppler}} + \mathbf{F}_{\mathrm{Mag}} = m\mathbf{g} - \beta\,\dot{\mathbf{r}} - \alpha\,\mathbf{r}, \tag{4.6}$$

where $\alpha$ and $\beta$ are effective spring-like and damping-like constants, and $\mathbf{g} = (0, 0, g)$ represents gravity (with $g \approx 9.8\,\mathrm{m/s^2}$). Taking the one-dimensional case of Equation 4.6, the force can be approximated by employing a Taylor expansion near the trap minimum with these outlined values $v_z = v_0$ and $z = z_0$:

$$F_{\mathrm{1D,MOT}} \approx F(v_z = v_0, z = z_0) + \left.\frac{\partial F}{\partial v_z}\right|_{v_0} v + \left.\frac{\partial F}{\partial z}\right|_{z_0} z + \mathcal{O}(v_z^2, z^2). \tag{4.7}$$

Looking at Equation 4.6, we see that it resembles a damped harmonic oscillator, suggest-

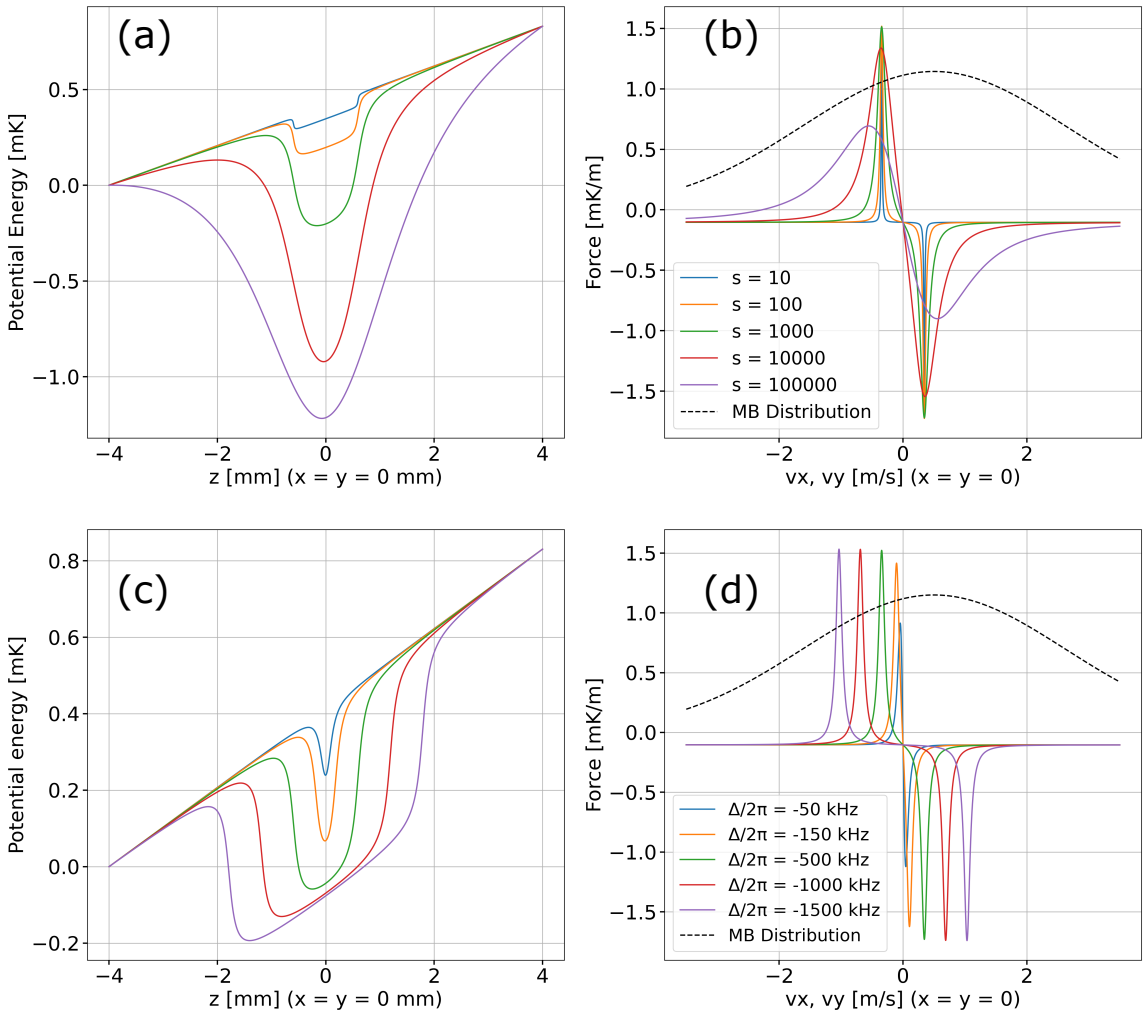


Figure 4.1: Potential energy and scattering force for a 1D Strontium MOT as a function of position and velocity. The top two (a,b) plots illustrate the effect of varying the saturation parameter ($s$) at a fixed detuning $\Delta = -2\pi \times 500$ kHz, while the bottom two (c,d) showing the effect of varying the detuning ($\Delta/2\pi$) at a fixed saturation parameter $s = 500$. The left plots (a,c) display the potential energy profile while demonstrating the effect of gravity. The right plot (b,d) presents the velocity-dependent scattering force, along with a Maxwell-Boltzmann (MB) distribution (dashed black line) with a $\Delta v = 3$[m/s]. This line illustrates the velocity distribution of atoms reaching the Doppler temperature limit in the blue MOT.

ing that atomic motion in the MOT can be classified into distinct regimes. In particular, analyzing Equation 4.7 and how the interplay between $s_0$ and $\Delta/\Gamma_E$ delineates three operational regimes in the narrow-line MOT. Adapted from the JILA group's characterization of the 689 nm transition in $^{88}$Sr [157], is done using a semi-classical model to detail the operation of the MOT at high saturation parameter $s \gg 1$. Followed by an explanation of when a full quantum treatment is required.

Before describing each regime, we can understand the unique conditions in the narrow

line red MOT by observing Figure 4.1. These plots illustrate the radiation pressure force and potential for various saturation parameters and detunings. Figures (b,d) represent the force exerted by a 1D single MOT beam as a function of atomic velocity. This analysis is based on a Maxwell-Boltzmann (MG) distribution of atoms released from the blue MOT, characterized by a temperature of $T = 3$ mK, as depicted by the black dashed line in Figure 4.1. The figure illustrates the overlap among the velocity classes, the operational range of the red MOT beam, and the velocity distribution of the thermal atomic cloud. The significant discrepancy between the red photon and the atoms from the blue MOT renders the transfer of atoms to the red MOT highly inefficient, necessitating an expansion of the red beam's spectral range. Looking at the potential (a,c), it is clear that gravity has an impact on the trapping of the atoms and their position. Due to gravity, the atomic cloud is sagging and displaced from the trap center.

### Standard Doppler cooling ($s_0 \gg 1$) and ($|\Delta/\Gamma_E| < 1$)

When the power-broadened linewidth ($\Gamma_E = \Gamma\sqrt{1+s_0}$) becomes comparable to the detuning, the atom dynamics is similar to a damped harmonic motion. The MOT operates similarly to a standard broad-line MOT, with the velocity-dependent force dominating, where the equilibrium temperature approaches a Doppler-like limit $\hbar\Gamma_E/2k_B$. In this regime, we can neglect higher orders of the $\mathcal{O}(v_z^2, z^2)$ and expand around $v_z = 0, z = 0$ as:

$$F_{1D,\mathrm{MOT}} \approx \frac{8\hbar\Gamma^3 k_z s_0 \Delta}{\left(4\Delta^2 + \Gamma_E^2\right)^2}\left[k_z v_z + \frac{g_J \mu_B \left|\partial_z B_z\right|}{\hbar} z\right] = -\beta_z v_z - \alpha_z z \tag{4.8}$$

where the damping and spring coefficients $\beta_z, \alpha_z$ can be written :

$$\beta_z = -\frac{8\Delta\hbar s_0 \Gamma^3}{\left(4\Delta^2 + \Gamma_{E,z}^2\right)^2} k_z^2 \ , \ \alpha_z = g_J \mu_B \frac{\left|\partial_z B_z\right| \beta_z}{\hbar k_z} \tag{4.9}$$

As the subsection 3.3.1 explains, the detuning sign determines whether the radiation pressure force in Equation 4.8 is repulsive and can decelerate the atom or attractive and lead to atom loss from the MOT.

In the presence of a spatially changing magnetic field, the detuning becomes polarization and position-dependent as the Zeeman shift forces the atoms in different positions toward the magnetic minimum. This ensures atoms are confined at the trap center and simultaneously cooled. In this regime, further cooling is limited, and the Doppler limit $\frac{\hbar\Gamma_E}{2k_B} \gg \frac{\hbar\Gamma}{2k_B}$ is not attainable. To overcome this issue, we can lower the scattering rate by a gradual decrease in the beam intensity. This results in fewer photons inducing heating, lowering the gas temperature, and leading to an increase in phase space density. However, prior to the power reduction, we want to increase our detuning compared to the effective resonance. This allows the atom to free fall inside the MOT "hard" walls potential, where it will eventually sit in the minimum point dominated by gravity.

### The single beam regime ($s_0 \gg 1$) and ($|\Delta/\Gamma_E| > 1$)

In this regime, the detuning dominates over the power-broadened linewidth, and single-photon processes govern the MOT dynamics and can take the atom out of resonance as seen in Figure 4.1 right side figures. As a result, the down-propagating red MOT beam becomes

detuned from the atomic resonance, thereby reducing its contribution to the cooling force. Consequently, the upward beam, remaining closer to resonance, dominates the restoring force on the atoms. By assuming only a single beam pushing the atom in the vertical direction, the equilibrium position $z_0$ changes. We can see this spatial shift by taking only the $\sigma_+$ in Equation 3.11 and comparing it to gravity ($F_{\mathrm{rp},+} = mg$); we find a balance point for the atomic cloud to sit in. Solving the equation assuming the atoms are at rest ($v_z = 0$), we get a stable point at

$$z_0^{\pm} = \frac{\hbar\Delta}{g_J\mu_B\left|\partial_z B_z\right|}\left(1 \pm \frac{\Gamma_E}{2\Delta}\sqrt{\frac{\Gamma\hbar k s_0}{2(1+s_0)mg} - 1}\right) = r_c\left(1 \pm \frac{\Gamma_E}{2\Delta}\sqrt{R_g s' - 1}\right) \tag{4.10}$$

We define respectively $R_g, r_c$ as the gravity recoil parameter in Table 4.1 and the capture radius of the MOT, which represents the area where atoms can be trapped. The $s' = s_0/(1+s_0)$ parameter is made for simplicity; by taking the assumption of this regime, we get that only the positive solution is stable and can be considered for the atom to reside as met by the $r_c$ parameter. Interestingly, we see that the stable point depends on the laser frequency, and one can move the cloud up or down (to a certain limit) by only shifting the detuning with sufficient beam power. If we look at Equation 4.7 Damping coefficient $\beta = \left.\dfrac{\partial F}{\partial v_z}\right|_{v_z=0}$ and insert our stable point solution $z_0^+$ we can observe that the saturation parameter primarily sets the atom energy loss and thus the equilibrium temperature in this regime, which is independent of the detuning.

**The single recoil photon regime ($s_0 \sim 1$)**

As the saturation parameter becomes on the scale of unity, the MOT enters a quantum regime where single-photon recoils govern the dynamics. This leads to two consequences, in the ensemble spatial and cooling aspects. First, the beam intensity has little effect on the equilibrium position, and small power changes can lead to high atom loss. However, with a magnetic offset field (several hundreds of mG), we can move the cloud, and we have used this effect to move the alignment purposes. Second, this regime allows cooling to half of the photon recoil limit, reaching temperatures as low as $T_{\min} \approx T_r/2 \approx 250$ nK [157]. The atomic ensemble exhibits sub-recoil cooling, a hallmark of narrow-line transitions, and the semi-classical treatment we used in the two other regimes is no longer valid [158]. This thesis will not address the full quantum treatment needed to understand this regime.

The reasoning for introducing all three regimes comes from the fact that the capture velocity is directly proportional to the detuning $kv_c \propto |\Delta|$. For the red MOT, this means that to transfer the hot atoms from the blue MOT to the red, we have to work first in the regime where the light detuning is much larger than the effective linewidth $|\Delta| > \Gamma_E$ and only after moving to the Doppler cooling regime. However, as explained in the single-beam section, the 689 nm transition is narrow, many atoms will not be affected, and only a small fraction of the atomic velocity distribution will be captured in the MOT beams. One can naively think that by increasing the power of the laser, we can broaden the spectrum. However, assuming a cloud with a velocity distribution on the blue MOT Doppler limit temperature scale 1 mK, the atoms experience a frequency upshift of roughly 5 MHz as they transfer to the red MOT. By plugging this shift into the effective broadening

$$|\Delta/\Gamma_E| \sim 1 \Rightarrow s_0 \approx \left(\frac{\Delta}{\Gamma}\right)^2 \tag{4.11}$$

The above calculation shows that one will need $s_0 \approx 4 \times 10^5$ for each beam, which, if we assume it has a waist of 1 cm, will need to have more than 15 W, thus rendering the idea as too be impossible with our available laser power. Instead, one can artificially broaden the spectrum by creating a frequency comb over the MOT beam light, where each peak is sufficiently intensified and the spectrum teeth are uniformly distributed with a constant separation. Thus, we syntactically broaden the spectrum to a few MHz, capturing many differently moving atoms and converging to a $\Delta = -100$ kHz single frequency where Doppler cooling takes place with only a few mW of power for each beam. In the following sections, we will see how this process works and what temperatures are accessible.

### 4.1.3 Spectral broadening for enhanced capture velocity

The four-order-of-magnitude difference in transition linewidth between the blue and red MOTs necessitates a sophisticated sequence for effective atomic transfer. To address this, we employ spectral broadening, introduced firstly by H. Wallis and W. Ertmer [159], by modulating the frequency drive of the MOT beams' AOMs temporally, increasing the red MOT capture range. Already executed by the Tokyo group [160] in 1999, this modulated light results in a broad spectrum with peaks across several MHz, depending on the modulation bandwidth. Despite the low saturation intensity associated with the red MOT's narrow line transition, the broadened spectrum, which can comprise over 250 distinct peaks in the Fourier domain with only 1.5 mW of power and a 0.4 cm beam waist per beam, provides peaks with intensities of approximately $I \approx 8I_{sat,red}$.

To better understand the underlying principle, let us consider a monochromatic planewave and convolute it with a linear sawtooth ramp. The resulting function will mimic the light beam emerging from the AOM and write:

$$E(z,t) = E_0 \cos(kz - \theta(t)) \rightarrow E(t) = E_0 \cos(\theta(t)), \quad \omega(t) = \partial_t \theta(t) \tag{4.12}$$

The fast-oscillating spatial part can be ignored as we are only looking at the frequency components and can focus only on the temporal part. Using the Fourier transform, this plane wave shows us how the frequency modulation affects the spectrum. The time-dependent phase $\theta(t)$ is related to the frequency omega by:

$$\theta(t) = \int_0^t \omega(t')dt' = \omega_0 t + \Delta \int_0^t f(t')dt', \tag{4.13}$$

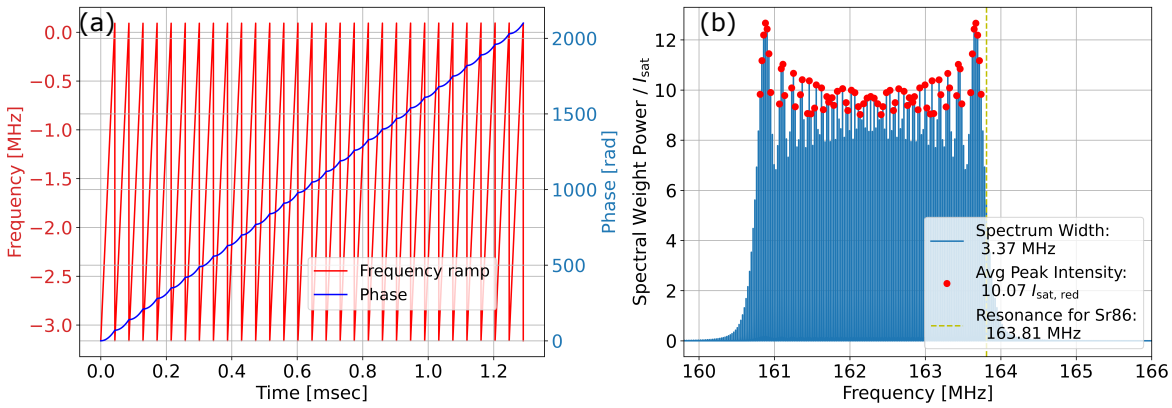


Figure 4.2: Frequency modulation and beam spectral broadening. (a) Illustration of a time-domain sawtooth modulation of the laser frequency, with a 3.26 MHz red-detuned span. A constant periodicity of $\Gamma_{\text{red}}$ is used to distribute spectral lines evenly, preventing atom loss during the convergence of the frequency sweep. The integrated phase increases linearly with a parabolic shape. (b) The corresponding normalized spectral weights in the Fourier domain demonstrate a broadened spectrum that matches the span of the time-domain modulation. The yellow dashed line indicates the resonance frequency for $^{86}$Sr at 163.81 MHz, which was used as an example, and the red dots represent sampling peaks in the broadened spectrum. The average peak intensity is approximately $\langle I(\omega)\rangle \approx 10 I_{sat,red}$ with around 35 peaks.

where $\omega_0$ represents the AOM operating frequency and $\Delta$ is the modulation bandwidth. The function $f(t')$ represents the frequency ramp, and for simplicity, we use a sawtooth profile, which is defined as follows:

$$f(x,T) = \sum_{n}^{N} \left(\frac{2x}{T} - 1\right) \chi_n;\ x \mod T \tag{4.14}$$

where $T$ is the periodicity time, $N$ is the number of periods applied during the red MOT, and $\chi_n$ is the indicator function of the interval $x \in [(n-1)T, nT]$ with $n \in \mathbb{N}$. The total time of applying the frequency ramp is given by $T_{\text{tot}} = TN$. This periodic modulation produces a frequency comb in Fourier space with components spaced by $1/T$. The relative amplitudes of these components depend on the symmetry of the modulation. By setting the modulation period to $T \approx 1/\Gamma_{\text{red}}$, we ensure that the frequency spacing of the modulated light is on the order of the red transition linewidth. This approach guarantees that all atomic velocity classes are addressed, thereby enhancing the cooling efficiency in the red MOT.

Through simulations using a Fast Fourier Transform (FFT), we can visualize the resulting spectrum and verify how the intensity is distributed. For example, by modulating the light for the $^{86}$Sr isotope over a 3.25 MHz bandwidth, the simulated spectrum reveals a distribution of peaks corresponding to our modulation. The left panel of Figure 4.2 shows the applied sawtooth ramps with a span of $\Delta = 70\Gamma_{\text{red}}$, for illustration purposes only, $N = 30$ periods were plotted. Note, however, that increasing the number of periods does not significantly alter the resulting spectrum. The right panel of Figure 4.2 shows the resulting spectral weights, with components detuned by approximately $2\Gamma_{\text{red}}$ from the resonance of $^{86}$Sr. Choosing the modulation period as $T = 1/\Gamma_{\text{red}}$ ensures a significant excitation probability across the entire modulation bandwidth. Although our simulations accurately predict the overall spectrum,

experimental measurements remain necessary to optimize the laser power, modulation bandwidth, and detuning.

The last part of the simulation is how the intensity per peak is distributed, as we saw before for each beam. This spectrum broadening represents the initial step in our cooling sequence. Further cooling requires the convergence of the broadband (BB) spectrum into the single-frequency (SF) regime. This technique allows for effective cooling of the atoms to below 1 $\mu$K, approaching quantum degeneracy.

## 4.2 Transition to Single-Frequency Cold Red MOT

After optimizing the capture efficiency of the broadband MOT, we transition to a single-frequency (SF) regime by rapidly switching to a small detuning without modulation. This change modestly increases the atomic density and reduces the temperature toward the Doppler limit. Although the converging ramp affects the number of atoms transferred to the SF MOT, its overall impact on the final atom number is limited, as well as on the final temperature of the cloud.

The trajectory that one chooses to ramp down the frequency can maximize the number of atoms retained in the SF red MOT at the end of the sequence. Evidently, we saw a lower atom number when no ramp was implemented, as the transition from the BB to the SF was initially done by instantaneously jumping from 5 MHz to 30 kHz. The result of adding a linear ramp increased the number of atoms by a factor of two in the SF red MOT. The implementation of the frequency ramps is limited by the finite bandwidth and detuning range of our AOMs, and attempts to modify it did not show significant effects on the atom number. Besides frequency, the beam intensity also plays a role and should be considered when we transition away from the BB regime. While high laser intensities increase the scattering rate, the red MOT beam sequence must be optimized to ensure that the spectral coverage adequately addresses the full range of atomic velocities during the transition to the single-frequency regime. However, at excessively low intensities, the atoms are no longer trappable, resulting in atom loss. Therefore, determining the optimal intensity profile in conjunction with the frequency ramp is critical for achieving both minimal temperature and minimal atom loss. As we optimize the saturation parameter $s_{\text{opt}} = I_{\text{opt}}/I_{\text{sat}}$ by reducing the final intensity $I_{\text{opt}}$ of the red beams, we are left with a cold red MOT (CrMOT) observing a density difference between a Fermionic MOT and a Boson one. This effect is due to the intrinsic nuclear spin of $^{87}$Sr and its hyperfine structure with 10 $m_F$-states, unlike bosons, which have no magnetic moment in their ground state.

### 4.2.1 Bosonic Case

As the frequency is ramped down, the atomic cloud transitions from the broadband regime to a more confined single-frequency regime, leading to a contraction of the initially large cloud. Concurrently, the magnetic field gradient is gradually reduced—a process initiated during the depumping of atoms from the reservoir state. To elucidate the spatial region where atoms become resonant with the cooling light in the SF MOT, we define a characteristic capture radius, $r_c$, This length scale represents the distance from the trap center at which the Zeeman shift induced by the magnetic field exactly compensates the laser detuning, and it is given by:

$$\mathbf{r}_c = \frac{\hbar\Delta}{m_J g_J \mu_B \nabla |\mathbf{B}|} \tag{4.15}$$

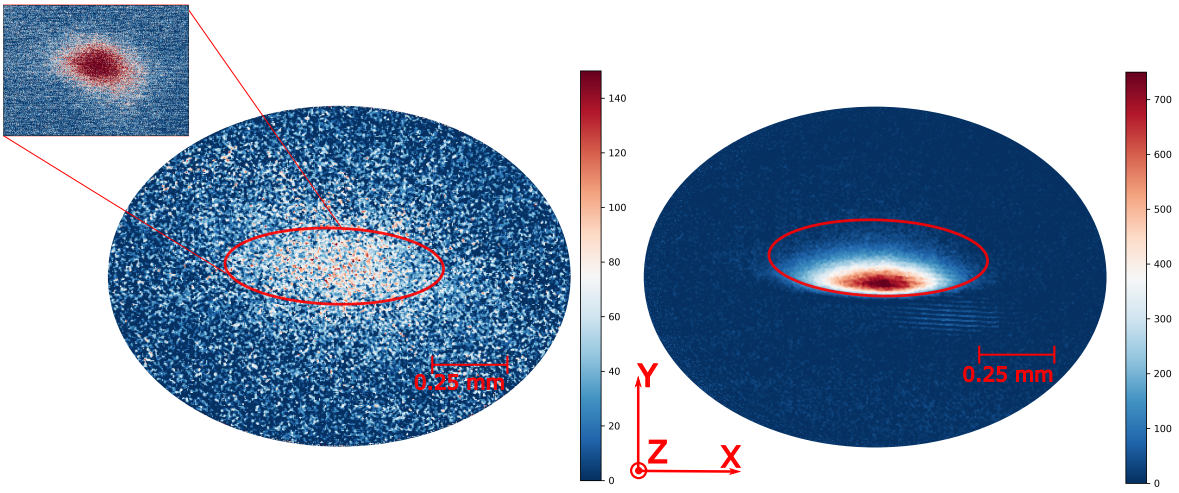


Figure 4.3: Red MOT absorption images. Two absorption images of both the $^{87}$Sr (left ellipse) and $^{88}$Sr (right ellipse) SF red MOT, taken with 100$\mu$s duration time of the imaging blue light. The red-colored ellipse corresponds to positions where the atoms get on resonance with the light. extracting the atom number from each image on the right side $3.6\times10^6$ and the left $0.24\times10^6$.The inset on the top left is the fluorescence image of the $^{87}$Sr with 0.1 ms imaging time.

Here Equation 4.15 represents a 3D ellipsoid picture. This boundary, where the atoms are captured, is engineered by the symmetry of our Anti-Helmholtz coils. By creating magnetic field gradients such that $\partial_z B_z = \partial_x B_x$, the size ratio of the MOT will be equal, making the cloud isotropic in the X-Z plane.[1] Initially at the BB phase the modulated MOT beam is spread over $\lceil \frac{\Delta}{\Gamma_{\text{red}}} \rceil \approx 250$ teeth in the spectrum to, thus the saturation intensity per comb line is around $s \approx 10$ with a lower bound of 50 kHz detuning from resonance. As bosons accumulate in the MOT, they are located at equilibrium points between the downforce of gravity and the dominant upwards beam accommodating ellipsoid-like shells generated at different radii governed by Equation 4.15 along the vertical axis.

At this phase, the average radial cloud size reaches $\langle \mathbf{r_c} \rangle \approx 0.4$ mm by assuming $\Delta = 2.5$ MHz and magnetic field gradient of 3 G/cm. After the atoms trapping is maximized by the extended light frequency comb, the second stage starts with converging ramps that shift towards a zero modulation span with detuning $4\Gamma_{\text{red}} \approx \Delta = 30$kHz. When dealing with a bosonic isotope such as $^{88}$Sr, one can estimate the horizontal size by taking a magnetic gradient 0.65 G/cm with a ground and excited state parameters $m_J + 1 = 1, g_J = 1.5$, which give an approximated size 0.37 mm, from Equation 4.15.

While the frequency broadening regime ensures efficient atom capturing, transitioning to the SF regime requires reducing the beam intensity to maintain effective Doppler cooling. As the frequency convergence occurs, the intensity is ramped down to several $I_{\text{sat}}$. At low intensities and for temperatures approaching 1 $\mu$K, the system enters a regime where the recoil energy sets the dominant scale. As the cloud reduces in size from 3-4 mm to a few hundred of $\mu m$, the phase space density increases significantly. The vertical size varies predominantly in the gravitational direction as all shells collapse into one, creating a thin, elongated shape that

[1] In our setup, the anti-Helmholtz coils have a diamond-shaped configuration, so the spatial profile of the resonant region does not conform to an elliptical shape

occupies the bottom part of the ellipsoid. Absorption imaging was performed using the blue imaging setup. For each experimental run, three images were acquired (one with atoms, one without but with the imaging beam on, and the last without atoms and light), suppressing background noise and enhancing the atomic signal. This procedure yields a spatially resolved image of the atomic cloud's density distribution at the CrMOT stage, where the cloud is cooled to only a few microkelvin. The atom number is then extracted from this density profile. In Figure 4.3, the right panel displays representative absorption images of $^{88}$Sr taken with a 100 $\mu$s square pulse through the atomic cloud, the transmitted light was recorded by the MANTA camera positioned in the Z–X plane. In the figure, the red circle represents an ellipse calculated with a major axis of $z_c \approx 366\ \mu m$ and an aspect ratio similar to the gradient field ratio.

The conditions for each bosonic isotope are a bit different, as more reservoir loading time is needed to accumulate enough atoms for a decent SF red MOT signal, with $^{84}$Sr being the most difficult to observe with 10-15 seconds loading time. At the time of this thesis, we have loaded all of strontium's stable isotopes into our red MOT trap.

### 4.2.2 Fermion case

When loading strontium-only stable fermion, the MOT shape determined by Equation 4.15 is distinctively different, which arises from its unique nuclear magnetic ground state. For $^{87}$Sr, the $m_F$-states are in resonance with the MOT beams at different shells, similar to an onion where the density is more uniformly distributed as seen in Figure 4.3. The first crucial part is that Equation 4.16 expression changes as different magnetic moments shift the excited and ground states and thus the detuning. In addition, each has a different magnetic quantum number, resulting in a transition-dependent force. Considering that the ground-state total angular quantum number is expressed as $F = J+I = 0+9/2$ as well as a much weaker magnetic moment due to its nuclear moment, makes the levels shift to be almost degenerate with 10 different nuclear $m_F$ sub-levels. Each state experiences an effectively different radiation force as the resonance position for each $m_F \to (m_F \pm 1)$ transition differs. Consequently, from the MOT configuration, the light is resonant with atoms in distinct $m_F$ states located on separate shells. For small detunings $\Delta$ or high saturation parameters $s$, these shells merge, resulting in the atoms occupying an ellipsoidal volume. This is in contrast to the bosonic case, where atoms are confined primarily to the lower surface of the MOT shape as shown in Figure 4.3. Assuming a one-dimensional MOT, an atom becomes resonant with the cooling light when the Zeeman shift compensates for the detuning and Doppler shift. In particular, the resonance condition for an atom at zero velocity is given by:

$$\Delta = (m_{F'} g_{F'} - m_F g_F)\, \mu_B B(z) = \tilde{\mu}\, (m_F(\rho - 1) \pm \rho))\, g_F \alpha z \tag{4.16}$$

Here $m_{F'} = m_F \pm 1$ depending on the polarization circularity, and $g_{F',F}$ are the Landé g-factor for the ground and excited state, respectively. In the second part of Equation 4.16 $\tilde{\mu} \approx 1.4$ MHz/G is the Bohr magnetron in atomic units, and we define $g_{F'}/g_F = \rho$ while setting the magnetic gradient of one MOT axis to a constant value $\partial_z B_z = \alpha$. For stable MOT operation, the resonance conditions must be negative for all $m_F$ states. This is ensured if the parameter $\rho$ falls within the bounds dictated by the ground and excited state fine structure coefficients:

$$\frac{F}{F+1} < \rho < \frac{F}{F-1} \quad (F \to F+1 \text{ transitions}) \tag{4.17}$$

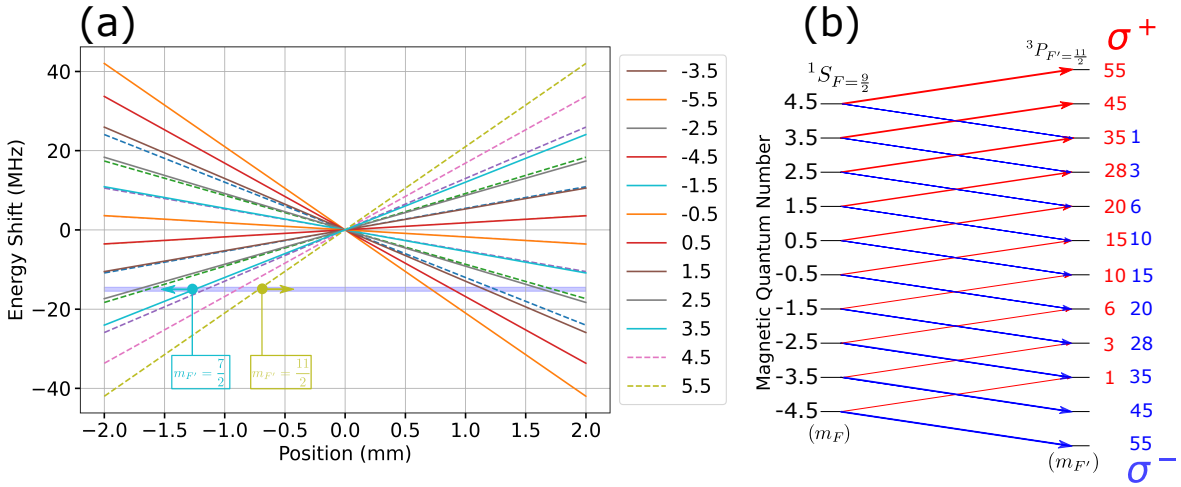


Figure 4.4: Zeeman splitting and transition probabilities in $^{87}$Sr. (a) Zeeman splitting in the MOT for all 10 ground-state nuclear magnetic moments. Using two polarizations $\sigma^-, \sigma^+$ (in cyan and yellow, respectively), an atom in state $m_F = \frac{9}{2}$ can be on the left-hand side of the zero magnetic field point and be driven away from the center of the trap or accelerated towards it. On Image (b) Clebsch-Gordan coefficients represent the relative strengths of each transition on the $F = \frac{9}{2} \rightarrow F' = \frac{11}{2}$.

In many alkali MOTs, these conditions are readily satisfied, so all $m_F$ states are addressed similarly by the MOT beams. For alkaline-earth atoms such as strontium, where the ground state has $J = 0$ and the magnetic sublevels are nearly degenerate, the resonance condition for a light field in a given magnetic field is dependent on the lower $m_F$-state. Under varying B-field, the effect is caused due to the $\rho \gg 1$, and the resonance positions are significantly different for each magnetic moment $m_F \rightarrow m_F \pm 1$ transition, which can be for some red-detuned while for other blue-detuned. Specifically, in $^{87}$Sr, as the ground-state magnetic constant is extremely small ($g_F \approx 1.3 \times 10^{-4}$ [161]) and the factors for the excited state are $g_{F'=9/2,11/2} = \{2/33, 3/11\}$ we thus get that $\rho \approx 2000 \gg 1$. This means that at a given position, the detuning from resonance can be negative or positive, depending on the ground-state moment and polarization $\sigma^+, \sigma^-$. Due to the variation in resonance conditions for the $m_F \rightarrow m_F \pm 1$ transitions, atoms in different magnetic sublevels experience markedly different radiation pressure forces. This variability can prevent the formation of a single, stable trapping potential, leading to some atoms being displaced from the MOT center.

An illustrative depiction of this phenomenon is presented in Figure 4.4 left plot. In the negative MOT region, $m_F = \frac{9}{2} \rightarrow m_{F'} = \frac{9}{2} \pm 1$ atoms experience either repulsive or attractive potentials, resulting in an acceleration away from or towards the MOT center upon interaction with a $\sigma^-(\sigma^+)$-polarized beam. The driving probability for each transition can be calculated using the Clebsch-Gordan coefficients [84], which gradually increase with higher magnetic moment and can be seen on the right panel of Figure 4.4 In the right figure, the probabilities for the previously depicted process are presented; for example, for every 55 trapped atoms in the $|F = \frac{9}{2}, m_F = -\frac{9}{2}\rangle$ one will be expelled from the MOT. Enabling a stable MOT for all sub-levels over many scattering processes requires shuffling the $m_F$ states so an atom feels an average restoring force. An additional beam, red-detuned to the $F = \frac{9}{2} \rightarrow F' = \frac{9}{2}$ transition, is typically used to stir the ground state. This "stirring beam" promotes an even

distribution among the magnetic sublevels [149]. The Zeeman shift of the stirring ($g_{F'=9/2}$) is approximately 4.5 smaller compared to the red MOT transition $g_{F'=11/2}$. This means that the magnetic coupling strength of the stirring beam is reduced by the same factor, resulting in a broadened resonance condition region by that factor. In the experiment, both beams are overlapped and sent to the same MOT fibers and are synchronized to go from the BB to the SF in an almost identical manner[2].

The lower abundance and the atomic loss that the stirring beam is aimed to mitigate are keeping the number of atoms in the red MOT much lower for $^{87}$Sr compared to the $^{88}$Sr. From absorption images of $^{87}$Sr as seen on the left in Figure 4.3, we see a smaller fraction of atoms, and therefore used also a short fluorescence imaging pulse of 100 $\mu s$ to reassure the homogeneous appearance. The fluorescence image can be seen as an inset in Figure 4.3. Calculating the expansion of the cloud due to the blue scattering light which on top of generating the fluorescence signal also heats the gas, was done by assuming the atoms move in a weak laser field with a momentum diffusion coefficient that scales with $D \sim (\hbar k)^2 \Gamma s_0$ [162]. The momentum and, therefore, the velocity variance can be expressed as $\Delta v = \Delta p/m = \sqrt{Dt}$, corresponding to a size increase of $d \approx 66 \mu m$, significantly smaller than the MOT size.

## 4.3 Red Laser System

Unlike blue laser systems, which operate above the UV regime, the 689 nm red laser systems have numerous commercially available laser diodes with instantaneous linewidths on the order of 100 kHz. Therefore, one main challenge for the red system is to stabilize the LD frequency well below the red transition linewidth of approximately $\Gamma/2\pi \approx 7.4$ kHz. For this purpose, we utilize a high-finesse, ultralow expansion (ULE) optical cavity to which we lock our laser.

The second challenge is to shift the laser's locking point by over 2.5 GHz to address different isotopes, similar to our blue laser locking scheme. To get the required frequency shifts for all isotopes, we employ a setup that involves both EOM and AOMs tuning the laser to the desired lock point. Lastly, the intensities required during the broadband phase are on the order of a few thousand $I_{\text{sat}}$, necessitating power amplification. These challenges were addressed with relatively low-budget, home-built setups designed and constructed in-house, enabling the observation of more than $6 \times 10^6$ atoms at a temperature $T < 1\ \mu K$ for $^{88}$Sr and $0.24 \times 10^6$ at $T < 1.5\ \mu K$ for $^{87}$Sr.

### 4.3.1 Cavity Frequency Locking

We employ a Toptica DLpro 689nm laser as our master laser. The laser has an instantaneous linewidth below 100 kHz, making it unsuitable for direct use on the narrow red transition ($\Gamma/2\pi \approx 7.4$ kHz). Laser frequency stabilization below a kHz is obtained by locking the laser to an ultra-low expansion (ULE) cavity. This cavity has a finesse of $F \approx 275,000$ and a free spectral range (FSR) of $\approx 1.5$ GHz, resulting in a cavity linewidth of $\Gamma_{\text{cav}} \approx 5.45$ kHz. The high-finesse cavity is mounted on a specialized BM-8 *Minus-K-Technology* stage for optimal vibration isolation, and its development and performance are detailed in the work of Lars Fischer [163].

[2] We set a smaller modulation BW for the stir beam as well as different power ramp down to the single-photon regime.

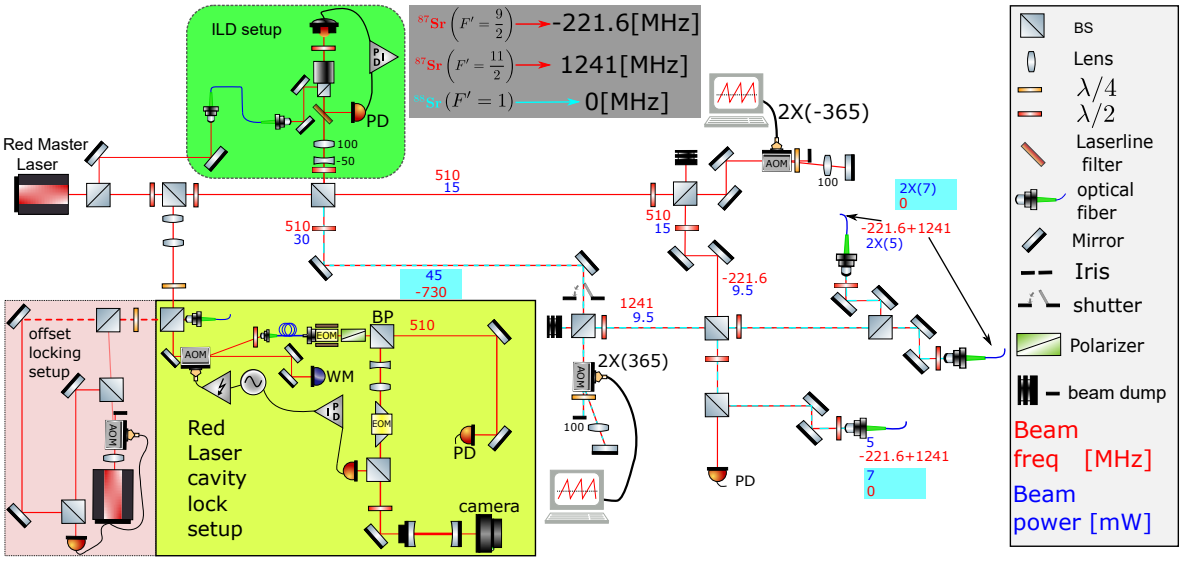


Figure 4.5: Red Laser System. The master laser output is divided into three paths: a locking arm for frequency stabilization to a high-finesse cavity and an injection-locked diode (ILD) amplification stage boosting the power to 90 mW. The last beam is combined with the amplified light from the ILD and sent to optical fibers via the two AOMs. For all bosonic isotopes (here for $^{88}$Sr), only one path is used (dashed light blue line); for the $^{87}$Sr, an additional stirring path is necessary. Note that parameters inside the light blue box refer to the bosonic red MOT.

The cavity is integrated into a frequency locking system based on an offset lock technique [164]. The system includes two electro-optic modulators (EOMs): a broadband fiber-coupled waveguide type from *Jenoptik PM705* with a phase modulation bandwidth tuning of 10 GHz and a free-space resonant crystal EOM *QUBIG PM7-NIR* with a bandwidth of 256 kHz. A power-stabilized 1 mW light is sent to a BB EOM to create sidebands at 1 GHz from the carrier. The beam is then directed to a second EOM, creating sidebands at ±25 MHz and sent to the cavity for frequency stabilization.

We employ the Pound-Drever-Hall (PDH) technique to lock the laser to a high-finesse ULE *Stable Laser Systems (SLS)* cavity. The fiber-based EOM allows us to arbitrarily adjust the laser frequency relative to the cavity mode, ensuring that the light is resonant with the red transitions for all isotopes. To bound the obtained laser linewidth and troubleshoot the frequency lock, another laser has been offset locked to the master laser, as indicated by the light red box in Figure 4.5. From the beat signal spectrum, shown on panel (a) in Figure 4.6, we can give an upper bound estimation on the master laser linewidth reduction. The scan reveals a main peak with a locked linewidth of 16 Hz, limited only by the resolution of the beat signal electronics and the spectrum analyzer's bandwidth (at 10 Hz). Note that additional sidebands, observed at ±5 MHz, likely originate from the offset locking to the second laser.

By scanning the $^{88}$Sr BB red MOT detuning via AOM modulation, we could track the resonance frequency over time. Over several weeks, we observed a slow drift in the red MOT resonance, attributed to the ULE cavity's frequency drift, which necessitates adjustment of the BB EOM setpoint. By tracking the atomic red MOT signal, we can accurately calibrate and compensate for this drift.

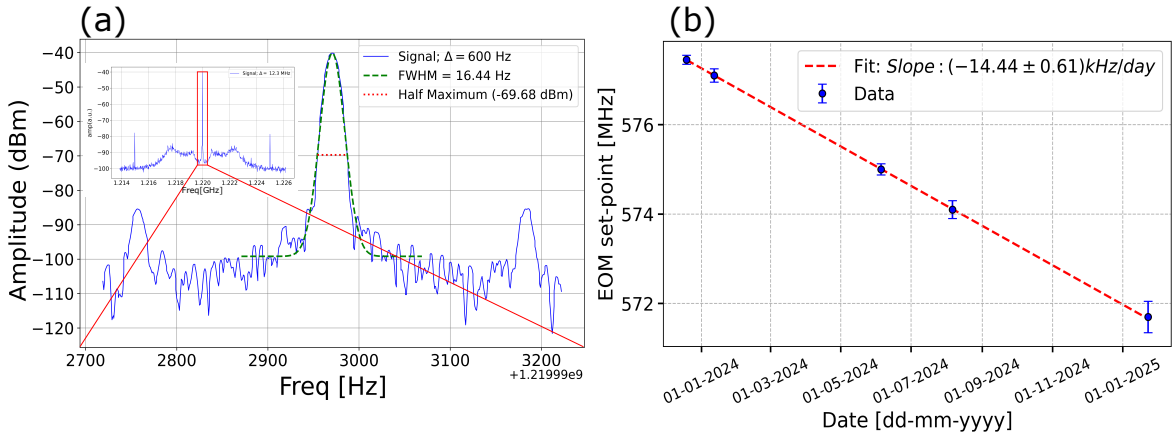


Figure 4.6: Beat lock spectrum and ULE cavity frequency drift. Using the offset locking setup, we could use the beat signal between the two lasers to estimate the linewidth of the locked laser. In the left image, we see a zoomed image to maximal resolution, measuring FWHM of 16 Hz from the inset. The right panel shows the cavity drift over approximately one year, where the position of the $^{87}$Sr red MOT resonance peak is a reference. The linear fit to the cavity drift and associated error bars, derived from the FWHM of the fitted Lorentzian, are also displayed.

In the bottom right of Figure 4.5, the linear trend of this drift is shown, with each point taken after peak resonance measurement and error bars derived from the peak FWHM. The slope indicates a drift of approximately $\approx$ 14.44(6)[kHz/day], which is slow enough to be corrected daily.

### 4.3.2 Injection Lock Diode for Laser Power Amplification

The initial power from the Master laser is around 23 mW, and after coupling to the MOT fibers, we have below 1 mW on the atoms. For beams with around 1 cm diameter, this is approximately 1000 $I_{\text{sat}}$. However, as modulation of the red MOT beams is necessary, this power is distributed over the full modulation span. For example, if we modulate over 4 MHz with a peak separation of 20 kHz, each peak power in the spectrum is below 10 $I_{\text{sat}}$, necessitating power amplification for all MOT beams.

Our approach to enhance the laser power is to use an injection-locked diode (ILD) seeded by the master laser, providing up to 90 mW at the LD output. The injected diode *Thorlabs-HL6750MG* center wavelength range is between 675 nm to 695 nm, making lasing in 689.2 nm fairly doable, and it can operate at a max current of 120 mA. We used a Thorlabs *ITC102* driver to control both the current and temperature with a custom-designed housing for mounting the diode with a temperature-stabilizing setup Appendix C.

We continuously monitor the injection locking diode (ILD) light using a Fabry–Pérot cavity and adjust the current as needed to maximize power while maintaining lock with the main laser through appropriate temperature corrections. In Figure 4.7, the ILD spectrum is shown when seeded and unseeded. The seeding operation is highly sensitive to alignment and seed beam shape and requires mode matching between the bare LD and the seed. The seeding power used to lock the ILD is $P \approx 0.2$ mW. The LD is operating around 22°, and the injection mode locking is reached in currents of $I_{\text{lock}} \approx 88.5, 99.1, 107.6$ mA where the maximum is

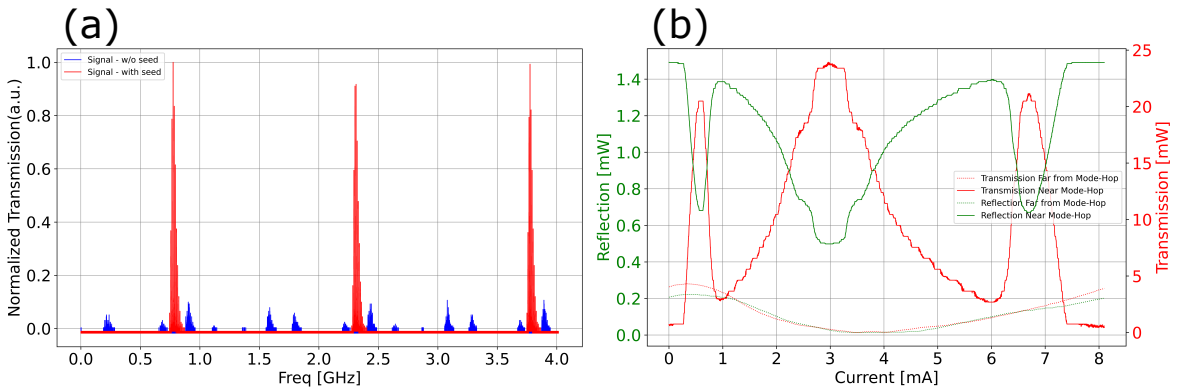


Figure 4.7: Red ILD FPI spectrum and auto relock error signal. The red ILD light is coupled to an FPI with an FSR $\approx$ 1.5 GHz to measure the spectrum together with the main laser. In the left panel, the blue spectra show the unseeded ILD, and in red, the seeded one. On the right panel, we measure the transmission and reflection from the 689 nm laser line filter when we are both far from the locked point of the ILD and near the mode-hop region. The correlation between reflection and transmission can be used to optimize the operating current of the ILD.

usually the working point. Stable injection locking is achieved with ILD current adjustments in the range of $0.1 - 0.3$ mA. When seeded, the ILD's maximum output power is around 65 mW after the isolator, with a roughly 1:2 aspect ratio elliptical shape and an average beam waist of 0.5 mm.

Similar to the Blue ILA and with the inspiration of [165], we add an auto-relock option to our red ILD, enabling automatic locking of the ILD. A simplified setup, illustrated in Figure 4.5 in the green section, takes advantage of inserting a narrow-line laser filter that is angle-dependent and transmits only a small bandwidth ($\sim$ 0.5 nm) of light that is matched to the acceptance angle of the filter (around 6°), and the reflected light from the filter is measured by a photodetector. When the diode is injection locked, the reflected light is minimized. This reduction in reflection generates an error signal for a feedback loop, enabling stable offset locking. By employing a Red-Pitaya Stemlab and its built-in locking PID GUI, an offset current can be chosen to match the minimum point in the current ramp, and the ILD will re-lock itself when needed. The right panel of Figure 4.7 shows the ILD power as a function of the ILD current of the transmission and reflection (red and green) both around the lock current $I_{\text{lock}}$ and way from it (solid and dashed lines). The figure shows the correlation expected when the current is ramped at a non-resonant point for the ILD as the filter acts far from its transmission point. However, as the current is ramped to any of the locking currents $I_{\text{lock}}$, an anti-correlation behavior with a strong gradient is observed. The setup had successfully re-locked the ILD, however, it is not currently used in the red laser system[3], The same setup could also be adapted to home-built blue ILA which tend to be less stable.

[3]The filter reflects 12% and seeing the high stability of the ILD overtime, it was decided to place it out of the beam path

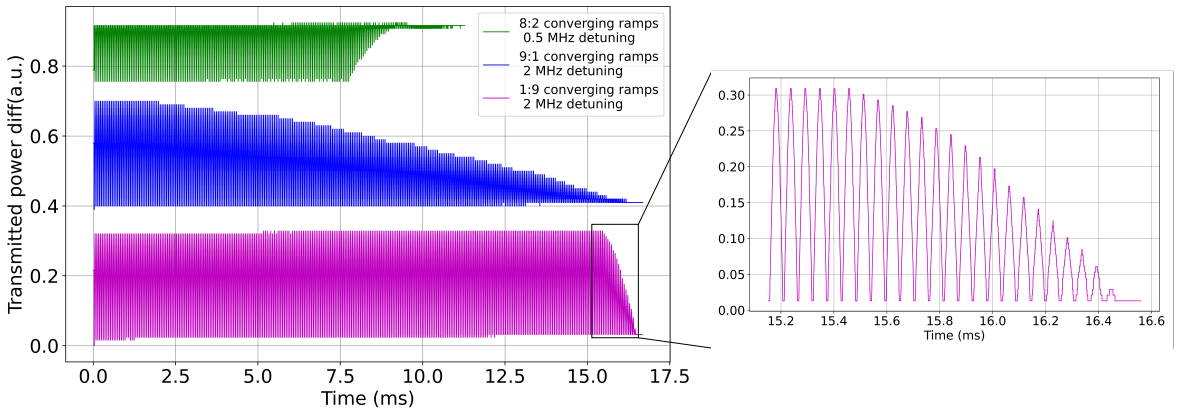


Figure 4.8: AOM power modulation in time and frequency domain. The left plot shows three different power ramps of the red MOT beams before the science cell Configured by the DDs. The magenta (blue) represents a measurement that has 180 (20) normal ramps followed by 20 (180) converging ramps with a time duration of 17 ms. In green, the detuning from the center AOM frequency is changed by 1.5 MHz, and the signal is set for only 100 ramps(80 normal and 20 converging), which shortens the duration. The inset is zoomed in to observe the individual modulations, specifically on the final part of the magenta plot as the ramping is converging.

### 4.3.3 Frequency Shifting and Modulation with Two AOM Arms

The amplified beam is then recombined with the initial split beam, and the two are sent to the main red MOT laser system. As shown in Figure 4.5, the two beams are sent to two DP AOMs (AOMO-350-125) with an operating frequency at $f_c = 350$ MHz and a bandwidth of $\delta_{1,2} = \pm 25$ MHz.

The achievable frequency difference between the two arms is thus $\Delta f_{\pm} = 1400 \pm 100$ MHz. This configuration bridges the gap between the two $^{87}$Sr $F' = \frac{9}{2}, \frac{11}{2}$ transitions to the $^3P_1$ manifold when using the 689 nm transition. As previously discussed, the separation of the state is roughly 1.46 GHz.

We refer to the first beam as the red MOT light and the other AOM arm as the stirring beam $F = \frac{9}{2} \rightarrow F' = \frac{9}{2}$, which is used to randomize the different $m_F$-states. After the DPs, we overlap the beams from each arm into a single PBS such that we get two beams, each having opposite polarization but the same two frequencies $f_1, f_2$. Then, using more PBSs and waveplates, we can equally distribute the light to three fibers and a PD.

Coupling two fibers with both beams is not simple, as the beams path and waist differ. However, by using a telescope on one path, we can adjust the beam's divergence, eventually reaching approximately 30% coupling efficiency for one beam and 45% coupling efficiency for the other. We can also alter the efficiency by small adjustments of the last mirror prior to the fiber's in-coupler. From there, the light is sent to the experimental table, where each beam has a waist of $w_0 \approx 4$ mm and a total power of 7.5 mW combined. They are polarization cleaned, sent to the atoms, and retro-reflected in a similar MOT configuration as we do for the blue MOT.

In our setup, individual isotopes are addressed simply by rotating a half-wave plate and adjusting the AOM and EOM frequencies. For bosonic isotopes, all available power is directed

into one AOM path to maximize the MOT loading. This two-AOM, two-EOM configuration is more cost-effective than systems that require separate AOMs for each isotope while still providing the necessary frequency control. When operating either with bosons or fermions, a preconfigured modulation scan is sent through the DDs to one or both AOMs. As one changes the frequency sent to the AOM, the powers varies due to a change of Bragg condition. Characterizing this loss in power shows less than 10% from max power over a scan of ±4 MHz around the peak, although for ±8 MHz this becomes around 50% with a beam waist of 0.5 mm.[4] When the AOMs are modulated, the resulting variations in beam power can be detected using a photodetector, as illustrated in Figure 4.8. Monitoring these power fluctuations facilitates sequence troubleshooting. The three colored graphs represent different ramps, which possess both normal and converging ramp periods with different aspect ratios. A normal ramp period means that both the initial set frequency and the final set frequency stay the same during the entire period. A converging ramp period means that while the initial set frequency is the same, the final one is reduced after each ramp with a constant subtraction (giving a linear shape as seen in the Figure 4.8) until it matches the initial frequency. The ratio between these periods (or number of ramps as the single ramp duration is constant) is the aspect ratio, which is shown in Figure 4.8. Other important parameters are the detuning of the signal compared to the AOM center frequency and the BW modulation, which is sent to the AOM. Modifications in the AOM detuning result in changes to the intensity profile, even with similar BW, as demonstrated in the green graph. This measurement serves as a useful tool for verifying the functionality and timing of the red MOT beams within the sequence. With the help of Fourier analysis on these datasets, the single ramp time is measured to be $t_{\text{ramp}} \approx 0.55$ ms $\approx 1/18.2$ kHz, which is close enough to our 20 kHz peak separation in the BB phase.

## 4.4 Red MOT Optimization and Characterization

A first signal from the red MOT is difficult to observe since finding the transition frequency means we search in sub-MHz steps throughout tens of MHz. An effective initial value is the literature frequency $\omega_{0,\text{red}} \approx 2\pi \times 434,829,121,300$ kHz [93], chosen for the red beam, aligning with the highest precision frequency observable with our wavemeter, which has a resolution of ± 15 MHz and absolute accuracy of 200 MHz. The red laser frequency is scanned by changing the BB EOM frequency while also modulating the AOM frequency and sending the light to the blue MOT. During the sequence, the fluorescence of the blue MOT is recorded on a camera, which is observed in real time. As the red MOT beam is tuned toward resonance, the blue MOT fluorescence intensity is synchronized with the red beam's frequency modulation. This effect is attributed to shelving, where atoms are transferred from the cooling cycle into long-lived, non-fluorescing metastable states[166, 167]. In essence, when the red MOT beam is near resonance, a significant fraction of atoms is "shelved" into these dark states, reducing their contribution to the blue fluorescence. Small detuning changes (on the order of 0.5–1 MHz) markedly affect the fraction of shelved atoms, resulting in the observed oscillations in the blue MOT signal. This technique is crucial in finding the transition frequency and helps with initial beam alignment. We can block all but one red MOT beam and align the light to hit the blue MOT until the effect is maximized. As the blue MOT is roughly 3-5 mm in size and the red beam diameter is 4 mm, we can find a point where almost the entire blue MOT

[4] The power gradient and max power depend on the beam size and give different numbers for smaller beams.

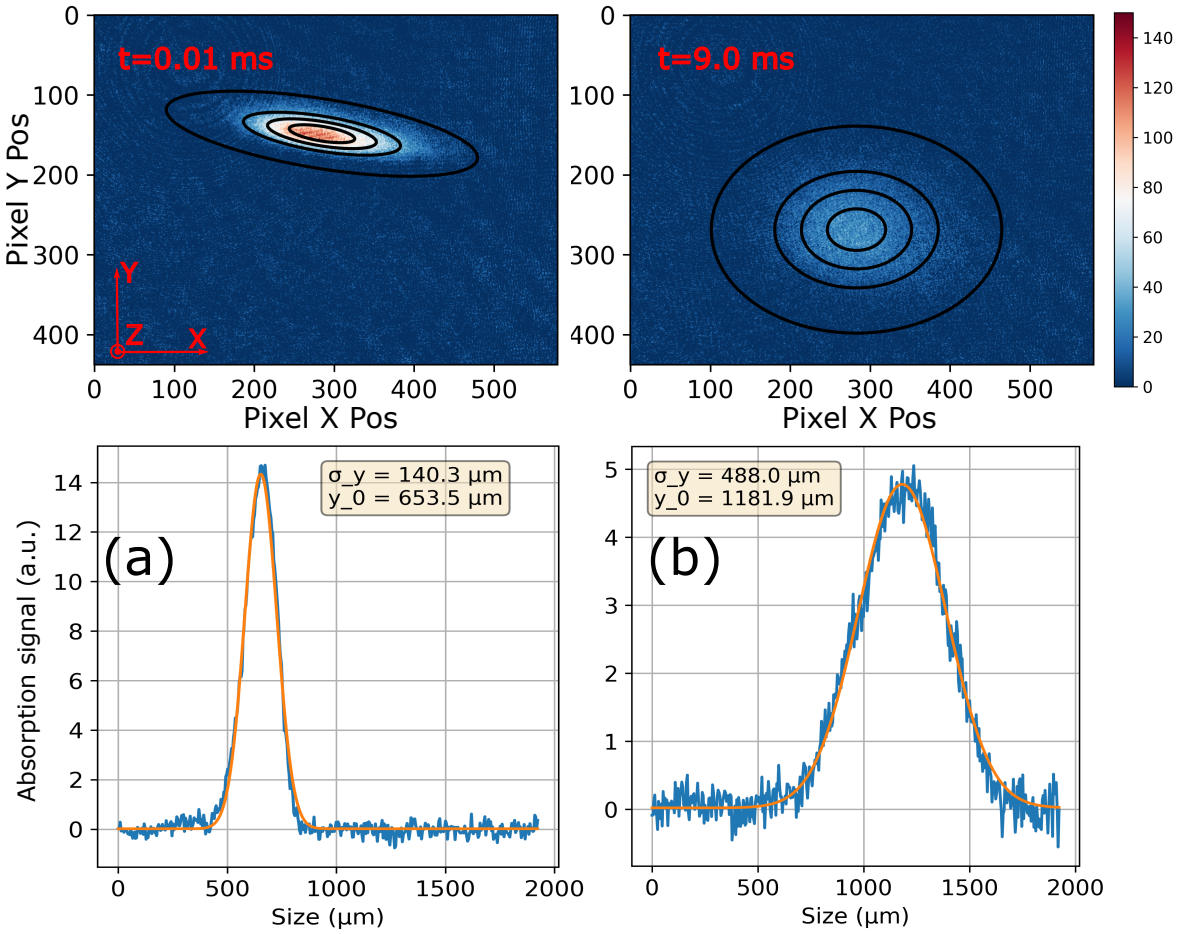


Figure 4.9: Time of flight images of $^{88}$Sr. In the top two absorption images, the CrMOT is presented for different ToF ($t = [0.01, 9]$ ms) with the arbitrary color bar to show high-density areas. The black contours show a 2D Gaussian model fitting to the cloud, which is used to plot the two bottom figures, and the red dashed line shows on which 1D cut they are taken. The time evolution of the vertical size (Y-axis) of the red MOT cloud is analyzed to determine the temperature, which is approximately 1.34$\mu$K.

blinks and afterward align the retro-reflecting mirror, increasing the signal. For each beam on the order of 3 mW of power is used, and we use waveplates before the fibers to distribute the power between the MOT axis unequally. From this point, all optimization, including power-balancing small alignments, is done by observing the BB or SF red MOT.

### 4.4.1 Boson Red MOT

By shifting the frequency of the EOM and relocking to the cavity, the system is tuned towards resonance with respect to the $^{88}$Sr isotope, our primary bosonic candidate for red MOT operation. The laser is locked using a *Toptica FALC pro* PID controller, with cavity transmission monitored via a camera and the laser wavelength continuously measured on the wavemeter for troubleshooting.

The experimental sequence proceeds by first capturing atoms in the reservoir during a non-

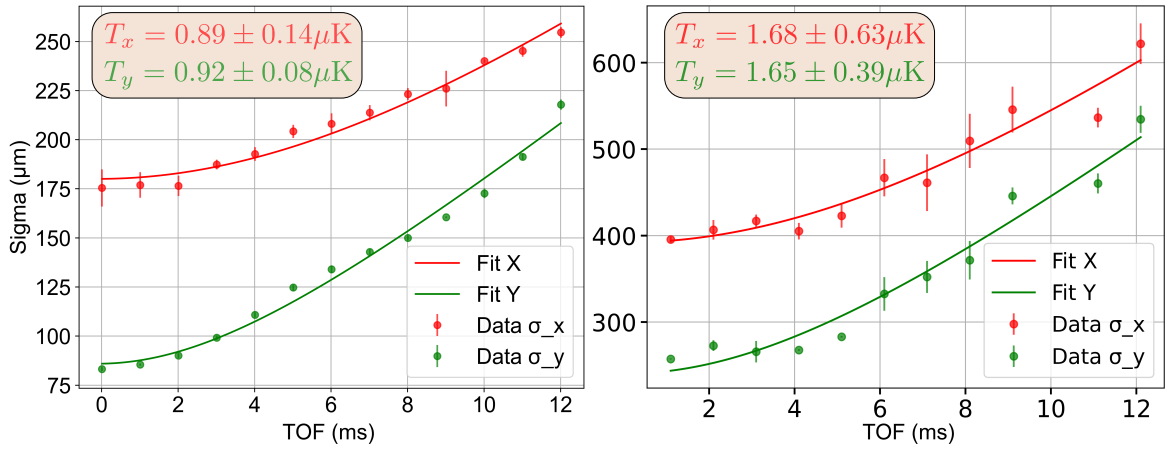


Figure 4.10: Single frequency red MOT temperatures. The expansion dynamics of the cloud during a time of flight gives access to the initial momentum spread of the cloud and hence its temperature along X (red) and Y (green), following Equation 4.18.

repumped blue MOT phase lasting 2 seconds. Subsequently, the atoms are depumped from the reservoir back to the ground state by illuminating them with both repumpers for 56 ms. During the initial 6 ms, the magnetic field is rapidly ramped down to roughly 3.22 G/cm and held constant until imaging. The broadband MOT frequency modulations start with 4 MHz peak-to-peak for each full ramp. As we go toward the SF crMOT, the power ramps down with a duration of 300 ms while the frequency span reduces. The beams power ramp down towards the SF regime is done by reducing the AOM signal amplification, reaching around $I/I_{\text{sat}} \approx 260$ in total intensity in the MOT. Going further down, the radiation force is too weak to hold to a cloud, and we see no atomic signal. Furthermore, the narrow linewidth of the SF red MOT results in a heightened sensitivity to small variations in the magnetic field.

### 4.4.2 Fermion red MOT

To create a red MOT for $^{87}$Sr, it is essential to address both the $F = 9/2 \rightarrow F' = 11/2$ transition with the MOT beam and the $F = 9/2 \rightarrow F' = 9/2$ transition with a stirring beam. The beam is split into two different AOMs to generate the required light for stirring and red MOT beams, to be later recombined and sent to the atoms.

In our setup, the 3D MOT beams are provided with approximately 7.5 mW of total power, while the stirring beams are maintained at around 2.5 mW. Each beam is modulated over a tailored frequency span, with independent detuning control, to optimize atom number and minimize temperature. This arrangement allows us to fine-tune the cooling without compromising overall system performance. Unlike the $^{88}$Sr case, the power ramp-down for $^{87}$Sr occurs over a much shorter time scale (approximately 100 ms), with distinct final power levels for each beam with final power levels corresponding to $I_{\text{MOT}}/I_{sat} \approx 420$ for the cooling and $I_{\text{stir}}/I_{sat} \approx 30$ for the stirring beam. At this stage, we evaluate the temperature, a critical step prior to loading the atoms into the dipole trap.

### 4.4.3 Time of flight measurement for temperature calibration

Observing the SF red MOT, we see a density increase, suggesting a colder sample.

To measure the temperature of the atoms, a time-of-flight (ToF) technique is used. The cloud is released from the MOT, and absorption or fluorescence imaging takes place for various expansion times of the atomic sample. Example absorption images with their corresponding 2D Gaussian fits are presented in Figure 4.9. These fits enable us to extract the cloud's size and position[5]. Assuming a Gaussian momentum distribution, the expansion of the atomic cloud is governed by initial momentum spread, which is directly related to the temperature. In practice, the MOT is released at $t = 0$ with an initial size $\sigma(t = 0)$; the subsequent free expansion yields a cloud size $\sigma(t)$ that reflects the temperature according to:

$$\sigma(t) = \sqrt{\sigma^2(t_0) + \langle v^2 \rangle (t - t_0)^2} \tag{4.18}$$

Here $\langle v^2 \rangle$ is the cloud velocity distribution RMS, and $t_0$ is the initial releasing time of the ToF.

The gravity direction in which the cloud falls is used to calibrate the magnification of our imaging system. From the free-fall dynamics, we find the magnification to be $M \approx 1.66(4)$ for $^{88}$Sr. From Boltzmann distribution, the RMS speed is connected to the temperature of the gas $T$ by the following relation

$$\langle v^2 \rangle = \frac{k_B T}{m}$$

Fitting Equation 4.18 to the observed expansion dynamics provides the temperature of the cloud, depending on which massive ($m$) isotope is imaged. In Figure 4.10 we present the ToF measurements of both axes for $^{88}$Sr and $^{87}$Sr. From the fit parameters, we get temperatures of below 1 $\mu K$ for $^{88}$Sr and around 1.66(3) $\mu K$ for $^{87}$Sr with roughly one million and 240 thousand atoms, respectively.

### 4.4.4 Lifetime and Cloud Characteristics

The optimization of the red MOT, in both BB and SF regimes, presents significantly greater challenges compared to the blue MOT. Specifically, the number of atoms trapped in the fermionic $^{87}$Sr MOT is reduced by more than 90% when the stirring beam is not incorporated into the experimental sequence from the BB phase. A shift of $\Delta\partial_y B_y \approx 0.086$ G/cm at an intensity of 10 $I_{\text{sat}}$ can displace the cloud's center-of-mass by 0.1 mm. To address these challenges, our optimization strategy involves a stepwise procedure.

We begin with the bosonic $^{88}$Sr isotope, maximizing the number of atoms and extending the trap lifetime by carefully tuning the sequence parameters. Subsequently, we adjust the magnetic field gradient and compensation coils to control the size and position of the SF red MOT. Using this optimized sequence, we routinely obtain 1-2 $\times 10^6$ atoms in the BB MOT, with a 20% loss during the SF MOT transition. In the low-intensity SF MOT, negligible atom loss is observed, and temperatures as low as 0.8 $\mu$K are achieved in some experiments. Using these numbers, we can roughly estimate the peak phase-space density (PSD), which is defined as $\rho_{\text{PSD}} = \frac{N}{(2\pi)^{3/2}\sigma_x\sigma_y^2}\lambda_T$, here $N, \sigma_{x,y}, \lambda_T$ are the number of atoms, the gaussian rms radii and Thermal de Broglie wavelength, respectively. The atomic cloud in the SF MOT exhibits PSD of approximately $\rho_{\text{PSD}} \approx 10.4 \times 10^{-4}$, and its spatial dimensions are $\sigma_x \approx 0.15$ mm (horizontal) and $\sigma_y \approx 0.04$ mm (vertical) giving an almost 1:4 spatial aspect ratio.

[5]The SF crMOT $^{88}$Sr may exhibit a slight tilt during equilibration, as seen in the top right image of Figure 4.9, but this does not affect the number of atoms or temperature.

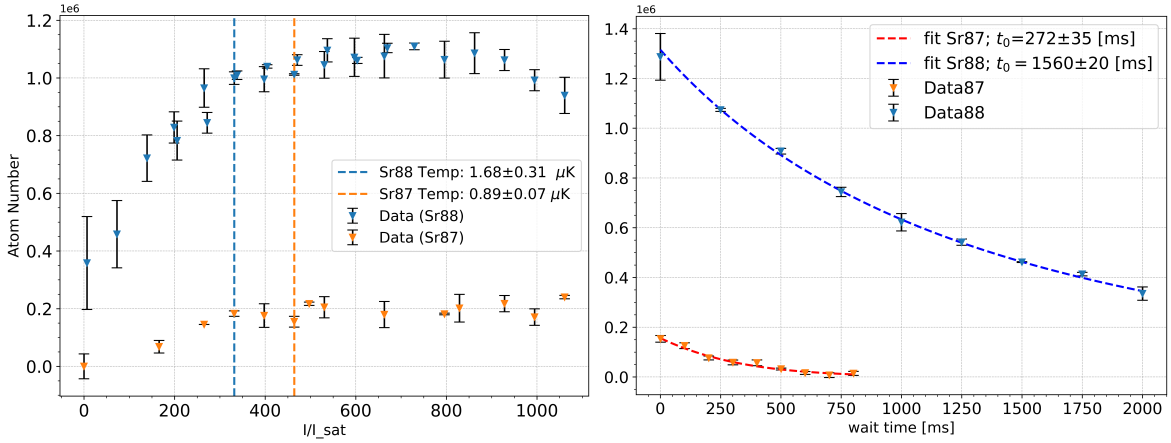


Figure 4.11: Lifetime and red beam Intensity ramp-down measurements for two different isotopes. On the Right panel, we see a holding time measurement in the SF red MOT for both Fermionic $^{87}$Sr and bosonic $^{88}$Sr atoms. The fitting function used is Equation 4.20, giving a lifetime of almost 2 seconds for the boson, however, the low initial number of atoms makes observing the Fermion difficult after more than 0.8 seconds. The intensity of the beams for each lifetime experiment is seen in the left panel in the two vertical line markers. In the plot, the intensity is ramped down while the number of atoms is counted, and the dashed lines are the optimal points we chose to perform ToF and lifetime measurements. Note that for the $^{87}$Sr, the stirring is also ramped down but with a different trajectory.

For the $^{87}$Sr fermionic sample, a typical number of atoms obtained $0.4 \times 10^6$ atoms in the BB MOT, with more than 40% loss during the transition to the SF MOT. In the low-intensity SF MOT, atom loss is minimal, and temperatures as low as 1.66 $\mu$K are achieved. Moreover, the atomic cloud in the SF MOT exhibits a peak PSD of approximately $\rho_{\mathrm{PSD}} \approx 3.1 \times 10^{-5}$. Notably, the cloud morphology is less anisotropic than its boson counterpart with average radii of $\sigma_x \approx 0.15$ mm (horizontal) and $\sigma_y \approx 0.1$ mm (vertical), the much higher 2:3 aspect reflects the effect of the hyperfine structure[6].

We optimized the previous values by finding the lowest intensity point in which the number of atoms is maximized while the temperature is minimized, as plotted in Figure 4.11 left panel. Below a critical red MOT beam intensity (normalized to the red saturation intensity), the atoms are no longer vertically confined and begin to fall from the trap. Therefore, identify the optimal intensity that maximizes the phase-space density and perform subsequent measurements, such as lifetime experiments, at this beam power setting. The lifetime is another parameter that is subject to optimization. observing at the MOT initial atom number, and its final, we can model this loss process as follows:

$$\frac{dN}{dt} = -a\,N - b\,N^2, \tag{4.19}$$

where the one-body loss rate $a$ represents density-independent losses (e.g., background collisions) and the two-body loss rate $b$ represents density-dependent losses by light-assisted collisions. This is a simplified model that neglects three-body collisions, which are rare events

[6]The PSD here is a rough estimation as MOT is not perfectly symmetric in the Y and Z axis.

that become dominant only closer to degeneracy. Solving Equation 4.19 is possible with an analytic solution in the form of:

$$N(t) = \frac{aN_0\, e^{-at}}{a + bN_0\,(1 - e^{-at})}. \tag{4.20}$$

In the SF MOT stage, cold atoms exhibit lifetimes exceeding several hundred milliseconds, which enables efficient loading into the dipole trap for further cooling. These lifetime measurements are presented in the right panel of Figure 4.11. These conditions are excellent for loading a conservative trap for further evaporation to degeneracy.

# Chapter 5

# Optical dipole trapping

Until now, we have focused on cooling the atomic cloud close to degeneracy with only the red MOT narrow line beams. Our next step involves loading the atoms into conservative traps for further cooling and experiments, offering further cooling and an opportunity to study the many-body physics in a lattice configuration. The envisioned cooling procedure will be pursued by first loading the atoms into an optical dipole trap of 1040 nm acting as a reservoir trap, to be transferred onto an even smaller dimple trap. The dimple trap with an additional light-shielding transparency beam, which shifts the atoms from the $^1S_0 \rightarrow {}^3P_1$ resonance, should bring the cloud to quantum degeneracy. Second, since the goal of our experiment is to study fermions in optical lattices with single-particle resolution, we introduce a spacing-tunable "accordion" optical lattice, which will be used to create 2D gases and to study the Fermi-Hubbard model. The chapter will start with a brief theory of optical dipole traps and the physics behind them. Then, a short discussion on our cooling technique inside the dipole trap and how it utilizes the transparency beam, followed by an explanation of what optical lattices are and how to create them. Finally, the vertical accordion lattice system will be presented and fully characterized to show its limitations and abilities to trap strontium atoms.

## 5.1 Final Cooling Stage

Although the narrow-line red MOT operating on the 689 nm transition cools strontium atoms to the microkelvin regime, it is photon re-scattering that limits the density by reheating the sample, thus preventing further cooling toward quantum degeneracy. To overcome these challenges, our strategy (adopted from [84, 69]) is to transfer atoms from the red MOT into a deep optical dipole trap, where they can be further cooled without the deleterious effects of near-resonant light. In the dipole trap, a secondary "transparency" laser is applied to induce a light shift on the excited state, effectively detuning the atoms from the cooling light. This decouples the cooling dynamics from photon reabsorption and light-assisted collisions, allowing elastic collisions to efficiently drive the accumulation of atoms into a tighter dimple potential. In this final stage, the combined effect of deep trapping and selective optical decoupling enables the system to approach the high phase-space density required for quantum degeneracy. The following sections detail the theory and experimental implementation of this scheme, along with the challenges encountered in optimizing the transfer from the red MOT to the optical dipole and dimple trap.

### 5.1.1 Theory of optical dipole traps

When an atom is coupled to a light field, two main contributions potentially affect it. First is a dissipative part, which is the radiation pressure, which we have detailed before, and secondly, the conservative part, which is the dipole force. Contrary to the radiation pressure force (used in the MOT), which dominates close to resonance, the dipole force cancels at zero detuning. However, for beams far-detuned from the resonance, the dipole force dominates, and the atoms can be trapped in the peak intensity or minima depending on the detuning sign. As the temperature reaches a few microkelvins, loading the atoms into an optical dipole trap calls for a high-intensity beam. The idea behind optical dipole traps originates from the dipole force (or potential) first demonstrated in 1986 [168] and fully detailed in [169], which we will partly follow here. The dipole force arising from the beam intensity gradient, which writes:

$$F_{\text{dip}}(\mathbf{r}) = -\nabla U_{\text{dip}} = -\frac{3\pi c^2}{2\omega_0^3}\left(\frac{\Gamma}{\omega_0-\omega}+\frac{\Gamma}{\omega_0+\omega}\right)\nabla I(\mathbf{r}) \tag{5.1}$$

Here, $\Gamma, \omega_0, c$, represent the linewidth, the on-resonance frequency, and the speed of light, respectively. In the rotating-wave approximation (RWA), which neglects the counter-rotating term [24], the dipole force scales as

$$F_{\text{dip}} \propto \frac{I}{\Delta}$$

where $I$ is the light intensity and $\Delta$ is the detuning. This dispersive force can offer trapping in two forms, red detuned ($\Delta < 0$), attracting atoms to the center of the beam intensity, or blue detuned ($\Delta > 0$), where the light is repelling the atoms. There are several transitions in Strontium to trap and cool (e.g. ${}^1S_0 \rightarrow {}^3P_1$), but the most suitable is at 460 nm. For this reason, blue-detuned traps are less common as they will reside in the UV spectrum [1]. For example, using the $\text{TEM}_{00}$ mode of a laser has a Gaussian form, and when shining it on the atoms, it generates a potential:

$$2\epsilon_0 c\,|E_{GB}(\mathbf{r})|^2 = I_{GB}(r,z) = \frac{2P}{\pi w^2(z)} e^{\frac{-2r^2}{w^2(z)}}\ ,\ w(z) = w_0\sqrt{1+\left(\frac{z}{z_R}\right)^2} \tag{5.2}$$

where we define $w_0, P$, and $z_R$, as the waist of the beam, the power of the beam, and the Rayleigh range, respectively. The Rayleigh range can be written as $z_R = \pi w_0^2/\lambda$, indicating the distance where the beam intensity is halved, with $\lambda$ being the light wavelength. Furthermore, inserting the intensity in Equation 5.2 to Equation 5.1, and expanding the resulting potential around $(r,z) = (0,0)$ we obtain:

$$U_{GB}(r,z) = \frac{3\pi c^2}{2\omega_0}\frac{\Gamma}{\Delta} I_{GB}(r,z) \approx U_0(\Delta, P)\left[\left(\frac{\sqrt{2}r}{w_0}\right)^2 + \left(\frac{z}{z_R}\right)^2\right] \tag{5.3}$$

This harmonic trap is characterized by its frequencies, i.e., the radial and vertical frequencies, $\omega_r = \sqrt{4U_0/mw_0^2}$ and $\omega_z = \sqrt{2U_0/mz_R^2}$, and $U_0$ can be calculated from the transition parameters and depend only on the detuning and beam intensity. The harmonic approximation made in Equation 5.3 is valid under the assumption of $\frac{k_B T}{U_0} \ll 1$, meaning the thermal distribution of the atomic sample is much smaller than the beam's axial and radial waists.

[1] There are proposals for such trapping [170], but to the best of my knowledge, not yet any demonstration

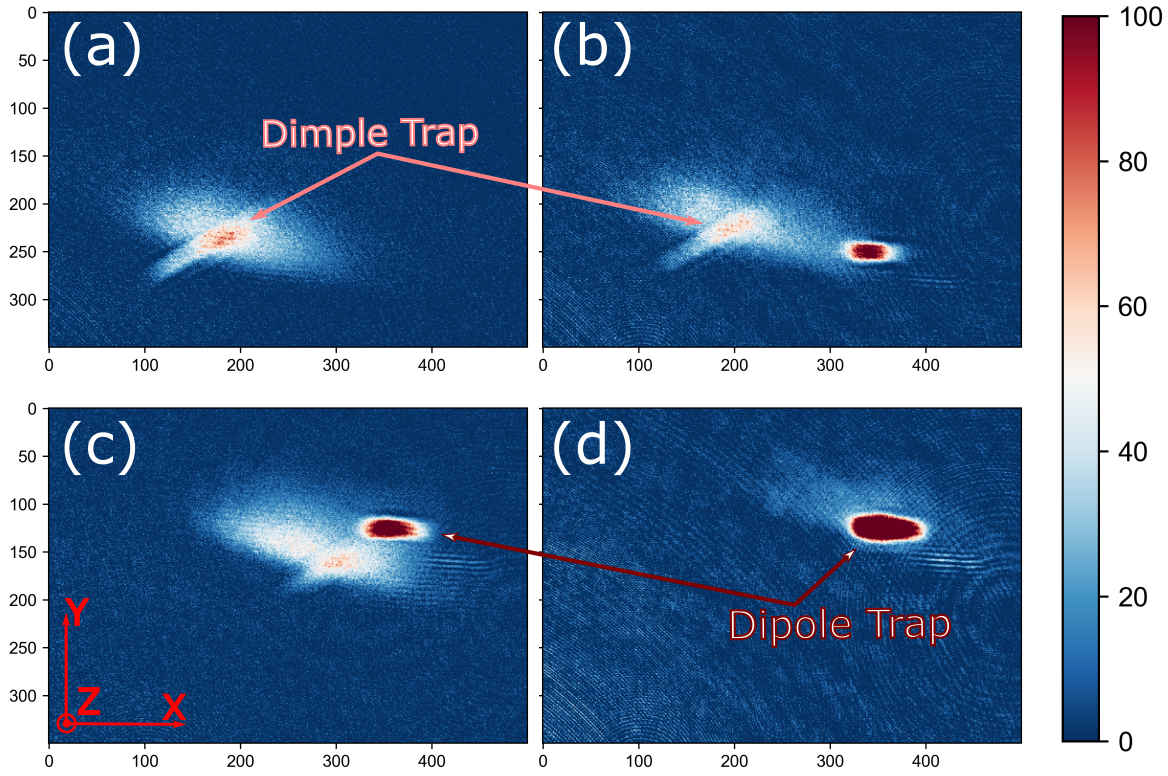


Figure 5.1: Absorption images of infrared dipole traps loading from $^{88}$Sr red MOT. The images show an overlap of the dimple trap (high-density region) with the red MOT. b,c). The trapping signal in both the dimple and reservoir dipole traps is misaligned. d) atoms loaded in the crossed dipole trap.

After confirmation that the trap depth is significantly larger than the atoms' thermal energy, which ensures a robust atomic confinement, we describe trapping frequencies. Because the gas is far from degeneracy, we can use the harmonic oscillator picture, assuming a classical (Boltzmann) gas at temperature $T$ inside a harmonic trap. In this picture, the trapped cloud has effective frequencies at which it moves due to the harmonic nature of the dipole trap. In our experiments, we determine the dipole trapping frequencies by directly measuring the atomic motion [171], which accurately characterizes the trapping efficiency. By using power modulation spectroscopy [172], the sample is parametrically driven with the laser at twice the trap resonance frequency. In this condition, the system experiences large losses. By scanning the modulation frequency, we can measure the trap resonance and, thus, determine its effective size.

### 5.1.2 Red MOT to dipole traps - towards quantum degeneracy

After measuring the temperature in the red MOT, further cooling is performed by employing a red-detuned 1040 nm ODT and aligning it to the red MOT position. The dipole and dimple traps building and characterization were performed by Thies Plaßmann. The seed laser is a

| Parameter | Dipole Trap | Dimple Trap |
|---|---|---|
| Wavelength | 1040 nm | 1040 nm |
| Beam waist | $w_z \approx 22\ \mu$m, $w_x \approx 186\ \mu$m | $w_r \approx 10\ \mu$m |
| Power Range | 4 W | 0.4 W |
| Trap Depth, $U_0/k_B$ | $\sim 22\,\mu$K | $\sim 23\,\mu$K |
| Radial Trap Frequency, $f_r$ | $\sim 344$ Hz | $\sim 900$ Hz |
| Longitudinal Trap Frequency, $f_z$ | $\sim 1.5$ Hz | $\sim 10$ Hz |

Table 5.1: Main parameters for the Dipole and Dimple traps. Trap depth $U_0/k_B$ is given in $\mu$K, and trap frequencies are reported in Hz.

home-built laser that was built by former student Etienne Cardi [2] and is a homemade cat-eye ECDL following this design [173]. The seed is coupled to a high-power fiber amplifier *Toptica ALS-IR*, which can output up to 45W. The amplifier output beam is split into two: one beam is used for the reservoir and dimple dipole traps, and one beam is sent to an SHG module to obtain light at 520nm for the optical lattice, which will be described in the accordion lattices chapter. The reservoir dipole trap is sent directly to the atoms on the horizontal axis (Z-axis), which overlaps with the horizontal imaging beams using dichroic optics. The beam has an elliptical shape with a vertical waist of $w_{\mathrm{dip,z}} \approx 22\ \mu m$ and a horizontal waist $w_{\mathrm{dip,x}} \approx 186\ \mu m$. With beam power on the order of 4 W Watts, the dipole trap depth corresponds to around 36 microkelvins. The dimple dipole trap has 0.5 W peak power and is propagating diagonally on the X-Y plane and intersects the red MOT on a 22-degree angle from the X-Z plane. The dimple has a vertical waist of $w_{\mathrm{dip,y}} \approx 11\ \mu m$ and a horizontal waist $w_{\mathrm{dip,x}} \approx 10\ \mu m$. As the waist of the dimple is much smaller, only around 0.5 W is used to trap atoms as seen in Figure 5.1.

By using the parameter in Table 5.1, and assuming a harmonically trapped classical gas, we can estimate the PSD in the cross dipole-dimple. Under these assumptions, the $\rho_{\mathrm{PSD}} = N(\hbar\bar{\omega}/k_B T)^3$, where $N$, $\bar{\omega}$, $T$ are the number of atoms, the geometric mean trap frequency, and the temperature of the sample. With a temperature of $T \approx 4\ \mu K$, and a trap frequency being $\bar{\omega} \approx 2\pi \times 0.93$ kHz with the $\sim 10^5$ atoms, we get $\rho_{\mathrm{PSD}} \approx 0.14$, which is still one order of magnitude far from the degenerate condensed gas.[3] Bridging the gap of the phase-space density requires a way to further cool the atoms while shielding them from the harmful red resonance light, which is done with the use of a transparency beam.

### 5.1.3 Transparency Light

The crossed dipole trap alone is insufficient to reach the quantum degenerate regime and, therefore, further cooling and or density increase is needed. Following the approach from [84, 69], a beam shifting the resonance of the red transition is used to mitigate the effect of photon reabsorption in the dimple region. We call this beam the transparency beam, which operates near the $^3P_1 \rightarrow {}^3S_1$ transition at 688 nm wavelength. The beam shifting is engineered to create a localized region of transparency within the ODT. This region is intended to shield atoms from the resonant scattering of the red MOT beams.

[2] The design and build-up of the laser is documented on a locally saved report

[3] The dimple trap is not fully characterized specifically the cross area with the dipole trap so the PSD could be lower.

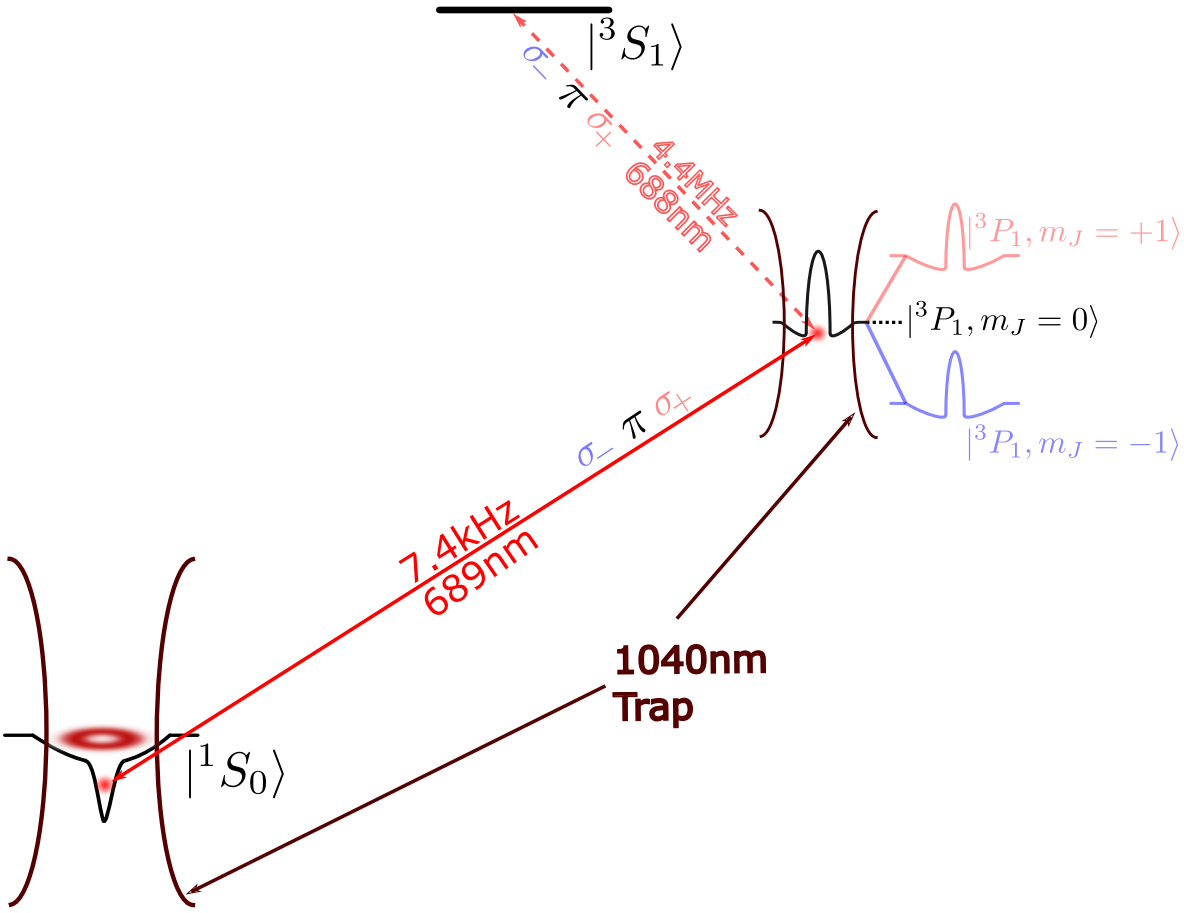


Figure 5.2: Light induced transparency in dimple trap. The light red dashed arrow depicts a transparency beam blue-detuned from the $^3P_1 \rightarrow {}^3S_1$ transition, inducing a light shift that renders atoms transparent to the red MOT cooling light. The light blue (red) color reflects a beam with a $\sigma^-, (\sigma^+)$ which couples to $m_J = -1$ $(+1)$ states inside the dimple trap. This creates a spatial region within the dipole trap (the dimple region) where atoms are shielded from resonant scattering, promoting higher densities and lower temperatures.

Through elastic collisions with the reservoir trap atoms, atoms accumulate in the dimple region, where they do not scatter red light anymore. Ultimately, this leads to the formation of a quantum degenerate gas [174, 175].

Figure 5.2 illustrates the energy level diagram, showcasing how the 688 nm beam induces a light shift by utilizing the $^3P_1 \rightarrow {}^3S_1$ transition. The transparency beam, characterized by a waist of $w_{\text{transp}} \approx 9.6\ \mu m$ and a frequency of 435.7315 THz, is spatially combined with the 1040 nm dimple beam via a dichroic mirror. As the power of the transparency light increases, the magnitude of the light shift and, consequently, the transparency effect increase. In our current setup, we use a power of 10 mW with a blue detuning of 9 GHz, following previous works [176, 69].

At the time of this writing, preliminary light-shielding signals have been observed in the dimple region. A subtle aspect of this scheme arises from the integer $J \rightarrow J$ nature of the transparency transition, which influences its optical properties and may affect the overall

cooling performance. In such equal angular momentum states, a dark state invariably exists. This dark state is a coherent superposition of the excited $^3P_1$ state (having three Zeeman sublevels $m_J = -1,\ 0,\ +1$), which is dependent on the polarization of the transparency beam.

For example, consider a $J = 1 \rightarrow J = 1$ transition illuminated solely with $\sigma^+$-polarized light. In this case, the selection rule $\Delta m_J = +1$ implies that the $m_J = -1$ and $m_J = 0$ states are driven (bright states), while the $m_J = +1$ state is not coupled by the light and remains dark. This yields the typical configuration for a $J = 1 \rightarrow J = 1$ transition: two bright states and one dark state.

Contrary to the bright states, which couple to the cooling light and experience an AC Stark shift, the dark state $|D\rangle$ remains decoupled due to destructive interference and does not undergo any light shift. Consequently, if the cooling light is tuned to induce transparency via light shifts, the dark state will not contribute, thereby limiting the effectiveness of the spatial transparency in the dimple region. This issue can be overcome by selecting a red-light polarization that minimizes the participation of the dark state in the cooling process [84].

Ideally, the optical Bloch equations can be solved to determine the precise dark state, and the transition to it can be prevented by carefully adjusting the polarization of both the transparency and cooling beams. Following [176], employing a $^3P_1 \rightarrow {}^3S_1$ transition with a ($\pi$) polarization, the two non-zero circular momentum states ($m_J = -1, +1$) are exclusively shifted, while the $m_J = 0$ must remain dark from selection rules considerations. This implies that setting the $^1S_0 \rightarrow {}^3P_1$ polarization to $\sigma_+$ or $\sigma_-$ will prevent excitation of the dark state, effectively shielding all atoms. In practice, achieving a clean single-component polarization is challenging and is invariably affected by any small optical element, such as our uncoated cell. However, creating such polarization can dramatically improve the cooling and shielding of atoms in the dimple trap.

## 5.2 Theory of Optical Lattices

Optical lattices offer a versatile platform for simulating solid-state physics phenomena. To mimic the behavior of electrons in a solid, ultracold fermionic atoms are confined in optical lattices created by interfering laser beams. In conventional solids, lattice spacings are on the order of a few angstroms (approximately 0.3–0.5 nm), and electron tunneling occurs at energy scales of several electron volts. By contrast, optical lattices offer much larger periodicity (typically 500 nm to several micrometers) and tunable tunneling rates in the range of a few hertz to several kilohertz. This significant difference in length and energy scales not only allows for better control over the system parameters but also enables the direct imaging and local addressing of individual atoms. Such capabilities provide unique insights into many-body phenomena and quantum correlations that are often inaccessible in conventional condensed matter systems.

Our imaging approach similar to that presented in [58], where an initial lattice with a tight spacing on the order of half the wavelength ($\lambda \approx 520$ nm) is formed; subsequent mirror shifts then enlarge the lattice spacing to facilitate imaging. This dynamic configuration, also known as an accordion lattice [177], is implemented using scanning galvo mirrors. In the subsequent section, we describe the basic principle behind the realization of the optical lattices in our experiment and provide a comprehensive account of the construction of the vertical lattice, which is used to confine atoms into 2D.

### 5.2.1 Sr atomic polarizability and the magic wavelength

Before designing our optical lattice, it is essential to choose the appropriate wavelength. Choosing a wavelength is determined by several factors: the desired lattice spacing, the detuning from atomic transitions to minimize off-resonant scattering, and the availability of high-power, low-noise laser sources to reduce heating. These considerations guide our selection to ensure efficient trapping with minimal unwanted photon scattering. Typically, commercial LDs for dipole trapping operate in the ranges of 515-540 nm, 760-922 nm, 1030-1090 nm, and 1550-1560 nm. In practice, both red and blue-detuned lattices are possible, but we decided to opt for a red-detuned option for broader availability of high-power lasers. Another aspect that needs to be considered when the wavelength of the trapping dipole trap is related to polarizability. Recalling Equation 5.1, the dipole force is related to the intensity gradient and the real part of the polarizability $\alpha(\omega, \hat{\epsilon})$.

As the wavelength changes, so does the polarizability and, subsequently, the dipole force. For varying energy states, the light shifts due to the polarizability are different, and they will feel a different trapping force inside the optical dipole trap. However, there exist frequencies at which two (or more) states experience the same light shift. Such a wavelength is referred to in the literature as a magic wavelength [119].[4]. Since 2003 [179], 813.4 nm light has been recognized as a magic wavelength for the clock transition in $^{87}$Sr [151]. At this wavelength, both the ground state and the clock state experience identical light shifts, enabling the creation of a transition-insensitive trap. Although 813.4 nm is used in the best optical clocks to date, its relatively low polarizability and the reliance on high-power Ti:Sapphire lasers, which are expensive, present challenges for large-scale trapping applications. Another magic wavelength between the ground state $^1S_0$ and narrowline cooling state $^3P_1$ is at 520 nm. Previously used in the Caltech group for single tweezer trapping [94], it will be used for optical lattice. This state-independent 520 nm lattice is engineered to remove the different trapping forces between the ground state and the $^3P_1$ state.

### 5.2.2 Optical lattice with two interfering beams

In the field of cooling and trapping atoms, one can take the interference of two beams to create a spatially oscillating trapping potential. Let's consider two propagating EM fields; then their joined intensity writes:

$$I(\mathbf{r}, t) = |E_1(\mathbf{r}, t) + E_2(\mathbf{r}, t)| = |E_1|^2 + |E_2|^2 + (E_1^* E_2 + E_1 E_2^*) \tag{5.4}$$

The last term is the interference term, where the first two are the amplitudes of each wave. As we work with monochromatic laser light in the visible regime, the temporal behavior is averaged out and we are left only with the position dependency. Taking a wave-plane solution with individual polarization $\vec{\epsilon}_1, \vec{\epsilon}_2$ and wave-vector $\vec{k}_1, \vec{k}_2$ then Equation 5.4 transform to:

$$I(\mathbf{r}) = I_1 + I_2 + 2\,|E_1 E_2|\,\Re\left[\vec{\epsilon}_1 \cdot \vec{\epsilon}_2^* e^{i(\vec{k}_1 - \vec{k}_2)\cdot\mathbf{r} + i\phi}\right] = 2I_0\left(1 + \Re\left[\vec{\epsilon}_1 \cdot \vec{\epsilon}_2^* e^{i\Delta\vec{k}\cdot\mathbf{r} + i\phi}\right]\right) \tag{5.5}$$

The last equality was made under the assumption of equal intensity and wavelength for both waves. Here $\phi, \Delta\vec{k} = \vec{k}_1 - \vec{k}_2$ are the relative phase between the two fields and the wave-vector difference, respectively. Looking in Equation 5.5 we see that polarization, the angle between

[4] For magnetically sensitive states, the polarizability can also be made magic by tuning the polarization direction or magnetic field orientation [94, 178]

the fields, and the phase difference all play a role in generating the optical lattice. Setting the parallel polarization axis of both waves and a $\phi = \pi$ we get:

$$I(\mathbf{r}) = 2I_0 \left(1 - \cos\left[\Delta\vec{k} \cdot \mathbf{r}\right]\right) = 4I_0 \sin^2\left[\Delta\vec{k} \cdot \mathbf{r}/2\right] \tag{5.6}$$

If we define the angle between the propagation of the waves as $\theta$ with the same wavelength $\lambda$, arbitrarily set the frame of reference such that $(r \to y)$, which then Equation 5.6 reads:

$$I(y) = 4I_0 \sin^2\left[\frac{2\pi y}{\lambda} \sin\left(\frac{\theta}{2}\right)\right] \tag{5.7}$$

and the nodes and spacing of this lattice are:

$$y_n = \frac{n\lambda}{2\sin(\theta/2)} \Rightarrow a = y_{n+1} - y_n = \frac{\lambda}{2\sin(\theta/2)} \ , n \in \mathbb{Z} \tag{5.8}$$

This is an important result, and it can easily be generalized to 2D and 3D configurations. In our setup, a two-dimensional lattice is generated by interfering pairs of coherent beams delivered through a high-$NA = 0.55$ objective microscope. Vertical confinement is achieved by using a pair of phase-coherent beams with a tunable relative angle, which allows us to dynamically adjust the lattice spacing. As shown in Equation 5.8, varying the interference angle continuously shifts the lattice spacing between its maximum value, set by the imaging system's projection capabilities, and the diffraction-limited minimum of $\lambda/2$, thereby defining the resolution of the lattice.

### 5.2.3 Green Vertical Accordion Lattice

Our main goal of having a vertical confinement is to reduce the dimensionality from 3D to 2D. In a plane, the mobility of particles is limited, and the vertical degrees of freedom are frozen. To reach this regime, one needs to scale the interactions and the temperature parameters of the system to be smaller than $\hbar\omega_y$, where $\omega_y$ is the trapping frequency of the vertical direction. For effective confinement, the scale of this trapping frequency should be on the order of several kHz. We can see that temperature-wise, by assuming a 20 kHz trap frequency, we will give a temperature scale of 1 microkelvin, which is slightly higher than our coldest red MOT sample. By doing so, the cold atomic sample cannot tunnel outside the potential barrier, and the system will reach 2D or quasi 2D regime (depending on the ratio between the cloud temperature and the trap depth). The implication of such a setup is to study phases in 2D and explore the dynamics of lower-dimensional quantum systems. A second goal involves counteracting the effect of gravity. Vertically gravitational force is pulling the atoms toward the lower part of the cell. Therefore, optical trapping prevents them from flying to the cell floor. To confine the atom in a plane tightly enough to oppose gravity, the trap depth needs to be adjusted with $U_0 \to U_g = U_0 - mg\Delta y/2$, where $\Delta y$ is the width of the trap in the vertical direction. This means that the criteria for vertical trapping write $\frac{k_B T_{\text{atom}}}{U_g} \ll 1$, and one has to account for the effect of gravity. For low enough temperature, the harmonic approximation is valid and we get that $\Delta y = \sqrt{\frac{\hbar}{m\omega_y}}$ where $\omega_y$ is the vertical lattice site trapping frequency, and that the potential from Equation 5.7 writes:

$$U(y) = U_0 \sin^2\left(k_y y \sin(\theta/2)\right) \approx U_0 \left(k_y y \sin(\theta/2)\right)^2 \tag{5.9}$$

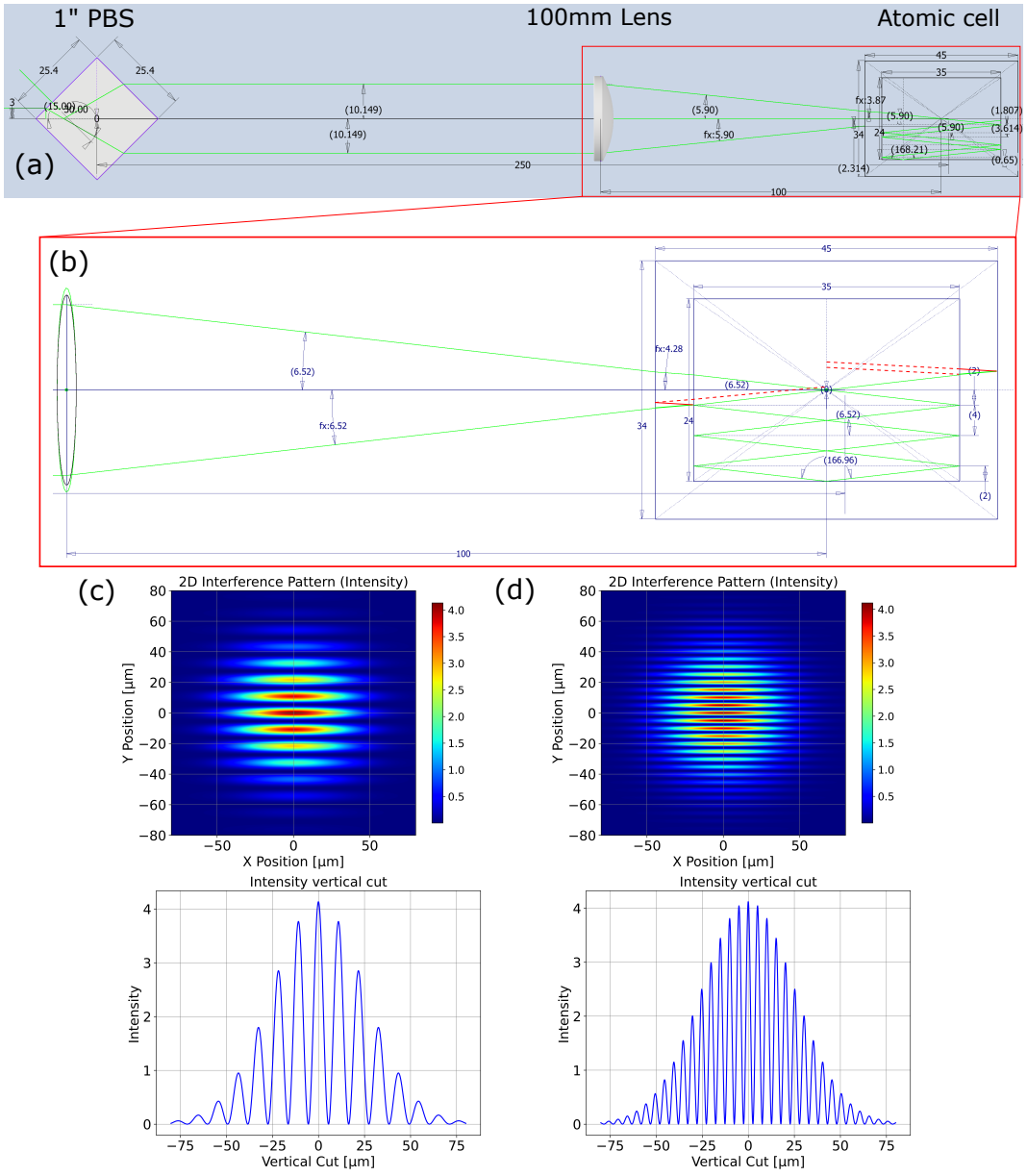


Figure 5.3: The beam path of the vertical lattice and the interference patterns simulations. The top image (a) illustrates the beam path from the PBS cube to the atom inside the cell, where the reflection from the cell walls is presented for the upper incoming beam. In (b), there is a closeup of the science cell with a special condition of the incident angle in degrees $\theta \approx 6.52° \approx \cot^{-1}\left(\frac{35}{24} \times 6\right)$, and the beam is reflecting backwards on the same path it entered the cell. Figures (c) and (d) are the interference patterns generated in the atom plane(also the focus point) for two angles ($\theta \approx [5.44°, 11.8°]$), respectively. By assuming the beams are $TEM_{00}$ mode, with a resolution of $1024 \times 1024$ points, the 2D intensity can be simulated, and a 1D cut along the vertical direction is shown below them.

By comparing it to the ground-state energy, the trap frequency writes:

$$\frac{m(\omega_y y)^2}{2} = U(y) \Rightarrow \omega_y = \sqrt{\frac{2U_0}{m}} k_y \sin\left(\frac{\theta}{2}\right) \tag{5.10}$$

For the equation above $k_y = \frac{2\pi}{a}$ and plugging it to the trapping condition of the atoms $U_0/k_BT \gg 1 \rightarrow (U_0 - g\sqrt{\hbar m/4\omega_y}) \gg k_BT$. For a trap with 1 kHz, the shift due to gravity is 44 nanoKelvins, which is negligible as the confinement is expected to be much higher.

For the side imaging system, to distinguish between atoms in a different layer the lattice spacing should be on the order of more than the effective pixel size $a \gg M\sigma_{\text{pix}}$, for the MANTA camera this is around 4.4 $\mu m$ with a magnification around $M \in [1 - 1.6]$, by taking the maximal magnification the spacing between vertical planes should be:

$$a = \frac{\lambda}{2\sin(\theta/2)} > M\sigma_{\text{pix}} = 1.6\sigma_{\text{pix}} \Rightarrow \theta < 2.42\,\text{deg} \tag{5.11}$$

At this level, when using beam power of $P = 200$ mW, the trap temperature $\hbar\omega_y/k_B \approx 6.1$ $\mu$K and trapping frequency $\sim$ 127 kHz. This confinement surpasses the thermal energy and chemical potential of the atoms in the single plane, behaving as if they are in a quasi 2D system. The concept behind an optical accordion lattice is straightforward. A pair of parallel, phase-coherent beams, arranged symmetrically with respect to the optical axis of a lens, interfere in the focal plane with an angle $\theta$, thereby creating a periodic optical lattice. By adjusting the distance of these beams from the optical axis, the lattice spacing can be dynamically tuned. With a lens parameter $f, D$ as the focal length and lens size respectively, the sine inner term in Equation 5.7 is limited by the numerical aperture $\sin\theta/2 < D/2f$, and an aspherical lens is necessary to avoid inhomogeneous trapping. Several approaches have been pursued [180, 181] to use such dynamical lattices. We follow a similar approach presented already in 2019 by the Harvard group [182], this setup generates two beams and redirects them to the atoms in the SC, as explained.

### 5.2.4 Green Lattice trapping potential simulation

Before building the accordion setup, we want to simulate the lattice beams inside the science cell, where the atoms reside. The reason is our non-coated glass whose interior, which reflects all beams, duplicating the interference pattern in an unclear manner which one should asses as the atoms might be harmfully affected by it. Using the optical ray approach first, we can visualize how the beams entering the cell are reflected from the glass walls. At shallow angles, the rays can travel back and forth many times before hitting the atoms again. The beam is split into two green beams (after PBS), which are focused on the atom inside the SC as illustrated at Figure 5.3, over 100 mm. Observing the top incoming beam after the lens angle at 5.9 degrees from the optical axis, one can see (from symmetry, the bottom beam will have the same path) how it is diffracted and then reflected in the cell as set by Snell's law. Given the system NA $\approx 0.127$, the angle between the beam and lens axis is limited to $\theta \approx 7.3°$, and using the lower bound from Equation 5.10, the beam bounces from the inside walls 5-8 times. There exists a set of incidence angles, such that the ray reflects backward on the same path it entered and hits the atoms again. This angular condition depends on the inner cell geometry, which writes:

$$\cot(\theta_n) = \frac{W}{H}n = \frac{35\text{ mm}}{24\text{ mm}}n \Rightarrow \theta_n = \cot\left(\frac{35}{24}n\right) \tag{5.12}$$

where $W, H$ are the width and height of the SC, respectively, and $n$ is the number of times the beam hits the cell walls as seen in Figure 5.3 in the closeup inset (not including the floor). It is useful to identify these angles to avoid them if possible, preventing reflection

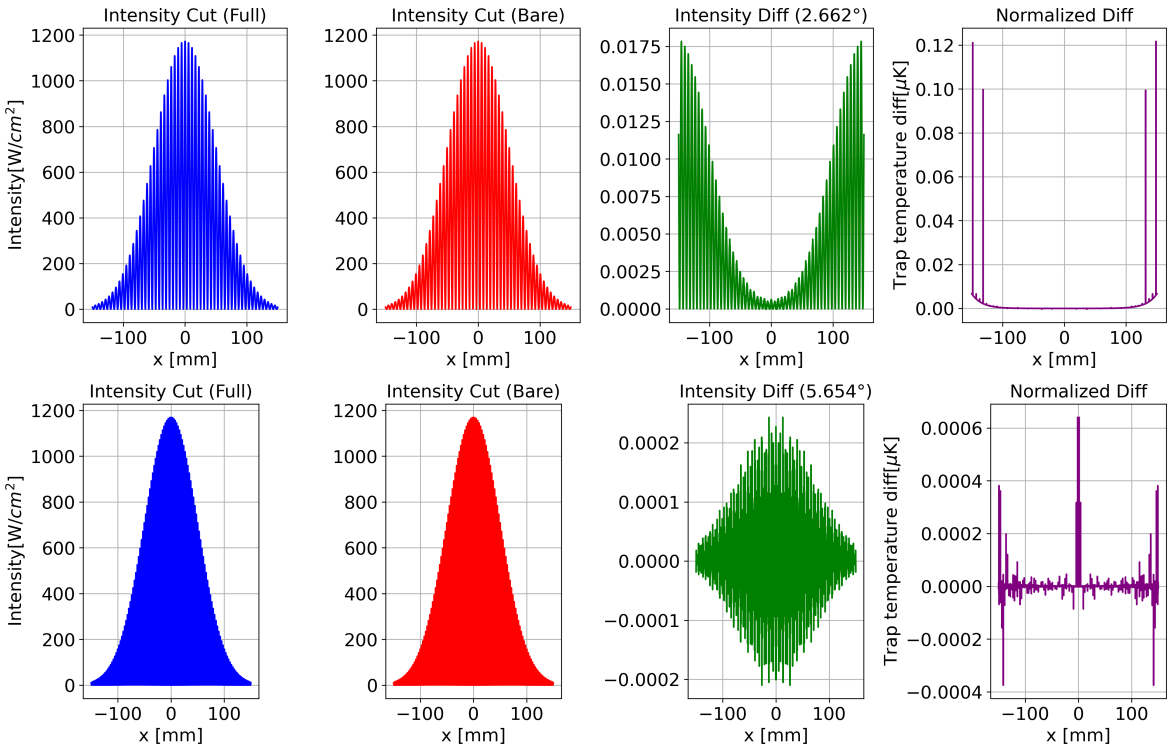


Figure 5.4: A 1D cut of two and eight beams with their difference. The eight plots above are the bare intensity and full accounting when the amplitude of the reflected beams is zero and when it follows the 4% reflection of the glass. The difference between the signals is taken as well as the normalized one, which is used in the last plot to show the fluctuations in the temperature at the bottom of the trap. These are at the nano Kelvin regime for all relevant angles, and $\theta/2$ is written above the last figure.

from hitting the atomic cloud. Nevertheless, seeing that back-propagating beams can reach the atoms again, an optical interference simulation was made by having additional beams with appropriate intensities and angles. In Figure 5.3, an interface pattern simulation for just two angled beams shows the optical lattice generated at the atom position. A vertical cut along the zero point of the X position is seen below the 2D images. In our simulation, the primary beams were modeled as Gaussian beams with a 100 µm waist and normalized intensity (amplitude = 1). Two primary beams were combined at the focal point for each selected angle in the explored range. Each secondary beam generated by a reflection from the glass cell was assumed to retain 4% of the intensity per reflection. In total, eight beams were simulated in the vicinity of the atoms. The resulting 2D intensity distributions were recorded, and vertical cross-sections were extracted for further analysis. In Figure 5.4, there are two simulations for different angles, where the intensity along the vertical cut ($x = 0$) of both eight beams and the bare two beams is shown. Using the angles $\theta/2 \approx [2.66°, 5.654°]$, which correspond to a spacing of $a \approx [5.6, 2.63]\mu m$, we can see the effect of reflections from the glass cell in the position of the focus for each angle. The observable intensity difference is calculated as seen below:

$$I_{\text{Diff}} = 2\frac{I_{8B} - I_{2B}}{I_{8B} + I_{2B}} = \frac{\Delta I}{\langle I \rangle} \tag{5.13}$$

Here, $I_{8B}$ is the intensity with all eight beams, and $I_{2B}$ is with only two. From the definition above, we can extract the normalized effect by adding more reflection on the intensity profile of the atoms seen at varying angles. In Figure 5.3, the green plots are representing $\Delta I$ ,whereas the purple two most right plots shows $I_{\text{Diff}}$ from Equation 5.13 multiply by trap depth temperature $\frac{U_{0,\text{vert}}}{k_B} \approx 9.7\ \mu$K. It is clear that in the center of the trap, the fluctuation in temperature due to residual light from the cell walls is 3-4 orders of magnitude smaller, thus, we expect that these will not affect the atom inside the lattice for all angles.

## 5.3 Accordion Lattice Setup

This final section of the chapter describes the construction and implementation of the accordion lattice. The initial assembly and characterization of the setup were performed on a breadboard physically separated from the science chamber. A galvanometer with a fixed thin mirror was used to direct the beam toward a camera, allowing for the assessment of beam quality and comprehensive characterization prior to integration around the sensitive region of the science chamber. As testing concluded, the entire setup was removed and mounted around the cell on the X-Z plane. The lattice light was then sent to the red MOT, and the first trapping attempts were made.

### 5.3.1 Galvanometer and Beam Characterization

Accordion optical lattices can be realized through a variety of techniques [180, 177], all based on the fundamental principle of combining two monochromatic beams of equal frequency and varying their angular separation over time to modulate the lattice spacing. Initially, we considered employing an acoustic-optic deflector (AOD) to split the beam due to its rapid control[5] and high angular tunability, which is directly proportional to the applied frequency. However, the resulting beam quality following AOD diffraction proved to be unsatisfactory for the formation of ODT traps, exhibiting wavefront errors comparable to the wavelength. To implement beam displacement, a galvanometer-controlled mirror was employed in conjunction with a precisely positioned lens and a polarizing beam splitter (PBS) cube. The incident beam was carefully aligned onto the galvanometer mirror, which then reflected the beam to a lens positioned at its focal point. The resulting collimated beam was directed at a 45 angle of incidence onto the entrance face of the PBS cube, with the splitting surface oriented parallel to the optical table. This configuration, as depicted in the top images of Figure 5.3, results in the beam being split into two spatially separated beams directed towards the final focusing lens. The galvanometer (MediaLas MicroAmp II), a voltage-controlled device with a maximum deflection angle of 25° at 25,000 points per second (PPS) using a ±24V operating voltage (or 8° at 50,000 PPS with ±30V), facilitates precise beam steering. A lightweight mirror (6 × 11 × 0.6 mm, W × H × T) affixed to the galvanometer shaft enables angular control of the reflected beam proportional to the input voltage. To elucidate the operational parameters of this system, a geometrical analysis was performed to establish the relationship between the galvanometer mirror's angular deflection and the resulting optical lattice spacing in the atomic plane. Employing a ray optics approach, with the galvanometer mirror at a fixed position, the incident beam is reflected towards a lens positioned one focal length ($f_1$) away. With an

[5] The response time of the AOD is related to the phonon mode shear velocity of the crystal, typically ranging from 1-5 microseconds.

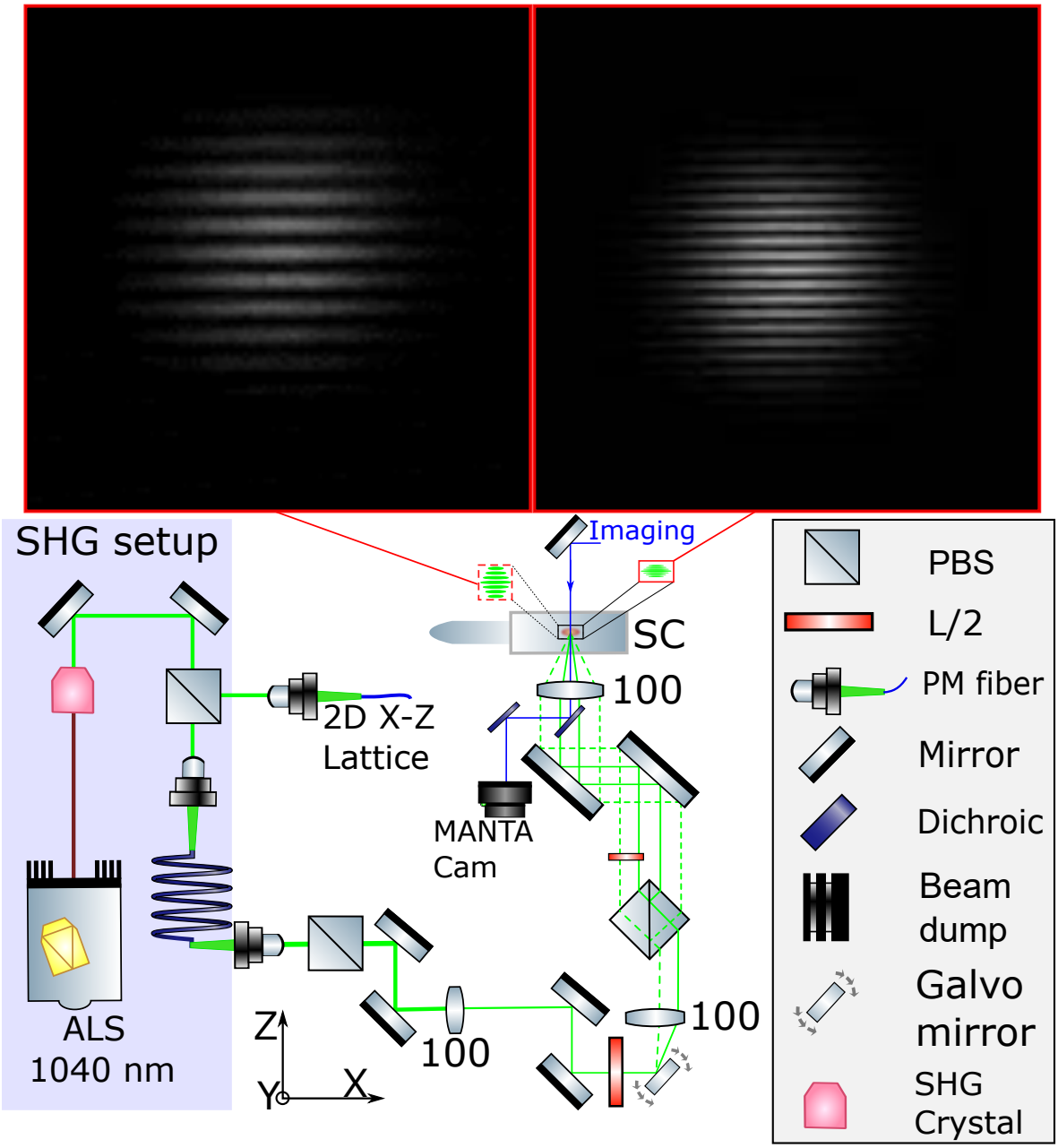


Figure 5.5: The accordion lattice setup. The full setup for generating the intensity interference pattern is shown above. The beam is frequency doubled and coupled to a high-power fiber. The images above the illustration are taken with a camera positioned at the focus point of the last lens, and shifting the galvanometer angle creates a smaller optical lattice spacing. Note that the rest of the green power is used for our 2D green lattice, which is imaged from below the atoms.

angular deflection of the galvanometer mirror, $\theta_1$, the height of the beam upon entering the PBS cube is $h = f_1 \tan\theta_1$. The PBS cube, characterized by a diagonal length $D$ and refractive index $n_2$, is positioned such that the incident beam strikes the entrance face at 45°. Applying

Snell's law, the angle of refraction within the cube, $\beta$, is given by:

$$n_1 \sin\theta_1 = n_2 \sin\theta_2 \rightarrow \sin(\pi/4) = n_2 \sin\beta \rightarrow \sin\beta = \frac{\sqrt{2}}{2n_2}, \tag{5.14}$$

where $n_1$ is the refractive index of air ($n_1 \approx 1$). The displacement of each beam from the optical axis is then:

$$2\Delta y = |D(1 - \tan\beta) - 2f_1 \tan\theta_1| \tag{5.15}$$

Where $\beta = 15$ (set by the PBS manufacturer) and $D$ is the cube diagonal length. From these equations, we see that the maximal beam separation is determined by the cube parameters and is independent of the lens or galvanometer settings. For our specific configuration, the maximum achievable beam separation, $y_M = \max|2\Delta y| \approx 26.3$ mm, with the parameters $D \approx 25.4$ mm, which is slightly bigger than a one-inch lens, but a bigger lens will not help. For zero beam difference between the split PBS beams (i.e., $\Delta y = 0$), the galvo angle needs to be $\theta_1 \approx 7.5$, therefore, the galvo angular range is sufficient for the required beam separation of the accordion lattice. The final step is the second $f_2 = 100$ mm, which overlaps both parallel beams with a crossing angle:

$$\theta = \tan^{-1}\left(\frac{y_M - 2f_1 \tan\theta_1}{2f_2}\right) \Rightarrow a = \frac{\lambda}{2\sin(\theta)} \tag{5.16}$$

The equation above[6] together with the $f_2$ lens size determined that the minimal spacing possible is $1.2\mu m$. From all the calculations above, it is clear that galvo can be used to generate the lattice and next, we had to measure the relation between voltage to angle and the beam's wavefront after the galvo mirror. Setting the operating voltage at 30 V and applying a voltage ramp to the galvanometer driver resulted in a voltage-to-displacement conversion factor of $\gamma = 55$ mrad/V $\rightarrow f_1 \tan\gamma = 55$ mm/V. This relationship between angle and voltage was done by a linear extrapolation between the voltage ramp to the beam displacement imaged via a $f_1 = 100$ mm lens onto a camera, where it was recorded. The quality of the beam after the galvo was also tested. A Shack-Hartmann wavefront sensor (*Axiom optics-HASO4*) was employed to characterize the beam's wavefront directly after the fiber. This measurement revealed a peak-to-valley (PV) aberration of $0.022\mu m \approx \lambda/24$ and a root mean square (RMS) aberration of 0.004 $\mu m$ at a beam power of 0.3W with a waist of 0.375 mm.

To assess the optical quality, we have implemented the following measurement. First, a collimated 520 nm beam was sent to a 0.5-inch *Thorlas-E02* mirror directly, and from the mirror to the wavefront sensor. We found that the mirror added minimally to PV = 0.023 $\mu m$ and RMS = $0.005\mu m$. Then, replacing the 0.5-inch mirror with the galvo mirror resulted in a PV of 0.038 $\mu m$ and an RMS of 0.008 $\mu m \approx \lambda/14$. The addition of the galvo mirror increased both aberration metrics, but all of them remain significantly below one-tenth of the wavelength, suggesting its suitability for our experimental goal.

Additionally, the astigmatism of the beam was evaluated by translating a camera along the beam axis around the focal point, recording the beam profile. The variation between the measured horizontal and vertical beam waists remained below $3\mu m$ across a range of $\pm 200$ mm from the focal point, comparable to the camera pixel size (3.4 $\mu m$). These measurements indicate no significant astigmatism introduced by the system.

[6] In our setup, both lenses have the same focal length $f_1 = f_2$ so Equation 5.16 can be simplified

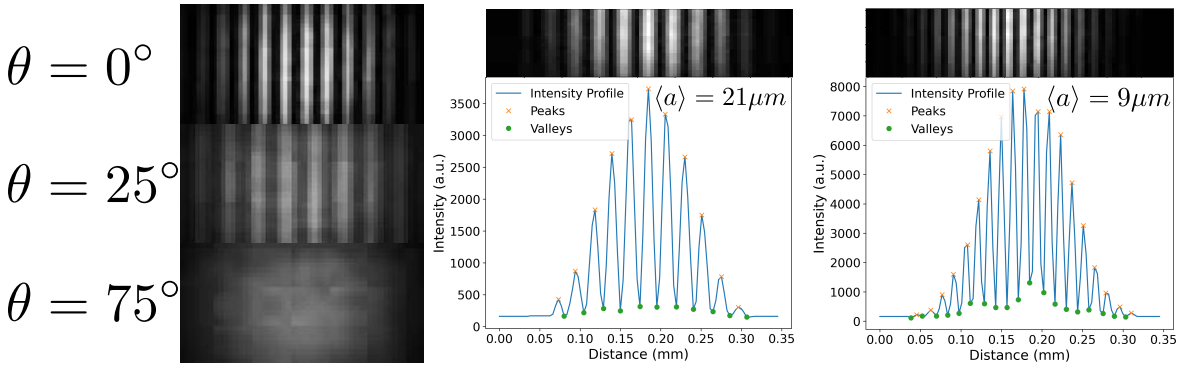


Figure 5.6: Impact of input beam polarization and resulting lattice structures. The left side panel displays images obtained with varying angles of a half-waveplate positioned after the 1-inch PBS cube. The 0° angle represents the point of optimal contrast. On the right, a cropped section of an interference pattern is shown, along with a 1D intensity profile obtained along the center of the beam for two distinct lattice spacings.

### 5.3.2 Lattice Design and Construction

The laser system to generate 520 nm light has been developed by my colleague Leon Schäfer. The 1040 nm beam at the fiber amplifier output is frequency doubled in a PPLT crystal to generate up to 10W of green power. The green beam is divided into two paths for creating a 3D accordion lattice. One path constitutes the 2D lattice generated beneath the science chamber and is directed through the objective microscope. The details of the 2D accordion lattice setup will be presented by Leon Schäfer in his respective dissertation.

The second beam is then coupled into a high-power fiber (*OZ optics*[7]) equipped with a metal jacket and a specialized in-coupling adapter before being redirected to a breadboard surrounding the science chamber to generate the lattice. As shown in Figure 5.5, the output from the fiber is shaped to achieve a 0.1 mm diameter on the galvanometer mirror. The lens after the galvo is mounted on a micrometer-controlled Z-axis stage. To precisely set the distance made by the lens after the galvo, a 10 Hz scan of the galvo angle is made to measure the edges of the beam after the lens in two spatially distant locations separated by 500 mm from one another. The lens is then shifted on the optical axis until both lengths are within the error difference of less than 10 $\mu m$, i.e. the beam after the lens is parallel to the optical axis. After the lens, a special cube mount is placed with a 1-inch PBS, and the beam is split into a top and bottom beam, where the lower one goes through a $\lambda/2$ waveplate. The waveplate is crucial as the PBS outputs beams have opposite polarization, meaning that when the beams are recombined, any perpendicular polarization does not interfere (see Figure 5.6 left panel). From Equation 5.5, the dependency of the polarization angle is shown. It goes as $\cos(\theta_{\text{pol}})$, and indeed by changing the polarization of one beam, the interference pattern vanishes.

The last focusing lens has the highest effect on the lattice potential in this setup, and therefore, an aspherical 100 mm lens (*Aspherical-520 nm*) was placed to suppress aberrations. By placing a camera at the focal point of the lens and imaging the lattice, as seen from two different angles, the corresponding spacing distance is found. A crop region of the lattice was picked, and a 1D cut was chosen to represent the peaks and valleys positions to estimate the

[7] QSMJ-A3HPMA3HPM-488-3.5/125-3AS-10

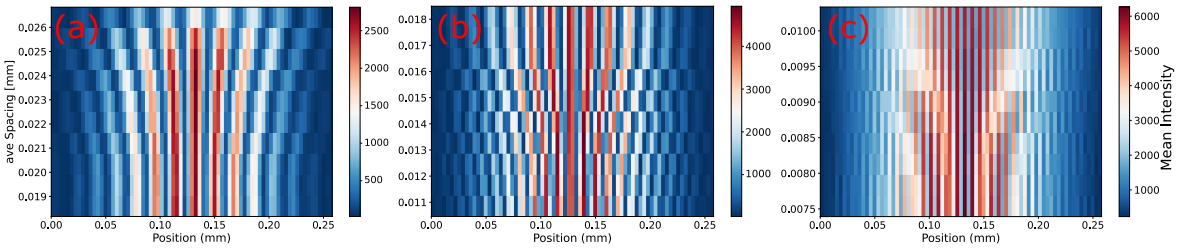


Figure 5.7: Influence of varying the lattice spacing on the interference pattern. The plots are made by taking a cropped section of the beam at a decreased spacing of the accordion lattice. By placing them from the largest spacing at $a \approx 26\mu$m on the top of (a), to the smallest resolved by the camera at $a \approx 7.5\mu$m (c). Note the different intensity color bars due to fluctuation in the intensity between measurements.

minimal spacing captured by the camera. In Figure 5.6 right panel, the lattice is imaged at 21 $\mu m$ and at 9 $\mu m$ spacing. The minimal lattice spacing imaged was 7 $\mu m$. However, below this scale, the camera resolution becomes comparable with the spacing size, and no clear pattern is visible. When scanning the lattice spacing, all maximal but the central fringe move, indicating high stability and minimal phase change when expanding the lattice. However, as the beams move, the global position of the lattice minimum and maximum can shift as if they accumulate a phase. As all but the center peak are repositioned over time, observing if the main peak has shifted can tell us about the lattice phase stability. The effect of this shift can push the atoms from their original lattice position, inducing heat and losing them in the process of creating a stronger confinement. In Figure 5.7, we monitor the shift of the lattice as the spacing is varied. In this experiment, the top beam has a waist of 0.094(3) mm, and the bottom is at 0.092(2), the angle between them was varied to have lattice spacing in the range of 26 $\mu m$ to 7.5 $\mu m$. Two 100 mm lenses were tested; one is an aspherical lens, and the other is a spherical high-power lens. At the moment, an identical spherical lens is mounted in front of the SC and is also used for the reservoir ODT; therefore, the phase test will also reveal the amount of aberration created by a spherical lens. In Figure 5.7, the three figures show the lattice spacing at three different regimes. On the right plot, the peaks are separated by a single pixel, and no apparent effect is shown as the angle between the beams increases. The first and last plots are taken with the spherical lens, and the middle is taken with the aspherical lens. Qualitatively, the aberrations are not severe, and it is hard to differentiate between the phase stability generated for each lens, with only a slightly better uniformity on the aspherical one. The more reliable observable is the atoms, and imaging them in the lattice will show quantitatively how much the phase shift is detrimental to the cloud. Afterward, all optical elements were transferred to the experimental breadboard around the cell. The beam path was then carefully realigned to ensure spatial overlap with the dichroic mirror of the 1040 nm ODT reservoir beam and the blue imaging beam. The 520 nm beam is split and focused using a final lens positioned 100 mm before the atoms inside the science chamber, as seen in Figure 5.5. The lattice alignment to the atom is done with 200 mW of power and a beam diameter of 0.1 mm. At the time of this writing, the lattice beams have been delivered to the atomic sample, and initial trapping attempts have been successfully performed. The next steps involve characterizing the trapping frequencies and assessing the phase stability of the lattice critical parameters for studying the 2D $SU(N)$ Fermi-Hubbard model.

# Chapter 6

# Outlook - The simulator near and far future

Predicting the exact course of our simulator is impractical, as inevitable events can always happen (as we learned from our Zeeman slower). However, in the following section, we will attempt to do so to the best of our abilities. This last chapter will cover the prospects for the proximate future and the long-term goals. Recent experiments include in-tweezer trapping measurements, free-falling imaging of single atoms, and an optical Stern-Gerlach scheme. Our motivation lies in the ability to spin-resolve individual atoms of $^{87}$Sr, first in a single trap and later in 2D optical lattices. By doing so, we can start shedding some light on the effect of magnetism in the $SU(N > 2)$ Fermi-Hubbard model. A short explanation of this plan will be given with a simulation of how distinct spins are imaged using our quantum gas microscope.

## 6.1 Single atom Spin-resolved imaging

During the writing of this thesis, three major parts were included in the experiment. An optical tweezer, operating at a wavelength of 813.4 nm with a radial trapping frequency of around 0.1 MHz, was implemented to trap atoms from the cold red MOT. An associated microscope objective, with a single-photon sensitivity EMCCD camera, facilitates imaging single atoms within the tweezer. These new features in our simulator have enabled single-atom detection in optical tweezers. As shown in the left panel of Figure 6.1, light-assisted collisions [94] yield a binary signal, indicating either zero or one atom per trap. This parity projection, implemented using 689 nm light and imaging as in [94], confirms the unity occupancy of the tweezer. Shown on the right plot of Figure 6.1, we plot the occurrence of counts in the trap over hundreds of images. The signature double peaks histogram is observed, indicating the zero background highest probability at low counts, and the higher counts shallow peak for a single atom. Using this method, both $^{88}$Sr and $^{87}$Sr were captured and imaged in the tweezer for 150 seconds. The detection fidelity can be found by fitting the histogram of the ROI-summed counts to a double-Gaussian model (red fitting in Figure 6.1) and selecting an optimal threshold that maximizes the probability of correct classification. This method yields a fidelity exceeding 99.99% for both isotopes.

The third major add-on is a supplementary blue light port that introduces counter-propagating photons relative to the existing imaging beam, as detailed in the Blue MOT chapter. By configuring these beams to operate in opposition, we can image single atoms in

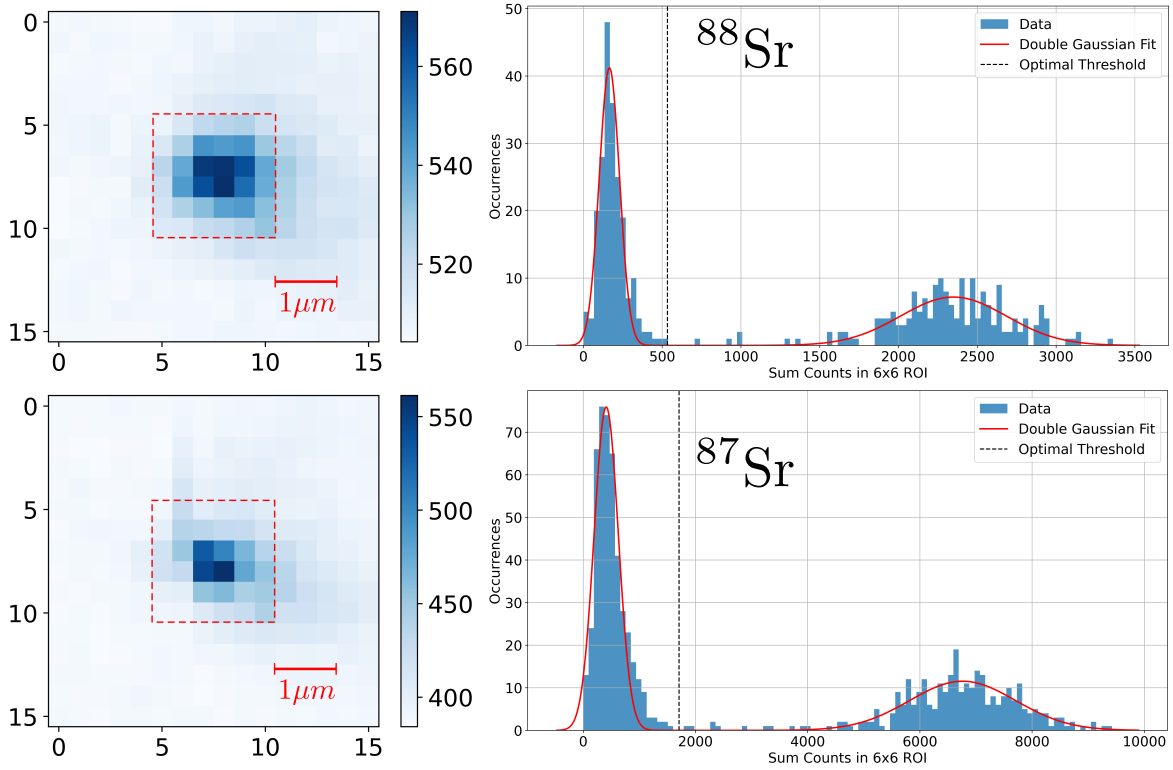


Figure 6.1: Single Atom in an optical tweezer. The left figures present images (taken by Leon Schäfer and Thies Plaßmann) of an atom held in a tweezer, with the upper and lower images corresponding to $^{88}$Sr and $^{87}$Sr, respectively. The red square indicates the region employed for binning to generate the histograms on the right side. The Y-axis shows the number of occurrences for a given number of counts in an ROI, and the X-axis is the sum of counts within the ROI. For $^{87}$Sr, the measured detection fidelity is 99.9962% with an optimal threshold (black dashed line) of 1706.81, and for $^{88}$Sr, it is 99.9956% with an optimal threshold of 549.736.

free space. This method, as demonstrated by previous groups [183, 58], extends the effective imaging time of free-falling atoms due to the broad linewidth on the blue transition and strontium's relatively large mass. The next step involves an optical Stern-Gerlach (OSG) force on the $^1S_0 \rightarrow ^1P_3$ transition, using the Fermion isotope of strontium. The OSG potential is desirable for single spin detection, and we briefly discuss this scheme and its usefulness.

### 6.1.1 Optical Stern-Gerlach for single atom

Similarly to the first experiment made by Otto Stern and Walther Gerlach [184], we want to spatially separate the nuclear spins depending on their $m_F$-states. However, due to the weak coupling of the $^{87}$Sr nuclear spin to a magnetic field, we will use a light field to push the $m_F$-states as they are released from the optical tweezer. The idea is as follows: we load $^{87}$Sr atoms into the tweezer trapped directly from the SF red MOT. The 3D red MOT beams are turned off, and a dedicated 689 nm parity projection beam is applied for 0.5 s to leave either a single atom or none in the tweezer. Further Sisyphus cooling on the 689 nm [185] cools the remaining atom near the motional ground state in the trap. Another $\sigma^+$ polarized

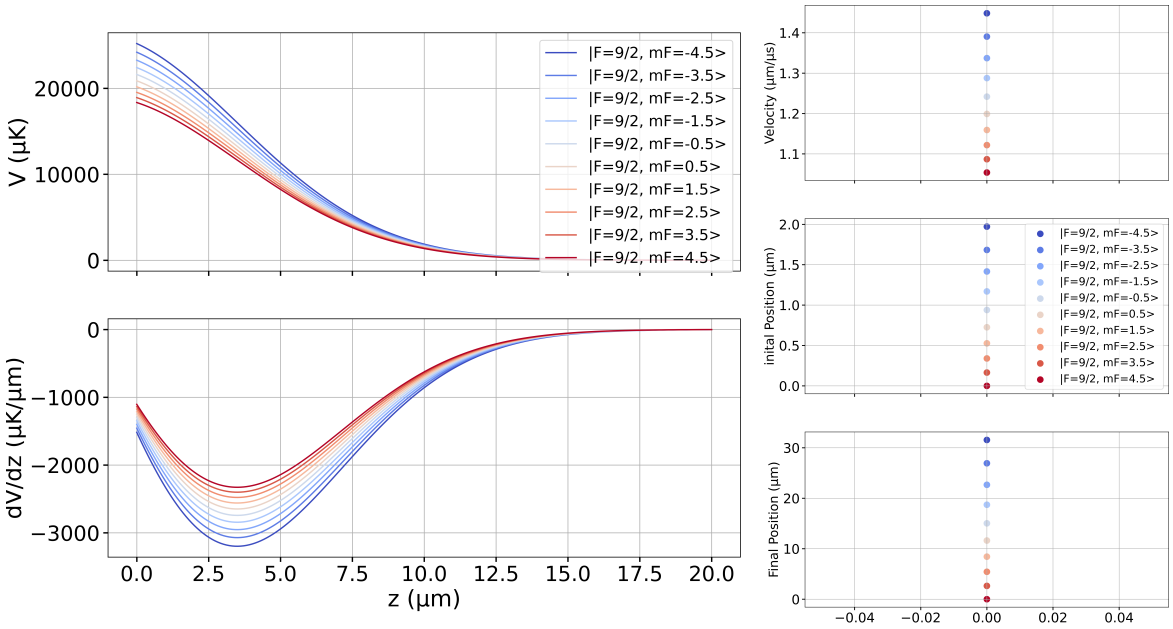


Figure 6.2: OSG light potential $^{87}$Sr. On the left, the top plot illustrates the potential the OSG beam creates, and the corresponding force is shown below. The intensity gradient of the blue-detuned 20 $\mu$m beam creates a repelling force at a position displaced by approximately 1.5 $\mu$m from the nominal trap center. With a pulse of $t_{\text{pulse}} = 10$ $\mu$s and an expansion time of $t_{\text{ToF}} = 100\mu$s, we can observe the corresponding velocities and position as seen on the right. This example provides an estimation, which still needs to be verified experimentally.

689 nm light is then sent through the microscope and focused to a waist of around $w_0 \approx 10\mu$m with around 2-10 mW of power. Utilizing this beam, we are able to exert variable forces on the atoms of $^{87}$Sr isotopes contingent on their nuclear magnetic moments. The light shift of each state consequently induces variations in the potential experienced by the atoms. We have estimated the effect on a freely falling atom subjected to an OSG light pulse. The pulse duration is 10$\mu$s, alongside a Time of Flight (ToF) of 100$\mu$s with an additional offset magnetic field of 3 Gauss. The results are depicted in Figure 6.2: the left section illustrates the applied force and potential, while the right section displays the velocities and displacements of atoms prior to and following expansion. Under the specified conditions, there is a discernible difference exceeding 30 $\mu$m between the lowest and highest magnetic states, with a minimum separation of approximately 2.5 $\mu$m, resolvable by our optical apparatus.

This technique is currently under investigation, showing promising preliminary results for atoms released from the optical tweezer. The subsequent phase involves transferring the atoms into a 520 nm accordion lattice, followed by the simultaneous application of the OSG sequence across all lattice sites. This spin-resolved imaging scheme, implemented within the lattice, will open new avenues to study the intriguing phase diagram of the $SU(N)$ Fermi-Hubbard model.

### 6.1.2 $SU(N > 2)$ magnetic ordering with quantum gas microscopy

After achieving spin detection through the OSG scheme with our quantum gas microscope, we can study the phase diagram of large spin systems. Assuming the simplest model of the $SU(N)$

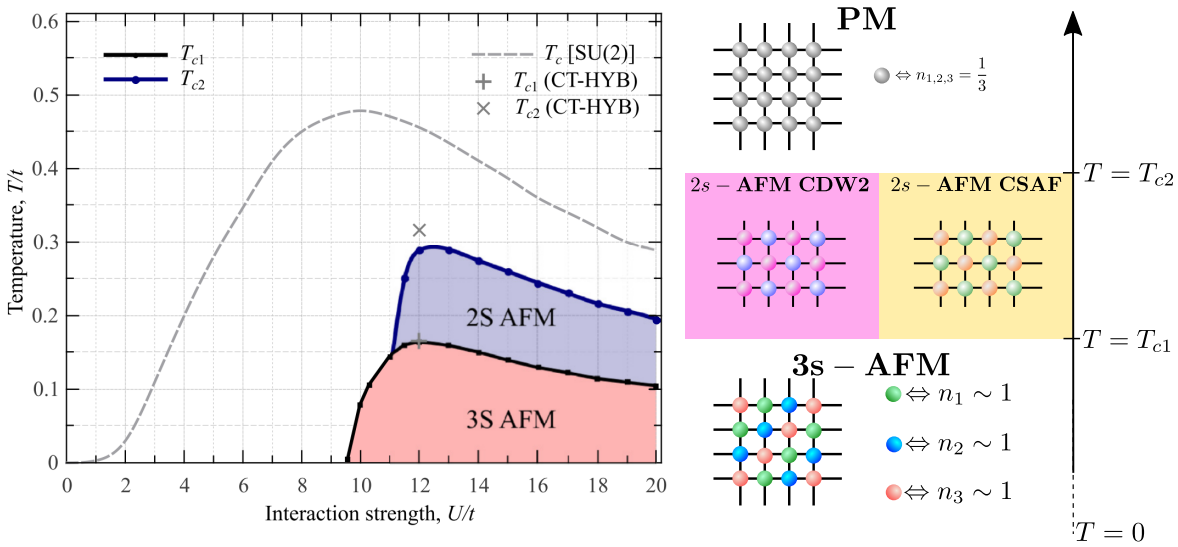


Figure 6.3: The phase diagram and schematic illustration of the magnetic ordering in the $SU(3)$-symmetric model. We see on the left plot (adopted from [186]) the theoretical phase diagram. The temperatures were numerically evaluated by continuous-time Monte Carlo hybridization (CT-HYB) [187, 188], and dynamical mean-field theory (DMFT) [189]. The right side illustrates the magnetic ordering that changes as we reduce the energy in the system.

Fermi-Hubbard model, we can set $N = 3$ and assign each spin a color flavor. Considering a 3D cubic (or a 2D square) lattice system at equal filling, meaning one particle per site (1/3 filling for each band), a finite temperature phase diagram appears. This prediction is based on a theoretical study aimed at better understanding many-body physics and showing new features beyond $SU(2)$ to be expected in a three-component ultracold fermi gas [190, 189]. The idea revolves around increasing the interaction parameter $U/t$ and observing a phase transition at critical temperatures. Using dynamical mean-field theory (DMFT) techniques [191], three important regions on the (T-U) phase diagram have been identified, as presented on the left of Figure 6.3. At high temperature $T/t \gg 1$ and a large range of interactions $U/t$, the spins are maximally disordered without any magnetic orientation, in a state referred to as the paramagnetic (PM). In the strong interaction $U/t \gg 1$ regime, decreasing the temperature leads to a spontaneous spontaneously broken phase with two-sublattice ordering. To understand why this happens, we need to map the Fermi-Hubbard system into an effective $SU(3)$-symmetric Heisenberg model [192, 193]. Under the condition of uniform lattice site confinement ($V_i = 0$), and filling one particle per site (meaning $n = 1$), the Hubbard Hamiltonian transforms into:

$$\hat{H}_{\text{eff}} = J \sum_{a=1}^{8} \sum_{\langle i,j \rangle} \hat{\sigma}_{ai} \hat{\sigma}_{aj} \tag{6.1}$$

Here, $J$ is coupling exchange parameters $J = 4t^2/U$ and $2\hat{\sigma}_{ai} = \hat{c}^{\dagger}_{\gamma i} \lambda_{a\gamma\beta} \hat{c}_{\alpha i}$ is a local pseudospin operator expressed using the Gell-Mann matrices [194]. The important part is that taking the expectation value $\langle \hat{\sigma}_{ai} \rangle$, for both single-site and two-local magnetization, reveal a spontaneous imbalance among the three color components. As the temperature is lowered in the strong-coupling regime, the superexchange interaction $J = 4t^2/U$ favors staggered alignments of the pseudospins, effectively reducing the full $SU(3)$ symmetry down to an effective

$SU(2)$ symmetry. This reduction is reflected in the formation of two distinct antiferromagnetic (2s-AFM) states—namely, the color-density wave (CDW2) and the color-selective antiferromagnetic (CSAF) phases—where one of the components becomes relatively suppressed, and the two remaining components develop complementary magnetization with a small residual net moment. As the temperature is further decreased, the system can undergo an additional transition into a three-sublattice (3S-AFM) phase, in which the lattice organizes into three interpenetrating sublattices characterized by distinct local pseudospin orientations. We can see these magnetic ordering phases on the right of Figure 6.3, showcasing how the transition happens as we move from $T_{c1}$ 2s-AFM phase to even lower setting $T_{c2}$ where the 3s-AFM phase exists. These assumptions can only occur between different quantum hyperfine states that interact equally with each other, making alkaline-earth atoms a perfect candidate. The spin correlation function can be directly measured with our microscope to reveal the relative occupations of each spin component, which can be expressed as:

$$m_j^{(3)} = \langle \hat{\sigma}_{3j} \rangle = \frac{1}{2}(n_{1,j} - n_{2,j}) \tag{6.2}$$

$$m_j^{(8)} = \langle \hat{\sigma}_{8j} \rangle = \frac{1}{\sqrt{3}}(n_{1,j} + n_{2,j} - 2n_{3,j}) \tag{6.3}$$

Here, $n_{s,i}$ is the occupation operator of spin $s$ at site $i$. These local magnetization parameters can be experimentally extracted and, when applied to the model previously described, provide insights into the state of the system. This demonstrates the capability of our simulator to investigate previously unexplored phases of matter.

# Appendix A

# Atomic jet momentum distribution

In contrast to free space, gases do not always expand isotropically, and they can be directed efficiently to a desired location through careful collection. A well-known method for achieving this employs an effusion oven, which consists of a nozzle tube attached to a large heating chamber where the material can be outgassed. The vapor is subsequently directed out of the nozzle, forming an effusive particle flow. We define the flux of particles escaping from this system as $\Phi_{\text{effusion}}$, which is controlled by parameters such as the temperature, pressure, and nozzle geometry. The flux can be determined by analyzing the rate at which atoms collide with and pass through the nozzle walls.

The effusion oven is widely used in cold atom experiments, as it enables atoms to move predominantly in a single direction. Assuming that the atoms follow a Maxwell-Boltzmann distribution and that the motion is limited primarily to the direction along the nozzle, we can consider an atom with a momentum component $p_z = p\cos\theta$ passing through an infinitesimal area $d\sigma$ over a short time interval $dt$. This setup allows us to define the particle distribution as

$$n(\mathbf{p}) = \int \frac{n(\mathbf{x},\mathbf{p})\, d^3\mathbf{x}}{(2\pi)^3} = \int \frac{n(x_i,p_i)\, dx\, dy\, dz}{(2\pi)^3} = \int p\cos\theta\, d\sigma\, dt \left(\frac{1}{2\pi m k_B T}\right)^{\frac{3}{2}} e^{-\frac{\mathbf{p}^2}{2mk_BT}} \tag{A.1}$$

where the last equality is obtained by transforming to the reference frame of the atom within the nozzle. From this, we observe that the flux of particles passing through a small cross-sectional area $d\sigma$ is proportional to

$$\frac{dn}{dt} \propto p\cos\theta \left(\frac{1}{2\pi m k_B T}\right)^{\frac{3}{2}} e^{-\frac{p^2}{2mk_BT}}. \tag{A.2}$$

Although the atomic trajectories are predominantly directed along the nozzle axis, atoms within the effusion oven can theoretically take any possible direction, as the density of states remains three-dimensional. To express this distribution in terms of spherical coordinates, we write

$$\frac{n(\mathbf{p})\, d^3\mathbf{p}}{d\sigma dt} = p_z \left(\frac{1}{2\pi m k_B T}\right)^{\frac{3}{2}} e^{-\frac{\mathbf{p}^2}{2mk_BT}}\, dp_x\, dp_y\, dp_z = \tag{A.3}$$

$$p\cos\theta \left(\frac{1}{2\pi m k_B T}\right)^{\frac{3}{2}} e^{-\frac{\mathbf{p}^2}{2mk_BT}} p^2\, dp\, \sin\theta\, d\theta\, d\phi = \underbrace{\left(\frac{p^2}{2\pi m k_B T}\right)^{\frac{3}{2}} \frac{e^{-\frac{p^2}{2mk_BT}}}{2}}_{n_{\text{jet}}(p)} \sin 2\theta\, dp\, d\theta\, d\phi$$

This expression, when combined with the flux weighting factor, yields the atomic jet momentum distribution, which is dependent only on the magnitude $p = |\mathbf{p}|$ raised to the third power, as expected from the flux-weighted distribution.

The mean momentum $\langle p \rangle$ can then be extracted by integrating over $p\, n_{\text{jet}}(p)$ in momentum space over the entire range of angles ($\theta \in [0, \pi], \phi \in [0, 2\pi]$) and momentum ($p \in [0, \infty]$). The flux $\Phi_{\text{effusion}}$ is defined as

$$\Phi_{\text{effusion}} = \frac{mN\sigma}{4V}\langle p \rangle = \frac{P\sigma}{4mk_BT}\langle p \rangle, \tag{A.4}$$

where $N$ is the number of particles in a closed volume $V$, and we have used the ideal gas law to derive the second expression where is the pressure of the gas.

Finally, to find the average momentum $\langle p \rangle$, we evaluate the following integral:

$$\langle p \rangle = \int_0^\infty p \cdot n_{\text{jet}}(p)\, dp. \tag{A.5}$$

Substituting $n_{\text{jet}}(p) = \left(\frac{1}{2\pi m k_B T}\right)^{3/2} p^3 e^{-\frac{p^2}{2mk_BT}}$, we obtain

$$\langle p \rangle = \int_0^\infty p \cdot \left(\frac{m}{2\pi k_B T}\right)^{3/2} p^3 e^{-\frac{p^2}{2mk_BT}}\, dp \tag{A.6}$$

$$= \left(\frac{m}{2\pi k_B T}\right)^{3/2} \int_0^\infty p^4 e^{-\frac{p^2}{2mk_BT}}\, dp. \tag{A.7}$$

Using the substitution $u = \frac{p^2}{2mk_BT}$, we get $p = \sqrt{2mk_BT\, u}$ and $dp = \frac{k_BT}{m}\, du$, giving

$$\langle p \rangle = \left(\frac{m}{2\pi k_B T}\right)^{3/2} \int_0^\infty (2mk_BT\, u)^{5/2} e^{-u} \frac{k_BT}{m}\, du \tag{A.8}$$

$$= \left(\frac{m}{2\pi k_B T}\right)^{3/2} (2mk_BT)^{5/2} \frac{k_BT}{m} \int_0^\infty u^{5/2} e^{-u}\, du. \tag{A.9}$$

Evaluating the integral using the Gamma function $\int_0^\infty u^{5/2} e^{-u}\, du = \Gamma(7/2) = \frac{15\sqrt{\pi}}{8}$, we obtain

$$\langle p \rangle = \sqrt{\frac{8mk_BT}{\pi}}. \tag{A.10}$$

This result provides the average momentum $\langle p \rangle$ in terms of the temperature $T$, which can be substituted back into the flux equation to give

$$\Phi_{\text{effusion}} = \frac{P\sigma}{4mk_BT}\langle p \rangle = \frac{P\sigma}{\sqrt{2\pi mk_BT}} \tag{A.11}$$

The flux of an effusion oven is following Equation A.11 and plugging some numbers from our Sr oven system we get

$$\Phi_{\text{effusion}} \approx 4.1 \times 10^{13} \left[\frac{\text{NoA}}{\text{sec}}\right]$$

. Which is on the order of the flux given by the datasheet for our oven [129]. It is important to mention that it seems that the rate is decreasing with high temperature, but this is not the case, as the temperature increase also increases the vapor gas and therefore the pressure in a nonlinear way, making the flux higher for elevated temperatures.

# Appendix B

# EOM and Digital PID setups

## B.1 Home-built EOM for Light-Induced Sidebands

The electro-optic modulator (EOM) used in our blue locking experiment is a custom-designed [195], featuring an anti-reflection (AR) coated lithium niobate ($LiNbO_3$) crystal (dimensions: 3×3×25 mm, CASIX Inc.) with no attached metallic electrodes at a lower cost. We placed the crystal between two specially designed copper electrodes and housed it in aluminum, as depicted in the top images of Figure B.1. We looped a conductive alloy wire around 25-27 times and soldered one side to the top cooper plate and the other to an output SMA port creating a solenoid inductor and isolated it from the rest of the casing using *Tesa* insulating tape, as seen in the right top panel of Figure B.1.

If we model our EOM as an RLC circuit we can make some assumptions allowing us to understand better what are the significant parameters in this system. The resonance frequency for this type of circuit depends on its resistance $R$, inductance $L$, and capacitance $C$, as described by:

$$2\pi f_{res} = \omega_{res} = \sqrt{\frac{1}{LC} - \frac{R^2}{L^2}} = \frac{1}{\sqrt{LC}}\sqrt{1 - \frac{CR^2}{L}} \approx \frac{1}{\sqrt{LC}}, \tag{B.1}$$

Here, $f_{res}, \omega_{res}$ are the resonance frequency in units of hertz and angular frequency, which is more commonly used because it is mathematically convenient, and where the last approximation holds for circuits with negligible resistance. To relate the modulation frequency and bandwidth to the circuit's electronic properties, we model the crystal's capacitance, $C_{crystal}$, as a rectangular cuboid with known dimensions and dielectric properties of lithium niobate, and assume a solenoidal coil configuration for the inductance, $L_{sol}$. These are estimated as:

$$C_{cry} = \epsilon\frac{A}{d}, \tag{B.2}$$

$$L_{sol} = \frac{\mu N^2 \pi r^2}{l}, \tag{B.3}$$

where $\epsilon$ is the permittivity of the material, $A$ the electrode surface area, and $d$ the distance between electrodes. For the solenoid, $\mu$ represents permeability, $N$ the number of turns, $r$ the inner radius, and $l$ the coil length. Inserting measured parameters, we calculate a resonance frequency of $\frac{1}{\sqrt{L_{sol}C_{crystal}}} \approx 2\pi \times 68.2$ MHz. Before we connected the EOM to

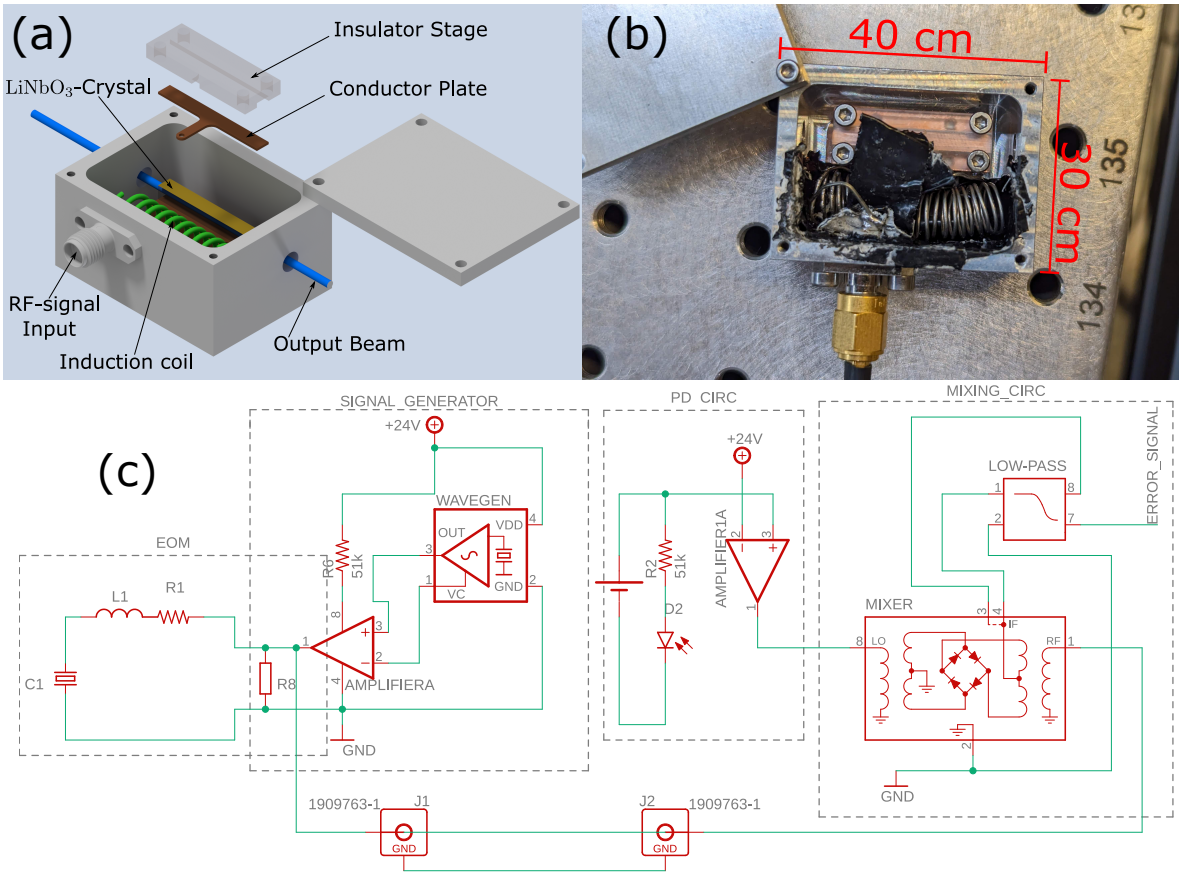


Figure B.1: The Home-built EOM. (a) Our design of the crystal housing is composed of an internal copper housing, which is electrically connected to a self-looped coil and SMA output. The electrodes sandwich the crystal, where a 5 mm diameter opening for the blue beam can pass through. (b) The fully built EOM is pictured on the right with the casing dimension. (c) The full electronic circuit we use to lock our laser has four sections. The EOM part is connected to an RF signal generation section with an amplifier. A fast photodiode circuit records the light beam signal passing through the EOM, which is then combined with the RF signal in the fourth section. By using a mixer, we can down-convert the photodiode sub-Doppler signal to an error signal, together with a low-pass filter to remove higher-order harmonics.

the full electronic circuit we used a spectrum analyzer measurement to obtain the resonance frequency using vector signal analyzer option (maybe in appendix) getting approximately 66.3 MHz with a bandwidth of 1.35 MHz, this deviation by 2.8% from our calculation,is likely due to residual coil resistance approximated here as zero and the accurate determination of the coil's induction. As shown in (c) of Figure B.1, the full locking circuit has many more elements integrated into it besides the EOM; therefore, more accurate measurements are needed to account for the non-negligible resistance.

To further characterize the EOM circuit, we introduce the quality factor ($Q$-factor), a dimensionless parameter that describes a resonator's efficiency and, specifically in an RLC circuit like ours, shows how underdamped the signal becomes. The $Q$-factor in a circuit is

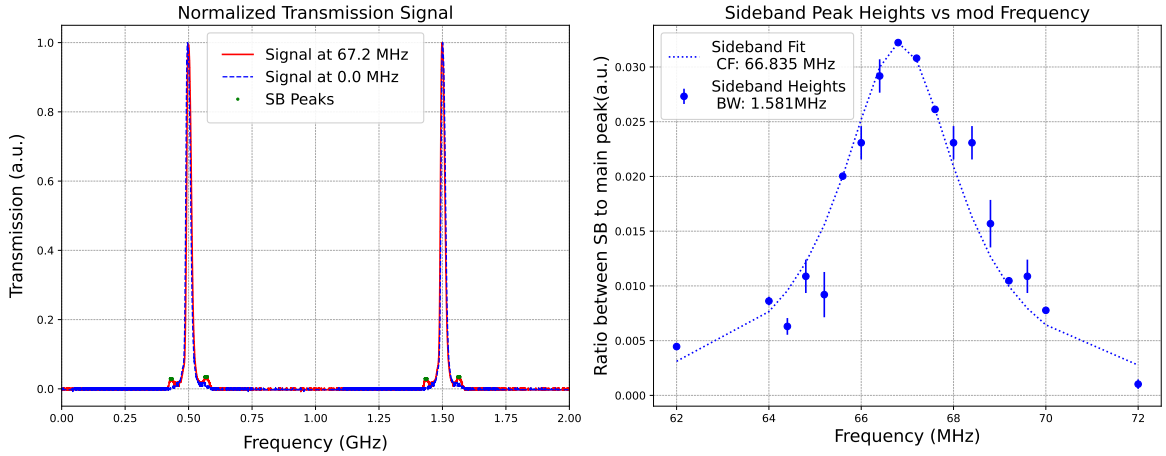


Figure B.2: SB measurement and $Q$-factor analysis. The left panel shows the normalized transmission signal where we align the zero modulation signal on top of the 67.2 MHz for compression. The SB heights (marked in green) are extracted and divided by the main peak height. (right panel)The ratio of SB peak height to the main peak is plotted against modulation frequency, with a Loranzin fit to find the central frequency (CF) and BW. From these measurements the a $Q$-factor can be calculated

defined as:

$$Q = \frac{\omega_{res}}{\Delta\omega} = \sqrt{\frac{L}{CR_T^2}} \tag{B.4}$$

Where $\Delta\omega, R_T$ represents the bandwidth and the resistance of the total system. The second equality holds for our circuit, indicating that a decrease in resistance improves the signal. Although the exact total resistance is complicated to calculate and is unknown to us, we can estimate the $Q$-factor and $R_T$ by measuring the SB amplitudes as a function of the input signal to the EOM and using a Lorentzian profile to extract the system respond to a modulation scan input[196].

Using a Fabry-Pérot interferometer with an FSR of approximately 1 GHz (Toptica FPI100), we sent a 460.8 nm pump beam through the crystal and observed the resulting signal as a function of the cavity spectrum, modulated by a piezoelectric element. We see in Figure B.2 (left panel) the transmission spectrum both with applying a 67.2 MHz sine wave at 19 dBm and without the modulation signal. Repeating this measurement takes around a minute, and due to the slow drift of the cavity, the spectrum in frequency and we realign it software-wise afterward to the zero modulation position. This shifting together with the significantly attenuated SB relative to the primary cavity mode, $\text{TEM}_{q00}$ seen in the data,(likely due to weak electric field coupling of in the absence of gold electrodes on the crystal) are big sources of errors which we need to take into account fitting the Lorentzian. Scanning one FSR allows us to calibrate the frequency axis and determine error bars. By fitting the SB peak ratio to the main peak over a 10 MHz scan range around resonance (as shown in Figure B.2, right panel), the data take the average of both SB in both peaks heights of (average over 4 points) and we estimate a $Q$-factor of approximately 40, sufficient for our requirements. From the $Q$-factor and the resonance frequency, and the capacity of the crystal, we derive the total

circuit resistance using Equation B.4 and Equation B.1 as:

$$Q = \frac{1}{R_T}\sqrt{\frac{L_{sol}}{C_{cry}}} = \frac{1}{R_T \omega_{res} C_{cry}} \Rightarrow R_T = \frac{1}{Q \omega_{res} C_{cry}} \approx 19.5 \text{ Ohm} \tag{B.5}$$

Initially, we connected the EOM directly to the wave generator, and we could observe a sub-Doppler signal by adding a 50-Ohm BNC cable, decreasing the resistance, and increasing the signal amplitude. We can estimate the effect of adding the cable to the circuit by assuming it is a parallel resistor, and the total resistance becomes:

$$\frac{1}{R_T} = \frac{1}{R_{BNC}} + \frac{1}{R_{T'}} \Rightarrow R_{T'} = \frac{R_{BNC} R_T}{R_{BNC} - R_T} \approx 32 \text{ Ohm}. \tag{B.6}$$

Here, $R_{BNC}, R_{T'}$ are the resistances of the BNC cable and the circuit before connecting it, we can see a reduction in resistance in the circuit by approximately 40%, thus enhancing its performance.

## B.2 Digital PID WM Lock for Repump Lasers

The frequencies of the repumping lasers significantly influence both the number of atoms and the lifetime of our MOT. We found that our initial configuration was suboptimal due to limitations in the ZS and the observed daily-timescale drift of the repumping laser frequencies, which was susceptible to environmental fluctuations. These frequency drifts, which could amount to 1 GHz or more, with a rate of approximately 0.15 GHz per hour in a random direction (towards blue or red detuning), resulted in significant variability in experimental outcomes.

To mitigate these issues, we implemented a digital locking system based on the WM readout. This system enables precise control of the laser frequencies and maintains them at the desired set points. This digital feedback system is crucial because neither the 707 nm nor the 679 nm repumping lasers are intrinsically locked to an atomic transition, leading to frequency variations during measurements. As these frequency drifts are slow, a slow PID controller was adequate for effective stabilization. As described in the previous section on the repumpers system, a small amount of light is directed to the WM for frequency readout. By cycling through the shutters, we can selectively send each laser beam to the WM and monitor its frequency, enabling precise readings of the frequency of all our lasers.

Using this information, a control script was developed to generate an error signal by subtracting the current WM-measured frequency from the desired setpoint. The error signal is then converted into a voltage and applied to an analog output channel of the Red Pitaya, which in turn sends a signal to the laser controller. This signal adjusts the laser's cavity piezo, effectively bringing the laser frequency closer to the setpoint and minimizing the error. The script utilizes a digital PID algorithm, calculating the error signal's derivative and integral at each iteration, thus requiring the error history over the loop time to perform the PID calculations. Since we employ two repumping lasers, two sets of PID parameters and two error history buffers are used in an alternating manner. To simplify user interaction, a custom GUI was developed allowing for adjusting PID parameters and setpoints, while providing manual control of the four shutters in the WM optical path, which allows for easy checkup when laser locking is not needed.

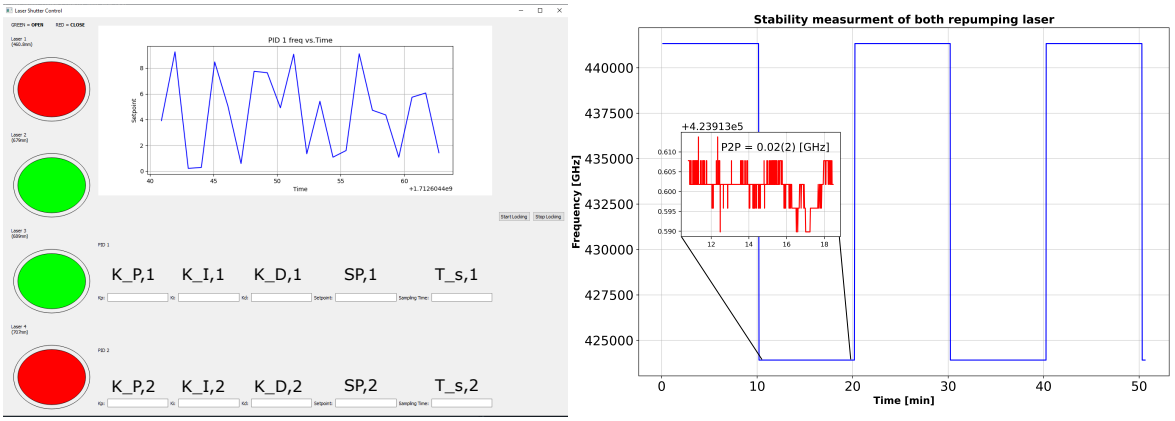


Figure B.3: Graphic User Interface (GUI) for the digital laser locking system and a representative wavemeter (WM) measurement. The left panel shows the custom GUI, displaying real-time error signals and setpoints for both repumping lasers. The GUI allows for setting the PID gains, setpoints, and sampling time. The right panel shows a stability measurement of both repumping lasers over an hour, where the frequencies of the different lasers are recorded while we cycle between them, with an inset showing a zoom on the locked region with a 20 MHz peak-to-peak. We can see the frequencies of each laser when the shutter in their path was activated.

As can be seen in the left panel of Figure B.3, the developed custom GUI allows manual control over each shutter in the WM path for daily checkups and provides an interface to set the PID parameters to control the locking loop. By configuring the PID parameters, setpoints, and the sampling time (which sets the time between iterations of the loop), a delay time of at least 0.1 seconds between each iteration was set to allow the script to execute correctly. After all the relevant fields have been filled, the user can activate the lock, initiating the locking sequence. During this sequence, we monitor and record the real-time error signal data on the GUI while comparing these data points to those from the WM to optimize the performance of the lock. In observing these parameters, we noticed that instability and ringing occur for values that are too high or too low in the $K_p$ and $K_I$ gain values. Furthermore, the switching time ($T_s$) between lasers, which was set to be $T_s \approx 10 - 20$ min to maintain lock stability, was optimized by considering that the lasers can drift over 50 MHz over a time scale of tens of minutes.

To assess the stability of the system, we recorded the frequency of each laser over an hour, switching between them every 11 minutes. As shown in the right panel of Figure B.3, the WM data demonstrates that this implementation of our digital lock allows for a stable, long-term lock of the repumping laser frequencies. The plot illustrates the time evolution of the measured frequencies while cycling through the different laser sources, with a zoomed inset to show the stability of the 707.2 nm laser is up to a peak-to-peak of 20 MHz, while our WM has a resolution of approximately 10 MHz. Overall, we observe that the maximum frequency change over a few hours is about 30 MHz, which is sufficient for our repumping scheme with both repump lasers, specifically when considering the more sensitive red MOT operations, which will be presented in the next chapter.

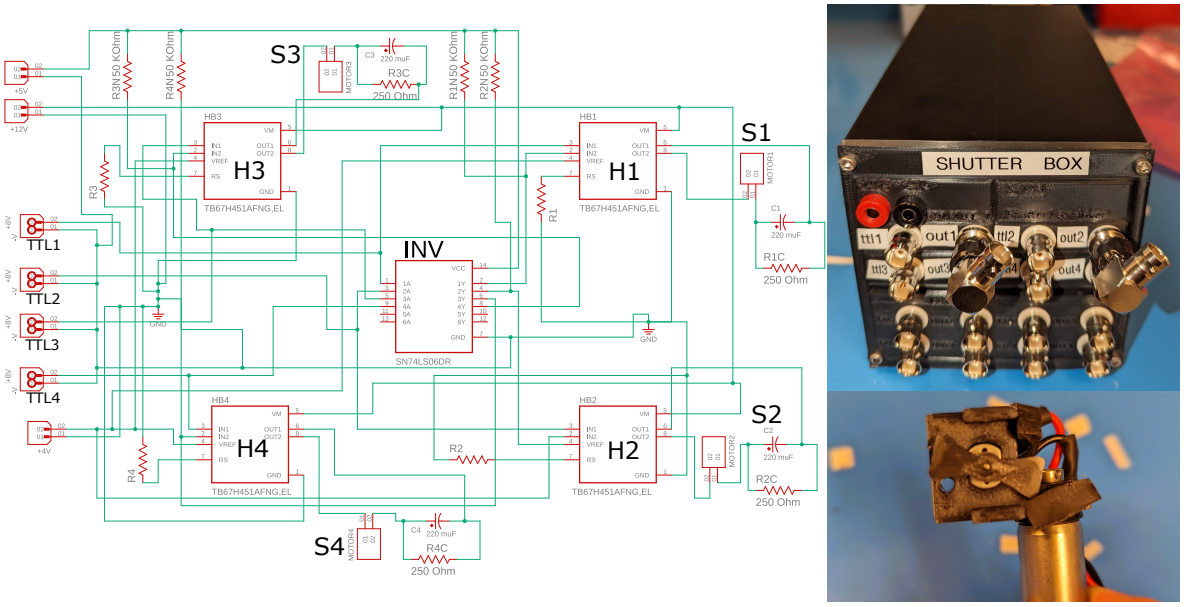


Figure B.4: Schematic of the home-built shutter system. The left panel shows the electronic circuit design, highlighting the four independent control channels each with an H-bridge configuration driven by a TTL input signal. The right panel displays a photograph of the assembled shutter box along with a close-up view of a single mechanical shutter mechanism. The mechanical shutters consist of a 3D-printed housing and blade, and include rubber flaps that limit the blade's range of motion, thus minimizing vibrations and noise.

### B.2.1 Home-Built Shutter System for the Repump and Other Systems

Leakage light, even at the microwatt level, can inadvertently transmit through AOMs and other optical switching elements. This residual light can significantly interfere with measurements, especially during the final stages of the cold red MOT, where precise control over atomic temperatures is crucial. To mitigate this, we implemented a physical shutter system, providing an additional layer of optical isolation and ensuring that no stray light reaches the atoms during sensitive cooling and trapping periods.

Inspired by the design presented in [197], we developed a custom-built shutter system optimized for our experimental parameters. The core mechanism comprises a DC electric motor that drives a rotating blade to selectively block or unblock the beam path. The blade and housing were designed using computer-aided design (CAD) software and fabricated through 3D printing. To enhance durability and reduce unwanted oscillations and noise, we incorporated rubber flaps to limit the blade's range of motion and minimize vibrations.

The electronic control of this shutter system centers on an H-bridge configuration, which reverses the current flow in the motor upon receiving a trigger signal, causing the blade to alternate between open and closed positions. As shown in the left panel of Figure B.4, the full electronic design enables the control of four independent shutters, using an inverter chip and H-bridges, powered by a minimum 12 V supply. A TTL input signal of at least 1.5 V is used to change the voltage potential of each H-bridge, driving the motor to rotate either clockwise or counterclockwise. This configuration provides precise and independent control over each shutter.

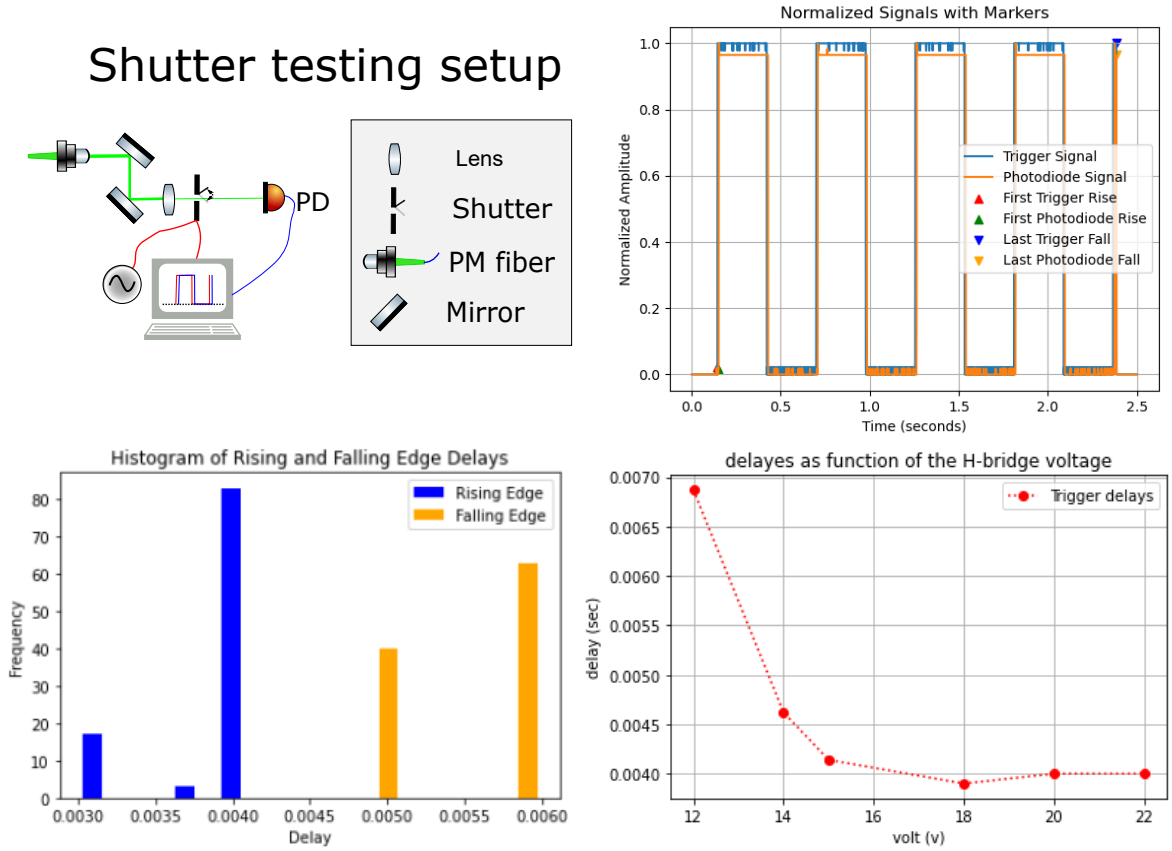


Figure B.5: Schematic of the shutter testing setup and the measured shutter response. The top-left panel depicts the optical setup: A laser beam passes through a series of optical elements and a mechanical shutter, controlled by an oscillating TTL trigger signal. The beam then reaches a PD, which provides an electrical signal that is recorded by an oscilloscope together with the shutter trigger signal. The top-right panel shows a plot of the normalized signals over time; the blue trace represents the TTL trigger signal, and the orange trace is the corresponding PD signal. The markers on the plot indicate the rising and falling edges of both the TTL signal and the PD signal. The bottom-left panel shows the histogram of the delays for both the rising and falling edges, displaying the distribution of these delays. The bottom-right panel displays the measured delays of the shutter, showing the dependence on the H-bridge voltage, which illustrates how we optimized the response of the system.

In our experimental setup, the mechanical shutters are strategically positioned along the beam paths of critical repumping and other auxiliary systems. For high-power light sources, additional layers of black anodized foil were added to the 3D-printed PLA housing to prevent heat-induced degradation. The electronic components of the system are powered by a single 18 V power supply, which is regulated and distributed to the motors, H-bridges, and the inverter.

The entire circuit is enclosed within a black anodized aluminum box, which houses eight TTL inputs and outputs (four of each). These inputs and outputs facilitate independent control of four mechanical shutters, and a representative image of such a box, along with a single mechanical shutter assembly, can be seen in the right panel of Figure B.4.

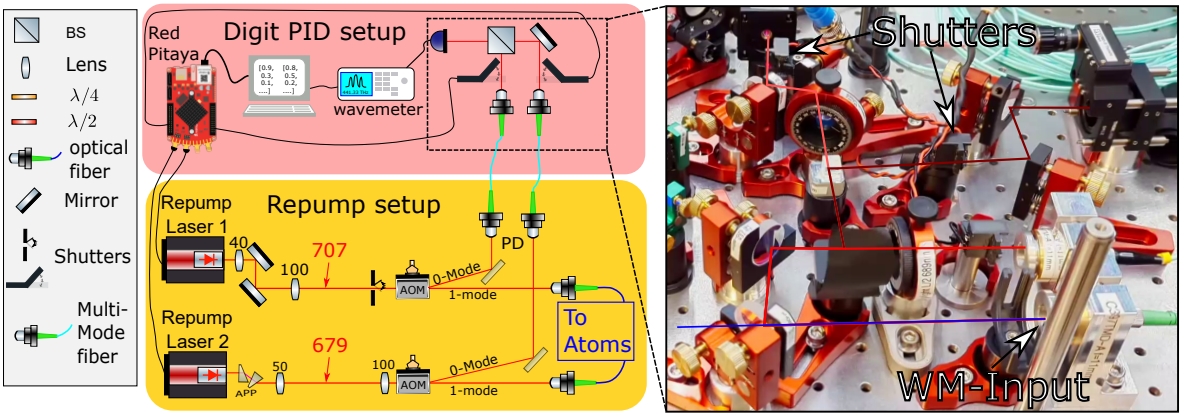


Figure B.6: Schematic and optical layout of the repumping and digital PID system. The left side of the figure shows an illustration of the optical setup containing two Toptica lasers and the associated optics, used to generate the 707.2 nm and 679 nm repumping beams. Each beam is guided through two AOMs, which produce a first-order diffracted beam sent to PM fibers aligned on the SC and a zero-order beam sent to multi-mode fibers used for simple alignment to the WM table. The image on the right panel shows the combined paths of the 460.8 nm blue laser (blue line), the 689 nm red laser (red line), the 707.2 nm repump laser (dark red line), and the 679 nm repump laser (light red line). Each beam path incorporates a mechanical shutter, remotely controlled by a trigger signal generated by a Red Pitaya, which allows control of which light reaches the WM input.

To evaluate the performance characteristics of the shutter system, a simple trigger and detection setup was designed and implemented. As shown in the top-left panel of Figure B.5, a pointer laser beam was directed through the shutter mechanism and onto a PD. Simultaneously, a trigger signal was sent to the shutter and an oscilloscope, which recorded both the trigger signal and the PD response. By analyzing the temporal delay between the trigger signal and the PD activation, the electronic parameters of the circuit, such as the TTL amplitude voltage and the voltage supplied to the H-bridge, were optimized. Additionally, the system was evaluated by collecting statistical data on the shutter's repetition rate, assessing whether delays exhibited variations over longer periods, and comparing the rise and fall times of the shutter response. Measurements were taken for several minutes under various conditions to analyze the effects of parameter changes.

As shown in the top-right panel of Figure B.5, a typical measurement for a specific parameter set shows the trigger and PD responses with the marked edges of each transition. We found that by manipulating the circuit parameters, the delay time could be tuned from 12 ms to 4 ms, which is an optimal point for our laboratory conditions. We also noted a dependence of the delay on the H-bridge voltage, although the most common signals we used (4.5 V and 3.3 V) gave similar delays. The bottom panels of Figure B.5 show how the H-bridge voltage affects the delay, and the statistical distribution of the rising and falling edge delays. It was also observed that increasing the voltage decreased the delay up to 18 V and that the rising and falling edges have different delay times, which may be related to the effect of gravity and the specific motor response. For our experimental setup, we optimized the parameters to a voltage of 18 V, together with a TTL trigger of 3.3 V - 4.5 V, which provided activation times below 4 ms.

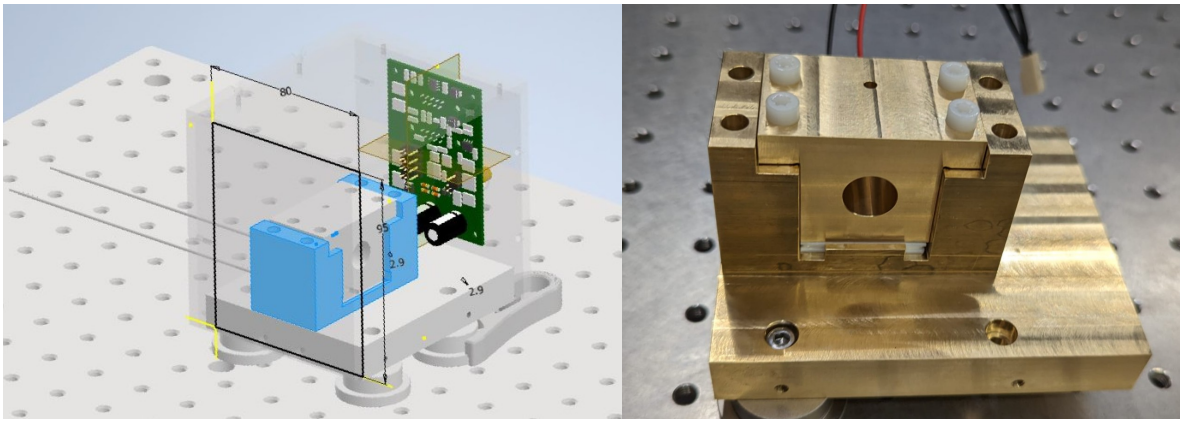


Figure B.7: The injection lock diode (ILD) module. The design of the ILD is shown both as an illustration and in a real image to show the final version.

## B.3 Red MOT injection lock diode design

As part of the red laser system, a new design of the housing for the injection lock diode (ILD) was made. The mount for the diode was made from brass material to improve thermal conductivity and was boxed with plastic-glass for external isolation. Using a simple electric breadboard and temperature and current controller *Thorlabs ITC-102*, the ILD was stabilized to around 20°C. The mount of the ILD was cooled by coupling it to a thermoelectric cooling (TEC) element, which transfers heat to a large brass plate below the TEC, which acts as a heat sink. The TEC was sandwiched between two custom-made parts, which are shown in Figure B.8 in a sketch. In Figure B.7, the full module for the ILD is presented to give an overview of how it is placed on the optical table.

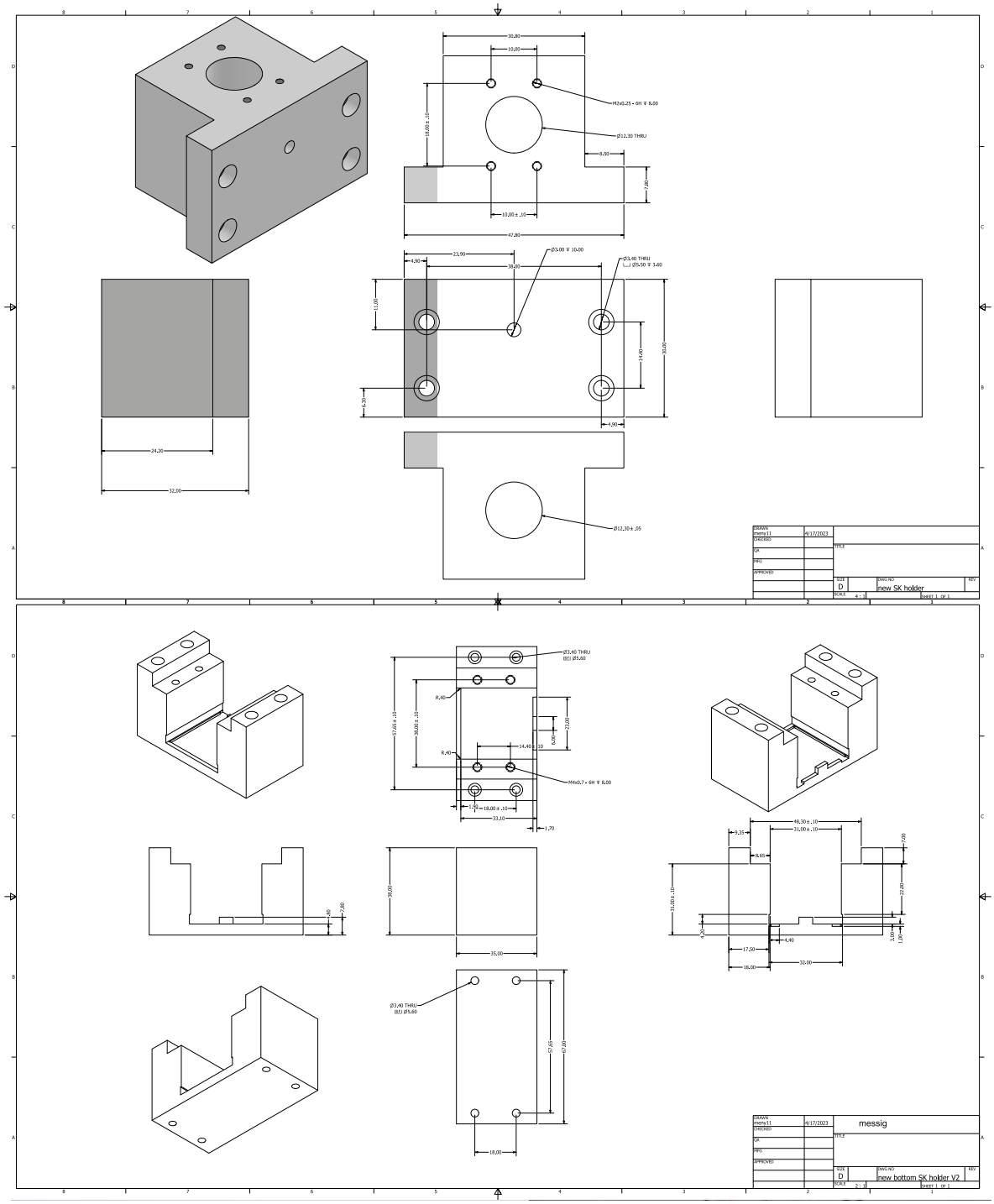


Figure B.8: The injection lock diode mount. The sketches of both the mount that holds the laser diode and the one that transfers heat to the brass plate. These bottom and top parts were carefully designed to place the TEC element to optimize heat conductivity.

# Appendix C

# novel ECDL for atomic Experiment

During the building of the blue 460.8 nm laser, which was meant for the Zeeman slower testing, an issue came to mind while testing the laser. To ensure single-mode operation within the initial cat-eye ECDL configuration, a back-reflecting optical component is employed to establish a cavity that forces the diode to operate in a single mode. The partially reflective mirror is affixed to a piezoelectric mount, allowing adjustments to the cavity length, facilitating the adjustment to a desired frequency, and compelling the laser to operate within that mode. To avoid replacing the reflecting partial mirror due to too much or too little seeding light, we designed and constructed a new type of ECDL cat-eye laser. The laser has tunability on the seeding, thus easing the coupling of the back-reflected light onto the diode. The ECDL, as shown in Figure C.1, is a monolithic casing with a designated mount for a cube PBS and a quarter waveplate. By placing a diode and a narrow band filter (0.5 nm) afterward, with a mirror attached to the piezo-electric mount, a cavity is formed that we can tune in size with voltage on the piezo. The two add-ons in the middle (PBS and waveplate) allow for power tuning by rotating the waveplate, which changes the polarization of the reflected beam from the mirror. By also tuning the mount of the LD, the power can be maximized after the first beam incident in the PBS by looking at the transmission after. This design is similar to a previous work [198], but with a much higher wavelength at 785 nm, our blue LD is inherently more difficult to stabilize due to its much smaller wavelength. Characterizing the laser, we start with the effect of changing the polarization of the reflected beam We set up our setup on the Laser table and placed a power meter to see how power is reflected using the cube and the $\lambda/4$ WP with the light passing twice through it, We observed how changing the angle affects the beam power outside the laser body. We can see in Figure C.2 on the top the periodic power change in percentage. The maximum power after the PBS is only 81%, meaning that the waveplate is not making a clean linear polarization before the PBS. The beam is then coupled to a wavemeter to observe a single-mode behavior.

We perform a linear ramp of the laser diode current and look at both ports of the laser body marked as $P_{1,2}$ as seen in the bottom of Figure C.1. We see in (b,c) plots the power from each port as a function of the diode current. By varying the waveplate, we can shift the threshold current for lasing, for both the bare signal (b) and the beam after passing twice through the PBS (c). It is clear that when sending too much power to the diode, the bare signal is decreasing, while in the output beam, we see an increase, probably from reflection from the diode itself. We observe optimal single-mode behavior when the first reflection $P_1$ is maximized. This point corresponds to about 29.6% (red line in Figure C.2 b) of feedback

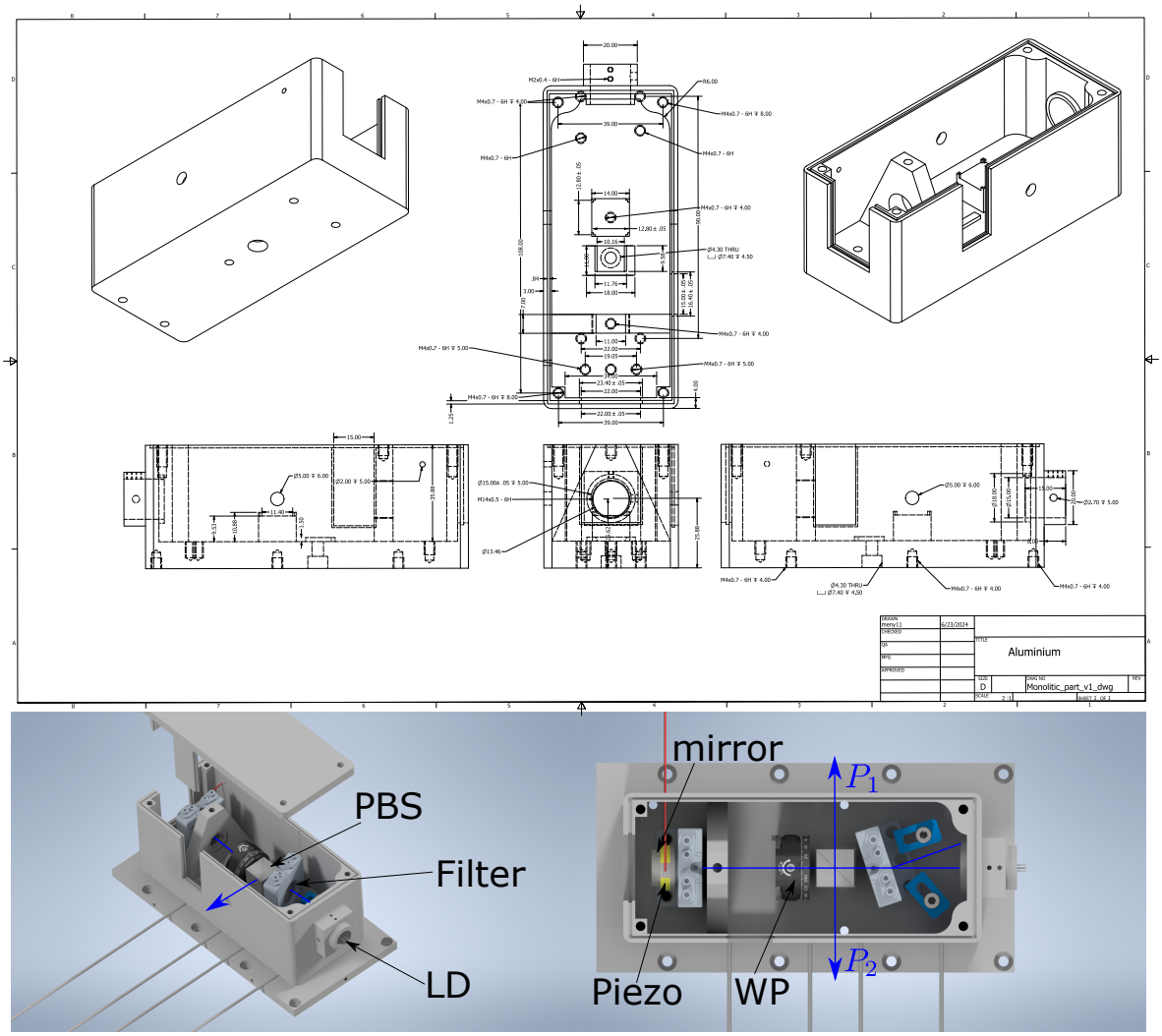


Figure C.1: The novel ECDL 2D sketch and 3D illustration. The sketches of the main body is shown in the top part (without the lid) that holds the LD and all other elements. On the bottom images are the side and top view of the inside of the ECDL with all the parts included.

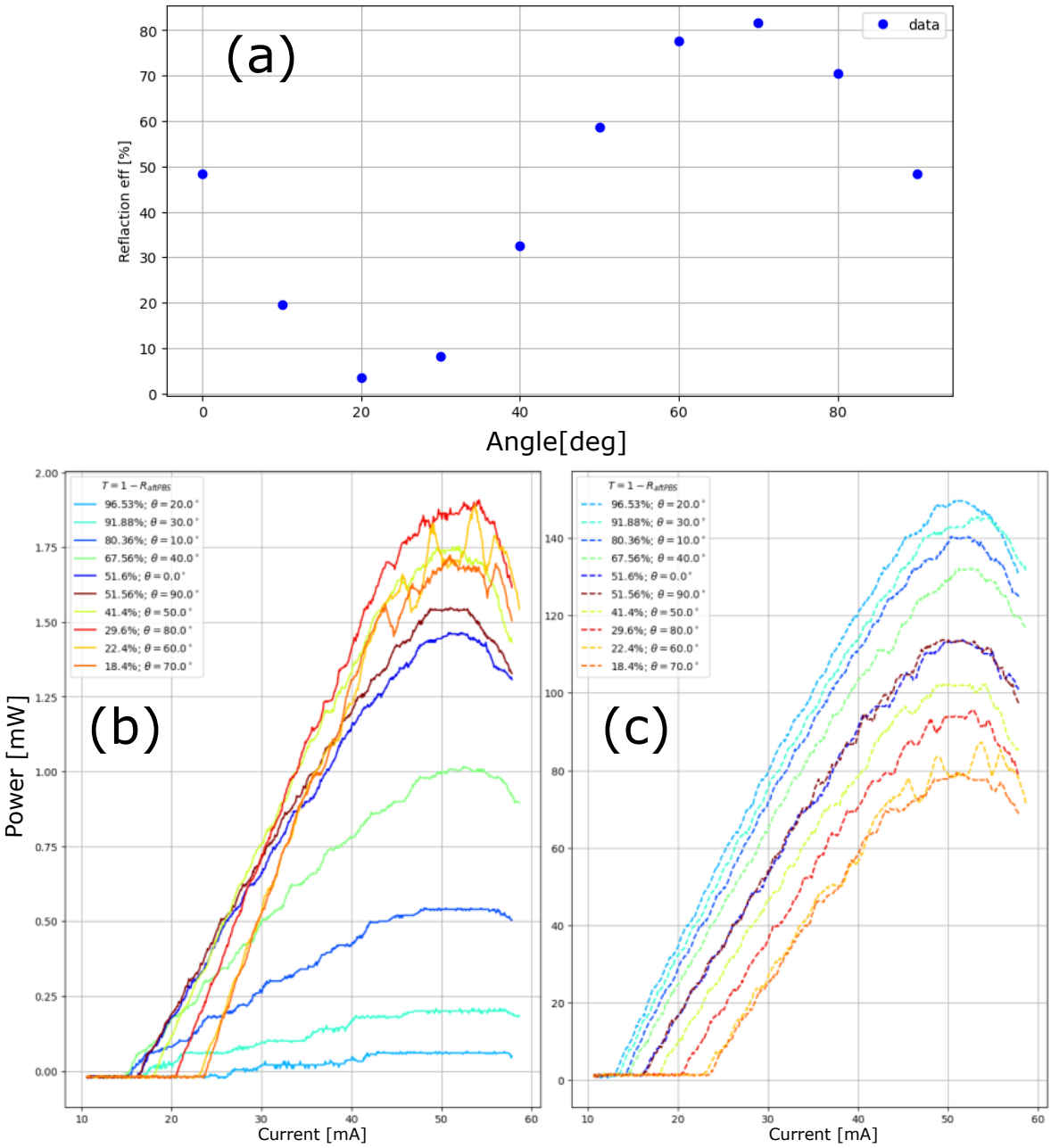


Figure C.2: Initial ECDL measurements. (a) The reflection of the beam after the PBS is normalized by the power before the mirror inside the ECDL. Both the mount that holds the laser diode and the one that transfers heat to the brass plate. These bottom and top parts were carefully designed to place the TEC element to optimize heat conductivity.

transmission sent back to the diode. This feedback is in good agreement with the other work [198], where they work with around 30% feedback light. The next step is to find the linewidth of the laser, to characterize the ECDL and see its spectrum. This can be done by measuring the spectral density of the laser [199], using a delayed self-heterodyne setup [200]. We followed

a testing setup similar to what *Toptica* is doing when testing their laser [201], however, we have not finished this measurement.

# References


[1] Alberto Zannoni. "On the quantization of the monoatomic ideal gas". In: *arXiv preprint cond-mat/9912229* (1999).

[2] Paul Adrien Maurice Dirac. "The quantum theory of the electron". In: *Proceedings of the Royal Society of London. Series A, Containing Papers of a Mathematical and Physical Character* 117.778 (1928), pp. 610–624.

[3] Robert M Ziff, George E Uhlenbeck, and Mark Kac. "The ideal Bose-Einstein gas, revisited". In: *Physics Reports* 32.4 (1977), pp. 169–248.

[4] Walther Meissner and Robert Ochsenfeld. "A new effect at the onset of superconductivity". In: *natural sciences* 21.44 (1933), pp. 787–788.

[5] K. v. Klitzing, G. Dorda, and M. Pepper. "New Method for High-Accuracy Determination of the Fine-Structure Constant Based on Quantized Hall Resistance". In: *Phys. Rev. Lett.* 45 (6 Aug. 1980), pp. 494–497. DOI: 10.1103/PhysRevLett.45.494. URL: https://link.aps.org/doi/10.1103/PhysRevLett.45.494.

[6] Kendall B Davis et al. "Bose-Einstein condensation in a gas of sodium atoms". In: *Physical review letters* 75.22 (1995), p. 3969.

[7] Brian DeMarco and Deborah S Jin. "Onset of Fermi degeneracy in a trapped atomic gas". In: *science* 285.5434 (1999), pp. 1703–1706.

[8] J. Bardeen. "Theory of the Meissner Effect in Superconductors". In: *Phys. Rev.* 97 (6 Mar. 1955), pp. 1724–1725. DOI: 10.1103/PhysRev.97.1724. URL: https://link.aps.org/doi/10.1103/PhysRev.97.1724.

[9] Leon N. Cooper. "Bound Electron Pairs in a Degenerate Fermi Gas". In: *Phys. Rev.* 104 (4 Nov. 1956), pp. 1189–1190. DOI: 10.1103/PhysRev.104.1189. URL: https://link.aps.org/doi/10.1103/PhysRev.104.1189.

[10] Stefano Giovanazzi, Axel Görlitz, and Tilman Pfau. "Tuning the Dipolar Interaction in Quantum Gases". In: *Phys. Rev. Lett.* 89 (13 Oct. 2002), p. 130401. DOI: 10.1103/PhysRevLett.89.130401. URL: https://link.aps.org/doi/10.1103/PhysRevLett.89.130401.

[11] Tilman Esslinger. "Fermi-Hubbard physics with atoms in an optical lattice". In: *Annu. Rev. Condens. Matter Phys.* 1.1 (2010), pp. 129–152.

[12] Eduardo Fradkin. *Field theories of condensed matter physics*. Cambridge University Press, 2013.

[13] E. Can Artun and A. Nihat Berker. "Spin-$s$ spin-glass phases in the $d = 3$ Ising model". In: *Phys. Rev. E* 104 (4 Oct. 2021), p. 044131. DOI: 10.1103/PhysRevE.104.044131. URL: https://link.aps.org/doi/10.1103/PhysRevE.104.044131.

[14] Eddy Timmermans et al. “Feshbach resonances in atomic Bose–Einstein condensates”. In: *Physics Reports* 315.1-3 (1999), pp. 199–230.

[15] Cheng Chin et al. “Feshbach resonances in ultracold gases”. In: *Reviews of Modern Physics* 82.2 (2010), pp. 1225–1286.

[16] Mohit Randeria, W Zwerger, and M Zwierlein. “The bcs–bec crossover and the unitary fermi gas”. In: *The BCS-BEC Crossover and the Unitary Fermi Gas*. Springer, 2011, pp. 1–32.

[17] Thomas Chalopin. “Optical superlattices in quantum gas microscopy”. In: *Nature Reviews Physics* 3.9 (2021), pp. 605–605.

[18] *Quantum science with optical tweezer arrays of ultracold atoms and molecules*. Nature. URL: https://www.nature.com/articles/s41567-021-01357-2.

[19] Seo Ho Youn et al. “Dysprosium magneto-optical traps”. In: *Phys. Rev. A* 82 (4 Oct. 2010), p. 043425. DOI: 10.1103/PhysRevA.82.043425. URL: https://link.aps.org/doi/10.1103/PhysRevA.82.043425.

[20] Quentin Lavigne, Thorsten Groh, and Simon Stellmer. “Magneto-optical trapping of mercury at high phase-space density”. In: *Phys. Rev. A* 105 (3 Mar. 2022), p. 033106. DOI: 10.1103/PhysRevA.105.033106. URL: https://link.aps.org/doi/10.1103/PhysRevA.105.033106.

[21] MV Romalis et al. “New limit on the permanent electric dipole moment of 199 Hg”. In: *Physical Review Letters* 86.12 (2001), p. 2505.

[22] Sebastian Will, Deepak Iyer, and Marcos Rigol. “Observation of coherent quench dynamics in a metallic many-body state of fermionic atoms”. In: *Nature communications* 6.1 (2015), p. 6009.

[23] Charles Kittel and Paul McEuen. *Introduction to solid state physics*. John Wiley & Sons, 2018.

[24] Harold J. Metcalf and Peter van der Straten. *Laser Cooling and Trapping*. Springer, 1999. DOI: 10.1007/978-1-4612-1568-2.

[25] Albert Einstein. “Quantum theory of the monatomic ideal gas”. In: *Sitzungsberichte der Preussischen Akademie der Wissenschaften, Physikalisch-mathematische Klasse* 261 (1924), p. 44.

[26] ECG Sudarshan. “The fundamental theorem on the relation between spin and statistics”. In: *Proceedings of the Indian Academy of Sciences-Section A*. Vol. 67. 5. Springer. 1968, pp. 284–293.

[27] Detlev Koester and Ganesar Chanmugam. “Physics of white dwarf stars”. In: *Reports on Progress in Physics* 53.7 (1990), p. 837.

[28] Raphael Jannin et al. “Pauli blocking of stimulated emission in a degenerate Fermi gas”. In: *Nature Communications* 13.1 (2022), p. 6479.

[29] Luigi De Marco et al. “A degenerate Fermi gas of polar molecules”. In: *Science* 363.6429 (2019), pp. 853–856.

[30] Simon Stellmer et al. “Bose-Einstein Condensation of Strontium”. In: *Phys. Rev. Lett.* 103 (20 Nov. 2009), p. 200401. DOI: 10.1103/PhysRevLett.103.200401. URL: https://link.aps.org/doi/10.1103/PhysRevLett.103.200401.

[31] Y. N. Martinez de Escobar et al. "Bose-Einstein Condensation of $^{84}$Sr". In: *Phys. Rev. Lett.* 103 (20 Nov. 2009), p. 200402. DOI: 10.1103/PhysRevLett.103.200402. URL: https://link.aps.org/doi/10.1103/PhysRevLett.103.200402.

[32] B. J. DeSalvo et al. "Degenerate Fermi Gas of $^{87}$Sr". In: *Phys. Rev. Lett.* 105 (3 July 2010), p. 030402. DOI: 10.1103/PhysRevLett.105.030402. URL: https://link.aps.org/doi/10.1103/PhysRevLett.105.030402.

[33] Franco Dalfovo et al. "Theory of Bose-Einstein condensation in trapped gases". In: *Rev. Mod. Phys.* 71 (3 Apr. 1999), pp. 463–512. DOI: 10.1103/RevModPhys.71.463. URL: https://link.aps.org/doi/10.1103/RevModPhys.71.463.

[34] Lev Pitaevskii and Sandro Stringari. *Bose-Einstein Condensation and Superfluidity*. Oxford University Press, Jan. 2016. ISBN: 9780198758884. DOI: 10.1093/acprof:oso/9780198758884.001.0001. URL: https://doi.org/10.1093/acprof:oso/9780198758884.001.0001.

[35] Wolfgang Ketterle and Martin W Zwierlein. "Making, probing and understanding ultracold Fermi gases". In: *La Rivista del Nuovo Cimento* 31.5 (2008), pp. 247–422.

[36] Stefano Giorgini, Lev P. Pitaevskii, and Sandro Stringari. "Theory of ultracold atomic Fermi gases". In: *Rev. Mod. Phys.* 80 (4 Oct. 2008), pp. 1215–1274. DOI: 10.1103/RevModPhys.80.1215. URL: https://link.aps.org/doi/10.1103/RevModPhys.80.1215.

[37] Andreas Trabesinger. "Quantum simulation". In: *Nature Physics* 8.4 (2012), pp. 263–263.

[38] Yunseong Nam et al. "Ground-state energy estimation of the water molecule on a trapped-ion quantum computer". In: *npj Quantum Information* 6.1 (2020), p. 33.

[39] Sepehr Ebadi et al. "Quantum phases of matter on a 256-atom programmable quantum simulator". In: *Nature* 595.7866 (2021), pp. 227–232.

[40] Gil Kalai, Yosef Rinott, and Tomer Shoham. "Questions and Concerns About Google's Quantum Supremacy Claim". In: *arXiv preprint arXiv:2305.01064* (2023).

[41] Frank Arute et al. "Quantum supremacy using a programmable superconducting processor". In: *Nature* 574.7779 (2019), pp. 505–510.

[42] Dolev Bluvstein et al. "Logical quantum processor based on reconfigurable atom arrays". In: *Nature* 626.7997 (2024), pp. 58–65.

[43] Wenchao Xu et al. "Fast Preparation and Detection of a Rydberg Qubit Using Atomic Ensembles". In: *Phys. Rev. Lett.* 127 (5 July 2021), p. 050501. DOI: 10.1103/PhysRevLett.127.050501. URL: https://link.aps.org/doi/10.1103/PhysRevLett.127.050501.

[44] Sepehr Ebadi et al. "Quantum optimization of maximum independent set using Rydberg atom arrays". In: *Science* 376.6598 (2022), pp. 1209–1215.

[45] Karen Wintersperger et al. "Neutral atom quantum computing hardware: performance and end-user perspective". In: *EPJ Quantum Technology* 10.1 (2023), p. 32.

[46] Fabian Böttcher et al. "Transient Supersolid Properties in an Array of Dipolar Quantum Droplets". In: *Phys. Rev. X* 9 (1 Mar. 2019), p. 011051. DOI: 10.1103/PhysRevX.9.011051. URL: https://link.aps.org/doi/10.1103/PhysRevX.9.011051.

[47] L. Chomaz et al. "Long-Lived and Transient Supersolid Behaviors in Dipolar Quantum Gases". In: *Phys. Rev. X* 9 (2 Apr. 2019), p. 021012. DOI: 10.1103/PhysRevX.9.021012. URL: https://link.aps.org/doi/10.1103/PhysRevX.9.021012.

[48] Vitaly L. Ginzburg. "Nobel Lecture: On superconductivity and superfluidity (what I have and have not managed to do) as well as on the "physical minimum" at the beginning of the XXI century". In: *Rev. Mod. Phys.* 76 (3 Dec. 2004), pp. 981–998. DOI: 10.1103/RevModPhys.76.981. URL: https://link.aps.org/doi/10.1103/RevModPhys.76.981.

[49] *Quantum simulations with ultracold atoms in optical lattices*. Science. URL: https://www.science.org/doi/10.1126/science.aal3837.

[50] Christian Gross and Waseem S Bakr. "Quantum gas microscopy for single atom and spin detection". In: *Nature Physics* 17.12 (2021), pp. 1316–1323.

[51] Waseem S Bakr et al. "A quantum gas microscope for detecting single atoms in a Hubbard-regime optical lattice". In: *Nature* 462.7269 (2009), pp. 74–77.

[52] Albert V Crewe, J Wall, and J Langmore. "Visibility of single atoms". In: *science* 168.3937 (1970), pp. 1338–1340.

[53] Lawrence W Cheuk et al. "Quantum-gas microscope for fermionic atoms". In: *Physical review letters* 114.19 (2015), p. 193001.

[54] C. Hölzl et al. "Motional ground-state cooling of single atoms in state-dependent optical tweezers". In: *Phys. Rev. Res.* 5 (3 Aug. 2023), p. 033093. DOI: 10.1103/PhysRevResearch.5.033093. URL: https://link.aps.org/doi/10.1103/PhysRevResearch.5.033093.

[55] Alexey V. Gorshkov et al. "Coherent Quantum Optical Control with Subwavelength Resolution". In: *Phys. Rev. Lett.* 100 (9 Mar. 2008), p. 093005. DOI: 10.1103/PhysRevLett.100.093005. URL: https://link.aps.org/doi/10.1103/PhysRevLett.100.093005.

[56] Hebin Li et al. "Optical imaging beyond the diffraction limit via dark states". In: *Phys. Rev. A* 78 (1 July 2008), p. 013803. DOI: 10.1103/PhysRevA.78.013803. URL: https://link.aps.org/doi/10.1103/PhysRevA.78.013803.

[57] Emil Wolf. *Progress in optics*. Vol. 47. Elsevier, 2005.

[58] Lin Su et al. "Fast single atom imaging for optical lattice arrays". In: *Nature Communications* 16.1 (2025), p. 1017.

[59] Martin W Zwierlein. "High-temperature superfluidity in an ultracold Fermi gas". PhD thesis. Massachusetts Institute of Technology, 2006.

[60] Elmar Haller et al. "Single-atom imaging of fermions in a quantum-gas microscope". In: *Nature Physics* 11.9 (2015), pp. 738–742.

[61] Philipp M. Preiss et al. "Quantum gas microscopy with spin, atom-number, and multilayer readout". In: *Phys. Rev. A* 91 (4 Apr. 2015), p. 041602. DOI: 10.1103/PhysRevA.91.041602. URL: https://link.aps.org/doi/10.1103/PhysRevA.91.041602.

[62] Martin Boll et al. "Spin-and density-resolved microscopy of antiferromagnetic correlations in Fermi-Hubbard chains". In: *Science* 353.6305 (2016), pp. 1257–1260.

[63] Richard T Scalettar. "An introduction to the Hubbard Hamiltonian". In: *Quantum materials: experiments and theory* 6 (2016).

[64] John Hubbard. "Electron correlations in narrow energy bands". In: *Proceedings of the Royal Society of London. Series A. Mathematical and Physical Sciences* 276.1365 (1963), pp. 238–257.

[65] Christian Hofrichter et al. "Direct Probing of the Mott Crossover in the SU($N$) Fermi-Hubbard Model". In: *Phys. Rev. X* 6 (2 June 2016), p. 021030. DOI: 10.1103/PhysRevX.6.021030. URL: https://link.aps.org/doi/10.1103/PhysRevX.6.021030.

[66] Alexey Vyacheslavovich Gorshkov et al. "Two-orbital SU (N) magnetism with ultracold alkaline-earth atoms". In: *Nature physics* 6.4 (2010), pp. 289–295.

[67] Miguel A Cazalilla and Ana Maria Rey. "Ultracold Fermi gases with emergent SU (N) symmetry". In: *Reports on Progress in Physics* 77.12 (2014), p. 124401.

[68] Shintaro Taie et al. "Realization of a SU (2)× SU (6) system of fermions in a cold atomic gas". In: *Physical review letters* 105.19 (2010), p. 190401.

[69] Lindsay Sonderhouse et al. "Thermodynamics of a deeply degenerate SU (N)-symmetric Fermi gas". In: *Nature Physics* 16.12 (2020), pp. 1216–1221.

[70] Daisuke Yamamoto and Katsuhiro Morita. "Engineering of a Low-Entropy Quantum Simulator for Strongly Correlated Electrons Using Cold Atoms with SU($\mathcal{N}$)-Symmetric Interactions". In: *Phys. Rev. Lett.* 132 (21 May 2024), p. 213401. DOI: 10.1103/PhysRevLett.132.213401. URL: https://link.aps.org/doi/10.1103/PhysRevLett.132.213401.

[71] Mingpu Qin et al. "Absence of Superconductivity in the Pure Two-Dimensional Hubbard Model". In: *Phys. Rev. X* 10 (3 July 2020), p. 031016. DOI: 10.1103/PhysRevX.10.031016. URL: https://link.aps.org/doi/10.1103/PhysRevX.10.031016.

[72] Robert Jördens et al. "A Mott insulator of fermionic atoms in an optical lattice". In: *Nature* 455.7210 (2008), pp. 204–207.

[73] Christian Hofrichter. "Probing the SU (N) Fermi-Hubbard model with ytterbium atoms in an optical lattice". PhD thesis. lmu, 2016.

[74] Thomas Chalopin et al. "Probing the magnetic origin of the pseudogap using a Fermi-Hubbard quantum simulator". In: *arXiv preprint arXiv:2412.17801* (2024).

[75] Martin Lebrat et al. "Observation of Nagaoka polarons in a Fermi–Hubbard quantum simulator". In: *Nature* 629.8011 (2024), pp. 317–322.

[76] Muqing Xu et al. "A neutral-atom Hubbard quantum simulator in the cryogenic regime". In: *arXiv preprint arXiv:2502.00095* (2025).

[77] Eduardo Ibarra-García-Padilla and Sayan Choudhury. "Many-body physics of ultracold alkaline-earth atoms with SU (N)-symmetric interactions". In: *Journal of Physics: Condensed Matter* 37.8 (2024), p. 083003.

[78] G. Pasqualetti et al. "Equation of State and Thermometry of the 2D SU($N$) Fermi-Hubbard Model". In: *Phys. Rev. Lett.* 132 (8 Feb. 2024), p. 083401. DOI: 10.1103/PhysRevLett.132.083401. URL: https://link.aps.org/doi/10.1103/PhysRevLett.132.08340.

[79] Miguel A Cazalilla, AF Ho, and M Ueda. "Ultracold gases of ytterbium: ferromagnetism and Mott states in an SU (6) Fermi system". In: *New Journal of Physics* 11.10 (2009), p. 103033.

[80] Congjun Wu. "Hidden symmetry and quantum phases in spin-3/2 cold atomic systems". In: *Modern Physics Letters B* 20.27 (2006), pp. 1707–1738.

[81] Salvatore R Manmana et al. "SU (N) magnetism in chains of ultracold alkaline-earth-metal atoms: Mott transitions and quantum correlations". In: *Physical Review A—Atomic, Molecular, and Optical Physics* 84.4 (2011), p. 043601.

[82] Arun Paramekanti and J Brad Marston. "SU (N) quantum spin models: a variational wavefunction study". In: *Journal of Physics: Condensed Matter* 19.12 (2007), p. 125215.

[83] Shintaro Taie et al. "An SU (6) Mott insulator of an atomic Fermi gas realized by large-spin Pomeranchuk cooling". In: *Nature Physics* 8.11 (2012), pp. 825–830.

[84] Simon Stellmer, Florian Schreck, and Thomas C Killian. "Degenerate quantum gases of strontium". In: *Annual Review of Cold Atoms and Molecules* (2014), pp. 1–80.

[85] Sandra Buob et al. "A Strontium Quantum-Gas Microscope". In: *PRX Quantum* 5 (2 Apr. 2024), p. 020316. DOI: 10.1103/PRXQuantum.5.020316. URL: https://link.aps.org/doi/10.1103/PRXQuantum.5.020316.

[86] Vladislav Gavryusev et al. "A new programmable quantum simulator with strontium rydberg atoms in optical tweezer arrays". In: *Quantum 2.0*. Optica Publishing Group. 2024, QTh2A–2.

[87] Shahir Masri et al. "Toxicant-induced loss of tolerance for chemicals, foods, and drugs: assessing patterns of exposure behind a global phenomenon". In: *Environmental Sciences Europe* 33.1 (2021), pp. 1–19.

[88] BL Tiller. "4.5 Fish and Wildlife Surveillance". In: *UNITED STATES DEPARTMENT OF ENERGY under Contract DE-AC06-76RL01830* (2001).

[89] Jan Trautmann. "The magnetic quadrupole transition in neutral strontium". PhD thesis. lmu, 2022.

[90] Mi Yan et al. "Controlling Condensate Collapse and Expansion with an Optical Feshbach Resonance". In: *Phys. Rev. Lett.* 110 (12 Mar. 2013), p. 123201. DOI: 10.1103/PhysRevLett.110.123201. URL: https://link.aps.org/doi/10.1103/PhysRevLett.110.123201.

[91] P Frank Winkler et al. "Magnetic moment of the proton in Bohr magnetons". In: *Physical Review A* 5.1 (1972), p. 83.

[92] Simon Stellmer, Rudolf Grimm, and Florian Schreck. "Detection and manipulation of nuclear spin states in fermionic strontium". In: *Phys. Rev. A* 84 (4 Oct. 2011), p. 043611. DOI: 10.1103/PhysRevA.84.043611. URL: https://link.aps.org/doi/10.1103/PhysRevA.84.043611.

[93] Martin M Boyd. "High precision spectroscopy of strontium in an optical lattice: Towards a new standard for frequency and time". PhD thesis. University of Colorado at Boulder, 2007.

[94] Alexandre Cooper et al. "Alkaline-earth atoms in optical tweezers". In: *Physical Review X* 8.4 (2018), p. 041055.

[95] HGC Werij et al. "Oscillator strengths and radiative branching ratios in atomic Sr". In: *Physical Review A* 46.3 (1992), p. 1248.

[96] Xinye Xu et al. "Cooling and trapping of atomic strontium". In: *JOSA B* 20.5 (2003), pp. 968–976.

[97] LR Hunter, WA Walker, and David Scott Weiss. "Observation of an atomic stark–electric-quadrupole interference". In: *Physical review letters* 56.8 (1986), p. 823.

[98] Jens Samland et al. "Optical pumping of 5 s 4 d 1 D 2 strontium atoms for laser cooling and imaging". In: *Physical Review Research* 6.1 (2024), p. 013319.

[99] Tomoya Akatsuka et al. "Three-stage laser cooling of Sr atoms using the 5 s 5 p P 2 3 metastable state below Doppler temperatures". In: *Physical Review A* 103.2 (2021), p. 023331.

[100] Roman Schwarz et al. "Long term measurement of the Sr87 clock frequency at the limit of primary Cs clocks". In: *Physical Review Research* (2020). URL: https://api.semanticscholar.org/CorpusID:218665271.

[101] Andrew D. Ludlow et al. "Systematic Study of the $^{87}$Sr Clock Transition in an Optical Lattice". In: *Phys. Rev. Lett.* 96 (3 Jan. 2006), p. 033003. DOI: 10.1103/PhysRevLett.96.033003. URL: https://link.aps.org/doi/10.1103/PhysRevLett.96.033003.

[102] Martin M. Boyd et al. "Nuclear spin effects in optical lattice clocks". In: *Phys. Rev. A* 76 (2 Aug. 2007), p. 022510. DOI: 10.1103/PhysRevA.76.022510. URL: https://link.aps.org/doi/10.1103/PhysRevA.76.022510.

[103] Karl N Blodgett et al. "Imaging a Li 6 atom in an optical tweezer 2000 times with $\lambda$-enhanced gray molasses". In: *Physical Review Letters* 131.8 (2023), p. 083001.

[104] D. C. McKay et al. "Low-temperature high-density magneto-optical trapping of potassium using the open $4S \rightarrow 5P$ transition at 405 nm". In: *Phys. Rev. A* 84 (6 Dec. 2011), p. 063420. DOI: 10.1103/PhysRevA.84.063420. URL: https://link.aps.org/doi/10.1103/PhysRevA.84.063420.

[105] Jan Trautmann et al. "S 0 1-P 2 3 magnetic quadrupole transition in neutral strontium". In: *Physical Review Research* 5.1 (2023), p. 013219.

[106] A. Heinz et al. "State-Dependent Optical Lattices for the Strontium Optical Qubit". In: *Phys. Rev. Lett.* 124 (20 May 2020), p. 203201. DOI: 10.1103/PhysRevLett.124.203201. URL: https://link.aps.org/doi/10.1103/PhysRevLett.124.203201.

[107] A Lurio, M Mandel, and R Novick. "Second-order hyperfine and zeeman corrections for an (sl) configuration". In: *Physical Review* 126.5 (1962), p. 1758.

[108] G Breit and Lawrence A Wills. "Hyperfine structure in intermediate coupling". In: *Physical Review* 44.6 (1933), p. 470.

[109] H -Jürgen Kluge and Hatto Sauter. "Levelcrossing experiments in the first excited 1 P 1 states of the alkaline earths". In: *Zeitschrift für Physik* 270 (1974), pp. 295–309.

[110] P Grundevik et al. "Radio-frequency and laser spectroscopy studies of low-lying states in SrI". In: *Zeitschrift für Physik A Atoms and Nuclei* 311 (1983), pp. 143–149.

[111] Irene Courtillot. "Première observation de la transition fortement interdite 1S0-3P0 du Strontium, pour une horloge optique à atomes piégés". PhD thesis. Université Pierre et Marie Curie-Paris VI, 2003.

[112] Stephan M Heider and Gilbert O Brink. "Hyperfine structure of Sr 87 in the P 2 3 metastable state". In: *Physical Review A* 16.4 (1977), p. 1371.

[113] Wenhui Li, Paul J. Tanner, and T. F. Gallagher. "Dipole-Dipole Excitation and Ionization in an Ultracold Gas of Rydberg Atoms". In: *Phys. Rev. Lett.* 94 (17 May 2005), p. 173001. DOI: 10.1103/PhysRevLett.94.173001. URL: https://link.aps.org/doi/10.1103/PhysRevLett.94.173001.

[114] C. Hölzl et al. "Long-Lived Circular Rydberg Qubits of Alkaline-Earth Atoms in Optical Tweezers". In: *Phys. Rev. X* 14 (2 May 2024), p. 021024. DOI: 10.1103/PhysRevX.14.021024. URL: https://link.aps.org/doi/10.1103/PhysRevX.14.021024.

[115] Théo DARDIER. "An optical tweezeres setup for a new Rydberg atom array experiment to quantum simulate lattice gauge theories". In: *Internship report, École Normale Supérieure Paris-Saclay, Institut de Ciències Fotòniques (ICFO), Barcelona* (2024).

[116] Giulia Semeghini et al. "Probing topological spin liquids on a programmable quantum simulator". In: *Science* 374.6572 (2021), pp. 1242–1247.

[117] Hannes Bernien et al. "Probing many-body dynamics on a 51-atom quantum simulator". In: *Nature* 551.7682 (2017), pp. 579–584.

[118] MA Norcia, AW Young, and AM Kaufman. "Microscopic control and detection of ultracold strontium in optical-tweezer arrays". In: *Physical Review X* 8.4 (2018), p. 041054.

[119] Masao Takamoto et al. "An optical lattice clock". In: *Nature* 435.7040 (2005), pp. 321–324.

[120] André Heinz et al. "State-dependent optical lattices for the strontium optical qubit". In: *Physical review letters* 124.20 (2020), p. 203201.

[121] W. Bowden et al. "Rydberg electrometry for optical lattice clocks". In: *Phys. Rev. A* 96 (2 Aug. 2017), p. 023419. DOI: 10.1103/PhysRevA.96.023419. URL: https://link.aps.org/doi/10.1103/PhysRevA.96.023419.

[122] Yang Chen et al. "Characterization of the magnetic field through the three-body loss near a narrow Feshbach resonance". In: *Phys. Rev. A* 103 (6 Sept. 2021), p. 063311. DOI: 10.1103/PhysRevA.103.063311. URL: https://link.aps.org/doi/10.1103/PhysRevA.103.063311.

[123] M. W. J. Romans and H. T. C. Stoof. "Bogoliubov theory of Feshbach molecules in the BEC-BCS crossover". In: *Phys. Rev. A* 74 (5 Nov. 2006), p. 053618. DOI: 10.1103/PhysRevA.74.053618. URL: https://link.aps.org/doi/10.1103/PhysRevA.74.053618.

[124] Y. N. Martinez de Escobar et al. "Two-photon photoassociative spectroscopy of ultracold $^{88}$Sr". In: *Phys. Rev. A* 78 (6 Dec. 2008), p. 062708. DOI: 10.1103/PhysRevA.78.062708. URL: https://link.aps.org/doi/10.1103/PhysRevA.78.062708.

[125] Yenny Natali Martinez de Escolar. "Bose-Einstein condensation of Strontium-84". In: *Ph. D. Thesis* (2010).

[126] Viatcheslav Kokoouline, Robin Santra, and Chris H Greene. "Multichannel cold collisions between metastable Sr atoms". In: *Physical Review Letters* 90.25 (2003), p. 253201.

[127] André Heinz. "Ultracold strontium in state-dependent optical lattices". PhD thesis. Ludwig Maximilians Universität München, 2020.

[128] Ivaylo Sashkov Madjarov. "Entangling, Controlling, and Detecting Individual Strontium Atoms in Optical Tweezer Arrays". In: (Jan. 2021). DOI: 10.7907/d1em-dt34.

[129] AOsense. *AOSense Cold Atomic Beam System Datasheet*. Available at: https://aosense.com/wp-content/uploads/2023/05/AOSense-Cold-Atomic-Beam-System-2023.pdf. 2023.

[130] Todd L Gustavson. "Cold Atom Gyros". In: *IEEE Sensors*. 2013.

[131] Moglabs. *Moglabs LDL Datasheet*. Available at: https://www.moglabs.com/products/tunable-lasers/littrow-lasers/MOGLabs_LDL_enhanced_A4_20220428.pdf. 2022.

[132] wieserlabs. *WL-FlexDDS-NG Rack Rack For Multi-Channel Agile Radio Frequency Source Datasheet*. Available at: https://www.wieserlabs.com/products/radio-frequency/flexdds-ng/WL-FlexDDS-NG-Rack-datasheet.pdf. 2024.

[133] I. Dede et al. *Development of an RF-driver for Acousto-optic Modulators*. Universität Hamburg, 2022. URL: https://books.google.de/books?id=6myvzwEACAAJ.

[134] X. Baillard A. Gauguet S. Bize P. Lemonde Ph. Laurent A. Clairon P. Rosenbusch. "Interference-filter-stabilized external-cavity diode lasers". In: (May 2006). DOI: https://doi.org/10.48550/arXiv.physics/0605046.

[135] P. W. Milonni and J. H. Eberly. "Lasers". In: New York, NY: John Wiley and Sons, 1988, p. 302.

[136] Eric David and Jean-Marie Gagne. "Frequency locking of laser diode using metallic vapor optogalvanic spectrum: UI". In: *Applied optics* 29.30 (1990), pp. 4489–4493.

[137] R. Wynands and A. Nagel. "Precision spectroscopy with coherent dark states". In: *Applied Physics B* 68 (1999), pp. 1–25.

[138] JF Eble and Ferdinand Schmidt-Kaler. "Optimization of frequency modulation transfer spectroscopy on the calcium 4 1 S 0 to 4 1 P 1 transition". In: *Applied Physics B* 88 (2007), pp. 563–568.

[139] DJ McCarron, SA King, and SL Cornish. "Modulation transfer spectroscopy in atomic rubidium". In: *Measurement science and technology* 19.10 (2008), p. 105601.

[140] Esa Jaatinen. "Theoretical determination of maximum signal levels obtainable with modulation transfer spectroscopy". In: *Optics Communications* 120.1-2 (1995), pp. 91–97.

[141] Tadas Pyragius. "Developing and building an absorption imaging system for Ultracold Atoms". In: *arXiv preprint arXiv:1209.3408* (2012).

[142] Christopher J Foot. *Atomic physics*. Vol. 7. Oxford university press, 2005.

[143] Elizabeth A Donley, Thomas P Heavner, and Steven R Jefferts. "Optical molasses loaded from a low-velocity intense source of atoms: an atom source for improved atomic fountains". In: *IEEE transactions on instrumentation and measurement* 54.5 (2005), pp. 1905–1910.

[144] William D Phillips and Harold Metcalf. "Laser deceleration of an atomic beam". In: *Physical Review Letters* 48.9 (1982), p. 596.

[145] Ryoto Takeuchi et al. "Continuous outcoupling of ultracold strontium atoms combining three different traps". In: *Applied Physics Express* 16.4 (2023), p. 042003.

[146] CH Feng et al. "High flux strontium atom source". In: *Quantum Science and Technology* 9.2 (2024), p. 025017.

[147] Oleksiy Onishchenko et al. “Frequency of the ultranarrow S-1 (0)-P-3 (2) transition in Sr-87”. In: *PHYSICAL REVIEW A* 99.5 (2019).

[148] Masami Yasuda and Hidetoshi Katori. “Lifetime measurement of the P 2 3 metastable state of strontium atoms”. In: *Physical review letters* 92.15 (2004), p. 153004.

[149] Simon Stellmer, Rudolf Grimm, and Florian Schreck. “Production of quantum-degenerate strontium gases”. In: *Physical Review A—Atomic, Molecular, and Optical Physics* 87.1 (2013), p. 013611.

[150] Irene Courtillot et al. “Accurate spectroscopy of Sr atoms”. In: *The European Physical Journal D-Atomic, Molecular, Optical and Plasma Physics* 33.2 (2005), pp. 161–171.

[151] Jun Ye et al. “Precision measurement based on ultracold atoms and cold molecules”. In: *International Journal of Modern Physics D* 16.12b (2007), pp. 2481–2494.

[152] KR Vogel et al. “Narrow line cooling of strontium to the recoil limit”. In: *1998 Conference on Precision Electromagnetic Measurements Digest (Cat. No. 98CH36254)*. IEEE. 1998, pp. 303–304.

[153] Wolfgang Ketterle and NJ Van Druten. “Evaporative cooling of trapped atoms”. In: *Advances in atomic, molecular, and optical physics*. Vol. 37. Elsevier, 1996, pp. 181–236.

[154] C. J. Myatt et al. “Production of Two Overlapping Bose-Einstein Condensates by Sympathetic Cooling”. In: *Phys. Rev. Lett.* 78 (4 Jan. 1997), pp. 586–589. DOI: 10.1103/PhysRevLett.78.586. URL: https://link.aps.org/doi/10.1103/PhysRevLett.78.586.

[155] Paul D. Lett et al. “Observation of Atoms Laser Cooled below the Doppler Limit”. In: *Phys. Rev. Lett.* 61 (2 July 1988), pp. 169–172. DOI: 10.1103/PhysRevLett.61.169. URL: https://link.aps.org/doi/10.1103/PhysRevLett.61.169.

[156] Shayne Bennetts et al. “Steady-state magneto-optical trap with 100-fold improved phase-space density”. In: *Physical review letters* 119.22 (2017), p. 223202.

[157] Thomas H Loftus et al. “Narrow line cooling and momentum-space crystals”. In: *Physical Review A—Atomic, Molecular, and Optical Physics* 70.6 (2004), p. 063413.

[158] Y Castin, H Wallis, and Jean Dalibard. “Limit of Doppler cooling”. In: *JOSA B* 6.11 (1989), pp. 2046–2057.

[159] H Wallis and W Ertmer. “Broadband laser cooling on narrow transitions”. In: *JOSA B* 6.11 (1989), pp. 2211–2219.

[160] Hidetoshi Katori et al. “Magneto-optical trapping and cooling of strontium atoms down to the photon recoil temperature”. In: *Physical Review Letters* 82.6 (1999), p. 1116.

[161] Ben-quan Lu et al. “Experimental Determination of the Landé g-Factors for 5s2 1S and 5s5p 3P States of the 87Sr Atom”. In: *Chinese Physics Letters* 35.4 (2018), p. 043203.

[162] K Berg-Sorenson et al. “Momentum diffusion of atoms moving in laser fields”. In: *Journal of Physics B: Atomic, Molecular and Optical Physics* 25.20 (1992), p. 4195.

[163] Lars Fischer. “Developing Laser Frequency Stabilization Systems for a Novel Strontium Quantum Simulation Platform”. Universität Hamburg, 2021.

[164] James I Thorpe, K Numata, and J Livas. "Laser frequency stabilization and control through offset sideband locking to optical cavities". In: *Optics express* 16.20 (2008), pp. 15980–15990.

[165] Ziting Chen et al. "Active control of a diode laser with injection locking using a laser line filter". In: *Review of Scientific Instruments* 92.12 (2021).

[166] I Manai et al. "Shelving spectroscopy of the strontium intercombination line". In: *Journal of Physics B: Atomic, Molecular and Optical Physics* 53.8 (2020), p. 085005.

[167] Jonatan Höschele et al. "Atom-Number Enhancement by Shielding Atoms From Losses in Strontium Magneto-Optical Traps". In: *Phys. Rev. Appl.* 19 (6 June 2023), p. 064011. DOI: 10.1103/PhysRevApplied.19.064011. URL: https://link.aps.org/doi/10.1103/PhysRevApplied.19.064011.

[168] Arthur Ashkin et al. "Observation of a single-beam gradient force optical trap for dielectric particles". In: *Optics letters* 11.5 (1986), pp. 288–290.

[169] Rudolf Grimm, Matthias Weidemüller, and Yurii B Ovchinnikov. "Optical dipole traps for neutral atoms". In: *Advances in atomic, molecular, and optical physics*. Vol. 42. Elsevier, 2000, pp. 95–170.

[170] Shengnan Zhang et al. "Blue-detuned Optical Lattice for Sr Long-range Interactions". In: *2022 Joint Conference of the European Frequency and Time Forum and IEEE International Frequency Control Symposium (EFTF/IFCS)*. IEEE. 2022, pp. 1–3.

[171] Joji Joykutty et al. "Direct Measurement of the Oscillation Frequency in an Optical-Tweezers Trap by Parametric Excitation". In: *Physical review letters* 95.19 (2005), p. 193902.

[172] T. A. Savard, K. M. O'Hara, and J. E. Thomas. "Laser-noise-induced heating in far-off resonance optical traps". In: *Phys. Rev. A* 56 (2 Aug. 1997), R1095–R1098. DOI: 10.1103/PhysRevA.56.R1095. URL: https://link.aps.org/doi/10.1103/PhysRevA.56.R1095.

[173] X. Baillard et al. "Interference-filter-stabilized external-cavity diode lasers". In: *Optics Communications* 266.2 (2006), pp. 609–613. ISSN: 0030-4018. DOI: https://doi.org/10.1016/j.optcom.2006.05.011. URL: https://www.sciencedirect.com/science/article/pii/S0030401806004561.

[174] Tino Weber et al. "Bose-Einstein condensation of cesium". In: *Science* 299.5604 (2003), pp. 232–235.

[175] DM Stamper-Kurn et al. "Reversible formation of a Bose-Einstein condensate". In: *Physical review letters* 81.11 (1998), p. 2194.

[176] SP Bennetts et al. "1000 times closer to a continuous atom laser: Steady-state strontium with unity phase-space density". In: (2019).

[177] RA Williams et al. "Dynamic optical lattices: two-dimensional rotating and accordion lattices for ultracold atoms". In: *Optics Express* 16.21 (2008), pp. 16977–16983.

[178] Govind Unnikrishnan et al. "Coherent control of the fine-structure qubit in a single alkaline-earth atom". In: *Physical Review Letters* 132.15 (2024), p. 150606.

[179] Masao Takamoto and Hidetoshi Katori. "Spectroscopy of the $^1S_0$–$^3P_0$ Clock Transition of $^{87}$Sr in an Optical Lattice". In: *Phys. Rev. Lett.* 91 (22 Nov. 2003), p. 223001. DOI: 10.1103/PhysRevLett.91.223001. URL: https://link.aps.org/doi/10.1103/PhysRevLett.91.223001.

[180] JL Ville et al. "Loading and compression of a single two-dimensional Bose gas in an optical accordion". In: *Physical Review A* 95.1 (2017), p. 013632.

[181] Klaus Hueck et al. "Two-dimensional homogeneous Fermi gases". In: *Physical Review Letters* 120.6 (2018), p. 060402.

[182] Gregory Alan Phelps. "A dipolar quantum gas microscope". PhD thesis. Harvard University, 2019.

[183] Andrea Bergschneider et al. "Spin-resolved single-atom imaging of $^6$Li in free space". In: *Phys. Rev. A* 97 (6 June 2018), p. 063613. DOI: 10.1103/PhysRevA.97.063613. URL: https://link.aps.org/doi/10.1103/PhysRevA.97.063613.

[184] Horst Schmidt-Bocking et al. "The stern-gerlach experiment revisited". In: *The European Physical Journal H* 41 (2016), pp. 327–364.

[185] Alexander Urech et al. "Narrow-line imaging of single strontium atoms in shallow optical tweezers". In: *Phys. Rev. Res.* 4 (2 June 2022), p. 023245. DOI: 10.1103/PhysRevResearch.4.023245. URL: https://link.aps.org/doi/10.1103/PhysRevResearch.4.023245.

[186] Andrii Sotnikov. "Critical entropies and magnetic-phase-diagram analysis of ultracold three-component fermionic mixtures in optical lattices". In: *Physical Review A* 92.2 (2015), p. 023633.

[187] Congjun Wu and Shou-Cheng Zhang. "Sufficient condition for absence of the sign problem in the fermionic quantum Monte Carlo algorithm". In: *Phys. Rev. B* 71 (15 Apr. 2005), p. 155115. DOI: 10.1103/PhysRevB.71.155115. URL: https://link.aps.org/doi/10.1103/PhysRevB.71.155115.

[188] Emanuel Gull et al. "Continuous-time Monte Carlo methods for quantum impurity models". In: *Rev. Mod. Phys.* 83 (2 May 2011), pp. 349–404. DOI: 10.1103/RevModPhys.83.349. URL: https://link.aps.org/doi/10.1103/RevModPhys.83.349.

[189] Andrii Sotnikov and Walter Hofstetter. "Magnetic ordering of three-component ultracold fermionic mixtures in optical lattices". In: *Physical Review A* 89.6 (2014), p. 063601.

[190] Tamás A Tóth et al. "Three-Sublattice Ordering of the SU (3) Heisenberg Model of Three-Flavor Fermions on the Square and Cubic Lattices". In: *Physical review letters* 105.26 (2010), p. 265301.

[191] Antoine Georges et al. "Dynamical mean-field theory of strongly correlated fermion systems and the limit of infinite dimensions". In: *Rev. Mod. Phys.* 68 (1 Jan. 1996), pp. 13–125. DOI: 10.1103/RevModPhys.68.13. URL: https://link.aps.org/doi/10.1103/RevModPhys.68.13.

[192] RW Helmes, TA Costi, and A Rosch. "Mott transition of fermionic atoms in a three-dimensional optical trap". In: *Physical review letters* 100.5 (2008), p. 056403.

[193] A. H. MacDonald, S. M. Girvin, and D. Yoshioka. "$\frac{t}{U}$ expansion for the Hubbard model". In: *Phys. Rev. B* 37 (16 June 1988), pp. 9753–9756. DOI: 10.1103/PhysRevB.37.9753. URL: https://link.aps.org/doi/10.1103/PhysRevB.37.9753.

[194] Howard Georgi. *Lie algebras in particle physics: from isospin to unified theories*. Taylor & Francis, 2000.

[195] Munich lithium group. *Build an EOM - Lithium*. PDF file attached to the project. https://www.quantum-munich.de/16130/Lithium-Quantum-Gas-Microscope. 2023.

[196] T. Satogata. "Oscillators, Resonances, and Lorentzians". In: *USPAS Accelerator Physics* (2013).

[197] Grace H Zhang et al. "Note: Fast compact laser shutter using a direct current motor and three-dimensional printing". In: *Review of Scientific Instruments* 86.12 (2015).

[198] Daniel J Thompson and Robert E Scholten. "Narrow linewidth tunable external cavity diode laser using wide bandwidth filter". In: *Review of scientific instruments* 83.2 (2012).

[199] wikipida. *Spectral density*. Available at: https://en.wikipedia.org/wiki/Spectral_density. 2024.

[200] Linden B Mercer. "1/f frequency noise effects on self-heterodyne linewidth measurements". In: *Journal of Lightwave Technology* 9.4 (1991), pp. 485–493.

[201] Toptica. *Toptica LINEWIDTH MEASUREMENT OF DIODE LASERS*. Available at: https://www.toptica.com/fileadmin/Editors_English/04_applications/10_application_notes/05_Linewidth_Measurement_of_Diode_Lasers/Linewidth-measurements-of-diode-lasers.pdf. 2023.